

UNIVERSIDADE DE SÃO PAULO

INSTITUTO DE QUÍMICA

**Graduate Program of Chemistry**

**LAÍSE MOURA FURTADO**

**Interactions between polydopamine and cellulose derivatives:  
Physicochemical aspects and applications**

Original version of the defended Thesis

**São Paulo**

The deposit date at the SPG

**20/06/2023**

Laíse Moura Furtado

Interactions between polydopamine and cellulose derivatives:  
Physicochemical aspects and applications

*Thesis presented at the Institute of Chemistry of the University  
of São Paulo to obtain the degree of Doctor in Chemistry.*

*Supervisor: Prof. Dr. Denise Freitas Siqueira Petri*

São Paulo

2023



Autorizo a reprodução e divulgação total ou parcial deste trabalho, por qualquer meio convencional ou eletrônico, para fins de estudo e pesquisa, desde que citada a fonte.

Ficha Catalográfica elaborada eletronicamente pelo autor, utilizando o programa desenvolvido pela Seção Técnica de Informática do ICMC/USP e adaptado para a Divisão de Biblioteca e Documentação do Conjunto das Químicas da USP

Bibliotecária responsável pela orientação de catalogação da publicação:  
Marlene Aparecida Vieira - CRB - 8/5562

F992i Furtado, Laise Moura  
Interactions between polydopamine and cellulose derivatives: physicochemical aspects and applications / Laise Moura Furtado. - São Paulo, 2023.  
198 p.

Tese (doutorado) - Instituto de Química da Universidade de São Paulo. Departamento de Química Fundamental.

Orientador: Petri, Denise Freitas Siqueira

1. polydopamine. 2. cellulose derivatives. 3. caffeine. 4. adsorption. 5. sugarcane bagasse. I. T. II. Petri, Denise Freitas Siqueira, orientador.

## Acknowledgements

Primeiramente eu quero agradecer aos meus pais, Isa Rejane e Kleiber Jr, por me encorajarem a embarcar nessa jornada, que acabaria sendo a experiência mais enriquecedora da minha vida até o momento.

À Deus e aos meus guias que me mantiveram sã e protegida ao longo de todo o caminho.

À Profª Drª Denise Freitas Siqueira Petri, por toda a guiança intelectual. Todo o conhecimento compartilhado, ideias incríveis, contribuições, puxões de orelha, confiança e paciência, que contribuíram para o meu amadurecimento profissional e pessoal ao longo desses anos.

Aos meus avós, Kleiber, Socorro, Teresinha e Raimundo Nonato que prepararam o caminho para que eu levantasse voos cada vez mais altos e que me ensinaram através do exemplo todo amor e resiliência que cultivo na minha vida.

Ao meu companheiro Giordano, por todo amor, paciência, compreensão, apoio e por estar comigo em todos os momentos de dificuldade e felicidade.

Aos meus amigos de infância que mesmo de longe davam um jeito de arrancar um sorriso meu e aproveitaram comigo o que São Paulo tinha de melhor para oferecer, Ana Clara, Marina, Thales e Beatriz.

Aos meus amigos e colegas de laboratório que traziam leveza para os meus dias. De conversas sobre música, cultura pop e skin care até discussão de resultados e troca de conhecimentos científicos, Emilli Fracchini, Camila Chiaregato, Pedro Bongiorno, Daiana Furlan, Alex Alavarse, Mario, Dairon Fuentes, Rafael Dezotti, Ícaro Francescato, Karina Hilamatu, Diego, Luciene, Victor Hugo, Izabô Meneses, Natalia Morita, Rafael Cruz, Stephanie Novaes, Talita Calheiros e Georgia Bloisi.

Ao Prof. Dr. Rômulo Ando (USP) por todas as contribuições, apoio, ensinamentos e colaboração científica ao longo dessa jornada.

Aos professores Drª Ana Maria Carmona, Dr. Pedro Vitoriano, Drª Ticiane Pinheiro, Dr Márcio Yee e suas equipes, pela colaboração científica e trocas de conhecimento

Aos órgãos de fomentos Conselho Nacional de Desenvolvimento Científico e Tecnológico (CNPq Grants 171250/2017, 306848/2017, 421014/2018, 304017/2021), Fundação de Amparo à Pesquisa do Estado

de São Paulo (FAPESP 2018/13492-2) pelo suporte financeiro, viabilizando minha dedicação exclusiva ao doutorado.

Ao CNPEM-LNNano, Campinas (Proposal XPS 24589, Proposal XPS 20220195 and Proposal MicroCT 26323) pelas análises.

*“Há de ser leve  
Um levar suave  
Nada que entrave  
Nossa vida breve  
Tudo que me atreve*

*A seguir de fato  
O caminho exato  
Da delicadeza  
E ter a certeza  
De viver no afeto  
Só viver  
No afeto.”*

***Lenine – Leve e Suave***

# RESUMO

Furtado, L. M. **Interações entre polidopamina e derivados de celulose: Aspectos físico-químicos e aplicações.** 2023. 198 páginas. Tese (Doutorado) – Programa de Pós-Graduação em Química. Instituto de Química, Universidade de São Paulo, São Paulo.

Esta tese teve como principal objetivo o estudo das interações entre polidopamina (PDA) e ésteres ou éteres de celulose. Essas interações permitiram explorar o desenvolvimento de adsorventes eficientes para tratar resíduos sintéticos e reais. O **Capítulo 1** aborda os aspectos físico-químicos relacionados ao efeito da energia de superfície de diferentes substratos na adesão da PDA sobre eles. As interações favoráveis entre PDA e butirato acetato de celulose (CAB) levaram à criação de microesferas de CAB revestidas com PDA, que provaram ser adsorventes eficientes para cafeína em soluções aquosas. Os resultados do **Capítulo 1** inspiraram um estudo para entender melhor as interações entre CAB e cafeína, que é apresentado no **Capítulo 2**. Os principais resultados relatam a miscibilidade entre os grupos funcionais de CAB e cafeína e a liberação controlada de cafeína em filmes micrométricos de CAB/cafeína. O **Capítulo 3** mostra a combinação de micropartículas de bagaço de cana-de-açúcar e hidroxipropilmetil celulose (HPMC) com PDA para formar adsorventes com estabilidade química e mecânica em meio aquoso. O alto teor de micropartículas de bagaço de cana-de-açúcar (83 (m/m) %) foi um desafio, mas as propriedades adesivas da PDA ajudaram a manter as partículas unidas e o HPMC forneceu plasticidade para moldar os adsorventes. Os adsorventes foram eficientes na remoção de corante (azul de metileno), bisfenol A e na separação de óleo em uma mistura óleo/água. O **Capítulo 4** apresenta a criação de adsorventes à base de micropartículas de bagaço de cana (83 wt%) e carboximetilcelulose (CMC) mediados por PDA. Esses adsorventes foram aplicados com sucesso no tratamento do resíduo do laboratório de graduação, que é uma mistura complexa de 17 íons metálicos em pH 1. A relevância deste estudo está na demonstração de que os adsorventes foram produzidos predominantemente com resíduos agrícolas e trataram eficientemente um resíduo real de um laboratório de graduação.

**Palavras-chave:** Polidopamina. Acetato Butirato de Celulose. Carboximetilcelulose. Cafeína. Bagaço de cana-de-açúcar. Adsorção.

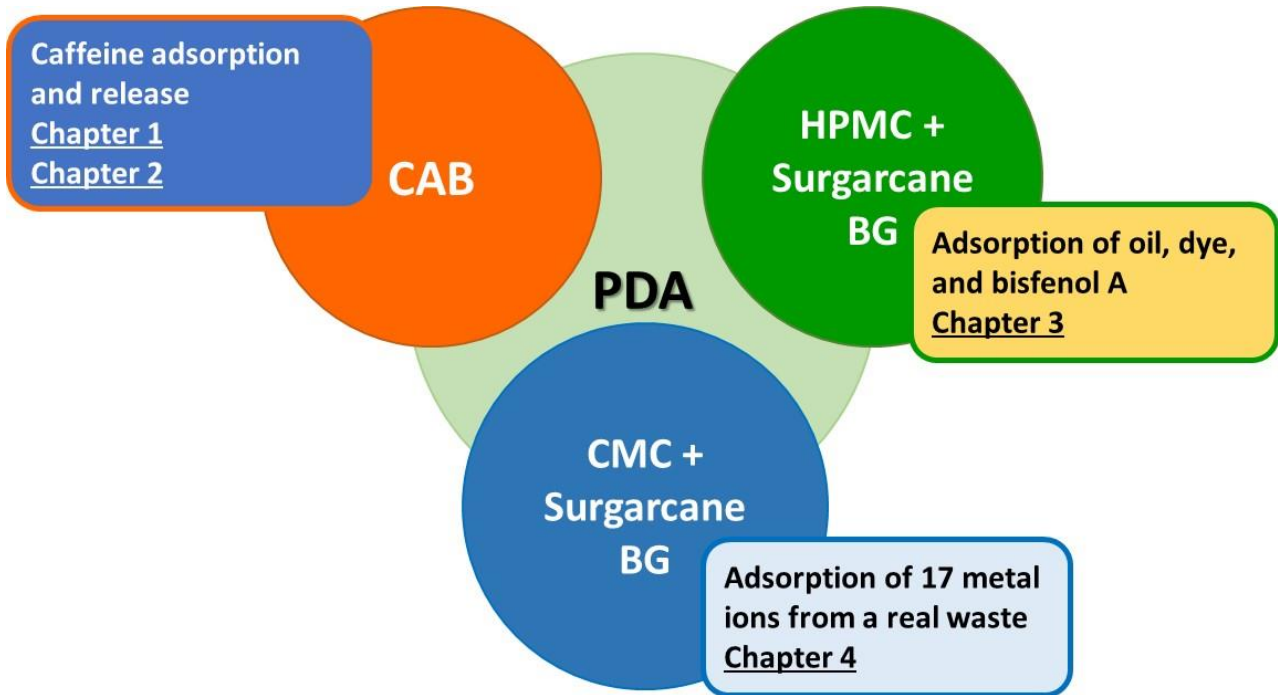


## Abstract

Furtado, L. M. **Interactions between polydopamine and cellulose derivatives: Physicochemical aspects and applications**. 2023. 198 pages. PhD Thesis – Graduate Program in Chemistry. Instituto de Química, Universidade de São Paulo, São Paulo.

This thesis focused on the comprehension about the interactions between polydopamine (PDA) and cellulose esters or ethers. Such interactions enabled to explore the development of efficient adsorbents to treat synthetic and real wastes. The **Chapter 1** comprises the physicochemical aspects regarding the effect of the surface energy of different substrates on the adhesion of PDA on them. The favorable interactions between PDA and cellulose acetate butyrate (CAB) led to the creation of PDA coated microbeads of CAB, which proved to be efficient adsorbents for caffeine from aqueous solutions. The results from the **Chapter 1** inspired a study to better understand the interactions between CAB and caffeine, which is presented in the **Chapter 2**. The main findings reported the miscibility between the functional groups of CAB and caffeine and the sustained release of caffeine from CAB/caffeine films. The **Chapter 3** shows the combination of sugarcane bagasse microparticles and hydroxypropyl methyl cellulose (HPMC) mediated by PDA to form adsorbents chemically and mechanically stable in aqueous medium. The high content of sugarcane bagasse microparticles (83 wt%) was challenging, but the adhesive properties of PDA helped keeping the particles together and HPMC provided plasticity to mold the adsorbents. The adsorbents were efficient towards the removal of dye (methylene blue), bisphenol A and to separate oil from water. The **Chapter 4** presents the creation of adsorbents based on sugarcane bagasse microparticles (83wt%) and carboxymethyl cellulose (CMC) mediated by PDA. These adsorbents were successfully applied to treat the waste of undergraduate laboratory, which is a complex mixture of 17 metal ions at pH 1. The relevance of this study is the demonstration that the adsorbents were produced predominantly with agrowaste and efficiently treated a real waste from an undergraduate laboratory.

**Keywords:** Polydopamine. Cellulose acetate butyrate. Carboxymethyl Cellulose. Caffeine. Sugarcane bagasse. Adsorption.



## List of Tables

<p><b>Table 3.1:</b> Fitting parameters determined for the deposition of PDA and C/PDA 1.0 on Si/SiO<sub>2</sub> wafers, PS and CAB films at <math>11 \pm 1</math> °C and <math>25 \pm 1</math> °C, using Equation 3.3. ....</p>	47
<p><b>Table 3.3:</b> Contact angle (<math>\theta</math>) measurements performed for MilliQ water and CH<sub>2</sub>I<sub>2</sub> droplets on PDA and C/PDA deposited (24 h) at <math>25 \pm 1</math> °C on Si/SiO<sub>2</sub>, PS and CAB, along with the surface energy (<math>\gamma_s</math>) values. <math>\gamma_{ps}</math> and <math>\gamma_{ds}</math> stand for the polar and dispersive components of the surface energy. N/C ratios determined from the XPS spectra obtained for PDA and C/PDA on Si/SiO<sub>2</sub> and PS, after 24 h deposition, at <math>25 \pm 1</math> °C .....</p>	55
<p><b>Table 3.4:</b> Some examples of polymeric systems used as adsorbents for caffeine along with the adsorption experiments conditions, <math>q_e</math> (mg/g) or removal (R) % values. <math>C_i</math> stands for initial caffeine concentration. <math>R = \frac{C_i - C_e}{C_i} \times 100\%</math>. ....</p>	62
<p><b>Table 4.1.</b> Glass transition temperature (<math>T_g</math>), initial decomposition temperature (<math>T_{5\%}</math>), degradation temperature (<math>T_{deg}</math>) and char residue at 500 °C determined for pure CAB and CAB/caf 2.5 wt%, CAB/caf 5 wt% and CAB/caf 7 wt% films.....</p>	81
<p><b>Table 4.2.</b> Some examples of polymeric delivery systems for caffeine and the corresponding highlight and reference. ....</p>	88
<p><b>Table 6.1.</b> Apparent density (<math>\rho_{app}</math>), specific surface area (<math>A_{sp}</math>), porosity (%) and swelling degree (gwater/g) calculated by CTAn software, swelling degree (gwater/g) and gel content (%) for CMC/BG and CMC/BG/PDA adsorbents. For comparison, the parameters corresponding to freeze-dried CMC/BG cryogels (BG 33 wt%) were also presented (Meneses et al., 2022). ....</p>	116
<p><b>Table 6.2.</b> Fitting parameters obtained for Pb<sup>2+</sup> on CMC/BG/PDA using Langmuir and Freundlich models. <math>q_{max}</math> (mg/g) and <math>K_L</math> (L/mg) stand for maximal adsorption capacity and Langmuir adsorption equilibrium constant, respectively. <math>K_F ((\text{mg/g})/(\text{mg/L}))^{1/n}</math> stands for Freundlich constant and indicates the relative adsorption capacity, and ‘n’ is related to the surface heterogeneity—the smaller n, the greater the heterogeneity. Literature data for the adsorption of Pb<sup>2+</sup> on BG and modified BG are presented for comparison. ....</p>	122

**Table 6.3.** Binding energy (BE, eV) and area (%) values corresponding to the deconvoluted peaks and references used for the assignments of the O 1s, Pb 4f, Ca 2p, C 1s and N 1s binding energy values. The BE and area values are mean values with standard deviations from three measurements in different points on the surface, for this reason, the sum of areas might larger than 100%. .....127

**Table 6.4.** Experimental conditions used in the column adsorption studies of Pb<sup>2+</sup> ions on CMC/BG/PDA, at pH 5.5: initial concentration ( $C_0$ ), flow rate ( $v$ ), adsorbent mass ( $m_{ads}$ ) and column height ( $H$ ). Fitting parameters obtained from Thomas model;  $K_{Th}$  and  $q_{Th}$  stand for the rate constant ( $L\ mg^{-1}\ min^{-1}$ ) and adsorption capacity (mg/g). Literature results for column adsorption studies of Pb<sup>2+</sup> ions on other biowastes.....131

**Table 6.5.** Concentration of 17 metals present in the undergraduate laboratory waste before treatment, after three steps of adsorption on the CMC/BG/PDA adsorbent and after the flocculation step with PDDA. Removal% after adsorption and flocculation..... 135

## List of Figures

- Figure 1.1:** (a) Schematic representation of the first steps of dopamine oxidation <sup>2</sup>. (b) Schematic representation of dopamine oxidation to dimers (red), trimers (blue) and tetramers (black) and their aggregation.....23
- Figure 3.1:** Schematic representation of chemical structures of (a) caffeine (C), (b) dopamine hydrochloride, (c) polystyrene (PS) and (d) cellulose acetate butyrate (CAB).....41
- Figure 3.2:** Photographs of (a) PDA and (b) C/PDA coatings on Si/SiO<sub>2</sub> wafers, PS and CAB films, respectively, taken after 1 h and 96 h contact with Tris buffer at pH 8.3. UV spectra determined for the supernatants of (c) PDA and (d) C/PDA coatings after 96 h contact at pH 8.3. The green line in (d) corresponds to the spectrum of pure caffeine solution at  $1.1 \times 10^{-4}$  mol/L.....49
- Figure 3.3:** Photographs of the (a) vials with PDA and C/PDA 1.0 coatings dissolved at pH 13, (b) PDA and C/PDA 1.0 coated Si/SiO<sub>2</sub> wafers, PS and CAB films before (0 min) and after 10 min contact with NaOH 0.1 mol/L, (c) vials with precipitated PDA and C/PDA at pH 1.0, after 96 h resting. (d) and (e) UV spectra of the supernatants observed in (c). The green line in (e) corresponds to the spectrum of pure caffeine solution at  $1.1 \times 10^{-4}$  mol/L.....52
- Figure 3.4:** AFM images (600 nm x 600 nm) of PDA and C/PDA 1.0 after 2 h deposition at  $25 \pm 1$  °C, on Si/SiO<sub>2</sub>, CAB and PS, along with the corresponding RMS values. ....53
- Figure 3.5:** (a) Experimental (red) and theoretical (light red) Raman, experimental (black) and theoretical (grey) FTIR spectra determined for C/PDA, the “\*” in the theoretical spectra indicates the bands that matches with the bands assigned in the experimental spectra. (b) Chemical structures of caffeine and PDA trimers used for the DFT calculations. (c) Snapshot from DFT simulation, where caffeine molecule approaches to PDA trimer by  $\pi$ - $\pi$  interactions and H bond by caffeine N(9).....59
- Figure 3.6:** (a) Confocal fluorescence images of CAB/PDA microbeads,  $\lambda_{\text{excitation}} = 467-498$  nm and  $\lambda_{\text{emission}} = 513-556$  nm (b) Adsorption isotherm of caffeine on the CAB/PDA microbeads at pH 5.5 and  $(24 \pm 1)$  °C, adsorption time 24 h, along with non-linear fitting for Freundlich model  $q_e = KF C_e(1/n)$ . The fitting parameters KF and n amounted to  $6.21 \text{ mgL} \times \text{g/mgL} \times \text{g}1n$  and 1.28, respectively,  $\chi^2 = 0.2469$  and  $R^2 = 0.9822$ .....61

**Figure 4.1:** Schematic representation of chemical structures of (a) CAB repeating units and (b) caffeine.....72

**Figure 4.2:** (a) and (b) SEM images of needle-shaped crystals of caffeine grown on Si/SiO<sub>2</sub> wafers by evaporation from acetone.(c) Optical microscopy and the corresponding and (d) CFM image of caffeine crystals on glass slides, after acetone evaporation. The concentration of caffeine in acetone was 2.0 g L<sup>-1</sup>. 75

**Figure 4.3:** SEM images of (a) CAB5/caf, (b) CAB10/caf, (c) CAB20/caf spin-coated films on Si/SiO<sub>2</sub> wafers. CFM images of (d) CAB5/caf films and (e) pure CAB films deposited from solution at 10 g L<sup>-1</sup> in EA, on glass slides. (f) SEM image of pure CAB spin-coated film from solution at 10 g L<sup>-1</sup> in EA, on Si/SiO<sub>2</sub> wafers. ....77

**Figure 4.4:** Photographs and transmittance of light at 600 nm through the CAB/caf films as a function of caffeine content ( $\phi_{caf}$ ). The red line corresponds to the exponential fit  $y = 0.75 \exp(-x/7.4)+0.036$ ,  $R^2 = 0.9530$ . The experimental data are mean values of duplicates, with standard deviations below 5%. ....78

**Figure 4.5:** SEM images of (a,b) pure CAB, (c,d) CAB/caf 2.5 wt%, (e,f) CAB/caf 5 wt% and (f,h) CAB/caf 7 wt% films.....80

**Figure 4.6.** FTIR-ATR determined for (a) pure caffeine as powder, pure CAB, CAB/caf 2.5 wt%, CAB/caf 5 wt% and CAB/caf 7 wt% films micrometric films, (b) pure caffeine as powder and caffeine dissolved in chloroform at 2.0 g L<sup>-1</sup>.....83

**Figure 4.7.** Snapshot of optimized geometries from DFT calculations of (a) caffeine, (b) CAB monomer and (c) caffeine and CAB interaction, where caffeine molecule approaches to CAB monomer by hydrogen bonding between CAB hydroxyl group and caffeine C=O(2). The interaction energy value was obtained from the difference of the energy of the isolated species.....84

**Figure 4.8.** Release profiles of caffeine from (a) CAB/caf 5 wt% and (b) CAB/caf 7 wt% in MilliQ at pH 5.5, 25 °C, in MilliQ water (blue triangle), NaCl 0.01 mol L<sup>-1</sup> (red circle) and NaCl 0.10 mol L<sup>-1</sup> (black square). Release profiles of caffeine from (c) CAB/caf 5 wt% and (d) CAB/caf 7 wt% at 25 °C, pH 2.0 (red circle), pH 5.5 (blue triangle), pH 7.4 (black square) and pH 9 (pink triangle). ....86

**Figure 4.9.** Schematic representation of caffeine release pH 7.4, from CAB/caf 2.5 wt%, CAB/caf 5 wt% and CAB/caf 7 wt%, over the period of 6 h and 48 h.....87

<b>Figure 5.1:</b> (a) HPMC/BG/PDA mixtures of F100 (left), F150 (center) and F200 (right) after 4h of DOPA oxidation packaged and stored in a refrigerator for later use/molding. (b) Mixtures of F100, F150 and F200 molded in cylindrical shape (c) Biomimetic filters after the steps of pre-crosslinking and crosslinking	100
<b>Figure 5.2:</b> SEM images of biomimetic filter (a) F100, (b) F150 and (c) F200.	100
<b>Figure 5.3:</b> (a) Photographs of F100, F150 and F200 filters in MilliQ water at pH 5.5 after 24 h under stirring. (b) Schematic representation of the esterification reaction between citric acid and HPMC hydroxyl groups.	101
<b>Figure 5.4:</b> Photographs of F150 filter (a) after MB adsorption and (b) after filter recovery through photooxidation with sunlight	102
<b>Figure 6.1.</b> Schematic representation of chemical structures of (a) CMC, with R = CH <sub>2</sub> -COO- Na <sup>+</sup> or -H, (b) dopamine hydrochloride, and (c) citric acid.	108
<b>Figure 6.2.</b> SEM images for (a) CMC/BG, (b) CMC/BG/PDA. Reconstructed 3D structures from microtomography data of (c) CMC/BG and (d) CMC/BG/PDA adsorbents. Parallelepiped (490 μm x 1070 μm x 1350 μm) from the central region of the samples are shown with the corresponding attenuation scales obtained by the transfer function in the software CTVox®.	116
<b>Figure 6.3.</b> CMC/BG/PDA adsorbents prepared in the presence of citric acid and PDA, heated at 172 °C for 10 min. Photographs of CMC/BG/PDA adsorbents after 0 h, 1 h, 3 h, 24 h, 48 h immersion in (a) pH 1, (b) pH 5.5 (MilliQ water) and (c) pH 8.5 media.	118
<b>Figure 6.4.</b> (a) Effect of pH on the Removal % of Pb <sup>2+</sup> ions (C <sub>0</sub> = 20 mg/L) by CMC/BG/PDA adsorbents (m ~ 40 mg) at pH 3.0, 4.5, 5.0, 5.5, 6.0 and 7.0 and the regeneration capacity by rinsing the adsorbents with HCl 0.1 mol/L, at 23 ± 1°C. (b) Cycles of adsorption and desorption of Pb <sup>2+</sup> ions (C <sub>0</sub> = 20 mg/L) using CMC/BG/PDA adsorbents (~ 40 mg) at 23 ± 1°C. The desorption was achieved with 5 mL of HCl 0.1 mol/L, 10 min contact.	121
<b>Figure 6.5.</b> Adsorption isotherms of Pb <sup>2+</sup> ions on CMC/BG/PDA adsorbents (53 ± 5 mg) in the absence (a) and in the presence (b) of Ca <sup>2+</sup> (C <sub>0</sub> = 5.0 mg/L) and Mg <sup>2+</sup> (C <sub>0</sub> = 5.0 mg/L) at pH 5.5, 19 ± 1 °C, one-hour	

contact,  $V = 5$  mL. The red and blue lines correspond to the nonlinear fittings for Langmuir and Freundlich adsorption models. .... 122

**Figure 6.6.** XPS high resolution spectra of O 1s for **(a)** CMC/BG/PDA before adsorption, **(b)** after adsorption of  $Pb^{2+}$  in the absence and **(c)** in the presence of  $Ca^{2+}$  and  $Mg^{2+}$  ions; Pb 4f after adsorption of  $Pb^{2+}$  **(d)** in the absence and **(e)** in the presence of  $Ca^{2+}$  and  $Mg^{2+}$  ions; **(f)** Ca 2p..... 126

**Figure 6.7.** Breakthrough curves for  $Pb^{2+}$  ions on CMC/BG/PDA at pH 5.5, **(a)** in the absence and **(b)** in the presence of the  $Ca^{2+}$  and  $Mg^{2+}$  ions. Column operational conditions  $C_0$ ,  $v$  and mass of adsorbent **(a)**: (1) 20 mg/L, 3.0 mL/min and 100 mg, (2) 20 mg/L, 1.5 mL/min and 100 mg, (3) 20 mg/L, 3.0 mL/min and 50 mg and (4) 8 mg/L, 3.0 mL/min and 50 mg. **(b)**  $v = 3.0$  mL/min,  $m_{ads} = 50$  mg. The solid lines are the non-linear fittings to Thomas model. .... 129

**Figure 6.8.** **(a)** Photographs of the residue after 3 sequential adsorption steps, using a new adsorbent in each step ( $m_{ads} = 0.2242 \pm 0.0024$  g), and of the CMC/BG/PDA adsorbents before and after each step. **(b)** Electronic spectra obtained for the original waste (R) after the first (R1), second (R2) and third (R3) steps of adsorption. **(c)** Concentration of each element found in the undergraduate laboratory waste before and after three adsorption steps. The concentration of Na and K was reduced to 1693 mg/L and 1503 mg/L, respectively. **(d)** Removal% after three adsorption steps (light green) followed by flocculation with PDDA (light purple). .... 134



# Summary

<b><u>1 INTRODUCTION.....</u></b>	<b><u>21</u></b>
1.1 POLYDOPAMINE .....	21
1.2 CAFFEINE.....	25
1.3 CELLULOSE DERIVATIVES POLYMERS .....	27
1.4 SUGARCANE BAGASSE .....	28
1.5 REFERENCES .....	28
<b><u>2 OBJECTIVE.....</u></b>	<b><u>36</u></b>
<b><u>3 CHAPTER 1 - POLYDOPAMINE COATED CELLULOSE ACETATE BUTYRATE</u></b>	
<b><u>MICROBEADS FOR CAFFEINE REMOVAL.....</u></b>	<b><u>37</u></b>
ABSTRACT.....	37
3.1 MOTIVATION.....	38
3.2 EXPERIMENTAL SECTION .....	40
3.2.1 MATERIALS.....	40
3.2.2 DEPOSITION OF PDA ON SOLID SUBSTRATES IN THE ABSENCE AND IN THE PRESENCE OF CAFFEINE .....	41
3.2.3 STABILITY OF PDA AND C/PDA COATINGS .....	42
3.2.4 CHARACTERIZATION OF PDA AND C/PDA COATINGS .....	42
3.2.5 RAMAN AND FTIR SPECTROSCOPY OF PDA AND C/PDA.....	44
3.2.6 DFT CALCULATIONS .....	45
3.2.7 PREPARATION OF PDA COATED MICROBEADS FOR CAFFEINE ADSORPTION.....	45
3.3 RESULTS AND DISCUSSION.....	46
3.3.1 DEPOSITION OF PDA OR C/PDA ON DIFFERENT SUBSTRATES .....	46
3.3.2 STABILITY OF PDA OR C/PDA LAYERS DEPOSITED ON DIFFERENT SUBSTRATES .....	48
3.3.3 CHARACTERIZATION OF PDA AND C/PDA COATINGS .....	52

3.3.4 SPECTROSCOPIC STUDY AND DFT CALCULATIONS .....	56
3.3.5 ADSORPTION OF CAFFEINE ON CAB/PDA MICROBEADS .....	59
<b>3.4 CONCLUSIONS.....</b>	<b>62</b>
<b>3.5 REFERENCES .....</b>	<b>63</b>

## **4 CHAPTER 2 - MISCIBILITY AND SUSTAINED RELEASE OF DRUG FROM CELLULOSE**

### **ACETATE BUTYRATE/CAFFEINE FILMS..... 69**

ABSTRACT.....	69
<b>4.1 MOTIVATION.....</b>	<b>70</b>
<b>4.2 EXPERIMENTAL SECTION .....</b>	<b>72</b>
4.2.1 MATERIALS .....	72
4.2.2 PREPARATION OF THIN FILMS BY SPIN-COATING AND CHARACTERIZATION.....	72
4.2.3 PREPARATION OF MICROMETRIC FILMS BY CASTING AND CHARACTERIZATION .....	73
4.2.4 IN VITRO RELEASE OF CAFFEINE FROM MICROMETRIC CAB/CAF FILMS.....	74
<b>4.3 RESULTS AND DISCUSSION.....</b>	<b>74</b>
4.3.1 CAB/CAF SPIN-COATED FILMS .....	76
4.3.2 CAB/CAF CAST FILMS .....	77
4.3.3 IN VITRO RELEASE OF CAFFEINE FROM CAB/CAF FILMS.....	84
<b>4.4 CONCLUSIONS.....</b>	<b>90</b>
<b>4.5 REFERENCES .....</b>	<b>90</b>

## **5 CHAPTER 3 - BIOMIMETIC FILTER FOR THE REMOVAL OF ORGANIC POLLUTANTS**

### **AND OIL/WATER SEPARATION ..... 96**

ABSTRACT.....	96
<b>5.1 MOTIVATION.....</b>	<b>97</b>
<b>5.2 EXPERIMENTAL SECTION.....</b>	<b>98</b>

5.2.1	PREPARATION OF BIOMIMETIC FILTER.....	98
5.2.2	CHARACTERIZATION OF BIOMIMETIC FILTERS .....	99
5.2.3	REMOVAL CAPACITY OF METHYLENE BLUE (MB) AND BISPHENOL A (BPA).....	99
5.2.4	OIL AND WATER SEPARATION .....	100
<b>5.3</b>	<b>RESULTS .....</b>	<b>100</b>
<b>5.4</b>	<b>CONCLUSIONS.....</b>	<b>102</b>
<b>5.5</b>	<b>REFERENCES .....</b>	<b>102</b>

**6 CHAPTER 4: CARBOXYMETHYL CELLULOSE/SUGARCANE BAGASSE/POLYDOPAMINE ADSORBENTS FOR EFFICIENT REMOVAL OF Pb<sup>2+</sup> IONS FROM SYNTHETIC AND UNDERGRADUATE LABORATORY WASTES..... 104**

	ABSTRACT.....	104
<b>6.1</b>	<b>MOTIVATION.....</b>	<b>105</b>
<b>6.2</b>	<b>EXPERIMENTAL SECTION .....</b>	<b>108</b>
6.2.1	MATERIALS.....	108
6.2.2	PREPARATION OF CMC/BG/PDA AND CMC/BG ADSORBENTS .....	109
6.2.3	CHARACTERIZATION OF CMC/BG/PDA AND CMC/BG ADSORBENTS.....	110
6.2.4	BATCH ADSORPTION STUDIES .....	111
6.2.5	FIXED-BED COLUMN ADSORPTION STUDIES .....	113
<b>6.3</b>	<b>RESULTS AND DISCUSSION.....</b>	<b>114</b>
6.3.1	CHARACTERIZATION OF CMC/BG AND CMC/BG/PDA ADSORBENTS.....	114
6.3.2	BATCH ADSORPTION STUDIES .....	120
6.3.3	BREAKTHROUGH CURVES FOR Pb <sup>2+</sup> IONS IN THE ABSENCE AND IN THE PRESENCE OF Ca <sup>2+</sup> AND Mg <sup>2+</sup> IONS	
	127	
6.3.4	REMOVAL OF Pb <sup>2+</sup> IONS FROM UNDERGRADUATE LABORATORY WASTE .....	132
<b>6.4</b>	<b>CONCLUSIONS.....</b>	<b>136</b>
<b>6.5</b>	<b>REFERENCES .....</b>	<b>137</b>

<b>7</b>	<b><u>GENERAL CONCLUSIONS</u></b>	<b><u>146</u></b>
<b>8</b>	<b><u>PERSPECTIVES</u></b>	<b><u>148</u></b>
<b>9</b>	<b><u>APPENDICES</u></b>	<b><u>150</u></b>
<b>9.1</b>	<b>PERMISSIONS</b>	<b>150</b>
9.1.1	CHAPTER 1:	150
9.1.2	CHAPTER 2:	151
9.1.3	CHAPTER 4:	151
<b>9.2</b>	<b>SUPPLEMENATARY MATERIAL</b>	<b>152</b>
9.2.1	CHAPTER 1:	152
9.2.2	CHAPTER 2:	172
9.2.3	CHAPTER 4:	181
<b>9.3</b>	<b>CURRICULAR SUMMARY</b>	<b>197</b>

# 1 INTRODUCTION

## 1.1 POLYDOPAMINE

Dopamine (3,4-hydroxyphenethylamine), DA, is a neurotransmitter responsible for the motor function of the human body (voluntary movements) and the decrease in its concentration in the body is related to Parkinson's (YU; FERNANDEZ, 2017). Because it is in the catecholamine group, it has been studied to functionalize molecules, such as polymers, for various applications, from electrochemical analyzes for their role in neuroscience to the development moisture-resistant adhesive materials (DUVALL; MCCREERY, 2000; LEE et al., 2007).

And this whole story began with the observation of the biological behavior of some species of mussels, which manage to remain adhered to rocks, even when completely submerged in sea water, which has inspired many research groups to develop new adhesives (BRUBAKER; MESSERSMITH, 2012). Mussels attach themselves to rocks by the byssus, which are composed of filaments and adhesive plates at the ends (BELL; GOSLINE, 1996).

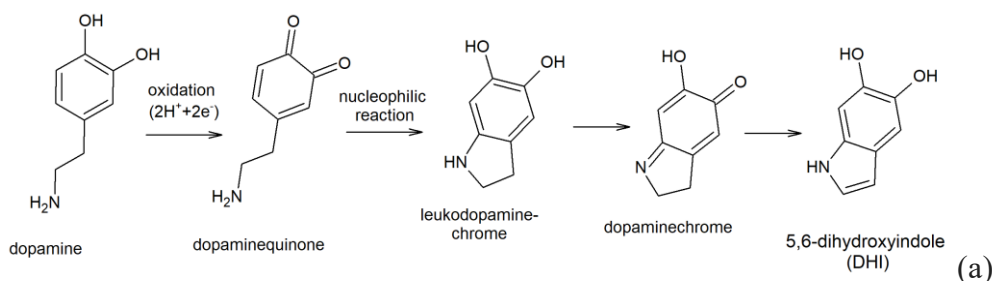
In studies carried out by Lee and collaborators, it was seen that the adhesive properties of the plates were related to the presence of L-dopa (3,4-dihydroxy-L-phenylalanine), which in most living beings is biosynthesized from L-tyrosine; Adhesion is promoted through many types of interactions, one of which is the  $\pi$ -cation interactions between  $\text{Fe}^{3+}$  or  $\text{Ca}^{2+}$  ions and the aromatic ring of L-dopa (LEE; LEE; MESSERSMITH, 2007; LEE et al., 2011). And this was the first important work on the development of adhesives based on polydopamine (PDA) inspired by the capacity of mussels adhere to rocks under water.

The authors demonstrate that the simple immersion of substrates in a dopamine solution in a slightly alkaline medium (pH  $\sim$ 8,5) led to dopamine self-polymerization with subsequent deposition

on the substrate. The tested substrates were noble metals, inorganic oxides, polymers, semiconductors and ceramics (LEE; LEE; MESSERSMITH, 2007).

Since then, PDA has been widely applied for surface modification due to strong adhesion in substrates with high or low surface energy, simplicity and high efficiency in the preparation.

The nature of PDA has been investigated by different research groups. The experimental results of solid state NMR spectroscopy and crystallographic techniques (DREYER et al., 2012) and high-performance liquid chromatography analysis coupled with mass spectrometry (HONG et al., 2012) allowed to conclude that PDA is not a polymer with the monomeric units covalently bonded, but it is an aggregate of different products of dopamine oxidation (DELLA VECCHIA et al., 2013). In the presence of O<sub>2</sub> and Tris-HCl buffer (pH 8.5), Vecchia et al. showed that at high concentration of dopamine (10 mmol/L), dopamine autoxidizes to dopamine quinone (**Figure 1.1a**), which undergoes dimerization and further oligomerization to catecholamine-based products, whereas at low concentration of dopamine (0.5 mmol/L) the intramolecular cyclization of dopamine to 5,6-dihydroxyindole (DHI) dominates (**Figure 1.1a**); the DHI-related products might undergo degradation to pyrrolicarboxylic acid fragments (DELLA VECCHIA et al., 2013). **Figure 1.1b** represents the chemical structure of dopamine and the most reported products of dopamine oxidation in the presence of O<sub>2</sub> and Tris buffer (pH 8.5), as well as their aggregation driven by H bonding,  $\pi$ - $\pi$  interactions and charge transfer among them (CHEN et al., 2014, 2017; KLOSTERMAN; RILEY; BETTINGER, 2015; KIM et al., 2016).



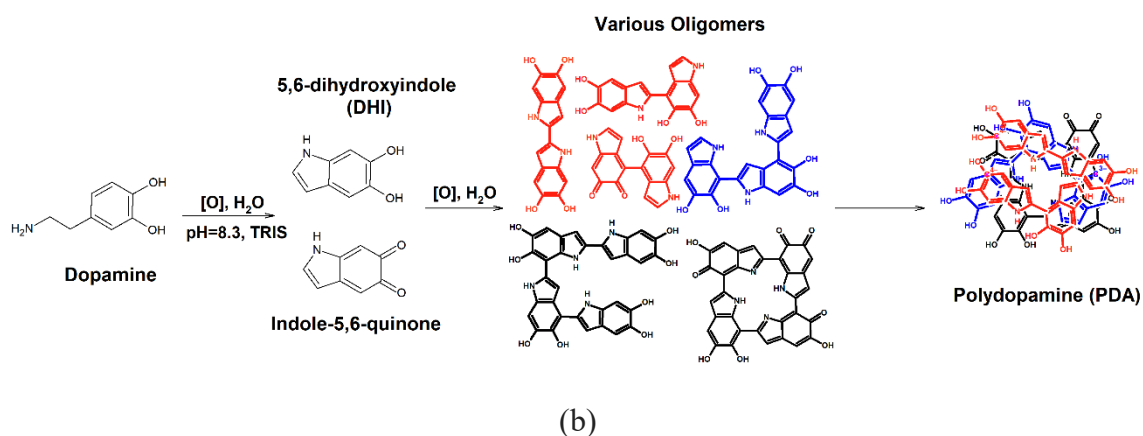


**Figure 1.1:** (a) Schematic representation of the first steps of dopamine oxidation (RYU; MESSERSMITH; LEE, 2018). (b) Schematic representation of dopamine oxidation to dimers (red), trimers (blue) and tetramers (black) and their aggregation.

The parameters that control the PDA formation are pH, addition of oxidant, initial concentration of dopamine, ionic strength and they were systematically investigated by different groups.

Briefly, at pH 8.5, Ball and co-workers demonstrated that the increase of initial dopamine concentration led to a linear increase of the thickness of PDA film onto Si/SiO<sub>2</sub> wafers (BALL et al., 2012). The type and concentration of buffer might play an important role on the products of dopamine oxidation. High concentration (~ 50 mmol/L) of Tris-HCl and low initial concentration of dopamine (from 0.5 to 2.0 mmol/L) favored the nucleophilic addition of Tris-HCl to the dopamine quinone (DELLA VECCHIA et al., 2014). The PDA particles synthesized under high ionic strength buffer (phosphate) were larger than those produced under low ionic strength (Tris-HCl or carbonate) buffer, due to charge-driven aggregation and salting out effects (DELLA VECCHIA et al., 2014). The chemical attachment of catechol groups to the surface is one of the explanations for the strong adhesion of PDA to various substrates. On the other hand, if the medium pH is higher than 9.5, which is close to the pK<sub>a</sub> of DHI catechol groups, the solubility of PDA increases and the thickness of adsorbed PDA decreases (KLOSTERMAN; RILEY; BETTINGER, 2015).

The PDA formation due to O<sub>2</sub> mediated dopamine oxidation requires pH ~ 8.5. However, it is also possible to oxidize dopamine under pH 5 if instead of O<sub>2</sub>, stronger oxidants, such as, copper sulfate (CS), sodium periodate (SP), or ammonium peroxodisulfate (AP), are used at dopamine/oxidant ratio of 1:2; being the PDA films produced in the presence of SP the most homogeneous and hydrophilic (PONZIO et al., 2016). The chemical composition and roughness of the substrate also affect the PDA deposition, e.g. the thickness of PDA films tend to increase with the substrate hydrophobicity and roughness (JIANG et al., 2011; KLOSTERMAN; RILEY; BETTINGER, 2015).

Recently, Lee and co-workers reported that the complete understanding of the detailed mechanism behind the formation of polydopamine is still a challenge, mainly due to the heterogeneity of the “monomeric” unit of DOPA (LEE; PARK; LEE, 2020).

Nevertheless, polydopamine continues to be widely applied as a functionalization platform for surfaces due to simple preparation, good biocompatibility, photothermal conversion efficiency and quenching effect with different applications.

For instance, Cheng et al reviewed preparation and polymerization of PDA in organic and inorganic nanomaterials for biomedical applications (CHENG et al., 2019). Liu et al summarized physical properties of polydopamine, such as optics, electricity and magnetics, and discussed interesting applications of polydopamine in the development of innovative technology for batteries, supercapacitors, and catalysts, highlighting its potential in the energy field due to its high carbon yield, robust wettability, high adhesion, and its characteristic of acting as a reducing agent agent (LIU; AI; LU, 2014).

In 2022, Liu et al highlighted a successful combination for water treatment: polysaccharides and polydopamine. The development of adsorbents with these features has many benefits, interconnected with sustainability and a circular economy such as such as biodegradability,



biocompatibility, renewability, and low cost. Furthermore, PDA provides functional groups (catechol, amine, and phenyl groups) that can bind inorganic and organic pollutants through various interactions ( $\pi$ - $\pi$  stacking, H-bonding, electrostatic, coordination, and chelating) and interfacial stability and compatibility (LIU et al., 2022). For this reason, polydopamine and its potential as a functionalization platform continued to be explored exponentially over the years.

Opportunities and challenges coexist in the development of PDA-based polysaccharide materials. In this thesis, cellulose derivatives and sugarcane bagasse were combined with the aid of polydopamine to develop new adsorbents for the adsorption of organic and inorganic pollutants. Understanding the physicochemical properties of PDA, up to its final application as a natural adhesive was essential for the development of the biomimetic filter for the treatment of wastes from an undergraduate laboratory of the Institute of Chemistry at USP.

## 1.2 CAFFEINE

Caffeine (1,3,7-trimethylxanthine) is a natural alkaloid found in many types of drinks that we consume daily, such as tea, coffee, yerba mate, guarana, among others (COLON; NERIN, 2014), that was reported for the first time in 1820 by Friedlieb Ferdinand Runge and synthesized 80 years later by Emil Fischer with reactions involving N-methylated uric acid (BUSSEMAS; HARSCH; ETTRE, 1994; KUNZ, 2002).

In human beings' organism, caffeine causes stimulating effects in the central nervous system, which acts as a cascade effect, increasing the respiratory rate through bronchodilation, diuretic action and lipolysis (NURMINEN et al., 1999). Most of these effects are associated with the caffeine metabolites, namely paraxanthine, theobromine and theophylline (GRACIA-LOR et al., 2017).

Outside the human body, caffeine has antioxidant, antibacterial, and antifungal properties, for instance, caffeine at  $26 \times 10^{-3} \text{ mol L}^{-1}$  is enough to prevent *C. albicans* growth, and, possibly

positive effect on the treatment of skin cancer (SHAKEEL; RAMADAN, 2010; VIGNOLI; BASSOLI; BENASSI, 2011; SLEDZ et al., 2015; CALHEIROS et al., 2020).

On the other hand, caffeine has been included in the group of emerging water organic pollutants in natural water (SOUSA et al., 2018). In Brazil, caffeine has been detected in surface water at 28.2 and 18.8  $\mu\text{g L}^{-1}$  (MACHADO et al., 2016; PETEFFI et al., 2018). Therefore, polymeric adsorbents might be useful to pre-concentrate caffeine and monitoring the caffeine concentration in wastes and natural waters (MARTÍN et al., 2012).

Interactions between caffeine and polysaccharides are often related to sustained released or adsorption process. Frachini et al. synthesized gelatin and alginate magnetic hydrogels with caffeine to evaluate the effects of the stimulant molecule in the viability of SH-SY5Y neuroblastoma cells. The authors claims that the system has a potential medical application (FRACHINI et al., 2023). Quesada et al. developed chitosan composite with activated carbons to adsorb caffeine from tap water and synthetic hospital wastewater (QUESADA et al., 2022).

The duality of caffeine properties demonstrates that depending on the concentration, the molecule can be good or bad for an ecosystem. Therefore, in this work, the effect of caffeine on the process of formation and deposition of polydopamine coatings was evaluated in order to develop a system for the adsorption of the organic pollutant. In addition, the miscibility of caffeine in micrometric films of cellulose acetate butyrate (CAB) and the influence of its properties on the sustained release of caffeine were studied for biomedical applications.

### 1.3 CELLULOSE DERIVATIVES POLYMERS

Cellulose derivative-based materials are widely applied in the development of new products, due to lower environmental impact with biodegradable and biocompatible potential and satisfactory mechanical properties (KALIA et al., 2011).

Chemical modifications in raw cellulose, such as esterification, enable interesting properties that improve materials processing through an extruder, injector, and dissolution in common organic solvents (EDGAR et al., 2001). Cellulose acetate butyrate (CAB) is a cellulose ester applied to coatings, paint, and sensors, because improves UV stability, flow, and leveling, reduces plasticizer migration, and dry time, controls viscosity and is a good film forming (EDGAR et al., 2001). CAB is an important component in pharmaceutical formulations, due to its hydrophobic character, biodegradability, and biocompatibility and has been reported as an interesting biopolymer for the sustained release of caffeine and nevirapine (FURTADO et al., 2020)(VARSHOSAZ et al., 2018).

Hydroxypropyl methylcellulose (HPMC) and carboxymethyl cellulose (CMC) are common industrial water soluble cellulose ethers, whose properties depend on the degree of substitution corresponding to methyl groups (DS) and molar substitution of hydroxypropyl groups (MS), in the case of HPMC (MARANI; BLOISI; PETRI, 2015), and to carboxymethyl groups (DS) in the case of CMC . Due to its hydrophilicity, water solubility, high chemical stability, nontoxicity to human health, biocompatibility, and biodegradability, cellulose ethers have been widely applied as rheological control agent, binder, emulsion stabilizer, and film former (SEDDIQI et al., 2021), excipients in sustained drug release (MARANI; BLOISI; PETRI, 2015), main matrix of porous materials with high surface area and swelling capacity with functional groups available for the adsorption of organic and inorganic pollutants (TOLEDO et al., 2019; MENESES et al., 2022; NOVAES; OLIVEIRA; PETRI, 2022a).

Cellulose ethers and esters are also being reported as an efficient alternative for the development of eco-inks for 3D printing, an exponentially growing technology (DAI et al., 2019). Therefore, these biopolymers have become increasingly relevant for the development of sustainable materials.

## **1.4 SUGARCANE BAGASSE**

Sugarcane bagasse is a source of lignocellulosic biomass, which is a byproduct of the sugar and alcohol industry (ANASTOPOULOS et al., 2017). As Brazil is currently the world's largest producer of sugarcane, producing 610 million tons, sugarcane bagasse is a low cost and abundant feedstock (CONAB, 2023). Its chemical composition consists of 40% cellulose, 24% hemicelluloses, and 25% lignin, approximately (REZENDE et al., 2011; MOORE; BOTHA, 2013).

Lignocellulosic materials are versatile feedstock due to their functional groups such as carbonyl, hydroxyl, and carboxyl, which allow chemical modifications to obtain fibers, nanocrystals, hydrogels, beads, and low cost and eco -friendly composites for adsorption of organic and inorganic pollutants (BLACHECHEN; FARDIM; PETRI, 2014; IWUOZOR et al., 2022).

Novaes et al. developed adsorbents of hydroxypropyl methylcellulose (HPMC) with different amounts of sugarcane bagasse (BG) microparticles to enhance cryogels mechanical properties and the optimized material was applied for 17 $\alpha$ -ethinylestradiol adsorption (NOVAES; OLIVEIRA; PETRI, 2022b). Furtado et al. evaluated the performance of a new composite with 83 wt% of BG microparticles for the removal of Pb<sup>2+</sup> ions from synthetic solutions and from an undergraduate laboratory waste containing other 16 metal ions (FURTADO et al., 2022).

## **1.5 REFERENCES**

ANASTOPOULOS, I. et al. A review on waste-derived adsorbents from sugar industry for

pollutant removal in water and wastewater. *Journal of Molecular Liquids*, v. 240, p. 179–188, 2017. Disponível em: <<http://dx.doi.org/10.1016/j.molliq.2017.05.063>>.

BALL, V. et al. Kinetics of polydopamine film deposition as a function of pH and dopamine concentration: Insights in the polydopamine deposition mechanism. *Journal of Colloid and Interface Science*, v. 386, n. 1, p. 366–372, 2012. Disponível em: <<http://dx.doi.org/10.1016/j.jcis.2012.07.030>>.

BELL, E. C.; GOSLINE, J. M. Mechanical design of mussel byssus: material yield enhances attachment strength. v. 199, p. 1005–1017, 1996.

BLACHECHEN, L. S.; FARDIM, P.; PETRI, D. F. S. Multifunctional cellulose beads and their interaction with gram positive bacteria. *Biomacromolecules*, v. 15, n. 9, p. 3440–3448, 2014.

BLACHECHEN, L. S.; SOUZA, M. A.; PETRI, D. F. S. Effect of humidity and solvent vapor phase on cellulose esters films. *Cellulose*, v. 19, n. 2, p. 443–457, 2012.

BRUBAKER, C. E.; MESSERSMITH, P. B. The Present and Future of Biologically Inspired Adhesive Interfaces and Materials. *American Chemical Society*, v. 28, p. 2200–2205, 2012.

BUSSEMAS, H. H.; HARSCH, G.; ETTRE, L. S. Friedlieb Ferdinand Runge (1794-1867): “Self-Grown Pictures” as Precursors of Paper Chromatography. *Chromatographia*, v. 38, n. 3/4, p. 243–254, 1994.

CALHEIROS, T. F. et al. Physicochemical and antifungal properties of waterborne polymer nanoparticles synthesized with caffeine. *Colloid and Polymer Science*, v. 298, p. 341–353, 2020. Disponível em: <<https://doi.org/10.1007/s00396-020-04615-6>>.

CHEN, C. T. et al. Excitonic effects from geometric order and disorder explain broadband optical absorption in eumelanin. *Nature Communications*, v. 5, n. May, p. 1–10, 2014. Disponível em: <<http://dx.doi.org/10.1038/ncomms4859>>.

CHEN, C. T. et al. Polydopamine and eumelanin molecular structures investigated with ab

initio calculations. *Chemical Science*, v. 8, n. 2, p. 1631–1641, 2017.

CHENG, W. et al. Versatile Polydopamine Platforms: Synthesis and Promising Applications for Surface Modification and Advanced Nanomedicine. *ACS Nano*, v. 13, n. 8, p. 8537–8565, 2019.

COLON, M.; NERIN, C. Molecular interactions between caffeine and catechins in green tea. *Journal of Agricultural and Food Chemistry*, v. 62, n. 28, p. 6777–6783, 2014.

CONAB, N. S. C. *Produção de cana chega a 610,1 milhões de toneladas na safra 2022/23 com melhora na produtividade nas lavouras*. Disponível em: <[https://www.conab.gov.br/ultimas-noticias/4977-producao-de-cana-chega-a-610-1-milhoes-de-toneladas-na-safra-2022-23-com-melhora-na-productividade-nas-lavouras#:~:text=e Promoção Institucional-,Produção de cana chega a 610%2C1 milhões de toneladas,melhora n](https://www.conab.gov.br/ultimas-noticias/4977-producao-de-cana-chega-a-610-1-milhoes-de-toneladas-na-safra-2022-23-com-melhora-na-productividade-nas-lavouras#:~:text=e%20Promo%C3%A7%C3%A3o%20Institucional-,Produ%C3%A7%C3%A3o%20de%20cana%20chega%20a%20610%2C1%20milh%C3%B5es%20de%20toneladas,melhora%20n)>. Acesso em: 17 jun. 2023.

DAI, L. et al. 3D printing using plant-derived cellulose and its derivatives: A review. *Carbohydrate Polymers*, v. 203, n. September 2018, p. 71–86, 2019. Disponível em: <<https://doi.org/10.1016/j.carbpol.2018.09.027>>.

DELLA VECCHIA, N. F. et al. Building-block diversity in polydopamine underpins a multifunctional eumelanin-type platform tunable through a quinone control point. *Advanced Functional Materials*, v. 23, n. 10, p. 1331–1340, 2013.

DELLA VECCHIA, N. F. et al. Tris buffer modulates polydopamine growth, aggregation, and paramagnetic properties. *Langmuir*, v. 30, n. 32, p. 9811–9818, 2014.

DREYER, D. R. et al. Elucidating the structure of poly(dopamine). *Langmuir*, v. 28, n. 15, p. 6428–6435, 2012.

DUVALL, S. H.; MCCREERY, R. L. Self-catalysis by Catechols and Quinones during Heterogeneous Electron Transfer at Carbon Electrodes. n. 122, p. 6759–6764, 2000.

EDGAR, K. J. et al. Advances in cellulose ether performance and application. *Prog. Polym. Sci.*, v. 26, p. 1605–1688, 2001.

FRACHINI, E. C. G. et al. Caffeine Release from Magneto-Responsive Hydrogels Controlled by External Magnetic Field and Calcium Ions and Its Effect on the Viability of Neuronal Cells. *Polymers*, v. 15, n. 7, 2023.

FURTADO, L. M. et al. Miscibility and sustained release of drug from cellulose acetate butyrate/caffeine films. *Journal of Drug Delivery Science and Technology*, v. 55, n. November 2019, p. 101472, 2020. Disponível em: <<https://doi.org/10.1016/j.jddst.2019.101472>>.

FURTADO, L. M. et al. Carboxymethyl cellulose/sugarcane bagasse/polydopamine adsorbents for efficient removal of Pb<sup>2+</sup> ions from synthetic and undergraduate laboratory wastes. *Journal of Cleaner Production*, v. 380, n. September, 2022.

GRACIA-LOR, E. et al. Estimation of caffeine intake from analysis of caffeine metabolites in wastewater. *Science of the Total Environment*, v. 609, n. June, p. 1582–1588, 2017.

HONG, S. et al. Non-covalent self-assembly and covalent polymerization co-contribute to polydopamine formation. *Advanced Functional Materials*, v. 22, n. 22, p. 4711–4717, 2012.

IWUOZOR, K. O. et al. A Review on the Mitigation of Heavy Metals from Aqueous Solution using Sugarcane Bagasse. *Sugar Tech*, v. 24, n. 4, p. 1167–1185, 2022. Disponível em: <<https://doi.org/10.1007/s12355-021-01051-w>>.

JIANG, J. et al. Surface characteristics of a self-polymerized dopamine coating deposited on hydrophobic polymer films. *Langmuir*, v. 27, n. 23, p. 14180–14187, 2011.

KALIA, S. et al. Cellulose-based bio- and nanocomposites: A review. *International Journal of Polymer Science*, v. 2011, 2011.

KIM, Y. J. et al. Evidence of Porphyrin-Like Structures in Natural Melanin Pigments Using Electrochemical Fingerprinting. *Advanced Materials*, v. 28, n. 16, p. 3173–3180, 2016.

KLOSTERMAN, L.; RILEY, J. K.; BETTINGER, C. J. Control of heterogeneous nucleation and growth kinetics of dopamine-melanin by altering substrate chemistry. *Langmuir*, v. 31, n. 11, p.

3451–3458, 2015.

KUNZ, H. Emil Fischer – Unequalled Classicist , Master of Organic Chemistry Research , and Inspired Trailblazer of Biological Chemistry. *Angewandte Chemie - International Edition*, v. 41, n. 23, p. 4439–4451, 2002.

LEE, B. P. et al. Mussel-Inspired Adhesives and Coatings. *The Annual Review of Materials Research*, v. 41, p. 99–132, 2011.

LEE, H. et al. Mussel-inspired surface chemistry for multifunctional coatings. *Science*, v. 318, n. 5849, p. 426–430, 2007.

LEE, H. A.; PARK, E.; LEE, H. Polydopamine and Its Derivative Surface Chemistry in Material Science: A Focused Review for Studies at KAIST. *Advanced Materials*, v. 32, n. 35, p. 1–20, 2020.

LEE, H.; LEE, B. P.; MESSERSMITH, P. B. A reversible wet / dry adhesive inspired by mussels and geckos. *Nature*, v. 448, p. 338–342, 2007.

LIU, F. et al. *Polydopamine-based polysaccharide materials for water treatment*. [s.l.] Springer Netherlands, 2022. v. 29

LIU, Y.; AI, K.; LU, L. Polydopamine and Its Derivative Materials : Synthesis and Promising Applications in Energy , Environmental , and Biomedical Fields. *Chemical Reviews*, v. 114, p. 5057–5115, 2014.

MACHADO, K. C. et al. A preliminary nationwide survey of the presence of emerging contaminants in drinking and source waters in Brazil. *Science of the Total Environment*, v. 572, p. 138–146, 2016. Disponível em: <<http://dx.doi.org/10.1016/j.scitotenv.2016.07.210>>.

MARANI, P. L.; BLOISI, G. D.; PETRI, D. F. S. Hydroxypropylmethyl cellulose films crosslinked with citric acid for control release of nicotine. *Cellulose*, v. 22, n. 6, p. 3907–3918, 2015.

MARTÍN, J. et al. Occurrence of pharmaceutical compounds in wastewater and sludge from



wastewater treatment plants : Removal and ecotoxicological impact of wastewater discharges and sludge disposal. v. 240, p. 40–47, 2012.

MENESES, I. P. et al. CTAB-modified carboxymethyl cellulose/bagasse cryogels for the efficient removal of bisphenol A, methylene blue and Cr(VI) ions: Batch and column adsorption studies. *Journal of Hazardous Materials*, v. 421, p. 126804, 2022.

MOORE, P. H.; BOTHA, F. C. *Sugarcane: Physiology, Biochemistry and Functional Biology*. 1st editio ed. [s.l.] Oxford: Wiley-Blackwell, 2013.

NOVAES, S. D.; OLIVEIRA, P. V.; PETRI, D. F. S. Hydroxypropyl methylcellulose-sugarcane bagasse adsorbents for removal of 17 $\alpha$ -ethinylestradiol from aqueous solution and freshwater. *Environmental Science and Pollution Research*, n. 0123456789, 2022a. Disponível em: <<https://doi.org/10.1007/s11356-022-20345-4>>.

NOVAES, S. D.; OLIVEIRA, P. V.; PETRI, D. F. S. Hydroxypropyl methylcellulose-sugarcane bagasse adsorbents for removal of 17 $\alpha$ -ethinylestradiol from aqueous solution and freshwater. *Environmental Science and Pollution Research*, v. 29, n. 42, p. 63936–63952, 2022b. Disponível em: <<https://doi.org/10.1007/s11356-022-20345-4>>.

NURMINEN, M. L. et al. Coffee, caffeine and blood pressure: A critical review. *European Journal of Clinical Nutrition*, v. 53, n. 11, p. 831–839, 1999.

PETEFFI, G. P. et al. Caffeine levels as a predictor of Human mastadenovirus presence in surface waters—a case study in the Sinos River basin—Brazil. *Environmental Science and Pollution Research*, v. 25, n. 16, p. 15774–15784, 2018.

PONZIO, F. et al. Oxidant Control of Polydopamine Surface Chemistry in Acids: A Mechanism-Based Entry to Superhydrophilic-Superoleophobic Coatings. *Chemistry of Materials*, v. 28, n. 13, p. 4697–4705, 2016.

QUESADA, H. B. et al. Caffeine removal by chitosan/activated carbon composite beads:

Adsorption in tap water and synthetic hospital wastewater. *Chemical Engineering Research and Design*, v. 184, p. 1–12, 2022. Disponível em: <<https://doi.org/10.1016/j.cherd.2022.05.044>>.

REZENDE, C. A. et al. Chemical and morphological characterization of sugarcane bagasse submitted to a delignification process for enhanced enzymatic digestibility. *Biotechnology for Biofuels*, v. 4, n. November, 2011.

RYU, J. H.; MESSERSMITH, P. B.; LEE, H. Polydopamine Surface Chemistry: A Decade of Discovery. *ACS Applied Materials and Interfaces*, v. 10, n. 9, p. 7523–7540, 2018.

SEDDIQUI, H. et al. *Cellulose and its derivatives: towards biomedical applications*. [s.l.] Springer Netherlands, 2021. v. 28

SHAKEEL, F.; RAMADAN, W. Colloids and Surfaces B: Biointerfaces Transdermal delivery of anticancer drug caffeine from water-in-oil nanoemulsions. v. 75, p. 356–362, 2010.

SLEDZ, W. et al. Antibacterial activity of caffeine against plant pathogenic bacteria. *Acta Biochimica Polonica*, v. 62, n. 3, p. 605–612, 2015.

SOUSA, J. C. G. et al. A review on environmental monitoring of water organic pollutants identified by EU guidelines. *Journal of Hazardous Materials*, v. 344, p. 146–162, 2018. Disponível em: <<http://dx.doi.org/10.1016/j.jhazmat.2017.09.058>>.

TOLEDO, P. V. O. et al. Carboxymethyl cellulose/poly(acrylic acid) interpenetrating polymer network hydrogels as multifunctional adsorbents. *Cellulose*, v. 26, n. 1, p. 597–615, 2019. Disponível em: <<https://doi.org/10.1007/s10570-018-02232-9>>.

VARSHOSAZ, J. et al. Formulation and characterization of cellulose acetate butyrate nanoparticles loaded with nevirapine for HIV treatment. *Journal of Drug Delivery Science and Technology*, v. 48, n. August, p. 9–20, 2018. Disponível em: <<https://doi.org/10.1016/j.jddst.2018.08.020>>.

VIGNOLI, J. A.; BASSOLI, D. G.; BENASSI, M. T. Antioxidant activity , polyphenols ,

caffeine and melanoidins in soluble coffee : The influence of processing conditions and raw material. *Food Chemistry*, v. 124, n. 3, p. 863–868, 2011.

YU, X. X.; FERNANDEZ, H. H. Dopamine agonist withdrawal syndrome : A comprehensive review. *Journal of the Neurological Sciences*, v. 374, p. 53–55, 2017. Disponível em: <<http://dx.doi.org/10.1016/j.jns.2016.12.070>>.

## 2 OBJECTIVE

The main goal of this thesis was to understand the physicochemical properties of polydopamine coatings on substrates with different surface energy and to manage them in order to develop biobased adsorbents for organic and inorganic pollutants.

### **3 CHAPTER 1 - Polydopamine coated cellulose acetate butyrate microbeads for caffeine removal**

Accepted version of article reproduced with permission from [ Furtado, L. M.; ANDO, Ando, R. A; Petri, Denise F.S. Polydopamine-coated cellulose acetate butyrate microbeads for caffeine removal. JOURNAL OF MATERIALS SCIENCE , v. 55, p. 3243-3258, 2019. Copyright 2019 Journal of Material Science]. The written permission is at Appendices 9.1.1 . The published version of this article can be accessed in the link: DOI: 10.1007/s10853-019-04169-1 ( <https://link.springer.com/article/10.1007/s10853-019-04169-1> )

#### **Abstract**

In this study, coatings of polydopamine (PDA) in the presence of caffeine were investigated upon their deposition on substrates with different surface energies. The physicochemical properties and stability of PDA coatings deposited in the absence and presence of caffeine (C/PDA) on Si/SiO<sub>2</sub> (high surface energy), cellulose acetate butyrate (CAB) (intermediate surface energy) and polystyrene (PS) (low surface energy) surfaces were investigated by means of ellipsometry, contact angle measurements and X-ray photoelectron spectroscopy (XPS). In order to gain insight about the interactions between caffeine and PDA at molecular level, Raman and infrared (FTIR-ATR) spectroscopy measurements were performed for PDA and C/PDA and the results were supported by density functional theory (DFT) calculations. In comparison to bare PDA, the C/PDA system displayed an increase of the deposition rate on all substrates, indicating co-deposition of caffeine and PDA. PDA and C/PDA coatings turned hydrophobic substrates into hydrophilic surfaces and vice-versa. PDA coatings on CAB and PS films were the most stable systems. CAB/PDA microbeads

were created and tested as new adsorbents for caffeine presenting adsorption capacity of  $10 \pm 1 \text{ mg g}^{-1}$ .

### 3.1 MOTIVATION

More than one decade ago polydopamine (PDA) was successfully presented as a versatile coating for organic and inorganic materials surfaces (LEE et al., 2007a; RYU; MESSERSMITH; LEE, 2018). The simple immersion of substrates into a dopamine solution containing dissolved  $\text{O}_2$ , under alkaline medium, led to the spontaneous formation and deposition of PDA on the surfaces. PDA is not a polymer with the monomeric units covalently bonded, it results from the aggregation of different products of dopamine oxidation process (dopamine quinone, 5,6-dihydroxyindole (DHI), catecholamine-based products) (DELLA VECCHIA et al., 2013; KLOSTERMAN; RILEY; BETTINGER, 2015; KIM et al., 2016; CHEN et al., 2017; MICILLO et al., 2017). The attachment of catechol groups to the surface is one of the explanations for the strong adhesion of PDA to various substrates. On the other hand, if the medium pH is higher than 9.5, which is close to the  $\text{pK}_a$  of DHI catechol groups, the solubility of PDA increases and the thickness of adsorbed PDA decreases (KLOSTERMAN; RILEY; BETTINGER, 2015). The chemical composition and roughness of the substrate also affect the PDA deposition, e.g., the thickness of PDA films tends to increase with the substrate hydrophobicity (JIANG et al., 2011; KLOSTERMAN; RILEY; BETTINGER, 2015) and roughness (JIANG et al., 2011). The adhesion forces between PDA coated silica nanoparticles and substrates with different surface energies indicated stronger affinity of PDA for hydrophobic surfaces (ZHANG et al., 2017).

Caffeine is a methylxanthine naturally found in coffee beans and leaves of tea plants. It stimulates signaling for the production and release of endogenous catecholamines, such as dopamine, in living beings (VOLKOW et al., 2015). Studies about the interaction between polymers and

caffeine are often related to adsorption process (ANDREEVA; DMITRIENKO; ZOLOTOV, 2010; LAVOINE et al., 2015). Polymeric adsorbents might be used to pre-concentrate caffeine from urine, considering that the caffeine concentration in urine might be low for the direct detection with conventional analytical methods. For instance, the maximal concentration of caffeine in athlete urine allowed by the International Olympic Committee is 12 mg/L (DE ARAGÃO et al., 2005), which is in the low limit of spectrophotometric methods. The development of adsorbents for caffeine pre-concentration is important for the determination of the caffeine concentration in wastewater and sludge from wastewater treatment (MARTÍN et al., 2012) because caffeine has been included in the group of emerging water organic pollutants (SOUSA et al., 2018).

Caffeine has two fused aromatic rings, two polar carbonyl groups, three nonpolar methyl groups and four nitrogen atoms, one of which can act as hydrogen-bond acceptor (**Figure 3.1a**). The solubility of caffeine molecules in water is limited at room temperature due to stacked aggregation, which is favored by the caffeine planar structure (TAVAGNACCO et al., 2018)(JOHNSON et al., 2017). Tavagnacco and co-workers showed by molecular dynamics simulations that caffeine molecules self-associate by a face-to-face stacking, but the interactions between caffeine and pyridine take place in a tilted-perpendicular orientation with some pair stackings (TAVAGNACCO et al., 2018).

The co-deposition of dopamine or PDA and co-components opens the possibility to create functional surfaces, as recently reviewed (QIU; YANG; XU, 2018). The final properties of such surfaces depend on the interactions between PDA and the added component. To the best of our knowledge, investigations about the interactions between PDA and caffeine are seldom reported in the literature, despite the relevance in biological systems. In a recent *in vivo* study, the administration of caffeine combined with dopamine increased *Daphnia*'s heart rate more than when each agent was administered alone (SINGH; KUNDU, 2018), evidencing synergistic activity between caffeine and

dopamine. The present study was conducted in view of the academic and practical need of understanding the PDA-caffeine interactions. In the first part of this work, the PDA-caffeine interactions were investigated by the deposition of PDA in the absence and presence of caffeine (C/PDA) on solid substrates. The deposition rates of PDA or C/PDA on Si/SiO<sub>2</sub> wafers, polystyrene (PS) and cellulose acetate butyrate (CAB) films were systematically investigated at pH 8.3 by means of ellipsometry. The criterion to choose the substrates was the surface energy. Thus, Si/SiO<sub>2</sub>, high surface energy, CAB, intermediate surface energy and PS, low surface energy substrates were used as model substrates. The physicochemical properties of resulting PDA and C/PDA coatings were carefully analyzed by chemical stability tests, contact angle measurements, atomic force microscopy (AFM) and X-ray photoelectron spectroscopy (XPS). In the second part, Raman and Fourier transform infrared (FTIR) spectroscopy measurements and density functional theory (DFT) calculations were performed in order to gain insight about the interactions between caffeine and PDA at molecular level. Based on the results from the first and second parts, the CAB/PDA system was successfully applied as a new adsorbent for caffeine.

## 3.2 EXPERIMENTAL SECTION

### 3.2.1 Materials

Dopamine hydrochloride (Sigma H60255, 189.64 g/mol), caffeine (Sigma W222402, 194.19 g/mol), Tris(hydroxymethyl) aminomethane hydrochloride (Tris-HCl) buffer (Sigma 10812846001, 157.60 g/mol), polystyrene (PS, Sigma 441147,  $M_w \sim 350,000$  g/mol), and cellulose acetate butyrate (CAB 551-0.2,  $M_v \sim 30,000$  g/mol, acetate, and butyrate degree of substitution,  $DS_{Ac} = 0.2$  and  $DS_{But} = 2.5$ ), kindly provided by Eastman Chemical Co., Brazil, were used without previous purification. **Figure 3.1** represents their chemical structures. Silicon (100) wafers with native SiO<sub>2</sub> layer (University Wafer, USA) were cleaned with isopropanol prior to use.



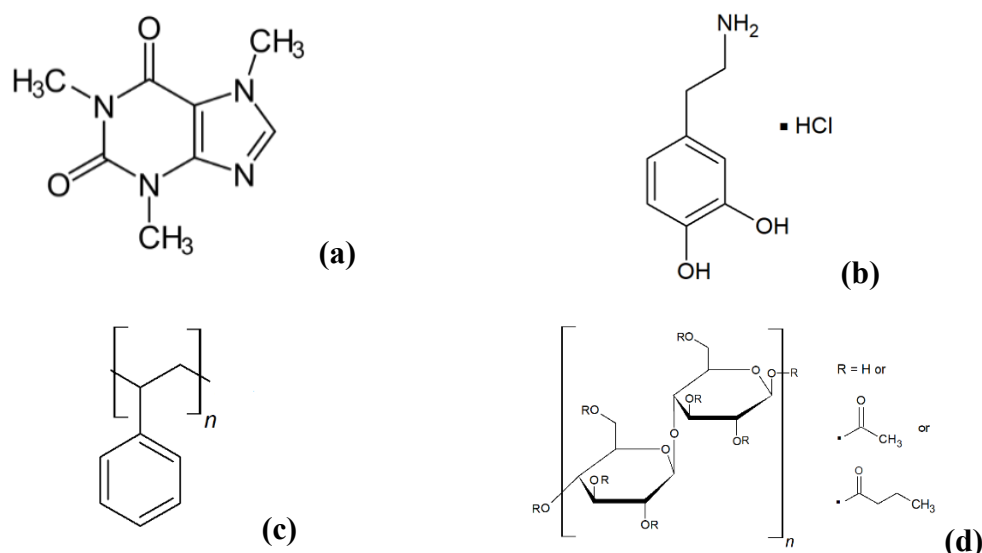


**Figure 3.1:** Schematic representation of chemical structures of (a) caffeine (C), (b) dopamine hydrochloride, (c) polystyrene (PS) and (d) cellulose acetate butyrate (CAB).

### 3.2.2 Deposition of PDA on solid substrates in the absence and in the presence of caffeine

Caffeine and dopamine were dissolved in 10 mM Tris-HCl buffer (pH 8.3) at the molar ratio caffeine:dopamine 1.0 (0.010 mol/L:0.010 mol/L). Dopamine and caffeine were dissolved separately in 10 mM Tris-HCl buffer at 0.010 mol/L (or 2.0 g/L), for control experiments. The Si/SiO<sub>2</sub> wafers were immersed in the solutions of caffeine:dopamine, neat caffeine and neat dopamine in open vials. After 0.25, 0.5, 1, 2, 3, 4, 5, 6 and 24 h contact, the substrates were withdrawn from the solution and then, they were extensively rinsed with MilliQ water and dried under a stream of N<sub>2</sub>. The effect of temperature on the film deposition on Si/SiO<sub>2</sub> wafers was investigated for solutions of caffeine:dopamine at molar ratio 1.0, at 11 ± 1 °C and 25 ± 1 °C. At temperatures larger than 35 °C, there was significant solvent evaporation, hindering the experiments. On the other hand, in closed vial. The O<sub>2</sub> content would not be comparable to that in the open vials. During the deposition experiments, the systems were not stirred.

CAB and PS films were also used as substrates; solutions of CAB in ethyl acetate or PS in toluene at 10 g/L were spin-coated on Si/SiO<sub>2</sub> wafers (Headway PWM32-PS-R790) at 3000 rpm for

30 s, at  $24 \pm 1$  °C and 65% relative air humidity. CAB and PS films were immersed into solutions of caffeine:dopamine at molar ratio 1.0, at  $11 \pm 1$  °C and  $25 \pm 1$  °C in open vials. After 0.25, 0.5, 1, 2, 3 and 24 h contact, the substrates were removed from the solution and then, they were extensively rinsed with MilliQ water and dried under a stream of N<sub>2</sub>.

### 3.2.3 Stability of PDA and C/PDA coatings

The stability of PDA and C/PDA coatings on Si/SiO<sub>2</sub> wafers, CAB and PS films was evaluated. Briefly, after 24 h deposition, the substrates were removed from the solution, rinsed with MilliQ water, and dried under a stream of N<sub>2</sub>. After that, the PDA- and C/PDA-coated substrates were immersed in phosphate saline buffer (PBS 0.010 mol/L, pH 7.4), Tris-HCl buffer (pH 8.3) and NaOH 0.1 mol/L (pH 13), at  $25 \pm 1$  °C, and kept in closed vials. After 10 min, 1 h, 3 h, 6h, 8h, 24 h, 72 h and 96 h of contact photographs were taken, the substrates were removed and analyzed by ellipsometry (see details below), whereas the supernatants were analyzed by UV spectrophotometry. In the case of pH 13, droplets of concentrated HCl were added to the supernatants until media pH  $\sim$  1.0; after that, tiny dark particles formed and settled to the bottom of the vials. The supernatants stemming from these systems at pH 1 were analyzed by UV spectrophotometry. The stability of neat Si/SiO<sub>2</sub> wafers, CAB and PS films at pH 7.4, pH 8.3 and pH 13 was evaluated under the same conditions.

### 3.2.4 Characterization of PDA and C/PDA coatings

The mean thickness of PDA and caffeine/PDA (C/PDA) films was determined in air by means of ellipsometry (DRE-EL02, Germany) with angle of incidence  $\Phi$  at 70° and wavelength  $\lambda$  of 632.8 nm. For data interpretation, a multilayer model composed of substrate, unknown layer and air was used. Then, the thickness ( $d_x$ ) and the refractive index ( $n_x$ ) of the unknown layer were calculated with

the ellipsometric angles  $\Delta$  and  $\Psi$ , the fundamental equation of ellipsometry and the interactive calculations with the matrices of Jones (AZZAM; BASHARA, 1996):

$$e^{i\Delta} \tan \Psi = \frac{R_p}{R_s} = f(n_k, d_k, \lambda, \phi) \quad 3.1$$

where  $R_p$  and  $R_s$  are the total reflectance coefficients of the parallel and perpendicular waves, which are a function of  $\Phi$ ,  $\lambda$ , the refractive index  $n_k$  and the thickness  $d_k$  of each layer of the model. From  $\Delta$  and  $\Psi$  values and the multilayer model composed of Si, SiO<sub>2</sub>, polymer layer (CAB or PS), layer of PDA or caffeine or C/PDA and air it is possible to determine the thickness of the last layer that is in contact with the air. First, the thickness of the SiO<sub>2</sub> layer was calculated considering the Si refractive index as  $\tilde{n} = 3.88 + i0.018$  and infinite thickness, the refractive indices of air and SiO<sub>2</sub> as 1.00 and 1.462 (PALIK, 1985), respectively. The mean thickness of the SiO<sub>2</sub> layer was determined over 220 samples as  $(2.0 \pm 0.2)$  nm. The mean thickness of the CAB and PS spin-coated films was calculated as  $(85 \pm 8)$  nm and  $(69 \pm 9)$  nm, respectively considering the refractive index of 1.475 (KOSAKA; KAWANO; PETRI, 2007) and 1.583 (PEREIRA et al., 2010), respectively. For the calculation of the thickness of deposited films, the index of refraction of PDA and caffeine were  $1.73 + i0.02$  (BERNSMANN et al., 2009) and 1.68 (CHEMSPIDER, 2019), respectively; their average (1.70) was used as index of refraction for C/PDA layer because there was no value reported for the mixture of caffeine and PDA. The mean thickness and corresponding standard deviation were determined for at least three different samples of the same system. The standard deviations achieved up to 20% of the mean value, due to partial light scattering on the surface of some rough films, particularly after 24 h deposition.

The contact angle measurements were performed by the sessile drop method (SEO Phoenix – I, Korea). The surface energy ( $\gamma_S$ ) of the PDA and C/PDA films deposited on Si/SiO<sub>2</sub> wafers, PS and CAB films was assessed by means of contact angles ( $\theta$ ) performed with droplets (10  $\mu$ L) of diiodomethane ( $\gamma_L = 50.8$  mJ/m<sup>2</sup>;  $\gamma_{pL} = 2.3$  mJ/m<sup>2</sup> and  $\gamma_{dL} = 48.5$  mJ/m<sup>2</sup>) and water ( $\gamma_L = 72.0$  mJ/m<sup>2</sup>;

$\gamma_p L = 50.2 \text{ mJ/m}^2$  and  $\gamma_d L = 21.8 \text{ mJ/m}^2$ ) (BOUALI et al., 1998). The polar ( $\gamma_p$ ) and dispersive ( $\gamma_d$ ) components of the surface energy were determined by Owens–Wendt's equation (OWENS; WENDT, 1969), also known as geometric mean equation. Atomic force microscopy (AFM) analyses were performed in the air at room temperature with Pico SPM-LE, Molecular Imaging (USA) microscope, in the intermittent contact mode, using silicon cantilevers with resonance frequency close to 300 kHz, all images were obtained with scan size  $0.6 \mu\text{m} \times 0.6 \mu\text{m}$ , the root mean square roughness (RMS) values were calculated with the PicoScan software. X-ray photoelectron spectroscopy (XPS, K-Alpha spectrometer, Thermo Fisher Scientific, UK) analyses were performed in order to determine the chemical composition on the surface of PDA and C/PDA films deposited on Si/SiO<sub>2</sub> wafers or PS films after 24 h. The X-ray source was the monochromatic Al K $\alpha$  ( $h\nu = 1486.6 \text{ eV}$ ). XPS survey spectra was developed with pass energy of 200 eV and 1.0 eV/step, which allowed determinate the ratio N/C followed by high-resolution spectra of C 1s, N1s and O1s with a pass energy of 50 eV and 0.1 eV/step, accumulating 30-50 scans. At least three films of the same composition were analyzed at different areas of the surface.

### 3.2.5 Raman and FTIR spectroscopy of PDA and C/PDA

Caffeine and dopamine were dissolved in 10 mM Tris-HCl buffer (pH 8.3) at the molar ratio caffeine:dopamine 1.0 (0.010 mol/L:0.010 mol/L). Dopamine and caffeine were dissolved separately in 10 mM Tris-HCl buffer at 0.010 mol/L (or 2.0 g/L), for control experiments. After 24 h, the samples were centrifuged at 2650 rpm for 10 min. The resonance Raman spectra of the supernatants were acquired in adapted NMR tubes in a rotating cell in a Horiba-Jobin-Yvon triple monochromator, T64000 spectrometer, excited at  $\lambda_0 = 405 \text{ nm}$  from a Toptica diode laser. The control experiments were also analyzed by Raman spectroscopy (Renishaw InVia Reflex coupled to a Leica DM2500 M microscope using an Olympus 50x objective, and a He-Ne Renishaw excitation laser at  $\lambda_0 = 632.8 \text{ nm}$ ). The precipitate was rinsed three times with MilliQ water, dried in oven at 45 °C overnight and

analyzed by Fourier transform infrared vibrational spectroscopy in the attenuated total reflectance mode in an Alpha FTIR-ATR, Bruker, with a diamond crystal, accumulating 64 scans at  $2\text{ cm}^{-1}$  of resolution.

### 3.2.6 DFT calculations

The calculations were performed using software Gaussian 09 (FRISCH et al., 2016) with the B3LYP functional and the 6-311++G(d,p) as basis set. The PDA structure chosen was based on a systematic DFT screening investigation of different possible PDA structures proposed by Chen and co-workers (CHEN et al., 2017). The vibrational analysis was performed revealing no negative frequencies, indicating the structures are in a minimum of the surface potential energy. The Raman and IR spectra were plotted using a Maple script considering  $5\text{ cm}^{-1}$  of FWHM and no scaling factor was applied.

### 3.2.7 Preparation of PDA coated microbeads for caffeine adsorption

Five mL of dopamine solution (10 mM Tris-HCl buffer) at 1.55 g/L was added to eight mL of CAB solution in ethyl acetate at 25 g/L under magnetic stirring at 50 °C. After 24 h stirring, the system was cooled down to 25 °C and centrifuged at 2,000 rpm for 10 min. The top dark phase was separated and dripped in 20 mL MilliQ water, where dark brown CAB/PDA microbeads were formed (**Supplementary Information S11**). Eight mL of PS solution in toluene at 25 g/L was added to 5 mL of dopamine solution (10 mM Tris-HCl buffer) at 1.55 g/L under magnetic stirring at 50 °C. After 24 h stirring, the system was cooled down to 25 °C and centrifuged at 530 g for 10 min. The top dark phase was separated and dripped in 20 mL MilliQ water, but no PS/PDA bead was formed, only a polymeric film was observed on the vial internal surface. Glass microbeads (200  $\mu\text{m}$  mean diameter, 10 g) were added to 10 mL of dopamine solution (10 mM Tris-HCl buffer) at 2.0 g/L under magnetic stirring at 50 °C, during 24 h. After that, the system was cooled down to 25 °C and centrifuged at 530

g for 10 min. The glass microbeads became dark brown and the supernatant turned light brown. The CAB/PDA microbeads were characterized by confocal fluorescence microscopy (Zeiss LSM 510, Germany).

For the adsorption of caffeine, typically 10 mg of dried adsorbent (CAB/PDA microbeads) was added to 2 mL caffeine solution prepared at the concentration range of 0.005 g/L to 2.0 g/L. The systems were shaken during 24 h; after that, the concentration of caffeine in the supernatant was determined by spectrophotometry ( $\lambda = 270$  nm). The concentration of adsorbed caffeine molecules onto CAB/PDA beads was determined as the difference between the initial caffeine concentration ( $C_0$ ) and that determined in the supernatant, or the equilibrium concentration ( $C_e$ ). The equilibrium adsorption capacity ( $q_e$ , mg g<sup>-1</sup>) was calculated dividing the concentration of adsorbed specie by the mass of dried adsorbent ( $m$ ) and multiplying by the solution volume ( $v$ ):

$$q_e = \frac{C_0 - C_e}{m} \times v \quad 3.2$$

### 3.3 RESULTS AND DISCUSSION

#### 3.3.1 Deposition of PDA or C/PDA on different substrates

**Supplementary Information SI2** shows the mean thickness values ( $d$ ) determined for the deposition of PDA in the absence and in the presence of caffeine at  $11 \pm 1$  °C and  $25 \pm 1$  °C, on Si/SiO<sub>2</sub> wafers, PS and CAB films, as a function of time. The exponential function fitted the experimental data (BALL et al., 2012):

$$d(t) = d(0) + d_{max}(1 - e^{-kt}) \quad 3.3$$

where  $k$  and  $d_{max}$  are the kinetic constant and maximal thickness, respectively.

**Table 3.1** presents the fitting parameter  $d_{max}$  for each system. The  $d_{max}$  values of C/PDA on Si/SiO<sub>2</sub>, PS and CAB were higher than those determined for neat PDA, regardless of the temperature and substrates. The largest  $d_{max}$  value (44 nm) was observed for C/PDA on Si/SiO<sub>2</sub> at 25 °C; it was

significantly larger than the  $d_{\max}$  value of PDA (20 nm) on Si/SiO<sub>2</sub> at the same temperature. One should notice that caffeine molecules did not adsorb onto any of the neat substrates, regardless of the temperature. Thus, one might consider two possibilities: (i) PDA and caffeine co-adsorb on the surface, making the C/PDA layers thicker or (ii) caffeine molecules adsorb on a PDA pre-adsorbed layer. In order to check the second hypothesis, caffeine (2 mL of caffeine solution at 0.020 mol/L) was added to the medium after 2 h of PDA deposition on Si/SiO<sub>2</sub> (2 mL, initial concentration of 0.010 mol/L). After 24 h, the  $d_{\max}$  value amounted to 32 nm (**Supplementary Information SI3**), which is larger than that observed for neat PDA (20 nm) on Si/SiO<sub>2</sub>, but smaller than that for C/PDA (44 nm). This finding allows concluding that the second hypothesis is wrong. Therefore, the pronounced adsorption from the C/PDA mixture implies the co-adsorption of caffeine and PDA on the substrates.

**Table 3.1:** Fitting parameters determined for the deposition of PDA and C/PDA 1.0 on Si/SiO<sub>2</sub> wafers, PS and CAB films at  $11 \pm 1$  °C and  $25 \pm 1$  °C, using Equation 3.3.

	T (°C)	System	$d_0$ (nm)	$d_{\max}$ (nm)	$k$ (h <sup>-1</sup> )	R <sup>2</sup>
Si/SiO <sub>2</sub>	11	PDA	0.36	20	0.11	0.9892
		C/PDA 1.0	0.30	26	0.11	0.9966
	25	PDA	0.63	20	0.11	0.9784
		C/PDA 1.0	-1.4	44	0.12	0.9898
PS	11	PDA	0.61	18	0.11	0.9565
		C/PDA 1.0	0.50	24	0.10	0.9912
	25	PDA	0.26	22	0.11	0.9767
		C/PDA 1.0	0.78	25	0.10	0.9503
CAB	11	PDA	0.044	17	0.14	0.9679
		C/PDA 1.0	$5.3 \times 10^{-4}$	22	0.10	0.9622
	25	PDA	-0.38	27	0.10	0.9929
		C/PDA 1.0	-2.4	34	0.18	0.8847

At 11 °C, the  $d_{\max}$  values determined for PDA and C/PDA tended to be smaller than those determined at 25 °C, regardless of the substrate. The decrease of the autoxidation of dopamine is not a plausible explanation because according to Henry's law, the dissolution of O<sub>2</sub> in water should

increase by cooling down, implying in thicker PDA and C/PDA coatings at low temperatures. Therefore, the tendency observed might be due to the adsorption process, which is weakened by decreasing the deposition temperature. On the other hand, the deposition kinetic constant  $k$  values showed no significant dependence on temperature or substrate. The  $k$  values determined for PDA onto Si/SiO<sub>2</sub> wafers at 11 °C or 25 °C amounted to 0.11 h<sup>-1</sup>, in agreement with the  $k$  value reported by Ball and co-workers (BALL et al., 2012).

For all substrates, the deposition behavior indicated that from the beginning up to 3 h, the thickness increased linearly with the time, being the slopes the initial deposition rates for PDA and C/PDA (**Supplementary Information SI4**). At 25 °C, the initial deposition rates of PDA and C/PDA were similar and amounted to  $2.7 \pm 0.5$  nm/h, consistent with the deposition rate determined for PDA (from initial concentration of 0.0106 mol/L) on Si/SiO<sub>2</sub> by Ball's group as 2.8 nm/h (BERNSMANN et al., 2009; BALL et al., 2012). The deposition experiments performed at 11 °C led to the initial deposition rates of PDA and C/PDA amounted to  $2.1 \pm 0.5$  nm/h, which is smaller than the value determined at 25 °C. This finding evidences that the temperature affects predominantly the initial stages of deposition. Jiang and coworkers observed similar behavior for PDA (initial concentration of dopamine at 0.010 mol/L) on Si/SiO<sub>2</sub> wafers and poly(vinylidene fluoride) in the temperature range of 20 °C to 40 °C; they attributed this effect to the surface roughness increase (JIANG et al., 2011). Noteworthy, probably the  $k$  values (Table 3.1) showed no significant dependence on temperature because they resulted from fits over the whole adsorption period (24 h).

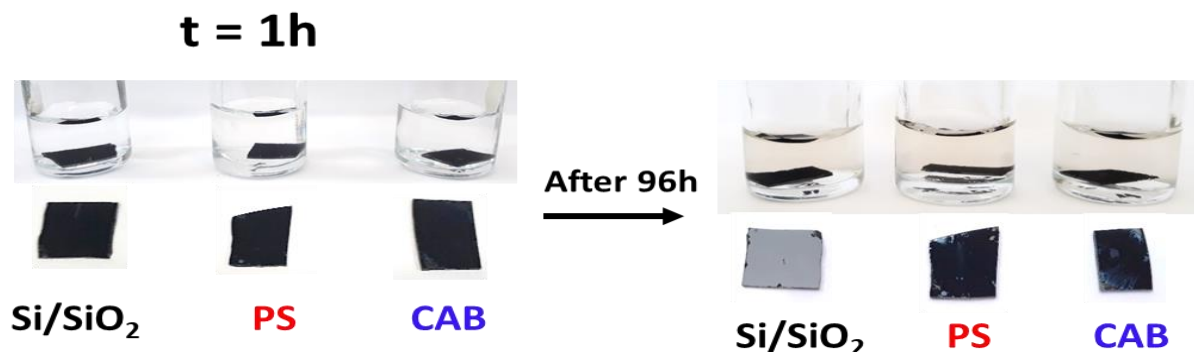
### 3.3.2 Stability of PDA or C/PDA layers deposited on different substrates

**Figure 3.2a** and **Figure 3.2b** shows the photographs of the PDA and C/PDA 1.0 coating systems, respectively, taken after 1 h and 96 h contact with Tris buffer at pH 8.3. The PDA and C/PDA 1.0 coatings on Si/SiO<sub>2</sub> wafers were stable during the first hour, but after 96 h the coatings were completely detached as large aggregates, leaving the substrates as they were originally, as



evidenced by ellipsometry. From PS and CAB the PDA and C/PDA coatings were more stable than on Si/SiO<sub>2</sub> wafers and only small regions detached from the part of the films after 96 h.

(a) PDA, pH 8.3



(b) C/PDA, pH 8.3

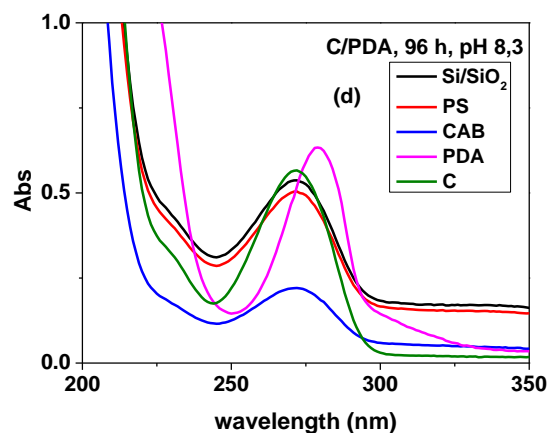
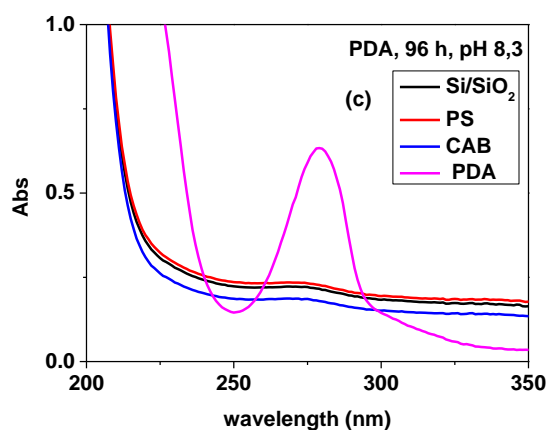


**Figure 3.2:** Photographs of (a) PDA and (b) C/PDA coatings on Si/SiO<sub>2</sub> wafers, PS and CAB films, respectively, taken after 1 h and 96 h contact with Tris buffer at pH 8.3. UV spectra determined for the supernatants of (c) PDA and (d) C/PDA coatings after 96 h contact at pH 8.3. The green line in (d) corresponds to the spectrum of pure caffeine solution at  $1.1 \times 10^{-4}$  mol/L.

The electronic spectra determined for the supernatants of PDA coatings after 1 h, 3 h, 6 h, 8 h, 24 h, 48 h, 72 h (Supplementary Information SI5) and 96 h (Figure 3.2c) contact with the liquid

media did not indicate significant amount of PDA dissolved in the medium. **Figure 3.2d** shows that caffeine was partially dissolved from the C/PDA (coatings or detached aggregates) after 96 h immersion in Tris buffer. The absorbance band at 272 nm (**Figure 3.2d**) was attributed to the caffeine  $\pi$ - $\pi^*$  electronic transitions (calibration curve available as **Supplementary Information SI6**). The concentration of caffeine released from C/PDA after 1 h or 96 h were similar and amounted to  $\sim 1 \times 10^{-4}$  mol/L from Si/SiO<sub>2</sub> wafers and PS, and to  $\sim 0.4 \times 10^{-4}$  mol/L from CAB, which corresponded to  $\sim 1\%$  and  $0.4\%$  of the original caffeine concentration (0.01 mol/L). In general, the amount of released caffeine over 96 h was too low, hindering a kinetics study. Ellipsometric measurements indicated that neat substrates (control experiment) presented no changes after 96 h, at pH 8.3. However, ellipsometric measurements were not performed for PDA or C/PDA coatings on CAB or PS because light was completely absorbed by the films. The stability of PDA and C/PDA coatings at pH 7.4 (PBS buffer, 10 mmol/L) was similar to that observed at pH 8.3, as presented in the **Supplementary Information SI7 and SI8**.

Particularly interesting were the experiments at pH 13. Immediately after contact with NaOH 0.1 mol/L, the PDA and C/PDA coatings dissolved to the medium, as shown in the movies at reference (FURTADO; ANDO; PETRI, 2019a) and (FURTADO; ANDO; PETRI, 2019b), respectively. **Figure 3.3a** and **Figure 3.3b** show the supernatants and substrates after 10 min contact, respectively. All supernatants stemming from C/PDA coatings were darker than those from PDA. The ellipsometric measurements performed for the substrates indicated total removal of PDA and C/PDA coatings on Si/SiO<sub>2</sub> wafers. In comparison to the  $d_{\max}$  values (**Table 3.1**), the reduction of PDA mean thickness on PS and CAB was  $\sim 70\%$  and  $\sim 50\%$ , respectively, evidencing better stability of PDA on CAB than on PS or Si/SiO<sub>2</sub> wafers. This finding is consistent with the stronger ( $\sim 5$ -fold larger) adhesion force of PDA to methyl terminated surfaces, in comparison to that that on hydroxyl-terminated surfaces (ZHANG et al., 2017). The reduction of C/PDA mean thickness on PS and CAB

was ~ 60% and 80 %, respectively. The qualitative analysis of Del Frari and co-workers about the stability of PDA coatings on ITO and glassy carbon in contact with sodium hypochlorite solution indicated that the degradation kinetics strongly depends on the nature of the substrate (DEL FRARI et al., 2012) The easy detachment of the PDA and C/PDA coatings are expected because at pH > 10 the SiO<sub>2</sub> surface begins to dissolve (NIIBORI et al., 2000). Regarding the PDA and C/PDA layers on PS and CAB, after 96 h at pH 8.3, the coatings did not change significantly and at pH 13 they dissolved partially. These findings indicate that the PDA and C/PDA coatings are more resistant on PS or CAB than on Si/SiO<sub>2</sub> wafers. Ellipsometric measurements indicated that neat substrates (control experiment) presented no significant changes after 96 h at pH 8.3 or after 10 min at pH 13, except for CAB, that the film was slightly damaged at pH 13 (**Supplementary Information SI9**).

The dissolved PDA and C/PDA at pH 13 formed brown solutions, it was only possible to observe aggregates in the PDA system, but not in the C/PDA system (Figure 3.3a). The addition of some droplets of concentrated HCl decreased the medium pH to 1.0. After one hour, tiny dark particles appeared suspended in the liquid phase, but after four h the particles settled to the bottom of the glass vials and the supernatants were clear (**Figure 3.3c**). Noteworthy, the particles did not adhere to the internal glass surface, it was very easy to disperse them by weak shaking. These findings allow concluding that under alkaline conditions, the dopamine oxidation products acquire negative charge, due to the deprotonation of carboxylic acid groups (SALOMÄKI et al., 2019), favoring the aggregates dissolution. On the other hand, under acidic conditions, the carboxylic acid groups are protonated, favoring H bonds and  $\pi$ - $\pi$  interactions among the dopamine oxidation products and their aggregation. The clear supernatants observed in **Figure 3.3c** were analyzed by UV spectrophotometry. The spectra in **Figure 3.3d** and **Figure 3.3e** correspond to systems stemming from PDA and C/PDA coatings, respectively. Regardless of the substrate, the spectra allowed identifying the presence of solution fractions of PDA and caffeine in the supernatants. The

supernatant stemming from C/PDA on PS contained a small amount of tiny aggregates that scattered the light, increasing the absorbance values (red line, in **Figure 3.3e**). The less intense band was observed for the supernatant from C/PDA on CAB, indicating that C/PDA on CAB was the most stable system under extreme alkaline and acid conditions.

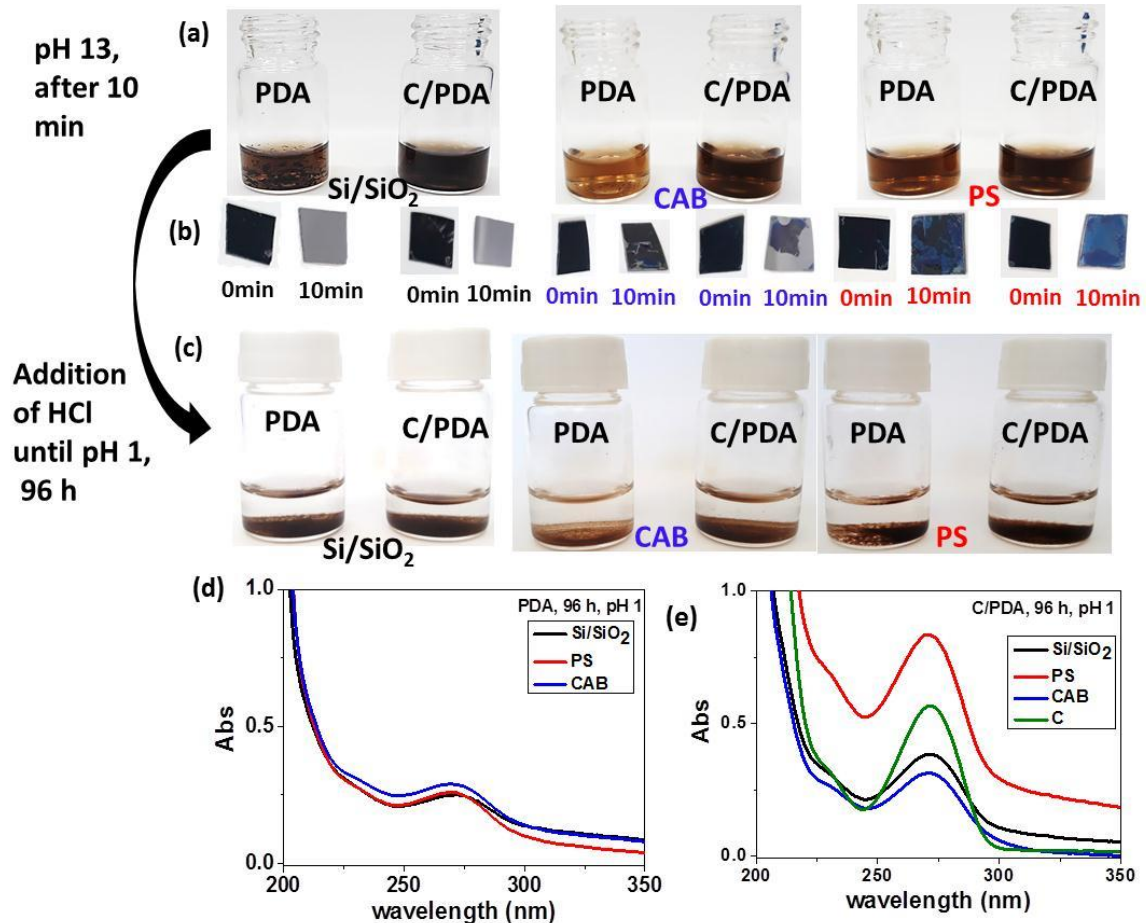


**Figure 3.3:** Photographs of the (a) vials with PDA and C/PDA 1.0 coatings dissolved at pH 13, (b) PDA and C/PDA 1.0 coated Si/SiO<sub>2</sub> wafers, PS and CAB films before (0 min) and after 10 min contact with NaOH 0.1 mol/L, (c) vials with precipitated PDA and C/PDA at pH 1.0, after 96 h resting. (d) and (e) UV spectra of the supernatants observed in (c). The green line in (e) corresponds to the spectrum of pure caffeine solution at  $1.1 \times 10^{-4}$  mol/L.

### 3.3.3 Characterization of PDA and C/PDA coatings

**Figure 3.4** shows AFM images (600 nm x 600 nm) images of PDA and C/PDA 1.0 after 2 h deposition at  $25 \pm 1$  °C on Si/SiO<sub>2</sub>, PS and CAB. The surfaces were covered by tiny spherical entities, which were assigned to the PDA aggregates adsorbed in the initial stages. Similar structures were observed for PDA on poly(diallyldimethylammonium chloride) (BERNSMANN et al., 2010). The

lowest surface roughness (RMS) was observed for PDA and C/PDA on PS. This tendency was also observed for PDA and C/PDA 1.0 deposited at  $11 \pm 1$  °C on Si/SiO<sub>2</sub>, PS and CAB (**Supplementary Information SI10**), where spherical aggregates and smooth surfaces were observed. The layers deposited at lower temperatures tended to be smoother than those adsorbed at higher temperatures, agreeing with literature data for PDA deposition (JIANG et al., 2011). The pristine Si/SiO<sub>2</sub>, PS and CAB surfaces presented RMS values of  $(0.3 \pm 0.1)$  nm,  $(2.7 \pm 0.1)$  nm and  $(5.8 \pm 0.1)$  nm, respectively. CAB was the roughest substrate due to the formation of breath figures (BLACHECHEN; SOUZA; PETRI, 2012) (**Supplementary Information SI10**) during the spin-coating process. In general, the deposition of PDA and C/PDA turned the PS and CAB surfaces smoother.

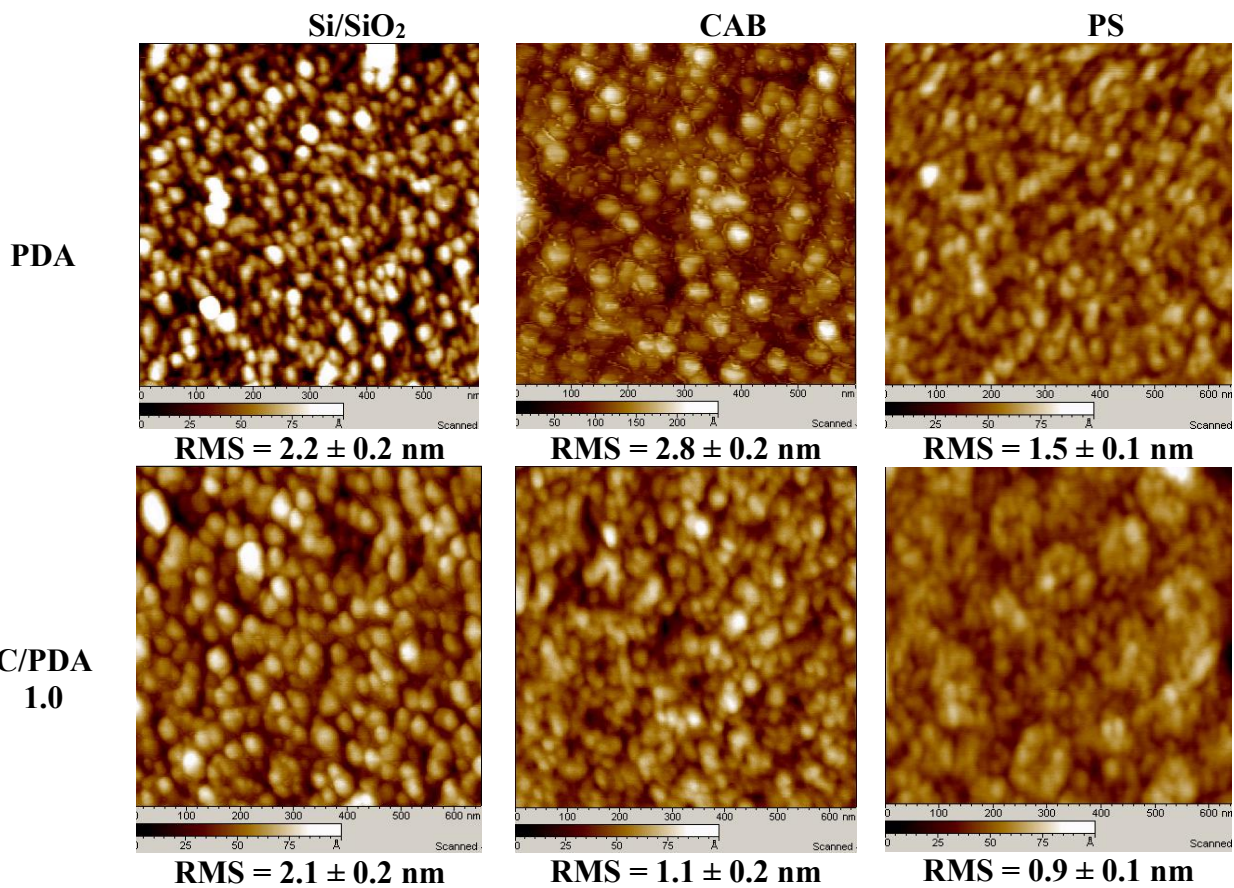


**Figure 3.4:** AFM images (600 nm x 600 nm) of PDA and C/PDA 1.0 after 2 h deposition at  $25 \pm 1$  °C, on Si/SiO<sub>2</sub>, CAB and PS, along with the corresponding RMS values.

The contact angle ( $\theta$ ) measurements performed for MilliQ water and CH<sub>2</sub>I<sub>2</sub> droplets on PDA and C/PDA deposited (24 h) at  $25 \pm 1$  °C on Si/SiO<sub>2</sub>, PS and CAB are shown in **Table 3.2**, along

with the surface energy ( $\gamma_s$ ) values ( $\gamma_{ps}$  and  $\gamma_{ds}$  stand for the polar and dispersive components of the surface energy). The  $\gamma_s$  values of pristine Si/SiO<sub>2</sub> (CACACE; LANDAU; RAMSDEN, 1997), CAB (AMIM et al., 2009) and PS (ROUXHET; GENET, 2011) substrates amount to 80.8 mJ/m<sup>2</sup>, 54.8 mJ/m<sup>2</sup> and 47 mJ/m<sup>2</sup>, respectively. The  $\gamma_s$  values determined for PDA and C/PDA 1.0 on Si/SiO<sub>2</sub> wafers were both 52.8 mJ/m<sup>2</sup>, indicating that the surface became more hydrophobic than the pristine substrate. Similarly, the  $\gamma_s$  value of neat CAB decreased from 54.8 mJ/m<sup>2</sup> to 50.1 mJ/m<sup>2</sup> and 51.9 mJ/m<sup>2</sup> after the deposition of PDA and C/PDA 1.0, respectively. On the other hand, the  $\gamma_s$  value of neat PS increased from 47 mJ/m<sup>2</sup> to 60.6 mJ/m<sup>2</sup> and 59.1 mJ/m<sup>2</sup> after the deposition of PDA and C/PDA 1.0, respectively, indicating that the surfaces became more hydrophilic. Similar behavior was observed for poly(ethylene terephthalate) (PET), whose surface energy increased from 41.3 mJ/m<sup>2</sup> to 50.2 mJ/m<sup>2</sup> after 12 h deposition of PDA at 30 °C (JIANG et al., 2011). The wettability of poly(ether ether ketone) (PEEK) increased considerably after 4 h deposition of PDA, making the PEEK/PDA scaffolds adequate for proliferation and mineralization of osteoblasts (WAN et al., 2019). The surface energy changes observed in

Table 3.2 indicate that upon adsorbing onto hydrophilic substrates the PDA and C/PDA orientated the hydrophilic residues to the surface and exposed the hydrophobic moieties to the air, whereas on hydrophobic substrate the orientation was reversed. These trends are consistent with the stability tests performed at pH 8.3 and pH 13, which clearly indicated that H bonds drive the initial deposition of dopamine oxidation products onto Si/SiO<sub>2</sub> surfaces, whereas onto PS and CAB it might be driven by  $\pi$ - $\pi$  and dipole-dipole interactions, respectively.

The  $\theta$  values determined for water on films of PDA and C/PDA deposited at  $11 \pm 1$  °C on Si/SiO<sub>2</sub>, PS and CAB during the initial deposition (up to 3 h) are available as **Supplementary Information SI11**. In the case of PDA and C/PDA on Si/SiO<sub>2</sub> wafers, the  $\theta$  values increased from 5°

(neat substrate) to  $\sim 50^\circ$  already in the first 15 minutes deposition. Mondal and co-workers (MONDAL; THAMPI; PURANIK, 2018) observed that 5,6-dihydroxyindole (DHI) formation is very fast, it takes less than 5 min. The  $\theta$  values determined for PDA and C/PDA on PS decreased gradually from  $89^\circ$  (pure PS) to the range of  $50^\circ$  to  $65^\circ$ , indicating that the molecular orientation on the hydrophobic surface evolved as the deposition proceeded. The changes of  $\theta$  values from  $68^\circ$  (pure CAB) to  $40^\circ - 55^\circ$  after deposition of PDA and C/PDA did not show any tendency as a function of deposition time.

**Table 3.2:** Contact angle ( $\theta$ ) measurements performed for MilliQ water and  $\text{CH}_2\text{I}_2$  droplets on PDA and C/PDA deposited (24 h) at  $25 \pm 1^\circ\text{C}$  on Si/SiO<sub>2</sub>, PS and CAB, along with the surface energy ( $\gamma_s$ ) values.  $\gamma_{ps}$  and  $\gamma_{ds}$  stand for the polar and dispersive components of the surface energy. N/C ratios determined from the XPS spectra obtained for PDA and C/PDA on Si/SiO<sub>2</sub> and PS, after 24 h deposition, at  $25 \pm 1^\circ\text{C}$

	$\theta \text{ H}_2\text{O} (^\circ)$	$\theta \text{ CH}_2\text{I}_2 (^\circ)$	$\gamma_{ps} (\text{mJ/m}^2)$	$\gamma_{ds} (\text{mJ/m}^2)$	$\gamma_s (\text{mJ/m}^2)$	N/C
<b>PDA on Si/SiO<sub>2</sub></b>	$66 \pm 1$	$26 \pm 1$	7.1	45.7	52.8	0.038
<b>PDA on PS</b>	$51 \pm 2$	$25 \pm 1$	14.5	46.1	60.6	0.069
<b>PDA on CAB</b>	$68.1 \pm 0.2$	$32.9 \pm 0.3$	7.1	43.0	50.1	-
<b>C/PDA on Si/SiO<sub>2</sub></b>	$64 \pm 1$	$32.0 \pm 0.3$	8.7	44.1	52.8	0.10
<b>C/PDA on PS</b>	$51.4 \pm 0.9$	$30 \pm 1$	15.0	44.1	59.1	0.066
<b>C/PDA on CAB</b>	$64 \pm 2$	$32.2 \pm 0.4$	8.6	43.3	51.9	-

The N/C ratios were determined from the XPS spectra obtained for PDA and C/PDA 1.0 on Si/SiO<sub>2</sub> and PS, after 24 h deposition, at  $25 \pm 1^\circ\text{C}$ , as presented in

Table 3.2. **Supplementary Information SI12 and SI13** present the XPS high-resolution spectra of C 1s, N 1s and O 1s and the corresponding binding energies, respectively. The XPS survey scan indicated that the ratio N/C increased from 0.038 (PDA) to 0.10 (C/PDA 1.0) on Si/SiO<sub>2</sub>, evidencing the presence of caffeine molecules on the uppermost layer. The comparison among the C



1s, N 1s and O 1s binding energies for PDA and C/PDA on Si/SiO<sub>2</sub> indicated as most significant changes the relative (i) decrease of intensities of C 1s at  $286.8 \pm 0.1$  eV ( $\underline{\text{C}}\text{-O}$ ) (XI et al., 2009; ROUXHET; GENET, 2011) and at  $292.18 \pm 0.1$  eV ( $\pi \rightarrow \pi^*$  shake up), both assigned to PDA (ZANGMEISTER; MORRIS; TARLOV, 2013a; WANG et al., 2017), (ii) increase of N 1s at  $400 \pm 0.1$  eV (substituted amine R-NH-R or indole groups) [44], which could be attributed to PDA and caffeine molecules and (iii) decrease of intensities of O 1s at  $532.9 \pm 0.2$  eV ( $\underline{\text{C}}\text{-OH}$ ), typical of PDA (ZANGMEISTER; MORRIS; TARLOV, 2013a). These features correlated well with the proposed model for C/PDA systems, where the caffeine and PDA co-adsorb on the substrates.

The C 1s, N 1s and O 1s binding energies observed for PDA and C/PDA on PS films revealed the presence of some functional groups on the surface, which were not observed on Si/SiO<sub>2</sub> and vice-versa. For instance, the binding energies of C 1s at 286.8 eV ( $\underline{\text{C}}\text{-O}$ ) and 288.7 eV ( $\underline{\text{C}}\text{=O-OH}$ ) assigned to polar functional groups were observed on Si/SiO<sub>2</sub>, but they were not observed on PS. On the other hand, the binding energy at 288.0 eV ( $\underline{\text{C}}\text{=O-NH-C}$ ) (ROUXHET; GENET, 2011)(DING et al., 2014), appeared only on PS. Possibly, during the deposition the preferential orientation of PDA and caffeine polar groups to the hydrophilic Si/SiO<sub>2</sub> surface and PDA and caffeine nonpolar groups to hydrophobic PS films induced different orientation of deposited molecules. The polar component of surface energy ( $\gamma_{ps}$ ) values determined for PDA or C/PDA on PS were approximately twice those determined for PDA or C/PDA on Si/SiO<sub>2</sub> wafers (

**Table 3.2**), indicating the preferential orientation of polar groups to the air, in the case of PS, or to the substrate, in the case of Si/SiO<sub>2</sub> wafers.

### 3.3.4 Spectroscopic study and DFT calculations

In order to gain insight about the interactions between caffeine and PDA at molecular level, Raman and FTIR-ATR spectra were acquired along with DFT calculations. **Figure 3.5a** shows the



experimental Raman and FTIR-ATR spectra along with the theoretical Raman and FTIR spectra resulting from DFT calculations considering a simple pair of a PDA oligomer interacting with caffeine. For comparison, the experimental and theoretical Raman and FTIR spectra determined for caffeine, dopamine and PDA were provided as **Supplementary Information SI14**.

Raman and FTIR-ATR spectra of caffeine presented the typical bands at  $\sim 1700\text{ cm}^{-1}$  (stretching C=O(2)) (JOHNSON et al., 2017),  $\sim 1645\text{ cm}^{-1}$  (stretching of conjugated C=O (6)) (JOHNSON et al., 2017) and  $\sim 1551\text{ cm}^{-1}$  (C=C stretching). Raman and FTIR spectra of dopamine show the characteristic catecholic C-OH (stretching) band at  $1288\text{ cm}^{-1}$  (JIANG et al., 2011). After 24 h autoxidation of dopamine, the intensity of this band decreased dramatically, but it did not disappear. Mondal and co-workers (MONDAL; THAMPI; PURANIK, 2018) observed by Raman spectroscopy that the complete consumption of dopamine and formation of PDA takes  $\sim 8$  days. On the other hand, an intense band at  $1425\text{ cm}^{-1}$  appeared in the PDA and C/PDA Raman and FTIR spectra, which was assigned to O-H bending and C=C stretching of PDA because this band is not characteristic of caffeine. Thus, the oxidation product of dopamine has a vibrational signature at  $\sim 1425\text{ cm}^{-1}$ ; in the theoretical spectra this band appears at  $\sim 1400\text{ cm}^{-1}$ . Mondal and co-workers (MONDAL; THAMPI; PURANIK, 2018) observed by Raman spectroscopy a vibrational signature of PDA formation at  $1616\text{ cm}^{-1}$ , attributed to the aromatic C-C stretching of benzene ring. Indeed, the oxidation of dopamine is a complex process and the experimental conditions (content of  $\text{O}_2$  during the reaction, time of reaction, etc) affect significantly the resulting products. Raman and FTIR spectra of C/PDA are similar to the spectra of PDA and caffeine (**Supplementary Information SI14**), and only subtle changes could be observed, probably due to the highly conjugated  $\pi$  system.

**Supplementary Information SI15** displays the approximately vibrational assignment corresponding to experimental Raman and FTIR spectra of C/PDA shown in Figure 3.5a, highlighting their corresponded bands in theoretical spectra (indicated by “\*”). The bands were

assigned to functional groups, which are presented in the chemical structures of caffeine and PDA trimers (ZANGMEISTER; MORRIS; TARLOV, 2013a) (**Figure 3.5b**) and by the visualization of each vibrational mode using the Gaussview 5.0 software. **Figure 3.5b** shows the optimized structures of caffeine and PDA trimer used for the DFT calculations. Considering the complexity of the samples, the experimental and calculated Raman and FTIR spectra presented a reasonable agreement, indicating that the chemical structures in the C/PDA aggregates are similar to the model proposed by DFT calculations. The discrepancies between the experimental and theoretical wavenumber values are expected, since the calculations were done in vacuum and no scaling factor was used.

The optimized DFT geometry of the PDA trimer interacting with caffeine shown in **Figure 3.5c**, whose geometry optimization steps are available as a movie at reference (FURTADO; ANDO; PETRI, 2019c) indicates that the interactions between caffeine and PDA trimer involve (i) a hydrogen bonding between the nitrogen 9 of the caffeine and the imidazolic N-H group of PDA trimer, and (ii)  $\pi$ - $\pi$  interactions between their aromatic rings. Noteworthy, the choice of the trimer structure to represent PDA was based on a previous work reported by Chen and co-workers, where among several PDA oligomers, the trimer considered in this work was the most stable (CHEN et al., 2017). Although it was considered a simple model to simulate the interaction between PDA and caffeine, the DFT optimized structure (**Figure 3.5c**) shows that the planarity of PDA is distorted by its interaction with caffeine, what may be responsible to the distinct behavior in the assembling of these materials (LIEBSCHER et al., 2013).

(a)

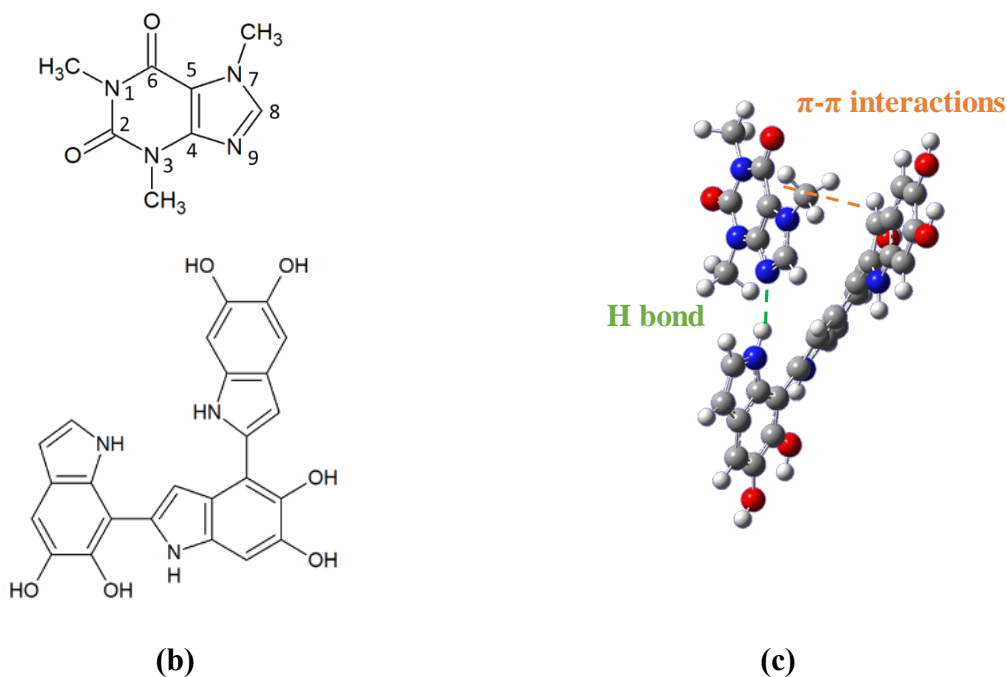
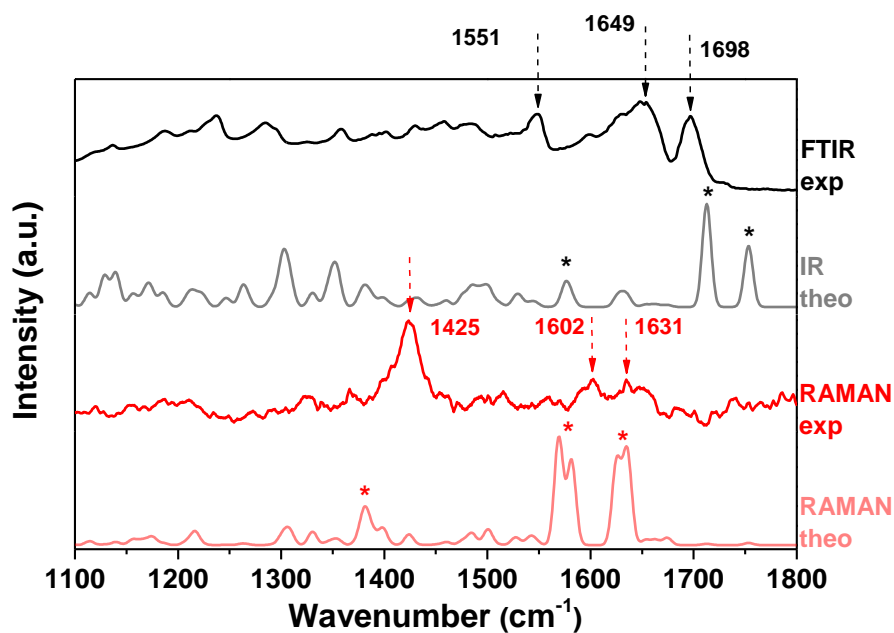


**Figure 3.5:** (a) Experimental (red) and theoretical (light red) Raman, experimental (black) and theoretical (grey) FTIR spectra determined for C/PDA, the “\*” in the theoretical spectra indicates the bands that matches with the bands assigned in the experimental spectra. (b) Chemical structures of caffeine and PDA trimers used for the DFT calculations. (c) Snapshot from DFT simulation, where caffeine molecule approaches to PDA trimer by  $\pi$ - $\pi$  interactions and H bond by caffeine N(9)

### 3.3.5 Adsorption of caffeine on CAB/PDA microbeads

So far, the systematic investigation on the deposition of C/PDA on solid substrates and the spectroscopic study revealed favorable interactions between caffeine and PDA. Considering that

PDA based adsorbents are particularly interesting for solid phase extraction towards the analysis of biological (MROWCZYNSKI, 2018) and environmental (POSATI et al., 2019) samples, the adsorption of caffeine on PDA coated surfaces was investigated.

For adsorption purposes, spherical substrates are more interesting than planar substrates because they provide larger surface area. PDA coated glass microbeads (~ 200 µm mean diameter) and CAB/PDA microbeads with diameter ranging from 50 to 100 µm (**Figure 3.6a**) were prepared to be applied as substrates for the adsorption of caffeine. The formation of PS/PDA microbeads by dripping was not successful. The PDA coated glass microbeads were not stable; after 24 h of interaction with caffeine solution (pH 5.5) under shaking, the PDA layer detached from the microspheres (**Supplementary Information SI16**), impairing the adsorption experiments. This finding is consistent with the low stability of PDA or C/PDA on Si/SiO<sub>2</sub> wafers. On the other hand, CAB/PDA microbeads were easily prepared and remained stable over one month in the caffeine solution, agreeing with the high stability observed for PDA or C/PDA on CAB films.

**Figure 3.6a** shows the fluorescence emission of CAB/PDA microbeads, which is typical for PDA (YU; LU; TAN, 2017). **Figure 3.6b** shows the adsorption isotherm of caffeine on the CAB/PDA microbeads at pH 6 and (24 ± 1)° C, along with the Freundlich model fitting (red line), which is represented by  $q_e = K_F C_e^{(1/n)}$  (FOO; HAMEED, 2010). The fitting parameters are the Freundlich constant ( $K_F$ ), the larger  $K_F$ , the higher the adsorption capacity, and  $n$ , which is related to the surface heterogeneity, the smaller  $n$  indicates greater heterogeneity (TIAN et al., 2017). Langmuir model<sup>45</sup> did not fit the experimental data (**Supplementary Material SI17**). The  $K_F$  and  $n$  values amounted to  $6.21 \left( \frac{mg}{L \times g} \right) / \left( \frac{mg}{L \times g} \right)^{\frac{1}{n}}$  and 1.28, respectively; these values were similar to those found for the adsorption of caffeine onto poly(acrylic acid) crosslinked with konjac glucomannan (TIAN et al., 2017). The  $n$  value of 1.28 indicated cooperative adsorption (FOO; HAMEED, 2010). The  $q_e$  values determined for caffeine on CAB/PDA increased with the caffeine  $C_e$ . Within the concentration

range investigated and for 10 mg of adsorbent, removal capacity was  $6 \pm 2$  % and the highest  $q_e$  value achieved was  $10 \pm 1$  mg/g, which is an excellent result, because the amount of adsorbent was relatively low (10 mg), in comparison to other adsorbents presented in **Table 3.3**. For a higher amount of adsorbent (100 mg) and initial concentration of caffeine at 1.0 g/L, the removal capacity increased to  $24 \pm 1$  %. These findings display the potential of CAB/PDA microbeads to be applied as adsorbents of emerging pollutants and as sensors for biomolecules (enzymes and proteins), where their fluorescent property might be advantageous.

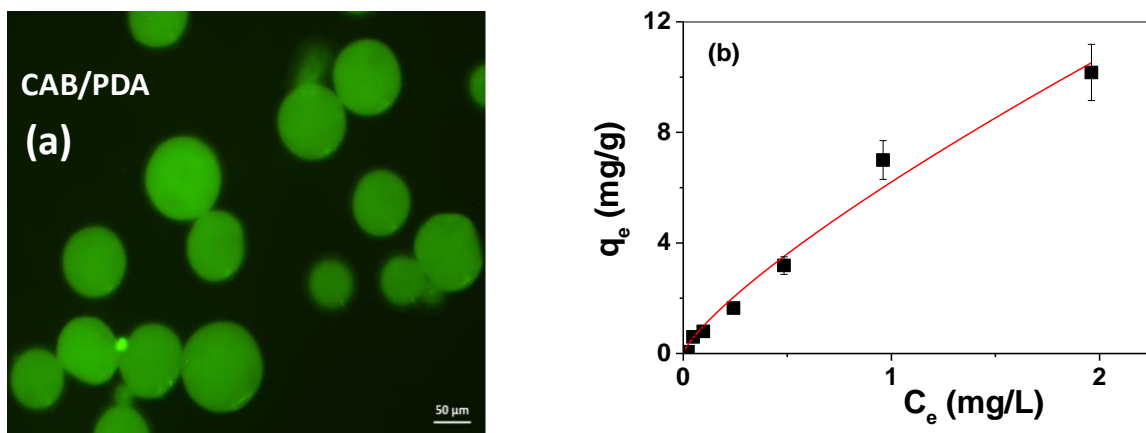


**Figure 3.6:** (a) Confocal fluorescence images of CAB/PDA microbeads,  $\lambda_{\text{excitation}} = 467\text{-}498$  nm and  $\lambda_{\text{emission}} = 513\text{-}556$  nm (b) Adsorption isotherm of caffeine on the CAB/PDA microbeads at pH 5.5 and  $(24 \pm 1)$  °C, adsorption time 24 h, along with non-linear fitting for Freundlich model  $q_e = KF C_e^{1/n}$ . The fitting parameters KF and n amounted to  $6.21 \left(\frac{\text{mg}}{\text{L}\times\text{g}}\right) / \left(\frac{\text{mg}}{\text{L}\times\text{g}}\right)^{\frac{1}{n}}$  and 1.28, respectively,  $\chi^2 = 0.2469$  and  $R^2 = 0.9822$ .

**Table 3.3:** Some examples of polymeric systems used as adsorbents for caffeine along with the adsorption experiments conditions,  $q_e$  (mg/g) or removal (R) % values.  $C_i$  stands for initial caffeine concentration.  $R = \left(\frac{C_i - C_e}{C_i}\right) \times 100\%$ .

Adsorbent	$C_i$ (g/L)	$m_{\text{adsorbent}}$ (mg)	$q_e$ (mg/g) or R (%)	Ref
Poly(triallyl isocyanurate-co-vinyl acetate)	0.026	200	1.17 mg/g	(PENG et al., 2012)
poly(acrylic acid) crosslinked with konjac glucomannan	Up to 2	100	21.67 mg/g	(TIAN et al., 2017)
poly(acrylic acid) crosslinked with ethylene glycol dimethacrylate	n.a.	n.a.	16.5 mg/g	(WEI et al., 2013)
Caffeine imprinted on poly(acrylic acid) crosslinked with ethylene glycol dimethacrylate	n.a.	n.a.	28.1 mg/g	(WEI et al., 2013)
Chitosan beads	0.05	80-260	8%	(ZARZAR et al., 2015)
Alginate beads	0.05	80-260	6%	(ZARZAR et al., 2015)
CAB/PDA microbeads	Up to 2	10	$10 \pm 1$ mg/g $6 \pm 2\%$	this work

n.a. = information not available

### 3.4 CONCLUSIONS

Caffeine and PDA co-adsorb on substrates with different surface energies. Particularly on CAB, the nanometric coatings present the highest stability over wide range of pH. Based on this, novel fluorescent CAB/PDA microbeads were created and proved to be efficient adsorbents for caffeine. The interactions between caffeine on PDA are driven by hydrogen bonds by the nitrogen 9 of the caffeine and imidazole N-H group of PDA trimer and the  $\pi$ - $\pi$  interactions between their aromatic rings, as revealed by spectroscopic analyses and DFT calculations. We believe that, this work describes for the first time, the mechanism behind the interactions between caffeine and PDA, which is relevant not only for the development of new functional stable coatings, but also for the understanding of biological systems behavior.

### 3.5 REFERENCES

AMIM, J. et al. Stability and interface properties of thin cellulose ester films adsorbed from acetone and ethyl acetate solutions. *Journal of Colloid and Interface Science*, v. 332, n. 2, p. 477–483, 2009. Disponível em: <<http://dx.doi.org/10.1016/j.jcis.2008.12.057>>.

ANDREEVA, E. Y.; DMITRIENKO, S. G.; ZOLOTOV, Y. A. Sorption of caffeine and theophylline on hypercrosslinked polystyrene. *Moscow University Chemistry Bulletin*, v. 65, n. 1, p. 38–41, 2010.

AZZAM, R. M. .; BASHARA, N. M. *Ellipsometry and Polarized Light*. 3rd. ed. Amsterdam: North Holland Publication, 1996.

BALL, V. et al. Kinetics of polydopamine film deposition as a function of pH and dopamine concentration: Insights in the polydopamine deposition mechanism. *Journal of Colloid and Interface Science*, v. 386, n. 1, p. 366–372, 2012. Disponível em: <<http://dx.doi.org/10.1016/j.jcis.2012.07.030>>.

BERNSMANN, F. et al. Characterization of dopamine-melanin growth on silicon oxide. *Journal of Physical Chemistry C*, v. 113, n. 19, p. 8234–8242, 2009.

BERNSMANN, F. et al. Melanin-Containing Films: Growth from Dopamine Solutions versus Layer-by-Layer Deposition. *ChemPhysChem*, v. 11, n. 15, p. 3299–3305, 2010.

BLACHECHEN, L. S.; SOUZA, M. A.; PETRI, D. F. S. Effect of humidity and solvent vapor phase on cellulose esters films. *Cellulose*, v. 19, n. 2, p. 443–457, 2012.

BOUALI, B. et al. Acid-base approach to latex particles containing specific groups based on wettability measurements. *Journal of Colloid and Interface Science*, v. 208, n. 1, p. 81–89, 1998.

CACACE, M. G.; LANDAU, E. M.; RAMSDEN, J. J. The Hofmeister series: salt and solvent effects on interfacial phenomena. *Q Rev Biophys*, v. 3, p. 241–277, 1997.

CHEMSPIDER. *Caffeine*. Disponível em: <<http://www.chemspider.com/Chemical->

Structure.2424.html>.

CHEN, C. T. et al. Polydopamine and eumelanin molecular structures investigated with ab initio calculations. *Chemical Science*, v. 8, n. 2, p. 1631–1641, 2017.

DE ARAGÃO, N. M. et al. Multivariate optimisation of the experimental conditions for determination of three methylxanthines by reversed-phase high-performance liquid chromatography. *Talanta*, v. 67, n. 5, p. 1007–1013, 2005.

DEL FRARI, D. et al. Degradation of polydopamine coatings by sodium hypochlorite: A process depending on the substrate and the film synthesis method. *Polymer Degradation and Stability*, v. 97, n. 9, p. 1844–1849, 2012.

DELLA VECCHIA, N. F. et al. Building-block diversity in polydopamine underpins a multifunctional eumelanin-type platform tunable through a quinone control point. *Advanced Functional Materials*, v. 23, n. 10, p. 1331–1340, 2013.

DING, Y. et al. Insights into the Aggregation/Deposition and Structure of a Polydopamine Film. *Langmuir*, v. 30, n. 41, p. 12258–12269, 2014.

FOO, K. Y.; HAMEED, B. H. Insights into the modeling of adsorption isotherm systems. *Chemical Engineering Journal*, v. 156, n. 1, p. 2–10, 2010.

FRISCH, M. J. et al. *Gaussian Revision A.02* Wallingford CT Gaussian Inc., , 2016. .

FURTADO, L. M.; ANDO, R. A.; PETRI, D. F. S. *Solubility of polydopamine coatings at pH 13*. Disponível em: <<https://www.youtube.com/watch?v=Zx5g-WbZkv8>>.

FURTADO, L. M.; ANDO, R. A.; PETRI, D. F. S. *Solubility of caffeine/polydopamine coatings at pH 13*. Disponível em: <<https://www.youtube.com/watch?v=xxIpziTTSGo>>.

FURTADO, L. M.; ANDO, R. A.; PETRI, D. F. S. *DFT calculations of polydopamine and caffeine molecules using the software Gaussian 09*. Disponível em: <<https://www.youtube.com/watch?v=FIXSQNvaFBw>>.



JIANG, J. et al. Surface characteristics of a self-polymerized dopamine coating deposited on hydrophobic polymer films. *Langmuir*, v. 27, n. 23, p. 14180–14187, 2011.

JOHNSON, N. O. et al. Anion-Caffeine Interactions Studied by <sup>13</sup>C and <sup>1</sup>H NMR and ATR-FTIR Spectroscopy. *Journal of Physical Chemistry B*, v. 121, n. 7, p. 1649–1659, 2017.

KIM, Y. J. et al. Evidence of Porphyrin-Like Structures in Natural Melanin Pigments Using Electrochemical Fingerprinting. *Advanced Materials*, v. 28, n. 16, p. 3173–3180, 2016.

KLOSTERMAN, L.; RILEY, J. K.; BETTINGER, C. J. Control of heterogeneous nucleation and growth kinetics of dopamine-melanin by altering substrate chemistry. *Langmuir*, v. 31, n. 11, p. 3451–3458, 2015.

KOSAKA, P. M.; KAWANO, Y.; PETRI, D. F. S. Dewetting and surface properties of ultrathin films of cellulose esters. *Journal of Colloid and Interface Science*, v. 316, n. 2, p. 671–677, 2007.

LAVOINE, N. et al. Modeling of caffeine release from a cellulosic substrate coated with microfibrillated cellulose. *Journal of Controlled Release*, v. 213, n. 2015, p. e83–e84, 2015. Disponível em: <<http://dx.doi.org/10.1016/j.jconrel.2015.05.139>>.

LEE, H. et al. Mussel-inspired surface chemistry for multifunctional coatings. *Science*, v. 318, n. 5849, p. 426–430, 2007.

LIEBSCHER, J. et al. Structure of polydopamine: A never-ending story? *Langmuir*, v. 29, n. 33, p. 10539–10548, 2013.

MARTÍN, J. et al. Occurrence of pharmaceutical compounds in wastewater and sludge from wastewater treatment plants : Removal and ecotoxicological impact of wastewater discharges and sludge disposal. v. 240, p. 40–47, 2012.

MICILLO, R. et al. Eumelanin broadband absorption develops from aggregation-modulated chromophore interactions under structural and redox control. *Scientific Reports*, v. 7, n. December

2016, p. 1–12, 2017. Disponível em: <<http://dx.doi.org/10.1038/srep41532>>.

MONDAL, S.; THAMPI, A.; PURANIK, M. Kinetics of Melanin Polymerization during Enzymatic and Nonenzymatic Oxidation. *Journal of Physical Chemistry B*, v. 122, n. 7, p. 2047–2063, 2018.

MROWCZYNSKI, R. Polydopamine-Based Multifunctional (Nano)materials for Cancer Therapy. *ACS Applied Materials and Interfaces*, v. 10, n. 9, p. 7541–7561, 2018.

NIIBORI, Y. et al. Dissolution Rates of Amorphous Silica in Highly Alkaline Solution. *Journal of Physical Chemistry B*, v. 4, n. 12, p. 3131, 2000.

OWENS, D. K.; WENDT, R. C. Estimation of the surface free energy of polymers. *Journal of Applied Polymer Science*, v. 13, p. 1741–1747, 1969.

PALIK, E. *Handbook of Optical Constants of Solids*. 1st. ed. London: Academic Press, 1985.

PENG, N. M. et al. Selective removal of caffeine from tea extracts using macroporous crosslinked polyvinyl alcohol adsorbents. *J. Sep. Sci.*, v. 35, p. 36–44, 2012.

PEREIRA, E. M. A. et al. Binding of dengue virus particles and dengue proteins onto solid surfaces. *ACS Applied Materials and Interfaces*, v. 2, n. 9, p. 2602–2610, 2010.

POSATI, T. et al. Polydopamine Nanoparticle-Coated Polysulfone Porous Granules as Adsorbents for Water Remediation. *ACS Omega*, v. 4, n. 3, p. 4839–4847, 2019.

QIU, W. Z.; YANG, H. C.; XU, Z. K. Dopamine-assisted co-deposition: An emerging and promising strategy for surface modification. *Advances in Colloid and Interface Science*, v. 256, p. 111–125, 2018. Disponível em: <<https://doi.org/10.1016/j.cis.2018.04.011>>.

ROUXHET, P. G.; GENET, M. J. XPS analysis of bio-organic systems. *Surface and Interface Analysis*, v. 43, p. 1453–1470, 2011.

RYU, J. H.; MESSERSMITH, P. B.; LEE, H. Polydopamine Surface Chemistry: A Decade of Discovery. *ACS Applied Materials and Interfaces*, v. 10, n. 9, p. 7523–7540, 2018.

SALOMÄKI, M. et al. Polydopamine Nanoparticles Prepared Using Redox-Active Transition Metals. *The Journal of Physical Chemistry B*, v. 123, p. 2513–2524, 2019.

SINGH, G.; KUNDU, A. Dopamine synergizes with caffeine to increase the heart rate of *Daphnia* [version 1; referees: 1 approved, 2 approved with reservations]. *F1000Research*, v. 7, p. 1–12, 2018.

SOUSA, J. C. G. et al. A review on environmental monitoring of water organic pollutants identified by EU guidelines. *Journal of Hazardous Materials*, v. 344, p. 146–162, 2018. Disponível em: <<http://dx.doi.org/10.1016/j.jhazmat.2017.09.058>>.

TAVAGNACCO, L. et al. Molecular Dynamics and Neutron Scattering Studies of Mixed Solutions of Caffeine and Pyridine in Water. *Journal of Physical Chemistry B*, v. 122, n. 21, p. 5308–5315, 2018.

TIAN, D. T. et al. Synthesis and Properties of Caffeine Molecularly Imprinted Polymers Based on Konjac Glucomannan. *Advances in Polymer Technology*, v. 36, n. 1, p. 68–76, 2017.

VOLKOW, N. D. et al. Caffeine increases striatal dopamine D2/D3 receptor availability in the human brain. *Translational Psychiatry*, v. 5, n. 4, p. e549-6, 2015. Disponível em: <<http://dx.doi.org/10.1038/tp.2015.46>>.

WAN, T. et al. Immobilization via polydopamine of dual growth factors on polyetheretherketone: improvement of cell adhesion, proliferation, and osteo-differentiation. *Journal of Materials Science*, v. 54, n. 16, p. 11179–11196, 2019. Disponível em: <<https://doi.org/10.1007/s10853-018-03264-z>>.

WANG, Z. et al. Polydopamine Generates Hydroxyl Free Radicals under Ultraviolet-Light Illumination. *Langmuir*, v. 33, n. 23, p. 5938–5946, 2017.

WEI, S. L. et al. Preparation of Caffeine Molecularly Imprinted Polymers and Application on Solid Phase Extraction. *Chinese J. Anal. Chem.*, v. 40, p. 1071–1075, 2013.

XI, Z. Y. et al. A facile method of surface modification for hydrophobic polymer membranes based on the adhesive behavior of poly(DOPA) and poly(dopamine). *Journal of Membrane Science*, v. 327, n. 1–2, p. 244–253, 2009.

YU, M.; LU, Y.; TAN, Z. Fluorescence growth of self-polymerized fluorescence polydopamine for ratiometric visual detection of DA. *Talanta*, v. 168, n. February, p. 16–22, 2017. Disponível em: <<http://dx.doi.org/10.1016/j.talanta.2017.03.010>>.

ZANGMEISTER, R. A.; MORRIS, T. A.; TARLOV, M. J. Characterization of Polydopamine Thin Films Deposited at Short Times by Autoxidation of Dopamine. *American Chemical Society*, v. 29, p. 8619–8628, 2013.

ZARZAR, A. et al. Insights into the Eco-Friendly Adsorption of Caffeine from Contaminated Solutions by Using Hydrogel Beads. *J. Environ. Anal. Chem.*, v. 2, p. 150–155, 2015.

ZHANG, C. et al. Deposition and Adhesion of Polydopamine on the Surfaces of Varying Wettability. *ACS Applied Materials and Interfaces*, v. 9, n. 36, p. 30943–30950, 2017.

## 4 CHAPTER 2 - Miscibility and sustained release of drug from cellulose acetate butyrate/caffeine films

Accepted version of article reproduced with permission from [Furtado, L. M.; Hilmatu, K. C. P.; Krishnasamy, B.; Ando, R. A.; Petri, Denise F.S. Miscibility and sustained release of drug from cellulose acetate butyrate/caffeine films. JOURNAL OF DRUG DELIVERY SCIENCE AND TECHNOLOGY, v. 55, p. 101472, 2019. Copyright 2019 Journal of Drug Delivery Science and Technology ]. The written permission is at Appendices 9.1.2 . The published version of this article can be accessed in the link: DOI: 10.1016/j.jddst.2019.101472 ( <https://doi.org/10.1016/j.jddst.2019.101472> )

### Abstract

The miscibility of caffeine and cellulose acetate butyrate (CAB) was investigated as a function of caffeine (caf) content and correlated with *in vitro* drug release studies. Films of CAB/caf with caffeine contents larger than 5 wt% presented partial miscibility, as revealed by scanning electron microscopy, turbidity measurements and thermogravimetric analyses. CAB/caf with 2.5 wt% or less were homogeneous films. Favorable interactions between CAB and caffeine was evidenced by the decrease of the glass transition temperature of CAB in 28 °C and by Fourier transform infrared vibrational spectra of the films, which displayed shifts to higher wavenumbers of caffeine bands assigned to the stretching of conjugated C=O(6) and isolated C=O(2) carbonyl groups of 16 cm<sup>-1</sup> and 9 cm<sup>-1</sup>, respectively. No drug released from completely miscible systems, regardless of the external medium. Partially miscible CAB/caf systems showed a two-step release process: in the first 6 h the segregated portion of caffeine dissolved in the medium and a second one, when the release of drug

located in the internal polymer matrix took place. After 48 h, at pH 7.4, the release of caffeine from CAB/caf 7 wt% was complete.

**Keywords:** Caffeine; cellulose acetate butyrate; drug release; miscibility; FTIR-ATR

## 4.1 MOTIVATION

The esterification of cellulose enables a range of properties that are impossible for raw cellulose; one of them is the possibility of extrusion, injection, and dissolution in common organic solvents. Such properties make cellulose esters useful for the development of coatings, paint, and sensors (EDGAR et al., 2001). Cellulose acetate butyrate (CAB) has been an important component for coating formulations because it reduces dry time, improves flow and leveling, and controls viscosity (EDGAR et al., 2001). CAB biocompatibility allows its application as drug release system (EDGAR, 2007; SOBRAL et al., 2008; SHOKRI; ADIBKIA, 2013; ALI; WALTHER; BODMEIER, 2018; VARSHOSAZ et al., 2018) and as efficient support for enzymes (KOSAKA; KAWANO; PETRI, 2007) and lectins (AMIM; PETRI, 2012).

Caffeine or 1,3,7-trimethylxanthine is an alkaloid belonging to the purine family, which exerts various stimulating effects on the central nervous system and can act as immunomodulatory (AL REEF; GHANEM, 2018). There is significant interest for caffeine carriers that allow its sustained release, because caffeine absorption is very rapid and reaches 99% absorption after 45 min ingestion (BLANCHARD; SAWERS, 1983). Among many reported carriers, polysaccharides have been often used to encapsulate caffeine due to their ability to swell, biocompatibility and nontoxicity (BELSCAK-CVITANOVIC et al., 2015; YEW; MISRAN, 2016; HASEEB et al., 2017;

MOHAMMADI; EHSANI; BAKHODA, 2018; NIKOO et al., 2018; NOOR et al., 2018) [11-16]. Cellulose and cellulose esters also present such advantageous properties and allow designing different architectures, such as macroporous beads (HARADA; NAKAMURA; UYAMA, 2019) and core-shell nanofibers (YANG et al., 2019). Microfibrillated cellulose coated paper served as an interesting carrier for caffeine, which was completely released after 10 h (LAVOINE; DESLOGES; BRAS, 2014). CAB combined with Eudragit®, a hydrophilic acrylate based copolymer, and triacetate citrate, a plasticizer, resulted in mechanically stable membrane to coat osmotic tablets for caffeine release (ALI; WALTHER; BODMEIER, 2018). Cellulose esters have been used as coating for osmotic tablets; the tablet is coated with a semi-permeable membrane (cellulose ester) and a laser drills holes in it. Upon contacting gastrointestinal fluids, the membrane swells by osmosis, dissolving the drug and pushing it towards the gastrointestinal tract (MALATERRE et al., 2009).

Despite the interesting reports available in the literature, a systematic study about the miscibility of caffeine and CAB and its influence on the sustained release of caffeine is still missing. In this study, the miscibility of caffeine and CAB was systematically investigated as nanometric spin-coated and micrometric cast CAB/caffeine films with different caffeine contents by means of morphological and structural analyses, turbidity and differential scanning calorimetry (DSC). DSC gives information about the glass transition temperature ( $T_g$ ) of polymer chains; in the presence of second component, the mobility of polymer chains might increase due to favorable interactions, decreasing the  $T_g$  value. Therefore, if CAB and caffeine are miscible, the  $T_g$  value of CAB is expected to decrease. The *in vitro* release behavior of caffeine from CAB/caffeine films under different pH and ionic strength was investigated and correlated with the miscibility of caffeine and CAB.

## 4.2 EXPERIMENTAL SECTION

### 4.2.1 Materials

Cellulose acetate butyrate (CAB, Eastman,  $DS_{Ac} = 0.2$ ,  $DS_{But} = 2.5$ ,  $M_v \sim 30,000 \text{ g mol}^{-1}$ , USA), caffeine (caf, Sigma W222402,  $194.19 \text{ g mol}^{-1}$ , purity 99.9 %) toluene (LabSynth, Brazil), ethyl acetate (EA, LabSynth, Brazil) and acetone (Ace, LabSynth, Brazil) were used as received. The chemical structures of CAB and caf are represented in **Figure 4.1**.

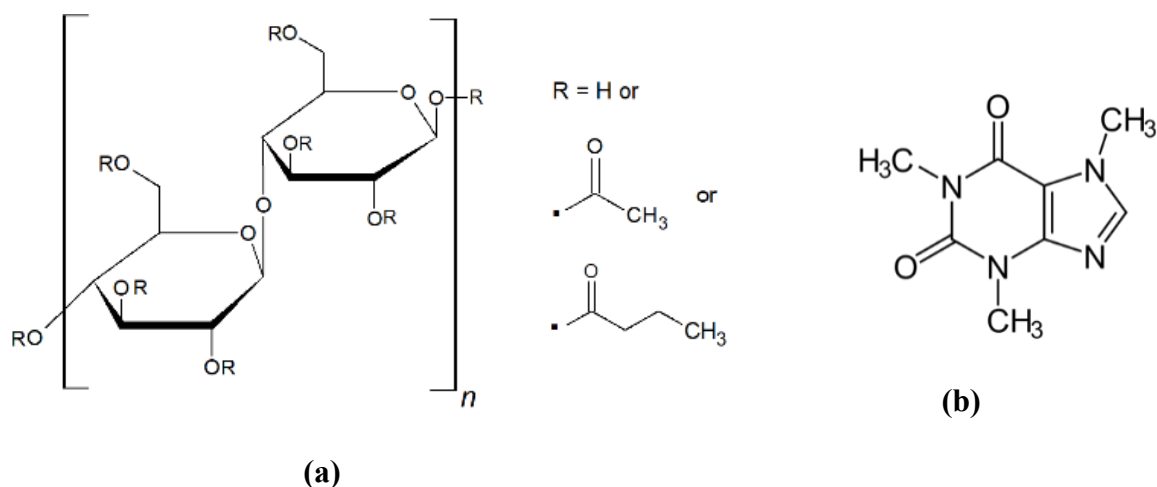


**Figure 4.1:** Schematic representation of chemical structures of (a) CAB repeating units and (b) caffeine.

### 4.2.2 Preparation of thin films by spin-coating and characterization

CAB was dissolved in ethyl acetate (EA) at  $10 \text{ g L}^{-1}$ ,  $20 \text{ g L}^{-1}$  and  $40 \text{ g L}^{-1}$ . CAB solution was mixed with caffeine (caf) dissolved in acetone at  $10 \text{ g L}^{-1}$ , at the volume ratio 1:1, so that the final concentrations were reduced to one-half their original values. The samples were coded as CAB5/caf, CAB10/caf, CAB20/caf. The initial concentration of caffeine was chosen at  $10 \text{ g L}^{-1}$  to ensure complete dissolution.



Thin films were prepared by spin-coating on Si/SiO<sub>2</sub> wafers and glass slides, with a Headway PWM32-PS-R790 spinner operating at 3000 rpm for 30 s, at (24 ± 1) °C and (75 ± 5) % of relative humidity. The thickness of the films was determined by ellipsometry in a vertical computer-controlled DRE-EL02 ellipsometer; the angle of incidence was set at 70.0° and the wavelength of the He–Ne laser was 632.8 nm (KOSAKA et al., 2007; AMIM; PETRI, 2012). The morphology of spin-coated films on Si/SiO<sub>2</sub> wafers was analyzed by scanning electron microscopy (SEM) in a SEM-FEG JEOL JSM7401F microscope; the surfaces were coated with a 2 nm thick gold layer prior to the analyses. Spin-coated films glass slides were characterized by confocal fluorescence microscopy (CFM) in a Zeiss LSM 510 equipment, the  $\lambda_{\text{excitation}}$  and  $\lambda_{\text{emission}}$  for caffeine were 559 nm and 637 nm, respectively.

#### 4.2.3 Preparation of micrometric films by casting and characterization

Micrometric films were prepared by casting CAB/caf solution on Petri dishes and heating at 60 °C until complete solvent evaporation. The thickness of the films was measured with a Mitutoyo Thickness Gage (Type ID-C1012XBS; Mitutoyo Manufacturing Co. Ltd, Kawasaki, Japan), being measured at three randomly chosen different positions of at least two films of same composition. Solutions of CAB in EA (20 g L<sup>-1</sup>) were mixed with caffeine solution in acetone at different concentrations, so that after drying the caffeine contents,  $\phi_{\text{caf}}$ , in the films were 0.1, 2.5, 5, 7, 10, 14.9 and 20 wt%, see **Supplementary Material SM1** for details.

The light transmitted through the films with thickness ranging from 100  $\mu\text{m}$  to 150  $\mu\text{m}$  was measured at 600 nm (at this wavelength there is no light absorbance), in a Beckmann-Coulter DU650 spectrophotometer. The morphology of films was evaluated by SEM in a SEM-FEG JEOL JSM7401F microscope. The images were taken from the top side and from internal region (cryofracture) of the films. The surfaces were coated with a 2 nm thick gold layer prior to the analyses.

Films were analyzed by Fourier transform infrared vibrational spectroscopy in the attenuated total reflectance mode in an Alpha FTIR-ATR, Bruker equipment, with a diamond crystal, accumulating 64 scans at  $2\text{ cm}^{-1}$  of resolution. Differential scanning calorimetry (DSC) analyses were performed in a Q10 TA Instruments equipment, at  $20\text{ }^{\circ}\text{C min}^{-1}$  heating rate from 20 to  $150\text{ }^{\circ}\text{C}$ . The glass transition temperature ( $T_g$ ) was determined from the second heating run. Thermogravimetric analyses (TGA) were performed with a Mettler Toledo TGA system, using temperature program from  $30\text{ }^{\circ}\text{C}$  to  $950\text{ }^{\circ}\text{C}$  at a heating rate of  $5\text{ }^{\circ}\text{C/min}$  under nitrogen atmosphere.

Density Functional Theory (DFT) calculations were performed using software Gaussian 09 [21] with the B3LYP functional and the 6-31+G(d,p) as basis set.

#### 4.2.4 In vitro release of caffeine from micrometric CAB/caf films

The release of caffeine from CAB/caf 2.5 wt%, 5 wt% and 7 wt% was investigated by immersing them (typically 10 – 15 mg film) in 7.0 mL of MilliQ water (pH 5.5), NaCl  $0.010\text{ mol L}^{-1}$  (pH 5.5), NaCl  $0.10\text{ mol L}^{-1}$  (pH 5.5), phosphate saline buffer (PBS, pH 7.4), HCl  $0.010\text{ mol L}^{-1}$  (pH 2) or NaOH  $1.0 \times 10^{-5}\text{ mol L}^{-1}$  (pH 9). An aliquot of 1.0 mL was withdrawn from the supernatant at pre-determined time intervals up to 48 h. After each sampling, the same volume of solvent was added to the medium to keep the solution volume constant. The release of caffeine to the medium was monitored by measuring the absorbance of withdrawn supernatants by UV spectrophotometry at 272 nm and  $(24 \pm 1)\text{ }^{\circ}\text{C}$ . The calibration curve of caffeine taken at 272 nm was provided as **Supplementary Material SM2**.

### 4.3 RESULTS AND DISCUSSION

Caffeine is soluble in solvents with high dielectric constant. Upon drying, the caffeine molecules tend to crystalize. **Figure 4.2a** and **Figure 4.2b** show SEM images of needle-shaped

crystals of caffeine grown on Si/SiO<sub>2</sub> wafers by evaporation from acetone. **Figure 4.2c** and **Figure 4.2d** show the optical microscopy and the corresponding CFM image of caffeine crystals on glass slides. The needle-shaped caffeine crystals were also observed after evaporation of nitromethane, dimethyl sulfoxide (EDDLESTON; JONES, 2010) and dichloromethane (SARFRAZ et al., 2011). The crystallization process is driven by self-assembling of caffeine molecules through  $\pi$ -stacking interactions (TAVAGNACCO et al., 2016) and hollow tubular structures result from a diffusion limited crystal growth (EDDLESTON; JONES, 2010). In the CFM image (**Figure 4.2d**) it is evident that part of caffeine molecules are arranged as long needles and part of them formed small aggregates.

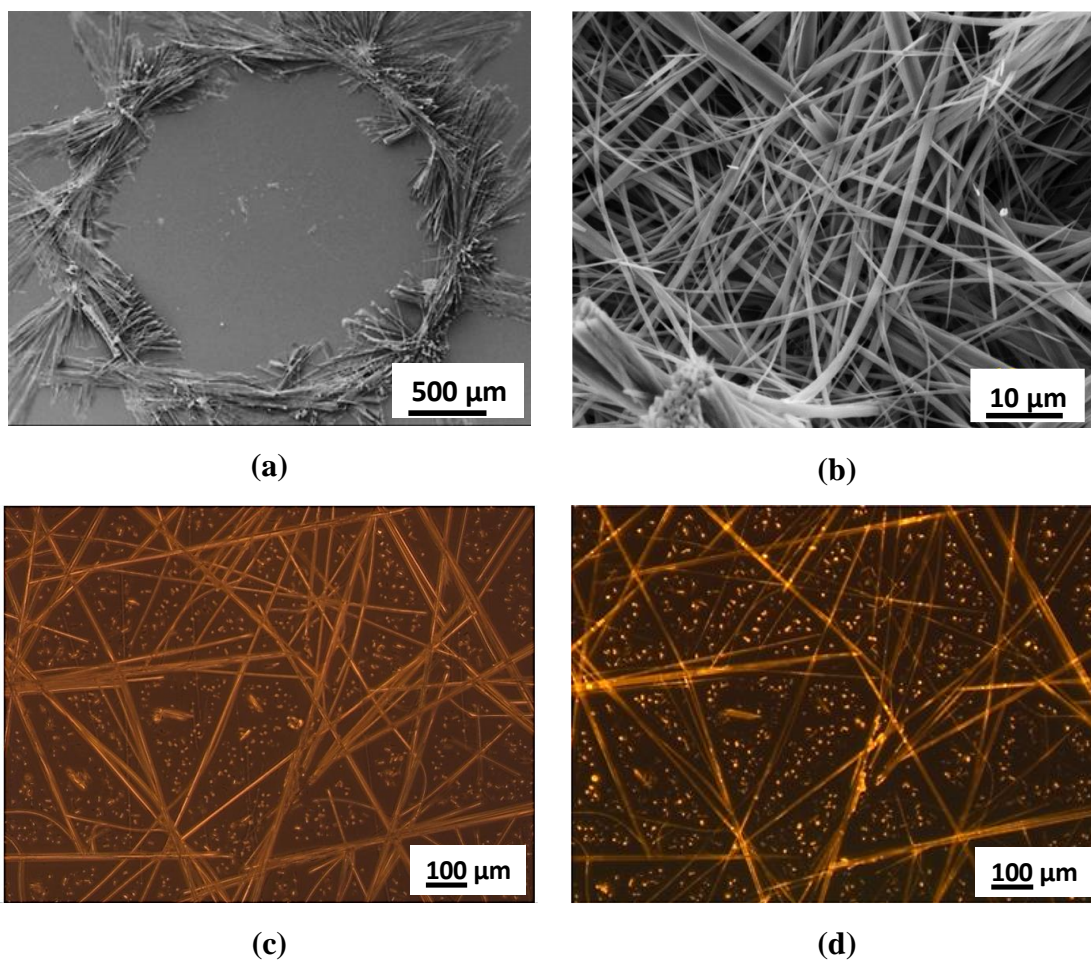


**Figure 4.2:** (a) and (b) SEM images of needle-shaped crystals of caffeine grown on Si/SiO<sub>2</sub> wafers by evaporation from acetone. (c) Optical microscopy and the corresponding and (d) CFM image of caffeine crystals on glass slides, after acetone evaporation. The concentration of caffeine in acetone was 2.0 g L<sup>-1</sup>.

### 4.3.1 CAB/caf spin-coated films

The effect of polymer concentration on the morphology of CAB5/caf, CAB10/caf, CAB20/caf spin-coated films is presented in the SEM images in **Figure 4.3a**, **Figure 4.3b** and **Figure 4.3c**. The thickness of spin-coated films ranged from  $\sim 40$  nm to  $\sim 80$  nm, as determined by ellipsometry. The solvents used to prepare CAB and caffeine solutions were EA and acetone, respectively. Regardless of the CAB concentration, the caffeine needles appeared buried in the polymer or appeared as short needles scarcely distributed on the surface, as indicated by the arrows in **Figure 4.3a**. The CFM images obtained for CAB5/caf films deposited on glass slides (**Figure 4.3d**) corroborated with the SEM images; the caffeine structures appeared in the CFM image as short needles. These morphological features evidenced affinity between caffeine and CAB. For comparison, pure CAB spin-coated film showed no fluorescence, it appears completely dark in **Figure 4.3e**. Pure CAB (**Figure 4.3f**) and CAB20/caf (**Figure 4.3c**) films presented “breath-figure” structures on the surface. “Breath figures” are cavities resulting from the condensation of the droplets of water on polymer solution during solvent evaporation and film formation (BLACHECHEN; SOUZA; PETRI, 2012) (WIDAWSKI; RAWISO; FRANÇOIS, 1994).

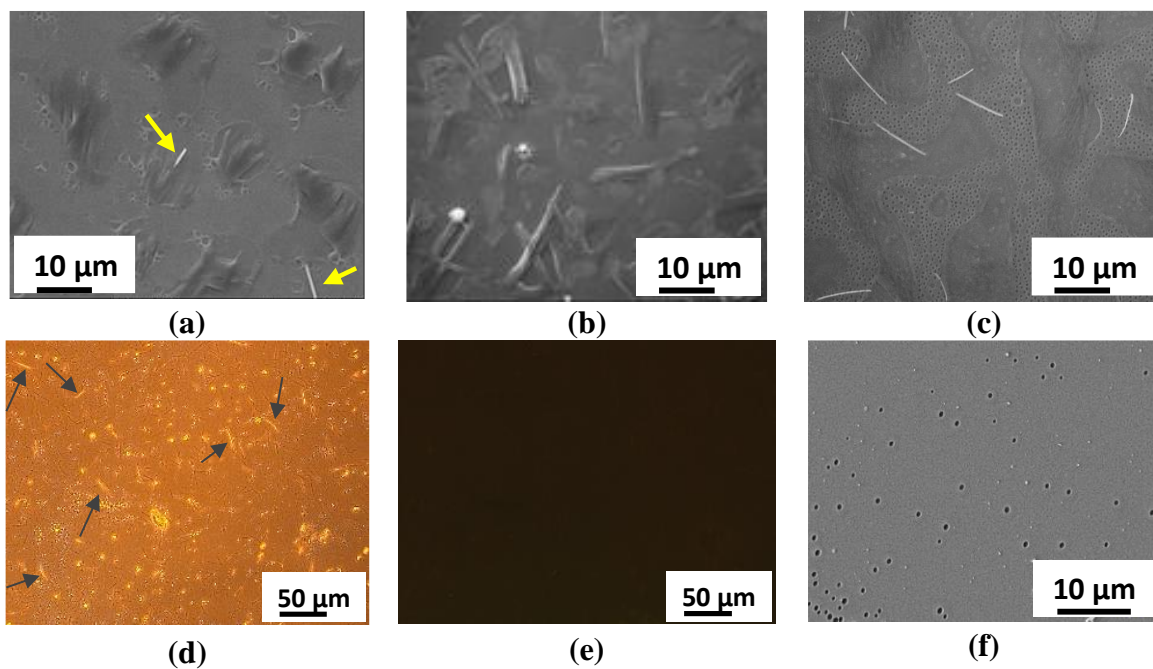


**Figure 4.3:** SEM images of (a) CAB5/caf, (b) CAB10/caf, (c) CAB20/caf spin-coated films on Si/SiO<sub>2</sub> wafers. CFM images of (d) CAB5/caf films and (e) pure CAB films deposited from solution at 10 g L<sup>-1</sup> in EA, on glass slides. (f) SEM image of pure CAB spin-coated film from solution at 10 g L<sup>-1</sup> in EA, on Si/SiO<sub>2</sub> wafers.

### 4.3.2 CAB/caf cast films

Films of pure CAB are transparent. However, as the caffeine content ( $\phi_{\text{caf}}$ ) increased in the CAB/caf films, the transmittance of light through the films decreased exponentially and turned opaque, as shown in **Figure 4.4**. Particularly, for  $\phi_{\text{caf}}$  higher than 5 wt%, the turbidity presented by the films indicated phase separation between CAB and caffeine. Noteworthy, all films presented similar mean thickness values, which ranged from 100  $\mu\text{m}$  to 150  $\mu\text{m}$ . **Figure 4.5** shows SEM images taken from the top side and from the internal region (cryofracture) of pure CAB, CAB/caf 2.5 wt%, CAB/caf 5 wt% and CAB/caf 7 wt% films. Pure CAB films (Figures 5a and 5b) presented the typical breath figures [25]. CAB/caf 2.5 wt% films (**Figure 4.5c** and **Figure 4.5d**) showed no caffeine crystals films and the breath figures were less frequent, indicating miscibility among CAB and caffeine and explaining the high transmittance (**Figure 4.4**). However, CAB/caf 5 wt% (**Figure 4.5e** and **Figure 4.5f**) and CAB/caf 7 wt% (**Figure 4.5g** and **Figure 4.5h**) films presented caffeine crystals buried in the matrix and exposed to the air, indicating phase separation. The exposed caffeine crystals probably scattered the light more efficiently, explaining the transmittance decrease (**Figure 4.4**).

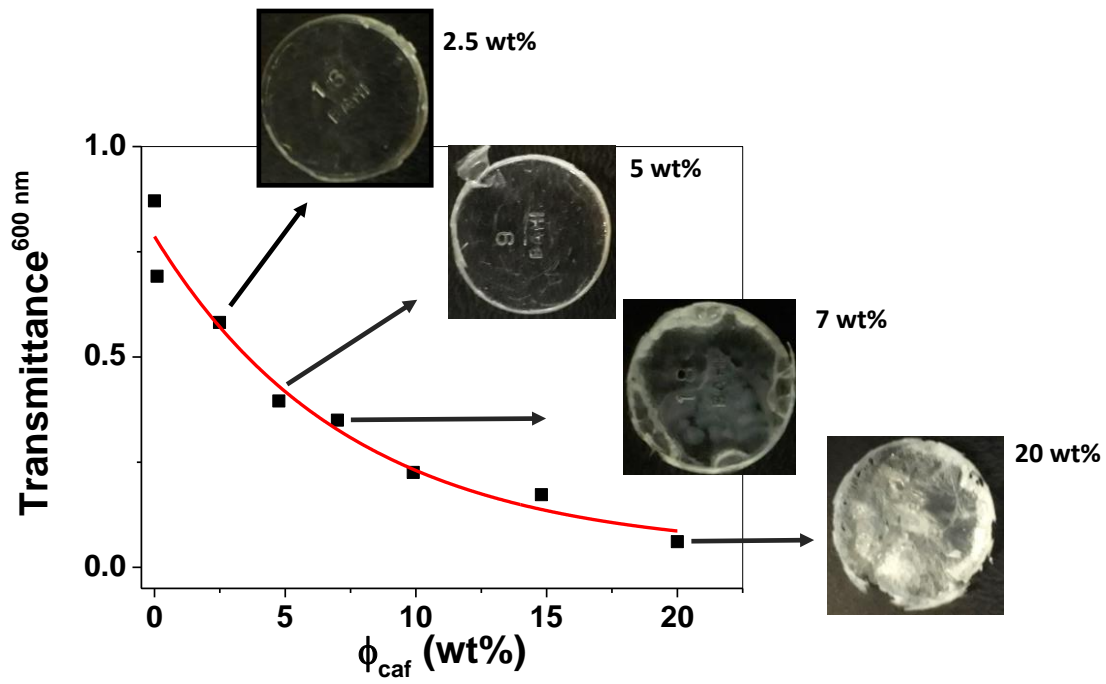


**Figure 4.4:** Photographs and transmittance of light at 600 nm through the CAB/caf films as a function of caffeine content ( $\phi_{caf}$ ). The red line corresponds to the exponential fit  $y = 0.75 \exp(-x/7.4) + 0.036$ ,  $R^2 = 0.9530$ . The experimental data are mean values of duplicates, with standard deviations below 5%.



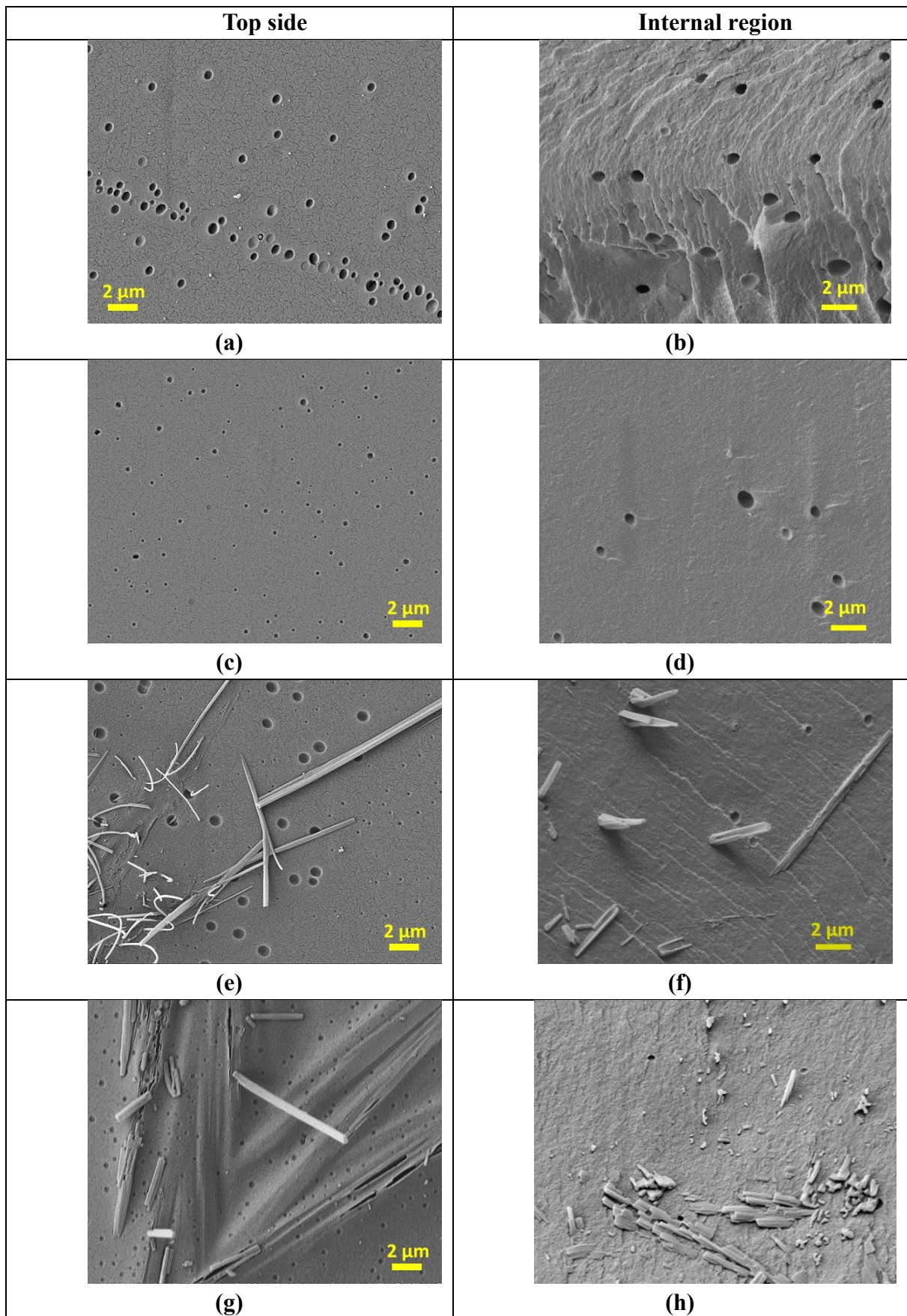


**Figure 4.5:** SEM images of **(a,b)** pure CAB, **(c,d)** CAB/caf 2.5 wt%, **(e,f)** CAB/caf 5 wt% and **(f,h)** CAB/caf 7 wt% films

The glass transition temperature ( $T_g$ ) values determined for pure CAB and CAB/caf films as a function of caffeine content ( $\phi_{caf}$ ) are presented in **Table 4.1**. Caffeine itself has no  $T_g$ , but it presents melting point at 235 °C (GOYANES et al., 2015). The  $T_g$  value determined for pure CAB ( $107 \pm 1$  °C) is in agreement with literature data (AMIM; BLACHECHEN; PETRI, 2012). The  $T_g$  values of CAB/caf films decreased linearly with  $\phi_{caf}$ , so that the addition of each 1 wt% caffeine to CAB reduced its  $T_g$  in 3.8 °C, indicating favorable interactions between caffeine and CAB (**Supplementary Material SM3**). The  $T_g$  of alginate based microcapsules decreased from 74 °C to 71 °C due to the intermolecular hydrogen bonding with caffeine molecules (MOHAMMADI; EHSANI; BAKHODA, 2018). Hydrogen bonds among caffeine molecules and poly(vinyl alcohol) also promoted the reduction of PVA  $T_g$  from 85 °C to 45 °C (GOYANES et al., 2015).

**Supplementary Material SM4** provides the thermogravimetric curves and the corresponding derivative curves of CAB, CAB/caf 2.5 wt%, CAB/caf 5 wt% and CAB/caf 7 wt% films. Table 1 shows the temperatures corresponding to the initial decomposition temperature ( $T_{5\%}$ ), thermal degradation ( $T_{deg}$ ) and char residue values at 500 °C. The initial decomposition temperature ( $T_{5\%}$ ) of pure CAB was noted at 315 °C and rest of the films exhibit ( $T_{5\%}$ ) at 293 °C, 238 °C and 244 °C for CAB/caf 2.5 wt%, CAB/caf 5 wt% and CAB/caf 7 wt% respectively. The above results indicated that presence of caffeine content ( $\phi_{caf}$ ) decreases the thermal stability of CAB. The CAB/caf 2.5 wt% films presented only one thermal event, which was assigned to the main degradation,  $T_{deg}$ , at 376 °C; it is 8 °C higher than that of pure CAB and might be due to favorable interactions with caffeine. For CAB/caf 5 wt% and 7 wt% films, beyond the main decomposition at 377 °C and 375 °C, respectively, a small fraction of material underwent degradation at 210 °C and 251 °C, respectively, which might correspond to the segregated caffeine molecules that were observed on the



film surface (**Figure 4.5e** and **Figure 4.5g**). The insignificant char residue obtained at 500 °C showed that CAB/caf systems undergo complete pyrolysis and decomposition.

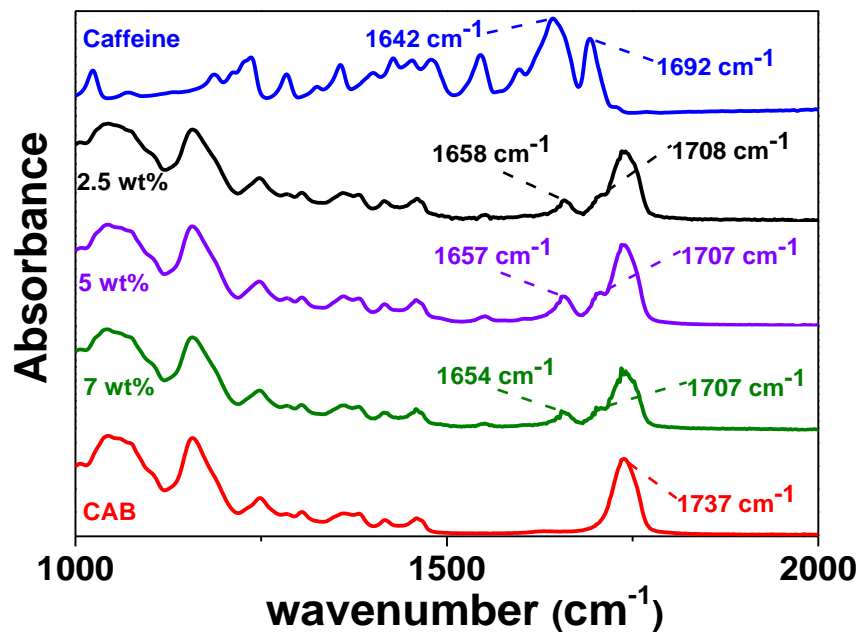
**Table 4.1.** Glass transition temperature ( $T_g$ ), initial decomposition temperature ( $T_{5\%}$ ), degradation temperature ( $T_{deg}$ ) and char residue at 500 °C determined for pure CAB and CAB/caf 2.5 wt%, CAB/caf 5 wt% and CAB/caf 7 wt% films.

Sample	$T_g$ (°C)	$T_{5\%}$	$T_{deg}$ (°C)	Char (%)
CAB	107 ± 1	315	368 ± 1	5.9
CAB/caf 2.5 wt%	96 ± 1	293	376 ± 2	6.1
CAB/caf 5 wt%	88 ± 1	238	210 ± 1 377 ± 1	7.5
CAB/caf 7 wt%	79 ± 1	244	251 ± 1 375 ± 2	6.7

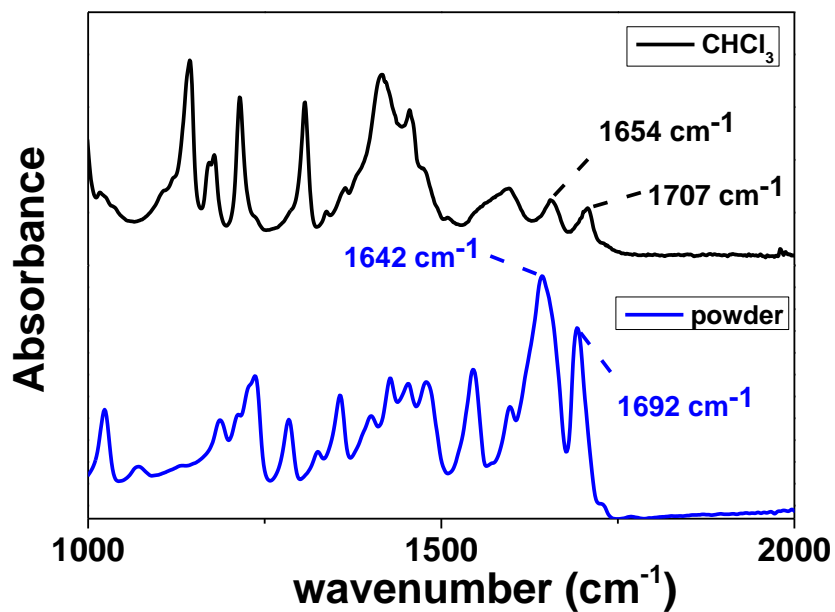
The interactions between caffeine and CAB were further investigated using FTIR-ATR spectroscopy. **Figure 4.6a** shows the FTIR-ATR spectra obtained for pure caffeine, pure CAB (powder), CAB/caf 2.5 wt%, CAB/caf 5 wt% and CAB/caf 7 wt% films, in the spectral range from 1000  $\text{cm}^{-1}$  to 2000  $\text{cm}^{-1}$ . Spectra with spectral range from 600  $\text{cm}^{-1}$  to 4000  $\text{cm}^{-1}$  and the corresponding bands assignments are provided as **Supplementary Material SM5**. The most interesting features concern the pure caffeine bands at 1642  $\text{cm}^{-1}$  and 1692  $\text{cm}^{-1}$ , assigned to the stretching of conjugated C=O(6) and isolated C=O(2) carbonyl groups (JOHNSON et al., 2017). In the presence of CAB, they shifted to higher wavenumber, for instance, CAB/caf 2.5 wt%, 5 wt% and 7 wt% films the C=O(6) bands shifted to 1658  $\text{cm}^{-1}$ , 1657  $\text{cm}^{-1}$ , and 1654  $\text{cm}^{-1}$ , respectively, whereas the C=O(2) band shifted to 1707  $\text{cm}^{-1}$ , in all compositions. The same effect was observed when the spectrum of caffeine powder was compared with the spectrum of caffeine dissolved in chloroform (**Figure 4.6b**). In chloroform, where the caffeine molecules are well solvated, the C=O(6) and C=O(2) bands appeared at 1654  $\text{cm}^{-1}$  and 1707  $\text{cm}^{-1}$ . Thus, such shifts to higher wavenumber clearly indicate

weakening of self-assembling of caffeine molecules and evidence favorable interactions between caffeine and CAB (MARSAC; LI; TAYLOR, 2009). Considering the CAB  $DS_{Ac}$  of 0.2 and  $DS_{But}$  of 2.5, dipole-dipole interactions and van der Waals interactions are expected to drive the miscibility.

One should notice that during the FTIR-ATR analysis, the evanescent wave penetrates the whole CAB/caf film because the films thicknesses ranged from 30  $\mu\text{m}$  to 50  $\mu\text{m}$  thick, so that the spectra reveal the vibrational bands of functional groups present on the surface and in the bulk film. Recently, FTIR-ATR was applied as analytical tool to estimate the amount of caffeine and loperamide hydrochloride printed on poly(ethylene terephthalate) films (PALO et al., 2016).



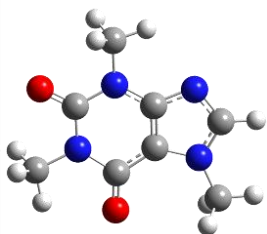
(a)



(b)

**Figure 4.6.** FTIR-ATR determined for (a) pure caffeine as powder, pure CAB, CAB/caf 2.5 wt%, CAB/caf 5 wt% and CAB/caf 7 wt% films micrometric films, (b) pure caffeine as powder and caffeine dissolved in chloroform at 2.0 g L<sup>-1</sup>.

DFT calculations were performed in order to gain insight about the interactions between caffeine and CAB monomer. The optimized DFT geometry of caffeine interacting with CAB monomer is displayed in **Figure 4.7**. The geometry optimization steps indicated hydrogen bonding between CAB hydroxyl group and caffeine C=O(2), with interaction energy of - 42 kJ/mol. The geometry optimization steps are available as a movie at (FURTADO et al., 2019)..



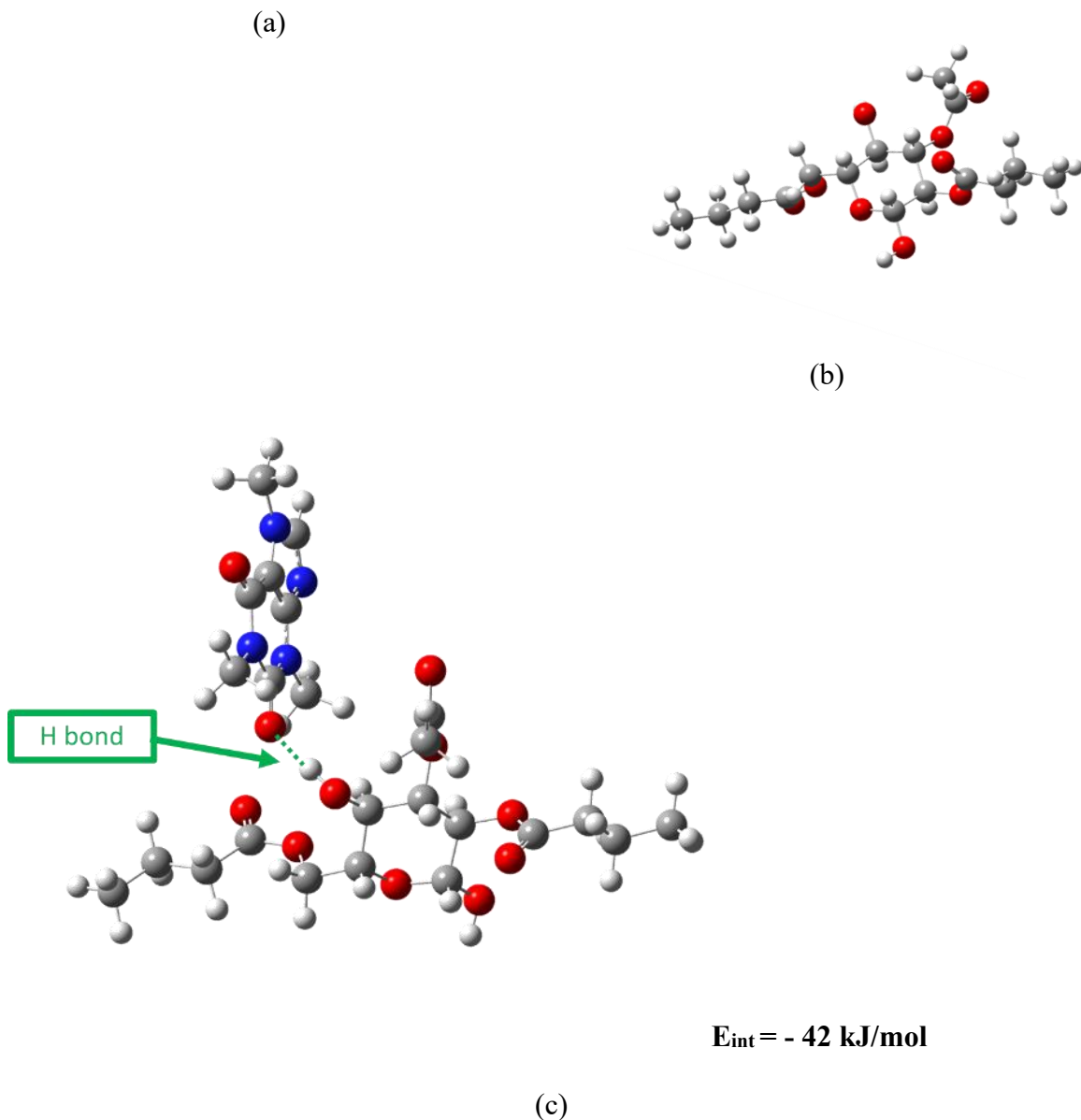


**Figure 4.7.** Snapshot of optimized geometries from DFT calculations of (a) caffeine, (b) CAB monomer and (c) caffeine and CAB interaction, where caffeine molecule approaches to CAB monomer by hydrogen bonding between CAB hydroxyl group and caffeine C=O(2). The interaction energy value was obtained from the difference of the energy of the isolated species.

#### 4.3.3 In vitro release of caffeine from CAB/caf films

The *in vitro* release of caffeine from CAB/caf 2.5 wt% films was negligible, regardless of the pH or ionic strength of external medium. The miscibility between CAB and caffeine at  $\phi_{caf}$  2.5 wt%

probably favored the homogeneous distribution of caffeine in the polymeric matrix, as evidenced in **Figure 4.5c** and **Figure 4.5d**, impairing the caffeine release to the medium.

**Figure 4.8a** and **Figure 4.8b** show the cumulative release of caffeine from CAB/caf 5 wt% and 7 wt%, respectively, at pH 5.5, in MilliQ water, NaCl 0.01 mol L<sup>-1</sup> and NaCl 0.10 mol L<sup>-1</sup>. It is possible to divide the release behavior into two regimes, a fast one up to 6 h, and a slow and continuous one for longer release time (48 h). The fast process probably corresponds to the dissolution and release of caffeine located at the film surface (**Figure 4.5e** and **Figure 4.5g**), whereas the slow one refers to the release of caffeine buried in the films, as observed in SEM images (**Figure 4.5f** and **Figure 4.5h**). Small defects in the film structure (microcracks, for instance) are already enough to promote the release of caffeine from the bulk film. In a similar process, the release of caffeine from nanoporous network formed by MFC coated on paper also presented a fast release in the first 30 min, and a slow step until the total release took place, after 10 h (LAVOINE; DESLOGES; BRAS, 2014). At 6 h release, the amounts of caffeine released from CAB/caf 5 wt% and CAB/caf 7 wt% in MilliQ water were the most pronounced,  $22.1 \pm 0.5\%$  and  $28 \pm 1\%$ , respectively. After 48 h, the highest cumulative releases amounted to  $43 \pm 6\%$  from CAB/caf 5 wt% in MilliQ water and  $55 \pm 2\%$  from CAB/caf 7 wt% in NaCl 0.10 mol L<sup>-1</sup>.

The fast (up to 6 h) and slow release stages were also observed for the release under different pH values (**Figure 4.8c** and **Figure 4.8d**). In the fast stage, the release from CAB/caf 5 wt% showed weak pH dependence; it ranged from  $14 \pm 3\%$  at pH 9 to  $22 \pm 3\%$  at pH 5.5. On the other hand, the release from CAB/caf 7 wt% was the highest at pH 2 ( $56 \pm 2\%$ ) and the lowest at pH 9 ( $25 \pm 3\%$ ). After 48 h, at pH 7.4, the release of caffeine from CAB/caf 7 wt% and CAB/caf 5 wt% films was  $98 \pm 2\%$  and  $50 \pm 2\%$ , respectively, which correspond to 1.5 g L<sup>-1</sup> and 0.5 g L<sup>-1</sup> caffeine.

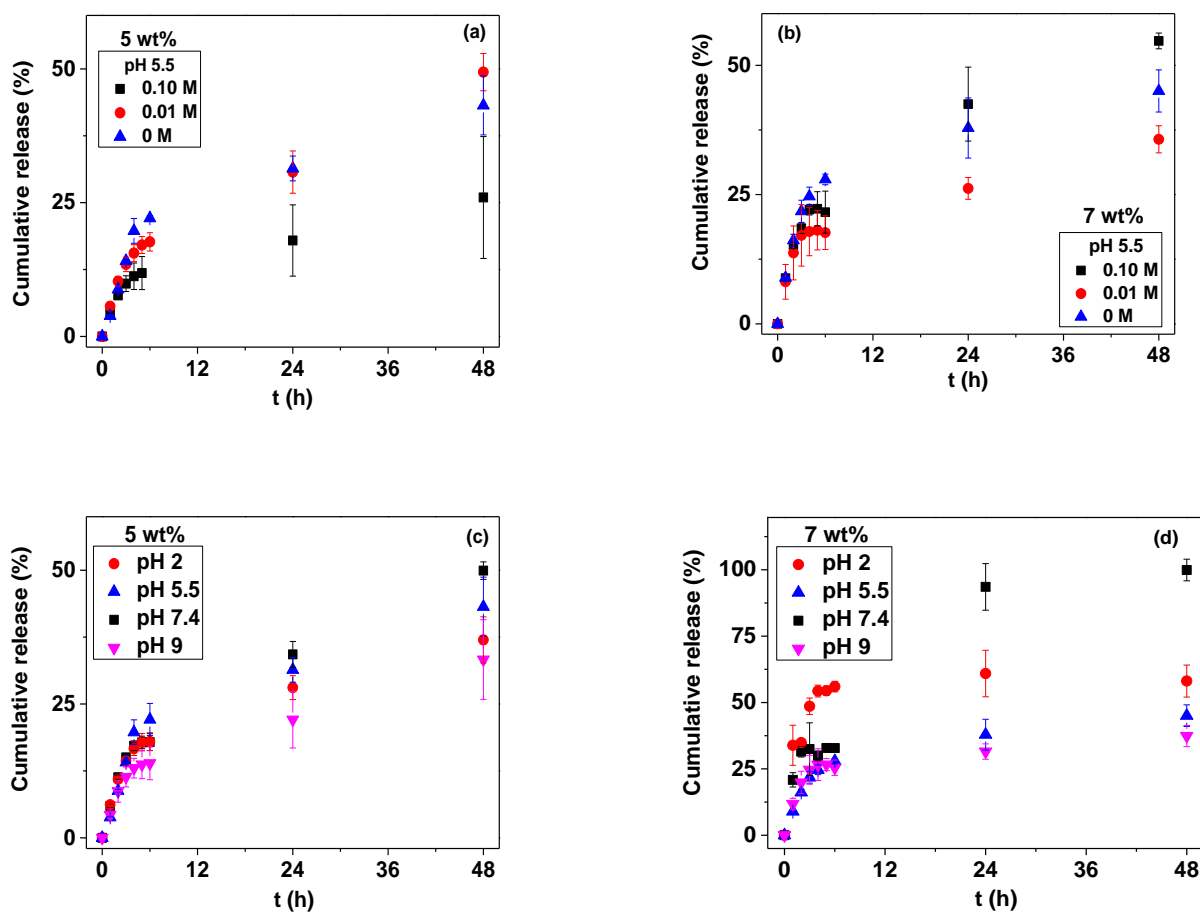


**Figure 4.8.** Release profiles of caffeine from (a) CAB/caf 5 wt% and (b) CAB/caf 7 wt% in MilliQ at pH 5.5, 25 °C, in MilliQ water (blue triangle), NaCl 0.01 mol L<sup>-1</sup> (red circle) and NaCl 0.10 mol L<sup>-1</sup> (black square). Release profiles of caffeine from (c) CAB/caf 5 wt% and (d) CAB/caf 7 wt% at 25 °C, pH 2.0 (red circle), pH 5.5 (blue triangle), pH 7.4 (black square) and pH 9 (pink triangle).

**Figure 4.9** shows schematically the release of caffeine at pH 7.4, from CAB/caf 2.5 wt%, CAB/caf 5 wt% and CAB/caf 7 wt%, over the period of 6 h and 48 h. In this model, caffeine molecules are not released from CAB/caf 2.5 wt% films due to complete miscibility with CAB, which does not swell in this medium. In the case of CAB/caf 5 wt% and CAB/caf 7 wt%, in the first 6 h, caffeine molecules located on the film surface dissolve in the medium. This first step is slow because caffeine molecules, which are not miscible with CAB, are well packed into organized structures on the outer surface, as observed in **Figure 4.5e** and **Figure 4.5g**. This process depends mainly on the amount of caffeine that segregated from the CAB matrix. After dissolution of external

caffeine molecules, caffeine molecules located in the interior of the CAB films can take advantage of breath figures or film degradation to come in contact with the external medium, and then, to diffuse to the medium. **Supplementary Material SM6** shows photographs of CAB/caf 2.5 wt% films and CAB/caf 7 wt% films and after 48 h, at pH 7.4. CAB/caf 2.5 wt% films kept their homogeneous and regular appearance, indicating that CAB was not eroded by the medium. On the other hand, CAB/caf 7 wt% films show empty (dark) spots, which probably were previously occupied by caffeine molecules.

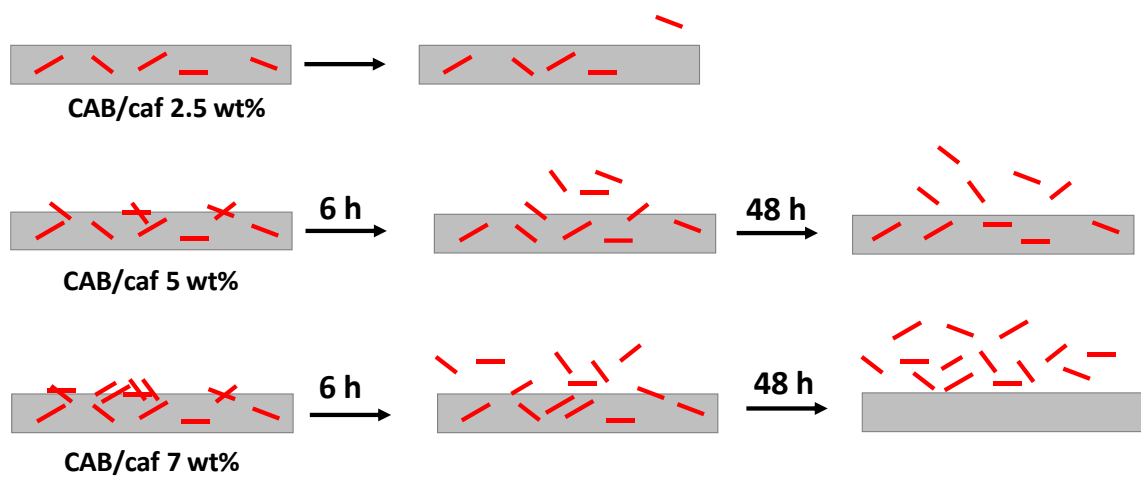


**Figure 4.9.** Schematic representation of caffeine release pH 7.4, from CAB/caf 2.5 wt%, CAB/caf 5 wt% and CAB/caf 7 wt%, over the period of 6 h and 48 h.

Many empirical models for drug release are designed for erodible polymers (MIRCIOIU et al., 2019), which is not the case of CAB under the experimental conditions. CAB is chemically stable in the pH range investigated (pH 2 to pH 9). **Supplementary Material SM7** provides an attempt to fit the experimental data to the Korsmeyer-Peppas model:

$$\frac{M^t}{M^{eq}} = kt^n \quad (1)$$

where  $M^t$  is the released amount at time “t”,  $M^{eq}$  is the released amount at equilibrium,  $k$  is a constant and “ $n$ ” is the diffusional coefficient, which is related to the interaction between drug and polymer matrix and describes the release mechanism. The fittings were performed for the first 6 h, where only the dissolution of segregated caffeine molecules takes place. The resulting “ $n$ ” values ranged from 0.67 to 1.0 (**Supplementary Material SM7**), indicating weak interaction between polymer and drug. This is consistent with the proposed model, which considers the first step as the dissolution period of segregated caffeine molecules. For period longer than 6 h, the release rate was estimated from linear fits (between 6 h and 48 h) in the range of  $5 \text{ mg.L}^{-1}.\text{h}^{-1}$  to  $8 \text{ mg.L}^{-1}.\text{h}^{-1}$ .

**Table 4.2** shows some literature examples, (WIDAWSKI; RAWISO; FRANÇOIS, 1994; BELSCAK-CVITANOVIC et al., 2015; HASEEB et al., 2017; MOHAMMADI; EHSANI; BAKHODA, 2018; NOOR et al., 2018), (LAVOINE; DESLOGES; BRAS, 2014) (LABAY; CANAL; CANAL, 2012; LI et al., 2013; ALAM; TAKAFUJI; IHARA, 2014; SILVA et al., 2014; AMIRI et al., 2017; CIRILLO et al., 2019; VILLEGAS; PÉREZ, 2019) which employed polymer matrices for the release of caffeine. Many of them are water soluble polymers or polymers that swell in aqueous media. However, in comparison to CAB/caf 7 wt%, most of them presented faster release of caffeine, pointing out that for hydrophilic drugs, as caffeine, water soluble polymers provide pronounced contact with water, speeding up the release.

**Table 4.2.** Some examples of polymeric delivery systems for caffeine and the corresponding highlight and reference.

System	Highlight	Ref.
Alginate-based blends consisting of carrageenan, pectin, chitosan or psyllium husk powder	Chitosan coated beads released 50% of caffeine after 13 min.	(BELSCAK - CVITANO VIC et al., 2015)



Beta-glucan, resistant starch, and beta-cyclodextrin microparticles		Caffeine release was more prevalent in simulated intestinal juice than gastric medium, displaying controlled release mechanism for such systems.	(NOOR et al., 2018)
Alginate-based matrix combined with different natural biopolymers		80% released in simulated mouth conditions after 30 min	(MOHAM MADI; EHSANI; BAKHODA, 2018)
Tablets with linseed polysaccharides		Buffers of pH 1.2, 6.8, 7.4, and DI water were used. Negligible drug release (<10%) was noted at pH 1.2 (2 h). Higher and sustained release was observed at pH 6.8 and 7.4 up to 16 h.	(HASEEB et al., 2017)
Microfibrillated cellulose coated paper loaded with caffeine at 7 g/m <sup>2</sup>		Release in 500 mL water, 100% caffeine release after 10 h.	(LAVOINE; DESLOGES; BRAS, 2014)
Acrylic acid (AAc), and 2- <i>N,N</i> -dimethylamino methacrylate grafted onto PVDF membrane.	ethyl	At pH 5, the maximum release was reached at 3 h, while at pH 7, it took 5 h.	(VILLEGA S; PÉREZ, 2019)
3D printed filaments of PVA/caffeine/paracetamol, with 4.7% and 9.5% caffeine		100% drug release in less than 360 min.	(GOYANE S et al., 2015)
Chitosan–quercetin-poly( <i>N</i> -isopropylacrylamide) hydrogels, 0.85 mg/mL caffeine loaded		After 30 min, at 40 °C and pH 2.0, 50% drug release (burst effect). At pH 7 and 25 °C or 40 °C, sustained release.	(CIRILLO et al., 2019)
Poly[ <i>N</i> -isopropylacrylamide-co-(3-methacryloxypropyltrimethoxysilane)] (pNS) copolymer chains as the backbone and silica nanoparticles (SiP) as crosslinkers		Release in 150 mL deionized water (pH 6.8) or pH 1.7. The release reached equilibrium (93% release) within 4 h at both pH conditions.	(ALAM; TAKAFUJI; IHARA, 2014)
Plasma treated polyamide 6,6 fibers impregnated with caffeine aqueous solution at 1%		Release in 150 mL PBS buffer at 37 °C. 90% release during the first hour.	(LABAY; CANAL; CANAL, 2012)
Electrospun nanofibers of PVA/caffeine at weight ratio 25:1	s.	Burst- caffeine released 100% within 60	(LI et al., 2013)
Biocellulose membrane loaded with caffeine at 8 mg/cm <sup>2</sup>		80% released in PBS after 5 min.	(SILVA et al., 2014)

Magnetic alginate beads loaded with 100 mg caffeine	Diffusion of drug from hydrogels was controlled by the pH of environment; maximal release was 60% after ~3 h.	(AMIRI et al., 2017)
CAB/caf 7 wt%	Sustained release over 48 h. Total (1.5 g L <sup>-1</sup> ) released in PBS after 48 h.	This work

## 4.4 CONCLUSIONS

The comprehension about the miscibility of drug and the polymer carrier is important to understand the release process over a specific duration. In this study, partial miscibility of CAB and caffeine was observed for caffeine contents higher than 5 wt%; total miscibility was observed for caffeine content lower than 2.5 wt%. The release from completely miscible systems was impaired. Systems partially miscible showed a two-step release process, namely, a first one corresponding to the dissolution of segregated drug and a second one related to the dissolution and release of drug located in the internal polymer matrix. CAB/caf 7 wt% films were particularly interesting because they provided total release of loaded caffeine at pH 7.4, for the prolonged period of 48 h. This feature is particularly advantageous for systems, which require prolonged release of caffeine. Moreover, CAB/caf 7 wt% systems might be interesting for hot melt extrusion because both components can be processed together and the caffeine content of 7 wt% is similar to those found in commercial tablets for headache as 6.5 wt% (DRUGS.COM, 2019).

## 4.5 REFERENCES

AL REEF, T.; GHANEM, E. Caffeine: Well-known as psychotropic substance, but little as immunomodulator. *Immunobiology*, v. 223, n. 12, p. 818–825, 2018. Disponível em: <<https://doi.org/10.1016/j.imbio.2018.08.011>>.

ALAM, A.; TAKAFUJI, M.; IHARA, H. Silica nanoparticle-crosslinked thermosensitive

hybrid hydrogels as potential drug-release carriers. *Polymer Journal*, v. 46, p. 293–300, 2014.

ALI, R.; WALTHER, M.; BODMEIER, R. Cellulose Acetate Butyrate: Ammonio Methacrylate Copolymer Blends as a Novel Coating in Osmotic Tablets. *AAPS PharmSciTech*, v. 19, n. 1, p. 148–154, 2018.

AMIM, J.; BLACHECHEN, L. S.; PETRI, D. F. S. Effect of sorbitan-based surfactants on glass transition temperature of cellulose esters. *Journal of Thermal Analysis and Calorimetry*, v. 107, n. 3, p. 1259–1265, 2012.

AMIM, J.; PETRI, D. F. S. Effect of amino-terminated substrates onto surface properties of cellulose esters and their interaction with lectins. *Materials Science and Engineering C*, v. 32, n. 2, p. 348–355, 2012. Disponível em: <<http://dx.doi.org/10.1016/j.msec.2011.11.004>>.

AMIRI, M. et al. Caffeine : A novel green precursor for synthesis of magnetic CoFe<sub>2</sub>O<sub>4</sub> nanoparticles and pH-sensitive magnetic alginate beads for drug delivery. *Materials Science & Engineering C*, v. 76, p. 1085–1093, 2017. Disponível em: <<http://dx.doi.org/10.1016/j.msec.2017.03.208>>.

BELSCAK-CVITANOVIC, A. et al. Improving the controlled delivery formulations of caffeine in alginate hydrogel beads combined with pectin, carrageenan, chitosan and psyllium. *Food Chemistry*, v. 167, p. 378–386, 2015.

BLACHECHEN, L. S.; SOUZA, M. A.; PETRI, D. F. S. Effect of humidity and solvent vapor phase on cellulose esters films. *Cellulose*, v. 19, n. 2, p. 443–457, 2012.

BLANCHARD, J.; SAWERS, S. J. A. The absolute bioavailability of caffeine in man. *European Journal of Clinical Pharmacology*, v. 24, n. 1, p. 93–98, 1983.

CIRILLO, G. et al. Chitosan–Quercetin Bioconjugate as Multi-Functional Component of Antioxidants and Dual-Responsive Hydrogel Networks. *Macromolecular Materials and Engineering*, 2019.

DRUGS.COM. *Acetaminophen / Caffeine Dosage*. Disponível em: <<https://www.drugs.com/dosage/acetaminophen-caffeine.html>, accessed in September 2019.>.

EDDLESTON, M. D.; JONES, W. Formation of tubular crystals of pharmaceutical compounds. *Crystal Growth and Design*, v. 10, n. 1, p. 365–370, 2010.

EDGAR, K. J. et al. Advances in cellulose ether performance and application. *Prog. Polym. Sci.*, v. 26, p. 1605–1688, 2001.

EDGAR, K. J. Cellulose esters in drug delivery. *Cellulose*, v. 14, n. 1, p. 49–64, 2007.

FRISCH, M. J. et al. *Gaussian Revision A.02* Wallingford CT Gaussian Inc., , 2016. .

FURTADO, L. M. et al. *DFT calculations for caffeine and cellulose acetate butyrate*. Disponível em: <<https://www.youtube.com/watch?v=IqaPsFcEaPc&feature=youtu.be>. >.

GOYANES, A. et al. 3D Printing of Medicines: Engineering Novel Oral Devices with Unique Design and Drug Release Characteristics. *Molecular Pharmaceutics*, v. 12, n. 11, p. 4077–4084, 2015.

HARADA, N.; NAKAMURA, J. I.; UYAMA, H. Preparation of macroporous cellulose beads through a single-step non-solvent induced phase separation method from a cellulose acetate solution. *Bulletin of the Chemical Society of Japan*, v. 92, n. 9, p. 1444–1446, 2019.

HASEEB, M. T. et al. Evaluation of superabsorbent linseed-polysaccharides as a novel stimuli-responsive oral sustained release drug delivery system. *Drug Development and Industrial Pharmacy*, v. 43, n. 3, p. 409–420, 2017.

JOHNSON, N. O. et al. Anion-Caffeine Interactions Studied by <sup>13</sup>C and <sup>1</sup>H NMR and ATR-FTIR Spectroscopy. *Journal of Physical Chemistry B*, v. 121, n. 7, p. 1649–1659, 2017.

KOSAKA, P. M.; KAWANO, Y.; PETRI, D. F. S. Dewetting and surface properties of ultrathin films of cellulose esters. *Journal of Colloid and Interface Science*, v. 316, n. 2, p. 671–677, 2007.

LABAY, C.; CANAL, M.; CANAL, C. Relevance of Surface Modification of Polyamide 6 . 6 Fibers by Air Plasma Treatment on the Release of Caffeine. *Plasma Processes and Polymers*, v. 9, p. 165–173, 2012.

LAVOINE, N.; DESLOGES, I.; BRAS, J. Microfibrillated cellulose coatings as new release systems for active packaging. *Carbohydrate Polymers*, v. 103, n. 1, p. 528–537, 2014. Disponível em: <<http://dx.doi.org/10.1016/j.carbpol.2013.12.035>>.

LI, X. et al. Electrospun polyvinyl-alcohol nanofibers as oral fast-dissolving delivery system of caffeine and riboflavin. *Colloids and Surfaces B: Biointerfaces*, v. 103, p. 182–188, 2013. Disponível em: <<http://dx.doi.org/10.1016/j.colsurfb.2012.10.016>>.

MALATERRE, V. et al. Oral osmotically driven systems: 30 years of development and clinical use. *European Journal of Pharmaceutics and Biopharmaceutics*, v. 73, n. 3, p. 311–323, 2009. Disponível em: <<http://dx.doi.org/10.1016/j.ejpb.2009.07.002>>.

MARSAC, P. J.; LI, T.; TAYLOR, L. S. Estimation of drug-polymer miscibility and solubility in amorphous solid dispersions using experimentally determined interaction parameters. *Pharmaceutical Research*, v. 26, n. 1, p. 139–151, 2009.

MIRCIOIU, C. et al. Mathematical modeling of release kinetics from supramolecular drug delivery systems. *Pharmaceutics*, v. 11, n. 3, 2019.

MOHAMMADI, N.; EHSANI, M. R.; BAKHODA, H. Development of caffeine-encapsulated alginate-based matrix combined with different natural biopolymers, and evaluation of release in simulated mouth conditions. *Flavour and Fragrance Journal*, v. 33, n. 5, p. 357–366, 2018.

NIKOO, A. M. et al. Electrospray-assisted encapsulation of caffeine in alginate microhydrogels. *International Journal of Biological Macromolecules*, v. 116, p. 208–216, 2018. Disponível em: <<https://doi.org/10.1016/j.ijbiomac.2018.04.167>>.

NOOR, N. et al. Microencapsulation of caffeine loaded in polysaccharide based delivery

systems. *Food Hydrocolloids*, v. 82, p. 312–321, 2018. Disponível em: <<https://doi.org/10.1016/j.foodhyd.2018.04.001>>.

PALO, M. et al. Quantification of caffeine and loperamide in printed formulations by infrared spectroscopy. *Journal of Drug Delivery Science and Technology*, v. 34, p. 60–70, 2016.

SARFRAZ, A. et al. Morphological Diversity of Caffeine on Surfaces: Needles and Hexagons Published as part of a virtual special issue of selected papers presented at the 2010 Annual Conference of the. *Cryst. Growth Des.*, p. 583–588, 2011.

SHOKRI, J.; ADIBKIA, K. Application of Cellulose and Cellulose Derivatives in Pharmaceutical Industries Chapter. In: *Cellulose - Medical, Pharmaceuical and Electronic Applications*. [s.l.] IntechOpen, 2013. p. 21.

SILVA, N. H. C. S. et al. Topical caffeine delivery using biocellulose membranes : a potential innovative system for cellulite treatment. *Cellulose*, v. 21, p. 665–674, 2014.

SOBRAL, M. C. C. M. et al. Ketotifen controlled release from cellulose acetate propionate and cellulose acetate butyrate membranes. *Journal of Materials Science: Materials in Medicine*, v. 19, n. 2, p. 677–682, 2008.

TAVAGNACCO, L. et al. Stacking and Branching in Self-Aggregation of Caffeine in Aqueous Solution: From the Supramolecular to Atomic Scale Clustering. *Journal of Physical Chemistry B*, v. 120, n. 37, p. 9987–9996, 2016.

VARSHOSAZ, J. et al. Formulation and characterization of cellulose acetate butyrate nanoparticles loaded with nevirapine for HIV treatment. *Journal of Drug Delivery Science and Technology*, v. 48, n. August, p. 9–20, 2018. Disponível em: <<https://doi.org/10.1016/j.jddst.2018.08.020>>.

VILLEGAS, G. M. E.; PÉREZ, G. G. Adsorption and release of caffeine from smart PVDF polyampholyte membrane. *Iranian Polymer Journal*, v. 28, n. 8, p. 639–647, 2019. Disponível em:

<<https://doi.org/10.1007/s13726-019-00730-6>>.

WIDAWSKI, G.; RAWISO, M.; FRANÇOIS, B. Self-organized honeycomb morphology of star-polymer polystyrene films. *Nature*, v. 369, p. 387–389, 1994. Disponível em: <<http://www.ncbi.nlm.nih.gov/pubmed/20576887>>.

YANG, Y. et al. Tunable drug release from nanofibers coated with blank cellulose acetate layers fabricated using tri-axial electrospinning. *Carbohydrate Polymers*, v. 203, n. August 2018, p. 228–237, 2019. Disponível em: <<https://doi.org/10.1016/j.carbpol.2018.09.061>>.

YEW, H. C.; MISRAN, M. Preparation and characterization of pH dependent  $\kappa$ -carrageenan-chitosan nanoparticle as potential slow release delivery carrier. *Iranian Polymer Journal (English Edition)*, v. 25, n. 12, p. 1037–1046, 2016.

## 5 CHAPTER 3 - Biomimetic filter for the removal of organic pollutants and oil/water separation

Accepted version of book chapter from [ FURTADO, Laíse M.; NOVAES, Stephanie D.; PETRI, Denise F. S.; "Biomimetic Filter for Removal of Organic Pollutants and Oil/Water Separation", p. 13 -17. In: 10º Workshop do Mestrado Profissional – Universidade de São Paulo, Instituto de Química. São Paulo: Blucher, 2022.]. The book is open access. The published version of this book chapter and the book can be accessed in the links, respectively: ISBN 9786555502084, DOI 10.5151/9786555502084-02 and <https://openaccess.blucher.com.br/article-list/9786555502084-593/list#undefined>.

### Abstract

Oil spill and water contamination resulting from human activities are potentially harmful to human health and aquatic organisms. Adsorbents based on sustainable materials, with low cost and high efficiency might mitigate the contamination problem. In this study, a biomimetic filter was obtained by combining sugarcane bagasse (BG) microparticles with hydroxypropyl methylcellulose (HPMC), and polydopamine (PDA), which conferred adherence between the components, chemical and mechanical stability for the adsorbents. The adsorbents were prepared from mixtures of HPMC (30 g/L), PDA (6 g/L) and BG at 100 g/L (F100), 150 g/L (F150) or 200 g/L (F200). SEM images showed that the filters have a porous and cohesive structure. The F150 biomimetic filter was stable for 24 h in aqueous medium at pH 5.5 and  $25 \pm 1$  °C, without loss of material or shape. In the absence of PDA the filters dissolved after 30 min in water. The F150 filter showed 70% and 100% removal



efficiency towards bisphenol-A (BPA) and methylene blue (MB), respectively, and oil retention of 100% from a mixture of 1:4, sunflower oil : water.

## 5.1 MOTIVATION

The control of substances released into the environment through industrial effluents, agricultural activities, domestic sewage, and wastewater from Sewage Treatment Plants has become a matter of great environmental concern in recent decades. Oil spills and water contamination by molecules resulting from human activities, such as endocrine disruptors, compounds potentially harmful to human health and aquatic organisms, demands new adsorbents based on sustainable materials, with low cost and high efficiency. Materials developed for pollutants adsorption from water must be mechanically stable, insoluble in water and recyclable. According to the National Supply Company (Conab), Brazil is the world's largest producer of sugarcane, having great importance for Brazilian agribusiness. The estimate for the harvest in 2022/23 was 610.1 million tons (CONAB, 2023). Sugarcane bagasse (BG) is the residue obtained after sugarcane processing, representing 30% of the initial biomass, corresponding to approximately 200 million tons in 2020/21 (BASSAM, 2010). The contents of holocellulose, lignin, and ash in the BG amounted to 79.0%, 20.5% and 0.2% (NOVAES; OLIVEIRA; PETRI, 2022). BG has great potential for removing heavy metals from effluents (EWULONU et al., 2019). Hydroxypropyl methylcellulose (HPMC) is a cellulose ether; the degree of substitution (DS) is related to substitution of hydroxyl groups by methyl groups, and the molar substitution (MS) is related to the insertion of hydroxypropyl groups (THIELKING; SCHMIDT, 2012). HPMC has been applied as rheological modifier, food additive, emulsion stabilizer and excipient in controlled release of drugs (MARANI; BLOISI; PETRI, 2015). Polydopamine (PDA) is a mussel-inspired adhesive, which has attracted the attention of researchers due to its simplicity, low cost and interesting coating properties. PDA coatings occur due to the

autooxidation of dopamine under alkaline medium (LEE et al., 2007b). Favorable interactions between PDA and cellulose esters allowed the development of adsorbents to remove caffeine (FURTADO; ANDO; PETRI, 2020). Therefore, in this work, the optimized combination of aqueous dispersions of BG microparticles, HPMC, and PDA led to a moldable material at room temperature. After water evaporation by heating, the material presented a highly cohesive porous structure with outstanding mechanical and chemical stability in water. Biomimetic filters showed high efficiency to separate oil from oil/water mixtures and to remove organic contaminants in water.

## 5.2 EXPERIMENTAL SECTION

### 5.2.1 Preparation of biomimetic filter

HPMC E4M (DS = 1.9 and MS = 0.25,  $M_w = 2.5 \times 10^5$  , g/mol), kindly supplied by Dow Chemical Company was dissolved in MilliQ® water at 30 g/ L, volume (V) of 20 mL. Then, BG (supplied by local market) microparticles were incorporated under vigorous stirring into the polymer matrix at 100 g/L, 150 g/L or 200 g/L; the systems were coded as F100, F150 and F200, respectively. Then 10 mL of a dopamine (Sigma-Aldrich H60255, 189.64 g/mol) solution at 6.0 g/L, prepared in Tris-HCl buffer (10 mM, pH 8.5), was added to the HPMC/BG mixtures. The oxidation reaction of dopamine into polydopamine took 4 h. **Figure 5.1a** shows the darker color of the mixtures evidencing the formation of PDA. For contaminant removal tests, the HPMC/BG/PDA mixtures were molded into a plastic Petri dish (diameter = 5.7 cm and thickness = 3 mm), as shown in **Figure 5.1b**. For sunflower oil separation from water/oil mixtures, HPMC/BG/PDA mixtures were molded in acrylic mold, with diameter = 10 mm and thickness = 6 mm. After this step, the materials were placed in oven at 60 °C for drying, during 4 h. Afterwards, the materials were placed in a glass Petri dish for pre-crosslinking on a heating plate at ~ 90 °C and slowly bathed with a crosslinking solution

containing 10 g/L citric acid (crosslinker, Labsynth, Brazil), 6.2 g/L succinic acid (crosslinker, Sigma-Aldrich) and 5.5 g/L sodium hypophosphite (catalyst, Labsynth, Brazil). For the crosslinking bath, it was fixed a ratio of 0.077 between the mass of the material being crosslinked and the volume of crosslinking solution incorporated ( $m_{\text{filter}} \text{ (g)} / V_{\text{solution}} \text{ (mL)}$ ). The dried filters were taken to oven at 172 °C for 10 min for crosslinking (esterification reaction) (**Figure 5.1c**). Finally, the materials were washed to remove unreacted molecules, after drying the F100, F150 and F200 biomimetic filters were characterized. F150 filter was chosen for the adsorption of organic pollutants and oil retention.

### 5.2.2 Characterization of biomimetic filters

Scanning electron microscopy (SEM) analyses were performed for F100, F150 and F200 coated with gold (~ 10 nm) in Jeol Neoscope JCM-5000 microscope operating at 10 kV. The chemical stability of the F100, F150 and F200 filters were evaluated at pH 5.5 (MilliQ water) for 24 h.

### 5.2.3 Removal capacity of methylene blue (MB) and bisphenol A (BPA)

Adsorption of methylene blue (MB, M9140 Sigma Aldrich, 319.85 g/mol) and bisphenol A (BPA, 133027 Sigma, 228.29 g/mol) was performed with F150 filter. The experiment was carried out in reduced pressure filtration system (~ 600 mbar), which the filter was placed directly into a Büchner funnel. The solutions of MB ( $V = 45 \text{ mL}$ ) and BPA ( $V = 25 \text{ mL}$ ) were prepared at initial concentration ( $C_0$ ) 5 mg/L and 388 mg/L, respectively. Separately, the solutions were pumped through the filter and the samples were quantified by spectrophotometer in the UV-Vis region (Beckman-Coulter DU640) for MB ( $\lambda_{\text{max}} = 662 \text{ nm}$ ) and BPA ( $\lambda_{\text{max}} = 276 \text{ nm}$ ). The removal capacity (%) of MB and BPA by F150 biomimetic filter was determined by:

$$\text{Removal (\%)} = \frac{C_0 - C_t}{C_0} \times 100 \quad 5.1$$

where  $C_0$  is initial concentration and  $C_t$  is concentration after a given contact time.

## 5.2.4 Oil and water separation

Sunflower oil and water mixture was prepared at a ratio of 1:4, sunflower oil: water ( $V = 5$  mL), this mixture was poured over the filter in a static column system and the volume of water after oil retention was measured by graduated cylinder.

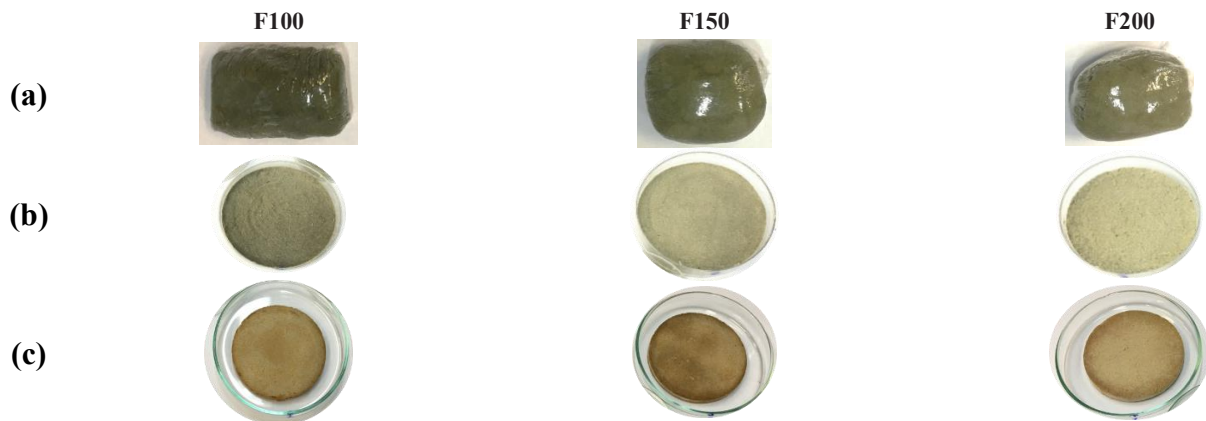


**Figure 5.1:** (a) HPMC/BG/PDA mixtures of F100 (left), F150 (center) and F200 (right) after 4h of DOPA oxidation packaged and stored in a refrigerator for later use/molding. (b) Mixtures of F100, F150 and F200 molded in cylindrical shape (c) Biomimetic filters after the steps of pre-crosslinking and crosslinking

## 5.3 Results

SEM images in **Figure 5.2a**, **Figure 5.2b** and **Figure 5.2c** shows the porous and cohesive structure of filters F100, F150 and F200, respectively; the presence of PDA did not affect the filters morphology. BG microparticles dominate the surface structure, because BG is the main component of these materials.

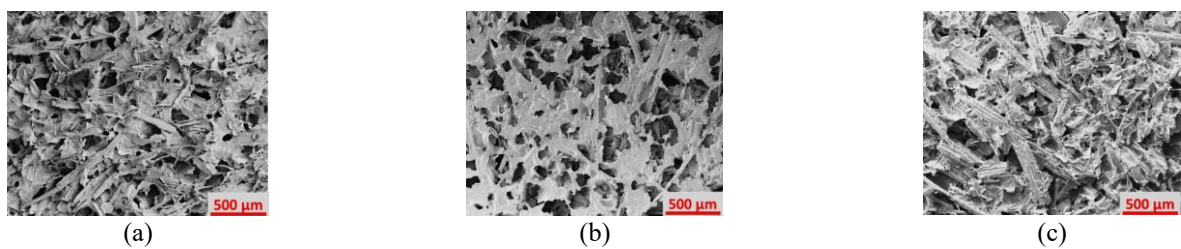


**Figure 5.2:** SEM images of biomimetic filter (a) F100, (b) F150 and (c) F200.

**Figure 5.3a** demonstrates the stability of F100, F150 and F200 filters at pH 5.5 after 24 h under stirring. The F100 filter was not chemically stable, the medium became yellowish because PDA was released to the aqueous medium, and F200 filter had loss of material after 24 h. On the

other hand, F150 filter showed excellent chemical and mechanical stability at pH 5.5. Meanwhile, the material without PDA dissolved completely after 30 min under stirring in water. Confirming that for materials with high content of BG, the esterification reaction (**Figure 5.3b**) was not efficient. Probably, the hydroxyl groups on BG particles were not available for crosslinking with citric acid molecules due to the strong intermolecular H bonds. Therefore, the combination of PDA and citric acid favored the adhesive properties of PDA in the system with high amount of BG, providing chemical stability for biomimetic filter F150 at pH 5.5.

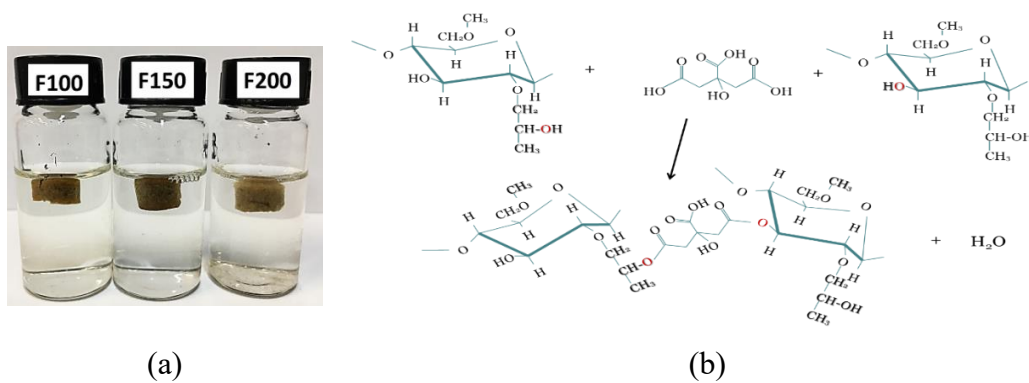


**Figure 5.3:** (a) Photographs of F100, F150 and F200 filters in MilliQ water at pH 5.5 after 24 h under stirring. (b) Schematic representation of the esterification reaction between citric acid and HPMC hydroxyl groups.

MB and BPA adsorption was performed with F150 filter in a reduced pressure filtration system. After pumping 45 mL of MB solution ( $C_0 = 5.0$  mg/L) through F150, the removal capacity yielded 100% (**Figure 5.4a**). The time required to treat 45 mL of solution was 30 seconds. This result indicated that this material has a high affinity for MB. The interactions between MB and the adsorbent might be driven by MB methyl groups and methyl groups on the polymer surface, and ion-dipole interactions with hydroxyl groups in BG. After adsorption, the filter was placed under sunlight for one week to promote the filter recovery by photooxidation of MB molecules (MARTINS; DE TOLEDO; PETRI, 2017).. **Figure 5.4b** shows that the adsorbent could be recovered for a next filtration process. The same filtration system was used for adsorption of BPA, after pumping 25 mL of BPA solution ( $C_0 = 388$  mg/L) the removal capacity was 70%. Probably, the adsorption of BPA occurred through the interactions of the methyl and aromatic groups of BPA and HPMC methyl

groups, and H bonds between BPA and HPMC hydroxyl groups. The time required for filtering 25 mL was 15 seconds. Another potential application for the F150 filter was presented with the 100% oil retention from a 1:4 mixture of sunflower oil: water ( $V = 5$  mL). The time required to collect 4 mL of water was 10 min, in a static column.

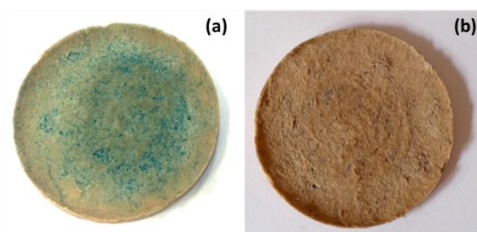


**Figure 5.4:** Photographs of F150 filter (a) after MB adsorption and (b) after filter recovery through photooxidation with sunlight

## 5.4 CONCLUSIONS

The HPMC/BG/PDA mixtures are moldable into filters that presented dimensional and chemical stability. The combination of PDA and crosslinking reaction with citric acid provided chemical and mechanical stability in aqueous media at pH 5.5 for the F150 filter. This filter showed great potential for adsorption of organic pollutants achieving removal of 100 % and 70 % for MB and BPA, respectively, and oil retention. Not less important, the cost to produce HPMC/BG/PDA filters at lab scale was estimated at US\$ 0.025/g, considering the local prices for HPMC, citric acid, DOPA, water, and energy.

## 5.5 REFERENCES

BASSAM, N. E. *Handbook of Bioenergy Crops: A Complete Reference to Species, Development and Applications*. 1st editio ed. [s.l.] Earthscan, 2010.

CONAB, N. S. C. *Produção de cana chega a 610,1 milhões de toneladas na safra 2022/23 com melhora na produtividade nas lavouras*. Disponível em: <[https://www.conab.gov.br/ultimas-noticias/4977-producao-de-cana-chega-a-610-1-milhoes-de-toneladas-na-safra-2022-23-com-](https://www.conab.gov.br/ultimas-noticias/4977-producao-de-cana-chega-a-610-1-milhoes-de-toneladas-na-safra-2022-23-com)



## 6 CHAPTER 4: Carboxymethyl cellulose/sugarcane bagasse/polydopamine adsorbents for efficient removal of Pb<sup>2+</sup> ions from synthetic and undergraduate laboratory wastes

Accepted version of article reproduced with permission from [ [Furtado, L. M.](#); Fuentes, D. P.; ANDO, R. A.; Oliveira, P. V.; Petri, D. F.S. Carboxymethyl cellulose/sugarcane bagasse/polydopamine adsorbents for efficient removal of Pb<sup>2+</sup> ions from synthetic and undergraduate laboratory wastes. JOURNAL OF CLEANER PRODUCTION, v. 380, p. 134969, 2022. Copyright 2022 Journal of Cleaner Production]. The written permission is at Appendice 9.1.3. The published version of this article can be accessed in the link: DOI: <https://doi.org/10.1016/j.jclepro.2022.134969>

### Abstract

Low-cost eco-friendly adsorbents are important as sustainable alternatives for water treatment. Carboxymethyl cellulose (CMC)/sugarcane bagasse (BG) adsorbents were prepared in the presence of polydopamine (PDA) and citric acid (crosslinker), which effectively removed Pb<sup>2+</sup> ions from aqueous synthetic and from an undergraduate laboratory waste containing other 16 metal ions. CMC/BG/PDA adsorbents presented apparent density, specific surface area and porosity of  $157 \pm 3$  kg/m<sup>3</sup>,  $246 \pm 10$  m<sup>2</sup>/kg and 56.5 %, respectively, outstanding chemical and dimensional stability. The adsorption isotherms of Pb<sup>2+</sup> ions on CMC/BG/PDA in the absence and in the presence of Ca<sup>2+</sup> and Mg<sup>2+</sup> ions fitted better to Langmuir models, yielding maximal adsorption capacity values of  $27.4 \pm 2.8$  mg/g and  $25.9 \pm 1.8$  mg/g, respectively. The  $\Delta H_{\text{ads}}$  and  $\Delta S_{\text{ads}}$  values of +5.7 kJ/mol and +48.3



J/(K.mol), respectively, indicated interactions between  $Pb^{2+}$  ions and CMC/BG/PDA hydroxyl groups, which were confirmed by XPS spectra. The fixed bed column adsorption studies indicated the highest adsorption capacity ( $q_{Th}$ ) for  $Pb^{2+}$  under optimal conditions as 70.3 mg/g. In the presence of  $Mg^{2+}$  and  $Ca^{2+}$  ions, the  $q_{Th}$  for  $Pb^{2+}$  decreased from 35.0 mg/g (single system) to 30.6 mg/g. CMC/BG/PDA in column removed 80% of  $Pb^{2+}$  ions from an undergraduate laboratory waste containing 16 other metal ions at pH 1.0. The simultaneous removal of the other metal ions from the laboratory waste was larger than 50%, disclosing the potential of CMC/BG/PDA adsorbents towards real wastes. The subsequent flocculation with a polycation removed.

98.7% of  $Pb^{2+}$  ions and 90% of other metal ions, disclosing the potential of combining adsorption and flocculation.

**Keywords:** carboxymethyl cellulose; polydopamine; sugarcane bagasse; adsorption; lead; citric acid

## 6.1 MOTIVATION

Water pollution caused by heavy metals and organic compounds is one of the most serious environmental problems resulting from urbanization and industrialization. For instance, lead contamination comes from lack of waste management from industrial activities as metal plating, mining operations, alloy, printed circuit board and battery industries (YANG et al., 2020). The presence of lead in the environment can bring about contamination in the food chain (KUMAR et al., 2020), leading to encephalopathy, cognitive problems, behavioral disorders, kidney damage, anemia and toxicity to the reproductive system (SHIBI; ANIRUDHAN, 2006; BRIFFA; SINAGRA; BLUNDELL, 2020). According to World Health Organization (WHO) the maximum permissible limit of lead in drinking water is 0.010 mg/L (0.01 ppm) (WORLD HEALTH ORGANIZATION, 2017). However, the amount of lead found in industrial wastewater might be far beyond this limit (~

200 to 500 mg/L) (ARBABI; HEMATI; AMIRI, 2015). Among the different strategies to remove heavy metal ions from aqueous wastewater, adsorption is advantageous because the surface can be tailored towards specific adsorbate, the adsorbent can be prepared using renewable materials and it offers the possibility to treat large volumes of waste (CRINI; LICHTFOUSE, 2019; VIEIRA et al., 2020; OLADOYE, 2022). Recently, the use of natural materials, industrial byproducts, agricultural and forest waste for the removal of lead was discussed in terms of cost and mass-scale applications (CHOWDHURY et al., 2022).

Lignocellulosic materials such as sugarcane bagasse (BG) have been applied in the development of porous materials such as sponges, filters and membranes to remove heavy metals from effluents due to their large availability, low cost and low environmental impact (KHOO; CHOW; ISMAIL, 2018; EWULONU et al., 2019). BG is composed of cellulose, hemicellulose and lignin, which present functional groups with potential for adsorption of water-soluble contaminants, as heavy metals (FAKHRE; IBRAHIM, 2018; VIEIRA et al., 2020). The BG surface can be chemically modified for enhancing the adsorption of  $Pb^{2+}$  ions from aqueous solution. Some successful modifications include the functionalization of BG with carbon nanotubes (HAMZA et al., 2013), magnetic amino groups (IRAWAN et al., 2021), EDTA dianhydride (KARNITZ et al., 2009), fungi (PALIN et al., 2016). Carboxymethyl cellulose (CMC) is a cellulose ether widely used in food, drug and cosmetic formulations due to their biocompatibility and non-toxicity (KREMPEL; GRIFFIN; KHOURYIEH, 2019; KANIKIREDDY et al., 2020; MARTINS et al., 2021). At pH higher than 4.5 it behaves as a polyanion, creating adsorption sites for metallic ions in aqueous media (HEINZE; KOSCHELLA, 2005). For instance, CMC/poly(acrylic acid)/polyacrylamide adsorbents presented adsorptive capacity for Pb(II) and methylene blue (CHEN et al., 2018); CMC/polyacrylamide hydrogels adsorbed efficiently Cu(II), Pb(II) and Cd(II) (GODIYA et al., 2019) and CMC/poly(acrylic acid) hydrogels successfully adsorb Cu<sup>2+</sup> ions methylene blue dye

(TOLEDO et al., 2019). Cryogels of CMC reinforced with BG particles (up to 33 wt%) and modified with cationic surfactants provided adsorption sites for Cr(VI), bisphenol A and methylene blue simultaneously (MENESES et al., 2022).

In this work, adsorbents containing BG microparticles (83 wt%), combined with CMC (16 wt%), polydopamine (PDA, 1 wt%) and citric acid were developed in a two-step heating process. PDA, a mussel-inspired coating, whose adhesive properties are due to catechol groups in its structure, favored chemical and mechanical stability of the adsorbents in aqueous medium (LEE et al., 2007b; LIN et al., 2007). PDA has been reported as a platform for functionalization of a wide range of polysaccharides as cellulose, cellulose acetate butyrate (FURTADO; ANDO; PETRI, 2020), chitin/chitosan (SAMYN, 2021; YANG et al., 2021) and cyclodextrin polymer microspheres (CHEN et al., 2020). Citric acid acts as a crosslinker by esterification reaction between citric acid carboxylic acid and BG or CMC hydroxyl groups (ALAVARSE et al., 2022). Thus, this study was based on the hypothesis that the combination of PDA and citric acid would render porous biomaterials with high chemical and dimensional stability. CMC/BG/PDA adsorbents were characterized by different techniques and applied in batch and column adsorption studies for the removal of  $\text{Pb}^{2+}$  ions from individual solutions and ternary mixtures of  $\text{Pb}^{2+}$ ,  $\text{Ca}^{2+}$  and  $\text{Mg}^{2+}$  ions. The effect of pH, temperature and column operational conditions (flow rate, initial concentration, and mass of adsorbent) were varied to understand the adsorption mechanism and to optimize the adsorption efficiency. Considering that the laboratory waste generated in practical classes of chemistry is a common problem in many educational institutions, the removal capacity of CMC/BG/PDA adsorbents towards an undergraduate laboratory waste containing  $\text{Pb}^{2+}$  ions and other 16 metal ions was also evaluated. The efficient clean-up of the undergraduate laboratory waste was achieved by combining filtration with CMC/BG/PDA adsorbents and post-flocculation with a polycation.

## 6.2 EXPERIMENTAL SECTION

### 6.2.1 Materials

Sodium carboxymethyl cellulose (CMC, 419303 Sigma, DS 0.9, 250,000 g/mol), dopamine hydrochloride (DOPA, Sigma H8502, 189.64 g/mol), citric acid (Labsynth, Brazil, 192.12 g/mol), sodium hypophosphite (HPS, Labsynth, Brazil, 105.99 g/mol),  $\text{Pb}(\text{NO}_3)_2$  (standard solution, 1000 mg/L, AccuStandard®),  $\text{Ca}(\text{NO}_3)_2$  (standard solution, 1000 mg/L, Fluka Analytical 69349),  $\text{Mg}(\text{NO}_3)_2$  (standard solution, 1000 mg/L, PerkinElmer) and Trizma® base (Sigma Aldrich 77-86-1, 121.14 g/mol) were used as received. **Figure 6.1** represents the chemical structures of CMC, dopamine hydrochloride, and citric acid.

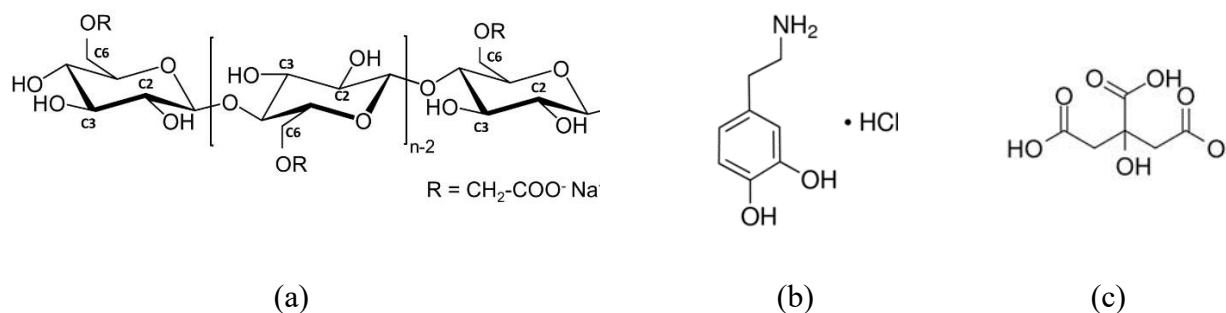


**Figure 6.1.** Schematic representation of chemical structures of (a) CMC, with R = CH<sub>2</sub>-COO<sup>-</sup>Na<sup>+</sup> or -H, (b) dopamine hydrochloride, and (c) citric acid.

Sugarcane bagasse (BG) waste from a local market was washed with tap water, dried, ground in a knife mill (Willye, TE-680, TECNAL), and sieved through a 400  $\mu\text{m}$  mesh (Retsch AS 200). BG particles smaller than 400  $\mu\text{m}$  were rinsed with distilled water under mechanical stirring (250 rpm) until the washing water showed a transmittance value (Beckmann-Coulter DU650 spectrophotometer) close to 100% and ionic conductivity of 10  $\mu\text{S}/\text{cm}$ . The particle size distribution analysis indicated two populations, namely, 104.9  $\mu\text{m}$  (13.5%) and 338.8  $\mu\text{m}$  (86.5%) (NOVAES; OLIVEIRA; PETRI, 2022). The BG particles were dried in oven at 60  $^{\circ}\text{C}$  overnight. The composition of BG was determined following the NREL Protocol (SLUITER et al., 2004). The content of holocellulose

(cellulose and hemicellulose), lignin, and ash in BG amounted to 79.0%, 20.5%, and 0.2%, respectively (NOVAES; OLIVEIRA; PETRI, 2022); these values are similar to those reported in the literature (HALYSH et al., 2019).

### 6.2.2 Preparation of CMC/BG/PDA and CMC/BG adsorbents

CMC solutions at 30 g/L were prepared in 10 mM Tris-HCl buffer (pH 8.5) to favor the oxidation of DOPA. The BG particles were incorporated into the gels under mechanical stirring (250 rpm) at a final concentration of 150 g/L until a homogeneous mixture was obtained. Then, DOPA solution (Tris buffer, 10mM, pH 8.5) at final concentration of 2.0 g/L was added to the mixture of CMC and BG. The oxidation reaction of DOPA to PDA took 4 h, under constant mechanical stirring (250 rpm), as evidenced by the darkening of the system (FURTADO; ANDO; PETRI, 2020). Citric acid (crosslinker) and sodium hypophosphite (HPS, catalyst) were added to the mixture under mechanical stirring (250 rpm) so that their final concentration amounted to 2.5 g/L and 1.25 g/L. The resulting adsorbent were coded as CMC/BG/PDA. In order to evaluate the effect of PDA on the filters, similar mixtures were prepared without PDA; these systems were coded as CMC/BG.

The mixtures were poured into acrylic molds (14 mm diameter, 10 mm height) and placed in an oven at 60 °C for solvent evaporation overnight. After drying, they were removed from the molds and heated at 172 °C for 10 min to promote the esterification reaction between citric acid carboxylic acid groups and hydroxyl groups of CMC chains and BG microparticles (MENESES et al., 2022). CMC/BG/PDA or CMC/BG adsorbents were washed with distilled water to remove unreacted molecules (450 mL of distilled water was used for each 1 g of material) until the water conductivity reached ~ 5  $\mu$ S/cm. They were dried in oven at 60 °C prior to the characterization.

### 6.2.3 Characterization of CMC/BG/PDA and CMC/BG adsorbents

The apparent density ( $\rho_{ap}$ ) of CMC/BG/PDA and CMC/BG adsorbents was determined in triplicate, weighing them in an analytical balance and measuring their dimensions with a pachymeter at  $23 \pm 1$  °C and relative humidity of  $70 \pm 10\%$ . Scanning electron microscopy (SEM) analyses were performed for CMC/BG/PDA and CMC/BG coated with gold (~ 10 nm) in Jeol Neoscope JCM-5000 microscope operating at 10 kV. Fourier transform infrared (FTIR) vibrational spectroscopy analyses were performed in the attenuated total reflection (ATR) mode, on diamond crystal, using a Bruker Alpha FTIR-ATR equipment; the spectra were obtained with an accumulation of 128 scans and resolution of  $2 \text{ cm}^{-1}$ .

The adsorbents were analyzed by X-ray microtomography (micro-CT) with the Bruker Skyscan 1272 equipment with the X-ray source operating at 20 kV and a current of 175  $\mu\text{A}$ . The samples were rotated  $0.6^\circ$  for each measurement, obtaining a resolution of 4  $\mu\text{m}$ . NRecon (v. 1.6.9.8, SkyScan) and CTVOx (v. 2.2.3.0, SkyScan) software were used for 3D reconstruction, from cross-sectional images, and image visualization and acquisition, respectively. The pore size distribution, pore connectivity density and specific area ( $A_{sp}$ ) of the volume of interest were determined with the CTan software (v. 1.14.4.1, SkyScan). The specific area was calculated by equation (1):

$$A_{sp} = \frac{A}{\rho \cdot VOI} \quad (1)$$

where VOI (volume of interest) is the reconstructed volume, in which the software performed the calculations, A is the internal area of the VOI, and  $\rho$  is the density of the material.

The chemical stability of the CMC/BG/PDA and CMC/BG adsorbents was evaluated at pH 1.0 (0.1 mol/L HCl), pH 5.5 (MilliQ water), pH 8.5 (buffer Tris-HCl 10 mM) for 48 h. The electronic spectra of the supernatants were measured in the UV-Vis region (Beckman-Coulter DU640). CMC/BG filters did not show chemical stability in aqueous media, after 30 min under stirring they dissolved completely at pH 5.5, as shown in the **Supplementary Material SM 1**. They also dissolved

at pH 1.0 and 8.5. These experimental observations clearly demonstrated the adhesive property of PDA. Therefore, the CMC/BG adsorbents could not be used for the adsorption studies.

The gel content (Gel %) was determined by

$$\text{Gel (\%)} = \frac{m_{\text{washed}}}{m_{\text{initial}}} \times 100 \quad (2)$$

where  $m_{\text{initial}}$  is the mass of the dry adsorbents just after preparation and  $m_{\text{washed}}$  is the mass of the adsorbents after washing to remove the unreacted molecules and drying.

The swelling degree (SD) values were determined with a precision tensiometer Krüss K100 at  $24.0 \pm 0.5$  °C, dividing the mass of MilliQ water sorbed (pH 5.5) at equilibrium ( $m_{\text{water}}$ ) by the mass of the dry filter ( $m_{\text{dried}}$ ):

$$SD = \left[ \left( \frac{m_{\text{water}}}{m_{\text{dried}}} \right) \right] \quad (3)$$

TG/DTG curves were obtained for CMC/BG/PDA, sugarcane bagasse and CMC powder (~ 2 mg) in the temperature range from 20 °C to 800 °C, using platinum crucibles, under dynamic N<sub>2</sub> atmosphere (60 mL/min) and with heating rate of 10 °C/min, in a TGA Q500 TA thermobalance. Elemental analysis (Perkin Elmer 2400) was performed for CMC/BG/PDA for the determination of carbon, nitrogen and hydrogen. X-ray photoelectron spectroscopy (XPS, K-Alpha spectrometer, Thermo Fisher Scientific, UK) analyses were performed for CMC/BG/PDA before and after adsorption of lead adsorption (single system and ternary system). The X-ray source was monochromatic Al K $\alpha$  1486.68 eV. XPS high resolution spectra of C 1s, N 1s, O 1s, Pb 4f and Ca 2p were obtained with a pass energy of 50 eV and 0.1 eV/step, accumulating 10 scans. The point of zero charge (pzc) of CMC/BG/PDA adsorbent was determined by titration (details provided as **Supplementary Material SM 2**) (MAHMOOD et al., 2011).

#### 6.2.4 Batch adsorption studies

The removal capacity (%) of Pb<sup>2+</sup> ions by CMC/BG/PDA adsorbents was determined by:

$$Removal (\%) = \frac{C_0 - C_t}{C_0} \times 100 \quad (4)$$

where  $C_0$  is initial concentration and  $C_t$  is concentration after a given contact time.

The equilibrium adsorption capacity ( $q_e$ , mg/g) was calculated dividing the concentration of adsorbed  $Pb^{2+}$  ions ( $C_0 - C_e$ ) by the mass of dried adsorbent ( $m$ ) and multiplying by the solution volume ( $V$ ):

$$q_e = \frac{C_0 - C_e}{m} \times V \quad (5)$$

Where  $C_e$  is the equilibrium concentration.

All  $Pb^{2+}$  solutions were prepared from a standard solution at 1000 mg/L in  $HNO_3$ . The concentration of  $Pb^{2+}$  ions was determined by inductively coupled plasma atomic emission spectrometry (ICP-OES, model iCAP 7400 Duo); the instrument specification and the instrumental set up are describe in **Supplementary Material SM 3**. Only CMC/BG/PDA adsorbents were used, CMC/BG had no stability in aqueous media.

Adsorption kinetics experiments of  $Pb^{2+}$  ions ( $C_0 = 90$  mg/L) on CMC/BG/PDA adsorbents were performed at  $(23 \pm 1)$  °C, using solution volume of 5 mL. The effect of pH on the removal of  $Pb^{2+}$  ions was investigated with  $Pb^{2+}$  solutions prepared at pH 3.0, 4.5, 5.0, 5.5, 6.0 and 7.0,  $C_0$  at 20 mg/L, and adsorbent mass ( $m$ )  $53 \pm 5$  mg, at  $23 \pm 1$ °C. The solution volume was 10 mL and pH adjustment was performed with HCl 0.1 mol/L and NaOH 0.1 mol/L. One should notice that pH higher than 7.0 was avoided due to the precipitation of  $Pb(OH)_2$ .

Adsorption isotherms of  $Pb^{2+}$  ions, in the absence and in the presence of  $Ca^{2+}$  ( $C_0 = 5.0$  mg/L) and  $Mg^{2+}$  ( $C_0 = 5.0$  mg/L), on CMC/BG/PDA adsorbents ( $53 \pm 5$  mg) were performed at pH 5.5,  $(19 \pm 1)$  °C, contact time of 1 h, and solution volume of 5 mL. After the adsorption experiments, the adsorbents were regenerated by rinsing the adsorbents with 5 mL of HCl 0.1 mol/L, at  $23 \pm 1$ °C. In order to determine the change of the thermodynamic functions ( $\Delta G$ ,  $\Delta H$  and  $\Delta S$ ) related to the



adsorption process, batch adsorption experiments were performed at  $(18 \pm 1) ^\circ\text{C}$ ,  $(35 \pm 1) ^\circ\text{C}$  and  $(40 \pm 1) ^\circ\text{C}$ .

## 6.2.5 Fixed-bed column adsorption studies

Column adsorption experiments were carried out in a 15 mL polyethylene column, coupled to Tygon® silicone tubes, which were connected to a peristaltic pump (Ismatec, Switzerland) for flow control (**Supplementary Material SM4**). The experiments were carried out at  $23 \pm 1 ^\circ\text{C}$ . The adsorbents were inserted into the column, fitting exactly to the inner diameter of the column (14 mm) (**Supplementary Material SM4**).

### 6.2.5.1 *Breakthrough curves for single solution and ternary mixtures*

The experiments were performed with flow rate ( $v$ ) ranging from 0.5 mL/min to 3.0 mL/min, adsorbent mass ( $m_{\text{ads}}$ ) varying from 50 mg to 200 mg and initial concentration ( $C_0$ ) of 8 mg/L and 20 mg/L for  $\text{Pb}^{2+}$  ions. The optimized parameters ( $v$ ,  $m_{\text{ads}}$  and  $C_0$ ) for single solution were applied for the breakthrough curves of the ternary mixture containing  $\text{Pb}^{2+}$ ,  $\text{Ca}^{2+}$  and  $\text{Mg}^{2+}$ .  $\text{Ca}^{2+}$  and  $\text{Mg}^{2+}$  were added to the mixture at the final concentration of 5 mg/L each. Based on the dependence of Removal (%) on pH, all  $\text{Pb}^{2+}$  solutions were prepared at pH 5.5.

The breakthrough curves were fitted to the Thomas model to estimate the maximum adsorption capacity ( $q_{\text{Th}}$ ) and mass transport constant ( $k_{\text{Th}}$ ). This model was chosen because it considers a Langmuir (favorable) isotherm shape (CHU, 2010; BARROS; ARROYO; SILVA, 2013):

$$\frac{C_t}{C_0} = \frac{1}{1 + \exp\left[\frac{K_{\text{Th}}}{v} q_{\text{Th}} m_{\text{ads}} - K_{\text{Th}} C_0 t\right]} \quad (6)$$

where  $K_{\text{Th}}$  is the rate constant ( $\text{L mg}^{-1} \text{min}^{-1}$ ),  $m_{\text{ads}}$  is the mass of adsorbent,  $q_{\text{Th}}$  is the maximal adsorption capacity (mg/g) and  $v$  is the flow rate ( $\text{mL} \cdot \text{min}^{-1}$ ).

### 6.2.5.2 Removal of $Pb^{2+}$ ions from undergraduate laboratory waste

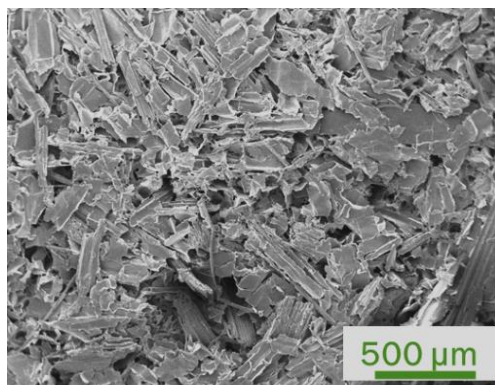
The Removal (%) of  $Pb^{2+}$  ions from a complex mixture, namely, a waste from an undergraduate laboratory containing 17 elements (identified by ICP-OES), at pH 1, was also evaluated. This is an example of a real complex sample because it contained solutions discarded by the students after practical classes of General Chemistry and Analytical Chemistry. The laboratory waste also contained chloride and nitrate ions. The laboratory waste was inserted at  $v$  of  $1.0 \text{ mL} \cdot \text{min}^{-1}$  into three consecutive columns, each one containing CMC/BG/PDA adsorbent ( $m_{\text{ads}} = 0.2242 \pm 0.0024 \text{ g}$ ). After the third filtration, the outlet (5 mL) was evaluated by ICP-OES. Flocculation metal ions was achieved by adding poly(diallyl dimethyl ammonium chloride) (PDAA solution 20 wt% in  $H_2O$ , Sigma Aldrich, 409014), so that the final concentration in the residue was 5 g/L. This concentration was optimized for the laboratory waste.

## 6.3 RESULTS AND DISCUSSION

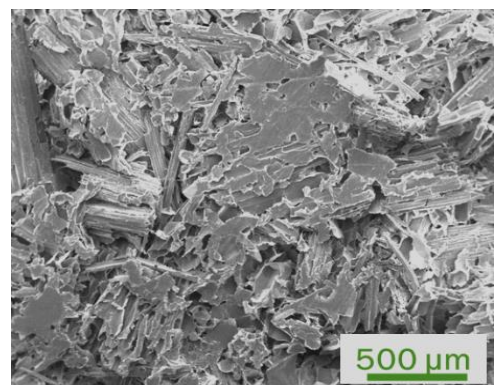
### 6.3.1 Characterization of CMC/BG and CMC/BG/PDA adsorbents

SEM images in **Figure 6.2a** and **Figure 6.2b** and show the porous structure of CMC/BG and CMC/BG/PDA, respectively; the presence of PDA did not affect the adsorbent morphology. As expected, BG microparticles dominate the structure because they account for 83 wt% of material composition. **Supplementary Material SM5** shows a typical SEM image of BG microparticles. **Figure 6.2c** and **Figure 6.2d** show the reconstructed 3D structures from microCT data of CMC/BG and CMC/BG/PDA adsorbents. **Table 6.1** shows the apparent density ( $\rho_{\text{ap}}$ ), specific surface area ( $A_{\text{sp}}$ ), and porosity, determined by analyzing the microCT data with the CTan<sup>®</sup> software. The  $A_{\text{sp}}$  values of  $236 \pm 10 \text{ m}^2/\text{kg}$  and  $246 \pm 10 \text{ m}^2/\text{kg}$  determined for CMC/BG and CMC/BG/PDA are similar to that reported for CMC/BG cryogels (BG 33 wt%) as  $223 \pm 11 \text{ m}^2/\text{kg}$  (MENESES et al., 2022), despite the different BG contents. In comparison to CMC/BG, CMC/BG/PDA presented slightly lower  $\rho_{\text{ap}}$

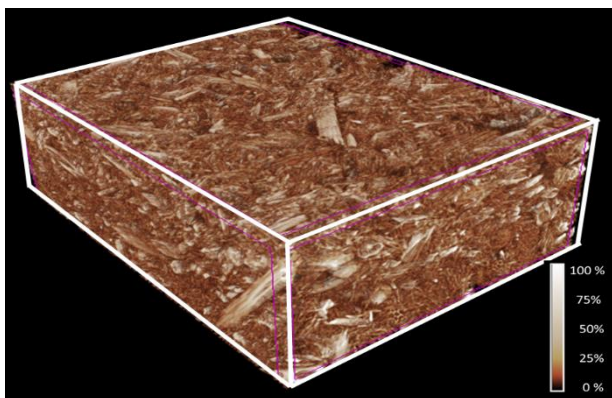
values and higher porosity, indicating that PDA had a small effect on the microstructure of the adsorbents. In contrast to freeze-dried CMC/BG (BG 33 wt%) cryogels, the oven dried adsorbents presented higher density and smaller porosity due to the high BG content (83 wt%) and the collapse of CMC chains upon oven drying. Cryogels produced by freeze-drying preserved better the porous structure in comparison to oven drying, but freeze-drying consumes more time and energy than oven drying does. Therefore, for the development of adsorbents for treating large volumes of waste, as is the case of the undergraduate laboratory waste, oven drying might be more appropriate because ovens are often available.



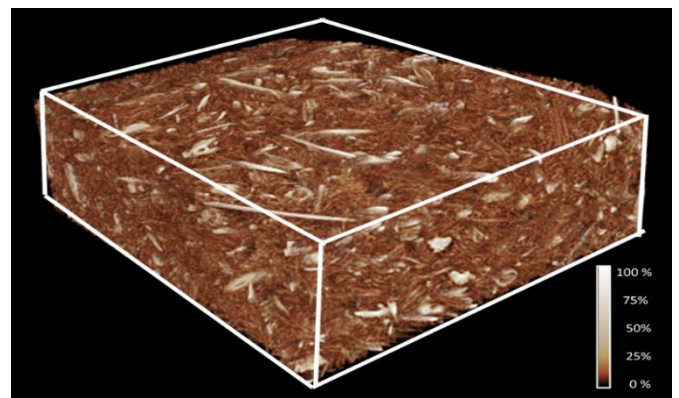
(a)



(b)



(c)



(d)

**Figure 6.2.** SEM images for (a) CMC/BG, (b) CMC/BG/PDA. Reconstructed 3D structures from microtomography data of (c) CMC/BG and (d) CMC/BG/PDA adsorbents. Parallelepiped (490  $\mu\text{m}$  x 1070  $\mu\text{m}$  x 1350  $\mu\text{m}$ ) from the central region of the samples are shown with the corresponding attenuation scales obtained by the transfer function in the software CTvox®.

**Table 6.1.** Apparent density ( $\rho_{\text{ap}}$ ), specific surface area ( $A_{\text{sp}}$ ), porosity (%) and swelling degree (gwater/g) calculated by CTAn software, swelling degree (gwater/g) and gel content (%) for CMC/BG and CMC/BG/PDA adsorbents. For comparison, the parameters corresponding to freeze-dried CMC/BG cryogels (BG 33 wt%) were also presented (Meneses et al., 2022).

Sample	$\rho_{\text{ap}}$ (kg/m <sup>3</sup> )	$A_{\text{sp}}$ (m <sup>2</sup> /kg)	Porosity (%)	SD (gwater/g)	Gel (%)
CMC/BG	168 $\pm$ 4	236 $\pm$ 10	49.8	-	-
CMC/BG/PDA	157 $\pm$ 3	246 $\pm$ 10	56.5	10.2 $\pm$ 0.4	89.3 $\pm$ 0.4
CMC/BG cryogel (BG 33 wt%)	67 $\pm$ 2	223 $\pm$ 11	91.1	21 $\pm$ 1	88 $\pm$ 1

CMC/BG adsorbents were prepared with citric acid (crosslinker). They dissolved after 30 min shaking in water (**Supplementary Material SM1**). Meneses and co-workers prepared CMC/BG cryogels with a BG content of 33 wt% or less and citric acid; they showed that the esterification reaction between the CMC and BG hydroxyl groups and citric acid carboxylic acid groups provided excellent chemical and mechanical stability (MENESES et al., 2022). In this work, where the adsorbents contain 83 wt% BG, the esterification reaction was not efficient. The hydroxyl groups on BG particles (main component of the adsorbent) probably were not available for crosslinking with citric acid molecules due to the strong intermolecular H bonds. On the other hand, CMC/BG cryogels prepared only with PDA, without citric acid, were not chemical stable (**Supplementary Material SM6a**) because PDA was released to the aqueous medium; after 24 h the medium became yellowish and PDA leached molecules were identified by UV spectrophotometry (**Supplementary Material SM6b**). CMC/BG/PDA prepared with PDA and citric acid showed excellent stability at pH 1, 5.5 and 8.5 up to 48 h (**Figure 2**). The UV spectra corresponding to each

medium and periods of contact revealed that the amount of PDA leached to the medium was not significant (**Supplementary Material SM7**). The evaluation of chemical stability is important because adsorbents should be stable over a broad range of pH and should not release any component to the medium. Therefore, the combination of PDA and citric acid favored the adhesive properties of PDA in the system composed predominately by BG, providing chemical stability for the adsorbents over a broad range of pH. PDA is the result of aggregation of different products of dopamine oxidation process, for instance dopamine quinone, 5,6-dihydroxyindole (DHI) and catecholamine-based products (DELLA VECCHIA et al., 2013; KLOSTERMAN; RILEY; BETTINGER, 2015; CHEN et al., 2017; MICILLO et al., 2017). Catechol groups in PDA provided excellent adhesive properties on substrates with surface energy values ranging from 80.8 mJ/m<sup>2</sup> to 47 mJ/m<sup>2</sup> (FURTADO; ANDO; PETRI, 2020).

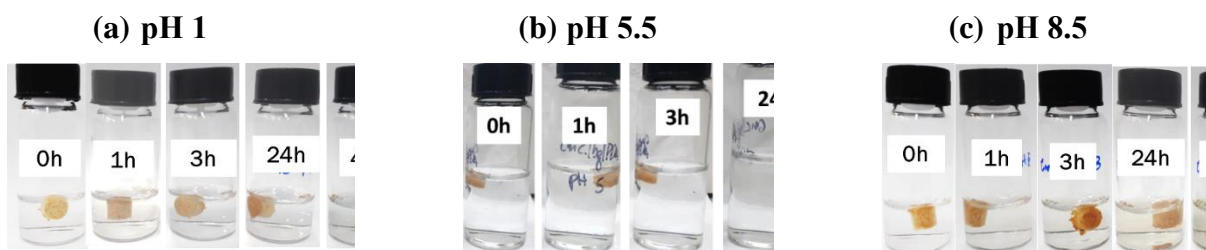


**Figure 6.3.** CMC/BG/PDA adsorbents prepared in the presence of citric acid and PDA, heated at 172 °C for 10 min. Photographs of CMC/BG/PDA adsorbents after 0 h, 1 h, 3 h, 24 h, 48 h immersion in (a) pH 1, (b) pH 5.5 (MilliQ water) and (c) pH 8.5 media.

CMC/BG/PDA adsorbents presented gel content of  $89.3 \pm 0.4 \%$  (**Table 6.1**). This value is comparable to that observed for CMC/BG cryogels with 33 wt% BG (MENESES et al., 2022). This finding clearly indicated that PDA provided catechol groups high adhesion among the BG particles and CMC, increasing the adsorbent stability in aqueous media. The high affinity between PDA and cellulose derivatives allowed the production of highly stable PDA/cellulose acetate butyrate microbeads for the removal of caffeine (FURTADO; ANDO; PETRI, 2020). The swelling kinetics of CMC/BG/PDA adsorbents at pH 5.5 (**Supplementary Material SM8**) showed that already after 15 min the swelling degree (SD) achieved  $\sim 9 \text{ g}_{\text{water}}/\text{g}$ . The swelling equilibrium was achieved after 6 h with SD of  $10.2 \pm 0.4 \text{ g}_{\text{water}}/\text{g}$  (**Table 6.1**). For comparison, this value is about half of the SD value determined for freeze-dried CMC/BG cryogels (BG 33 wt%) (MENESES et al., 2022); it is because the CMC/BG/PDA adsorbents have a more collapsed structure and a lower content of CMC (16 wt%) than the CMC/BG cryogels (BG 33 wt%).

**Supplementary material SM9a** shows the FTIR-ATR spectra for pure BG, CMC/BG and CMC/BG/PDA adsorbents. The spectra of BG and CMC/BG presented similar absorption bands. The characteristic bands of pure BG at  $\sim 1727 \text{ cm}^{-1}$ ,  $1600 \text{ cm}^{-1}$ ,  $1240 \text{ cm}^{-1}$ ,  $1163 \text{ cm}^{-1}$  and  $1033 \text{ cm}^{-1}$  overlapped the characteristic bands of PDA at  $\sim 1628 \text{ cm}^{-1}$  (C=O, quinone structures),  $1288 \text{ cm}^{-1}$  (C-OH stretching) and  $1034 \text{ cm}^{-1}$  (C-C and C-O stretching) and carboxylic acid/ester linkages ( $\sim 1728 \text{ cm}^{-1}$ ) (SUN et al., 2019; FURTADO; ANDO; PETRI, 2020). **Supplementary material SM9b**

presents the corresponding band assignments (HAN; LUO; ZHANG, 2012; MPATANI et al., 2020). The pzc of CMC/BG/PDA was determined as 4.1 (**Supplementary Material SM2**), which is related to the protonation of carboxylic acid groups of CMC and BG evidenced by the FTIR spectra.

The high content of BG particles in the adsorbent composition dominated the FTIR-ATR spectra and SEM images. On the other hand, elemental analyses indicated 0.25% of N in the CMC/BG/PDA adsorbent. Considering the N content of 9.14 % in dopamine, the amount of PDA incorporated was estimated as 2.74 wt%. In addition, XPS high resolution spectrum of N1s evidenced the presence of PDA in CMC/BG/PDA adsorbent with binding energy peaks at  $400.2 \pm 0.2$  eV and  $402.1 \pm$  assigned to R-NH-R and R-NH<sub>2</sub>, respectively (**Supplementary Material SM10 and SM11**) (LUO et al., 2013; ZANGMEISTER; MORRIS; TARLOV, 2013b).

**Supplementary Material SM12** shows the TG/DTG curves obtained for CMC/BG/PDA adsorbents. For comparison, TG/DTG curves of pure BG and CMC powder were also presented. From 19 °C to 100 °C, the weight loss was attributed to water release; it amounted to ~ 3%, ~ 5% and ~19% for CMC/BG/PDA, pure BG, and CMC powder, respectively. This finding indicated that the adsorbents and pure BG are not hygroscopic, contrarily to CMC powder. Materials with low hygroscopicity are advantageous because they do not provide suitable environment for the proliferation of microorganisms. The weight loss profiles for CMC/BG/PDA and pure BG were similar. Pure BG presented two events at 308 °C and 354 °C that were assigned to the degradation of hemicellulose and cellulose belonging to BG particles (PALIN et al., 2016). For CMC/BG/PDA these events were observed at 276 °C and 329 °C, indicating that the presence of CMC decreased slightly the thermal stability. The degradation of pure CMC was mainly observed at 282 °C. The char contents observed for CMC/BG/PDA, pure BG, and CMC powder at 800 °C amounted to 15.4%, 6% and 15.8%, respectively.

### 6.3.2 Batch adsorption studies

**Figure 6.4** shows the effect of pH on the Removal (%) of  $\text{Pb}^{2+}$  ions ( $C_0 = 20 \text{ mg/L}$ ) by CMC/BG/PDA adsorbents ( $\sim 40 \text{ mg}$ ) at  $23 \pm 1^\circ\text{C}$ , pH 3.0, 4.5, 5.0, 5.5, 6.0 and 7.0 and the regeneration capacity after rinsing the adsorbents with  $\text{HCl}$  0.1 mol/L ( $V = 5 \text{ mL}$ ) for 10 min. In the pH range from 3.0 to 7.0 (below and above the pzc) the adsorbents presented excellent removal capacity ( $\sim 97\%$ ), indicating that the ionizable carboxylic acids groups played no significant role on the interaction with  $\text{Pb}^{2+}$  ions. The formation of  $\text{Pb}(\text{OH})_2$  was not visually observed at  $\text{pH} > 5$ , although Vera and co-workers suggested to work with  $\text{Pb}^{2+}$  solutions in the pH range from 2 to 5 in order to avoid metal ion precipitation as hydroxides (VERA et al., 2019). Therefore, pH 5.5 (pH of MilliQ water) was chosen to proceed with the adsorption kinetics and isotherms. The adsorbents regeneration with  $\text{HCl}$  0.1 mol/L ( $V = 5 \text{ mL}$ ) was practically complete ( $\sim 95\%$ ) (**Figure 6.4a**). This outstanding behavior allowed running 5 cycles of adsorption (at pH 5.5) and desorption (pH 1.0) without efficiency loss (**Figure 6.4b**). **Supplementary Material SM13** shows that after one contact, the adsorbed amount ( $q_e$ ) of  $\text{Pb}^{2+}$  ions ( $C_0 = 90 \text{ mg/L}$ , pH 5.5) on CMC/BG/PDA adsorbents was already constant at  $7.9 \pm 0.1 \text{ mg/g}$ . For this reason, all adsorption isotherms were performed for one-hour contact.

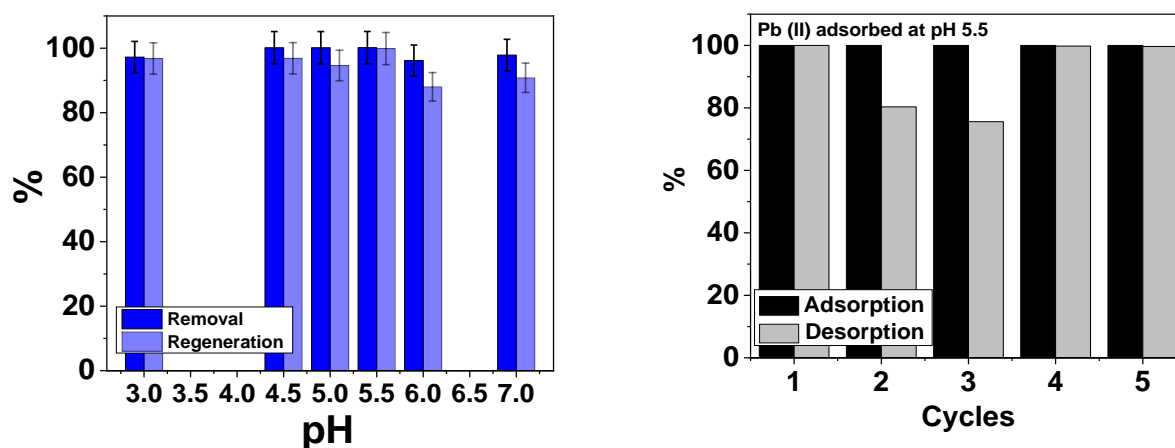




**Figure 6.4. (a)** Effect of pH on the Removal % of  $Pb^{2+}$  ions ( $C_0 = 20$  mg/L) by CMC/BG/PDA adsorbents ( $m \sim 40$  mg) at pH 3.0, 4.5, 5.0, 5.5, 6.0 and 7.0 and the regeneration capacity by rinsing the adsorbents with HCl 0.1 mol/L, at  $23 \pm 1^\circ C$ . **(b)** Cycles of adsorption and desorption of  $Pb^{2+}$  ions ( $C_0 = 20$  mg/L) using CMC/BG/PDA adsorbents ( $\sim 40$  mg) at  $23 \pm 1^\circ C$ . The desorption was achieved with 5 mL of HCl 0.1 mol/L, 10 min contact.

**Figure 6.5a** and **Figure 6.5b** show the adsorption isotherms of  $Pb^{2+}$  ions in the absence and in the presence of  $Ca^{2+}$  ( $C_0 = 5.0$  mg/L) and  $Mg^{2+}$  ( $C_0 = 5.0$  mg/L), respectively, on CMC/BG/PDA adsorbents ( $53 \pm 5$  mg) at pH 5.5,  $19 \pm 1^\circ C$ , after one-hour contact. The experimental data were fitted to Langmuir and Freundlich models, which correspond to equations 7 and 8, respectively (AL-GHOUTI; DA'ANA, 2020):

$$q_e = \frac{q_{max}K_L}{1+K_L C_e} \quad (7)$$

where  $K_L$  = adsorption equilibrium constant and  $q_{max}$  is the maximal adsorption capacity.

$$q_e = K_F C_e^{1/n} \quad (8)$$

where  $K_F$  is the Freundlich constant, the larger  $K_F$ , the higher the adsorption capacity, and  $n$  is related to the surface heterogeneity, the smaller  $n$ , the greater the heterogeneity.

**Table 6.2** shows the non-linear fitting parameters obtained for adsorption isotherms presented in **Figure 6.5** along with literature data. Langmuir model fitted better the experimental data, yielding  $q_{max}$  values of  $27.4 \pm 2.8$  mg/g and  $25.9 \pm 1.8$  mg/g for  $Pb^{2+}$  ions in the absence and in the presence of  $Ca^{2+}$  ( $C_0 = 5.0$  mg/L) and  $Mg^{2+}$  ( $C_0 = 5.0$  mg/L), respectively, on CMC/BG/PDA adsorbents. These findings indicated that the adsorption is not driven by electrostatic interactions, because the  $q_{max}$  values were not significantly affected by the increase of ionic strength.  $Pb^{2+}$  ions might form stable complexes with BG or CMC hydroxyl groups (ion-dipole interactions). **Table 6.2** shows that the  $q_{max}$  values determined for  $Pb^{2+}$  ions on CMC/BG/PDA adsorbents are on the same order of magnitude of those reported for pure BG in the literature (KARNITZ et al., 2009; DOS SANTOS et al., 2010; MARTÍN-LARA et al., 2010; HAMZA et al., 2013; PUTRA et al., 2014; PALIN et al., 2016); only

EDTA dianhydride modified BG led to much higher  $q_{\max}$  values (up to 333 mg/g), due to the favored complexation process (KARNITZ et al., 2009).

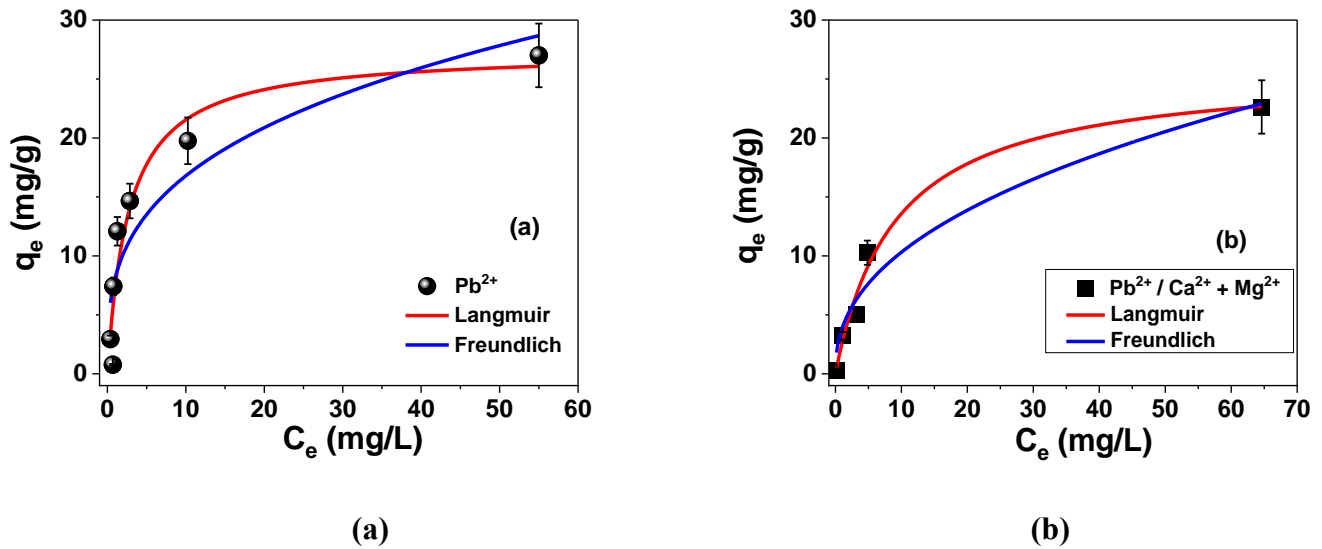


**Figure 6.5.** Adsorption isotherms of  $\text{Pb}^{2+}$  ions on CMC/BG/PDA adsorbents ( $53 \pm 5$  mg) in the absence (a) and in the presence (b) of  $\text{Ca}^{2+}$  ( $C_0 = 5.0$  mg/L) and  $\text{Mg}^{2+}$  ( $C_0 = 5.0$  mg/L) at pH 5.5,  $19 \pm 1$  °C, one-hour contact,  $V = 5$  mL. The red and blue lines correspond to the nonlinear fittings for Langmuir and Freundlich adsorption models.

**Table 6.2.** Fitting parameters obtained for  $\text{Pb}^{2+}$  on CMC/BG/PDA using Langmuir and Freundlich models.  $q_{\max}$  (mg/g) and  $K_L$  (L/mg) stand for maximal adsorption capacity and Langmuir adsorption equilibrium constant, respectively.  $K_F$   $((\text{mg/g})/(\text{mg/L}))^{1/n}$  stands for Freundlich constant and indicates the relative adsorption capacity, and ‘n’ is related to the surface heterogeneity—the smaller n, the greater the heterogeneity. Literature data for the adsorption of  $\text{Pb}^{2+}$  on BG and modified BG are presented for comparison.

		Langmuir			Freundlich			Ref.
		$K_L$	$q_{\max}$	$R^2$	$K_F$	n	$R^2$	
CMC /BG/PDA	$\text{Pb}^{2+}$ pH 5.5	$0.37 \pm 0.12$	$27.4 \pm 2.8$	0.906	$8.1 \pm 1.7$	$3.18 \pm 0.63$	0.806	This work
CMC /BG/PDA	$\text{Pb}^{2+} / \text{Ca}^{2+}$ and $\text{Mg}^{2+}$ pH 5.5	$0.1106 \pm 0.023$	$25.9 \pm 1.8$	0.981	$3.85 \pm 0.96$	$2.34 \pm 0.34$	0.948	This work
BG	$\text{Pb}^{2+}$ pH 6.0	0.05	21.3	0.948	2.12	2.19	0.979	(PUTRA et al., 2014)
BG	$\text{Pb}^{2+}$ pH 5.0	0.11	6.37	0.991	1.46	3.11	0.937	(MARTÍ N-LARA et al., 2010)
BG- H2SO4	$\text{Pb}^{2+}$	0.14	7.30	0.992	1.90	3.32	0.877	(MARTÍ N-LARA

	pH 5.0							et al., 2010)
<b>BG</b>	Pb <sup>2+</sup> pH 5.0	0.03	31.3	0.99	4.39	3.15	0.98	(PALIN et al., 2016)
<b>Fungi modified BG</b>	Pb <sup>2+</sup> pH 5.0	0.012	58.3	0.97	1.20	1.59	0.94	(PALIN et al., 2016)
<b>EDTA dianhydride modified BG</b>	Pb <sup>2+</sup> pH 3.0	0.600	238	0.999	-	-	-	(KARNI TZ et al., 2009)
	pH 5.3	0.205	333	0.992				
<b>BG</b>	Pb <sup>2+</sup> pH 5.0	0.087	11.6	0.932	0.16	0.143	0.325	(DOS SANTO S et al., 2010)
<b>Citric acid modified BG</b>	Pb <sup>2+</sup> pH 5.0	0.011	52.6	0.989	4.33	0.479	0.661	(DOS SANTO S et al., 2010)
<b>BG</b>	Pb <sup>2+</sup> pH 4.5	0.386	21.3	-	-	-	-	(HAMZ A et al., 2013)
<b>Carbon nanotubes-BG</b>	Pb <sup>2+</sup> pH 4.5	0.292	54.5	-	-	-	-	(HAMZ A et al., 2013)

The adsorption equilibrium constant  $K_{ads}$  values were calculated by the ratio between  $q_e$  and  $C_e$  ( $q_e/C_e$ ) (CHEN; DA; MA, 2021) determined at 18 °C (291 K), 35 °C (308 K), and 40 °C (313 K). The dependence of the adsorption constant ( $K_{ads}$ ) on the temperature and van't Hoff equation allowed estimating the adsorption enthalpy change ( $\Delta H_{ads}$ ) and entropy change ( $\Delta S_{ads}$ ), assuming that  $\Delta H_{ads}$  did not depend on the temperature, in the temperature range investigated (CHANG, 2000):

$$\ln K_{ads} = -\frac{\Delta H_{ads}}{R} \times \frac{1}{T} + \frac{\Delta S_{ads}}{R} \quad (9)$$

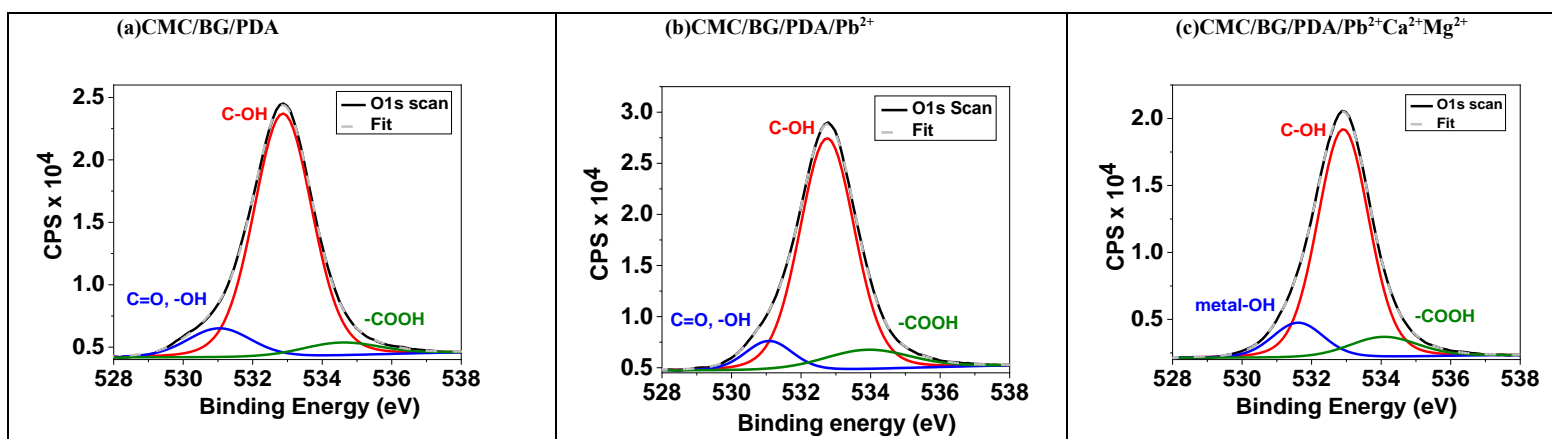
**Supplementary Material SM14** shows the dependence of  $\ln K_{ads}$  on  $1/T$ , along with the linear fittings. The slope and the intercept yielded the enthalpy change ( $-\Delta H_{ads}/R$ ) and entropy change ( $\Delta S_{ads}/R$ ), respectively, with  $R = 8.314 \text{ J mol}^{-1} \text{ K}^{-1}$ . The adsorption of  $\text{Pb}^{2+}$  ions on CMC/BG/PDA is a spontaneous process with  $\Delta G_{ads}$  ranging from  $-8.36 \text{ kJ/mol}$  (291 K) to  $-9.42 \text{ kJ/mol}$  (313K). The  $\Delta H_{ads}$  value of  $+5.7 \text{ kJ/mol}$  revealed an endothermic process and the  $\Delta S_{ads}$  value

amounted to + 48.3 J/(K mol). In order to adsorb, the  $\text{Pb}^{2+}$  ions have to release part of their hydration shell; this process requires heat (TAKA et al., 2018) and explains the endothermic process. Upon adsorbing, the  $\text{Pb}^{2+}$  ions and the substrate released hydration water molecules, increasing the entropy of the system. For the sake of comparison, the  $\Delta H_{\text{ads}}$  and  $\Delta S_{\text{ads}}$  values estimated for the adsorption of  $\text{Pb}^{2+}$  ions on (i) phosphorylated multiwalled carbon nanotube-cyclodextrin/silver doped titania amounted to + 1.223 kJ/mol and + 49.58 J/(K mol) (TAKA et al., 2018), respectively, (ii) lignin microspheres amounted to + 56.9 kJ/mol and + 225 J/(K mol), respectively (GE; QIN; LI, 2016); these adsorption processes also involved the release of hydration water molecules.

So far, the  $q_{\text{max}}$  values of  $27.4 \pm 2.8$  mg/g and  $25.9 \pm 1.8$  mg/g determined for  $\text{Pb}^{2+}$  ions on CMC/BG/PDA adsorbents, in the absence and in the presence of  $\text{Ca}^{2+}$  ( $C_0 = 5.0$  mg/L) and  $\text{Mg}^{2+}$  ( $C_0 = 5.0$  mg/L), respectively, and the thermodynamic data indicated that the adsorption is mainly driven by ion-dipole interactions between  $\text{Pb}^{2+}$  ions and hydroxyl groups. At pH 1.0, the desorption was complete (**Figure 6.4**) because such binding forces were severely weakened due to the surface hydroxyl protonation.

The proposed mechanism was confirmed by XPS measurements performed on CMC/BG/PDA adsorbents prior to the adsorption and after the adsorption of  $\text{Pb}^{2+}$  ions on CMC/BG/PDA in the absence and in the presence of  $\text{Ca}^{2+}$  ( $C_0 = 5.0$  mg/L) and  $\text{Mg}^{2+}$  ( $C_0 = 5.0$  mg/L) (**Figure 6.6** and **Table 6.3**). The XPS high resolution spectra of O 1s for CMC/BG/PDA prior to the adsorption (**Figure 6.6a**) presented a main peak at 533.1 eV (85%), assigned to the C-O-H bond, and two peaks at 531.1 eV (10%) and 534.3 eV (8.7%), attributed to C=O and COOH (carboxylic acid), respectively (LÓPEZ; CASTNER; RATNER, 1991; ARTEMENKO et al., 2021). These are typical functional groups of BG particles and CMC. After adsorption of  $\text{Pb}^{2+}$  ions on CMC/BG/PDA (**Figure 6.6b**), the areas of C-O-H (533.1 eV) and C=O decreased from 85% to 81% and 10% to 7%, respectively. **Figure 6.6d** shows the Pb 4f peaks at  $139.1 \pm 0.1$  eV (56%) and  $143.7 \pm 0.1$  eV (44%), which were

assigned to Pb 4f<sub>7/2</sub> and Pb 4f<sub>5/2</sub>, respectively; the peak at 139.1 eV indicated the interaction between lead and oxygen in O-C-O or cellulose CH<sub>2</sub>-OH group (CRUZ-OLIVARES et al., 2010; FU; XIE, 2020). After the adsorption of Pb<sup>2+</sup> ions on CMC/BG/PDA in the presence of Ca<sup>2+</sup> and Mg<sup>2+</sup> ions (**Figure 6.6c**), the area of C-O-H (533.1 eV) decreased considerably from 85% to 51% and a new deconvoluted band appeared at 531.8 eV with area of 42%, which was attributed to metal-OH bond (PUTRA et al., 2014). Interestingly, this band did not appear in the absence of Ca<sup>2+</sup> and Mg<sup>2+</sup> ions, but it was significant in the ternary mixture. After the adsorption of Pb<sup>2+</sup> ions on CMC/BG/PDA in the presence of Ca<sup>2+</sup> and Mg<sup>2+</sup> ions, the Pb 4f peaks appeared at the similar binding energy values as those in **Figure 6.6d** (absence of Ca<sup>2+</sup> and Mg<sup>2+</sup> ions), namely, at 139.1 ± 0.1 eV (54%) and 143.7 ± 0.1 eV (46%) assigned to Pb 4f<sub>7/2</sub> and Pb 4f<sub>5/2</sub> (**Figure 6.6e**). **Figure 6.6f** shows the Ca 2p peaks at 347.5 eV (64%) and 350.9 eV (31%) assigned to Ca 2p<sub>3/2</sub> and Ca 2p<sub>1/2</sub>, respectively. Noteworthy, the presence of Mg was not identified in the XPS spectra. The high-resolution spectra obtained for C 1s and N 1s presented irrelevant changes after the adsorption of Pb<sup>2+</sup> ions on CMC/BG/PDA in the absence or in presence of Ca<sup>2+</sup> and Mg<sup>2+</sup> ions (**Supplementary Material SM10 and SM11**).



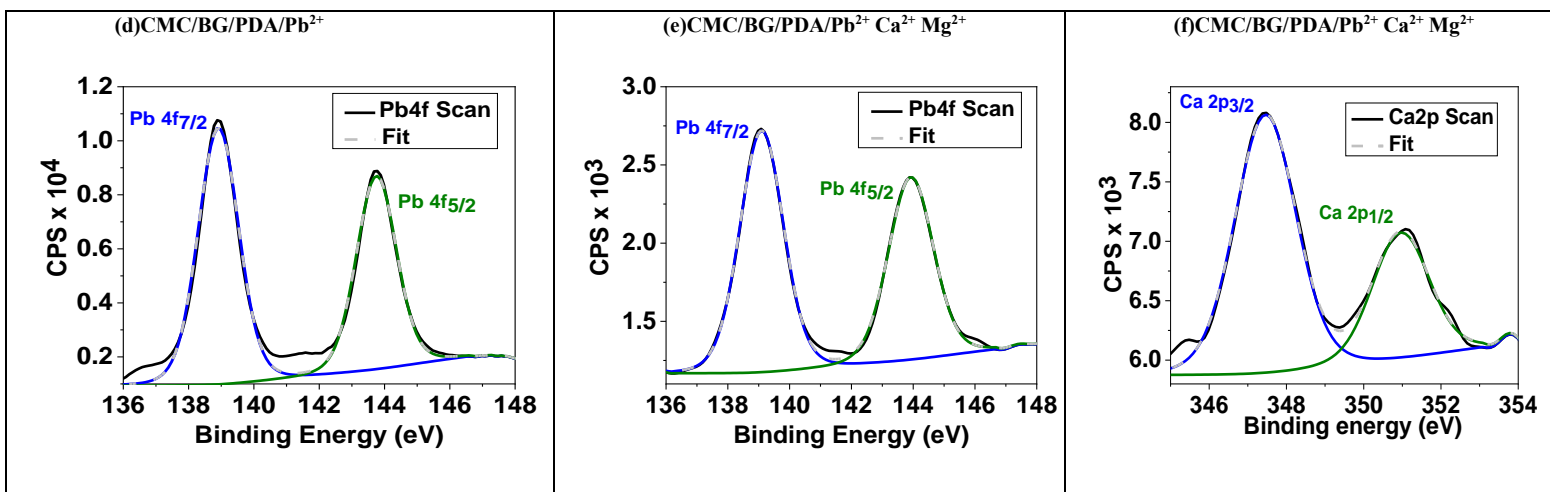


**Figure 6.6.** XPS high resolution spectra of O 1s for (a) CMC/BG/PDA before adsorption, (b) after adsorption of Pb<sup>2+</sup> in the absence and (c) in the presence of Ca<sup>2+</sup> and Mg<sup>2+</sup> ions; Pb 4f after adsorption of Pb<sup>2+</sup> (d) in the absence and (e) in the presence of Ca<sup>2+</sup> and Mg<sup>2+</sup> ions; (f) Ca 2p.

**Table 6.3.** Binding energy (BE, eV) and area (%) values corresponding to the deconvoluted peaks and references used for the assignments of the O 1s, Pb 4f, Ca 2p, C 1s and N 1s binding energy values. The BE and area values are mean values with standard deviations from three measurements in different points on the surface, for this reason, the sum of areas might larger than 100%.

	Peak position (eV)	Area (%)		Area (%)
		CMC/BG/PDA	CMC/BG/PDA/Pb <sup>2+</sup>	CMC/BG/PDA/Pb <sup>2+</sup> Ca <sup>2+</sup> Mg <sup>2+</sup>
O 1s	531.1 ± 0.2 (C=O, -OH)	10 ± 4	7.0 ± 0.9	-
	531.8 ± 0.2 (metal-OH)	-	-	42 ± 6
	533.1 ± 0.3 (C-OH)	85 ± 6	81 ± 5	51 ± 4
	534.3 ± 0.3 (-COOH)	8.7 ± 1.1	12 ± 5	8.2 ± 2.3
Pb 4f	139.1 ± 0.1 (Pb 4f <sub>7/2</sub> )	-	56 ± 1	54 ± 5
	143.7 ± 0.1 (Pb 4f <sub>5/2</sub> )	-	44 ± 1	46 ± 5
Ca 2p	347.5 ± 0.1 (Ca 2p <sub>3/2</sub> )	-	-	64 ± 5
	350.9 ± 0.1 (Ca 2p <sub>1/2</sub> )	-	-	31 ± 2

### 6.3.3 Breakthrough curves for Pb<sup>2+</sup> ions in the absence and in the presence of Ca<sup>2+</sup> and Mg<sup>2+</sup> ions

All fixed-bed column adsorption experiments were performed at pH 5.5. The column operational conditions initial concentration  $C_0$ , flow rate  $v$  and mass of adsorbent  $m_{ads}$  were varied in order to understand which parameters affect the maximum adsorption capacity ( $q_{Th}$ ), determined from the nonlinear fitting to Thomas model (eq. 6). **Figure 6.7a** shows breakthrough curves obtained

for  $\text{Pb}^{2+}$  ions under different operational conditions. The effect of flow rate was evaluated with  $C_0$  at 20 mg/L,  $m_{\text{ads}} = 0.10$  g, and  $v$  of 1.5 mL/min and 3.0 mL/min, blue and black symbols, respectively. The non-linear fit parameters in **Table 6.4** indicated that the reduction of flow rate ( $v$ ) from 3.0 mL/min to 1.5 mL/min increased the maximum adsorption capacity ( $q_{\text{Th}}$ ) from 61.1 mg/g to 70.3 mg/g, respectively. At lower flow rate ( $v = 1.5$  mL/min), the contact time between the adsorbent and adsorbate increased, improving the  $q_{\text{Th}}$  values (TATY-COSTODES et al., 2005); the column achieved 80% saturation only after 7 h. Decreasing the  $m_{\text{ads}}$  from 100 mg (black symbols) to 50 mg (pink symbols), the  $q_{\text{Th}}$  values reduced from 61.1 mg/g to 35.0 mg/g (57% less) (**Table 6.4**), because the adsorption sites available for interaction were halved. The decrease of  $C_0$  from 20 mg/L (pink symbols) to 8 mg/L (green symbols) led to the increase of  $q_{\text{Th}}$  values from 35 mg/g to 44.6 mg/g (**Table 6.4**); the column reached  $C_t/C_0 \sim 0.85$  after 78 min and 206 min, for  $C_0 = 20$  mg/L and  $C_0 = 8$  mg/L, respectively. For comparison, the fitting parameters reported for column adsorption studies of  $\text{Pb}^{2+}$  on other biowastes are provided in **Table 6.4**. Abdolalli et al. used lignocellulosic residues as adsorbent for  $\text{Pb}^{2+}$  adsorption achieving the maximal  $q_{\text{Th}}$  value of 54.5 mg/g with  $m_{\text{ads}} = 10$  g,  $C_0 = 20$  mg/L and  $v = 10$  mg/L (ABDOLALI et al., 2017). Long et al. obtained  $q_{\text{Th}}$  values ranging from  $\sim 58$  mg/g to  $\sim 68$  mg/g (LONG et al., 2014). Although these  $q_{\text{Th}}$  values are comparable to those achieved with CMC/BG/PDA adsorbents, the  $m_{\text{ads}}$  of CMC/BG/PDA was two orders of magnitudes smaller in comparison to the other biowastes.



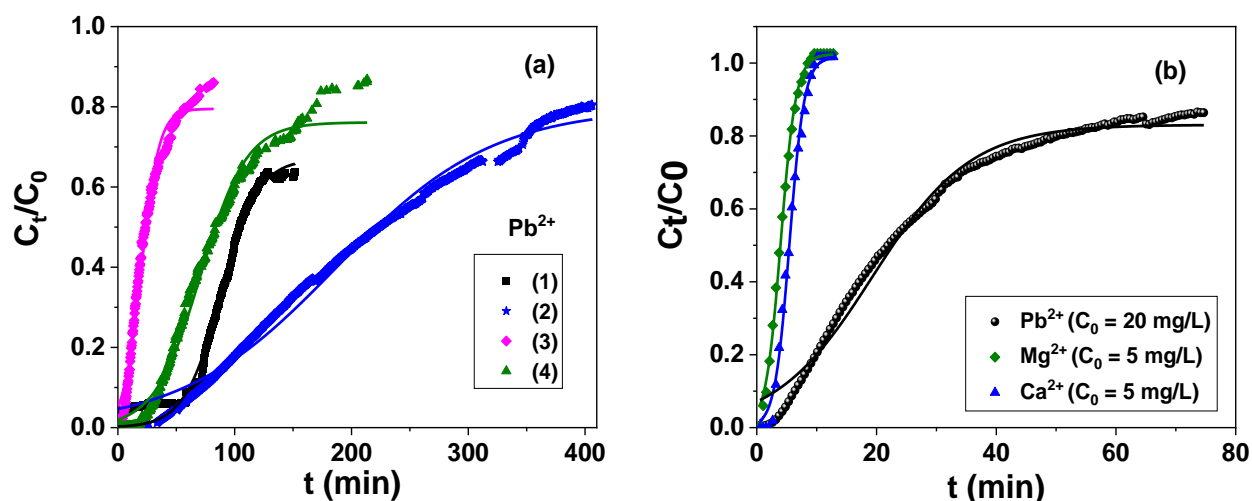


**Figure 6.7.** Breakthrough curves for Pb<sup>2+</sup> ions on CMC/BG/PDA at pH 5.5, (a) in the absence and (b) in the presence of the Ca<sup>2+</sup> and Mg<sup>2+</sup> ions. Column operational conditions C<sub>0</sub>,  $\nu$  and mass of adsorbent (a): (1) 20 mg/L, 3.0 mL/min and 100 mg, (2) 20 mg/L, 1.5 mL/min and 100 mg, (3) 20 mg/L, 3.0 mL/min and 50 mg and (4) 8 mg/L, 3.0 mL/min and 50 mg. (b)  $\nu = 3.0$  mL/min, m<sub>ads</sub> = 50 mg. The solid lines are the non-linear fittings to Thomas model.

**Figure 6.7b** shows the breakthrough curves obtained for Pb<sup>2+</sup> ions (black symbols) (C<sub>0</sub> = 20 mg/L) in the presence of Ca<sup>2+</sup> (blue symbols) and Mg<sup>2+</sup> (green symbols) ions at C<sub>0</sub> = 5.0 mg/L each,  $\nu = 3.0$  mL min<sup>-1</sup> and m<sub>ads</sub> = 50 mg. Already after ~ 5 min, the column was saturated with Mg<sup>2+</sup> ions, Ca<sup>2+</sup> ions. The saturation for Pb<sup>2+</sup> ions in the ternary mixture was achieved after ~ 60 min, similarly to pure Pb<sup>2+</sup> ions (**Figure 6.7a**, pink symbols). In comparison to pure Pb<sup>2+</sup> ions (**Figure 6.7a**, pink symbols), the q<sub>Th</sub> value obtained for Pb<sup>2+</sup> in the mixture decreased from 35.0 mg/g to 28.3 mg/g (**Table 6.4**), indicating that Ca<sup>2+</sup> (blue symbols) and Mg<sup>2+</sup> (green symbols) ions compete for some adsorbing sites. The q<sub>Th</sub> values determined for Ca<sup>2+</sup> (blue symbols) and Mg<sup>2+</sup> ions were ~ 1.4 mg/g and ~ 0.66 mg/g, respectively. This effect corroborates with the interaction between Ca<sup>2+</sup> ions and OH groups detected by the XPS high resolution spectra (**Figure 6.6f** and **Table 6.3**). The presence of Mg was not detected on the surface by XPS, probably due to its low amount on the surface. Breakthrough curves obtained for Pb<sup>2+</sup> ions (black symbols) (C<sub>0</sub> = 20 mg/L) in the presence of Ca<sup>2+</sup> (blue symbols) and Mg<sup>2+</sup> (green symbols) ions at C<sub>0</sub> = 5.0 mg/L each, at lower flow rate ( $\nu = 0.5$  mL min<sup>-1</sup>) and larger m<sub>ads</sub> (240 mg) are available as **Supplementary Material SM15**. The column

saturation took longer; it was saturated with  $\text{Mg}^{2+}$  and  $\text{Ca}^{2+}$  ions after  $\sim 20$  min. After 130 min,  $C_t/C_0$  was 0.13 for  $\text{Pb}^{2+}$  ions, similarly to the breakthrough curve obtained for pure  $\text{Pb}^{2+}$  ions.

The adsorption studies for  $\text{Pb}^{2+}$  ions on CMC/BG/PDA in the presence of  $\text{Ca}^{2+}$  and  $\text{Mg}^{2+}$  ions showed that (i) low flow rate, high mass of adsorbent and high initial concentration favored the adsorption and (ii) the presence of  $\text{Ca}^{2+}$  and  $\text{Mg}^{2+}$  ions decreased the adsorption capacity towards  $\text{Pb}^{2+}$  ions by  $\sim 20\%$  because they compete for the hydroxyl sites. Similar trends were observed for the simultaneous removal of  $\text{Pb}^{2+}$  (54.4 mg/g) and  $\text{Cd}^{2+}$  (36.8 mg/g) ions by columns ( $H = 25$  cm) of waste biomass-based biochar and alginate-based biopolymer; upon increasing the bed height or reducing the flow rate, the competitive adsorption decreased, increasing the adsorption efficiency (BISWAS et al., 2021). The  $q_{\text{Th}}$  values determined for  $\text{Pb}^{2+}$  ions ( $C_0 = 5$  mg/L) adsorbed on columns of iron coated zeolite in single solution and in a mixture containing  $\text{Zn}^{2+}$ ,  $\text{Cd}^{2+}$ ,  $\text{Cu}^{2+}$ ,  $\text{Cr}^{3+}$  at  $C_0 = 5$  mg/L each decreased from 2.03 mg/g to 0.95 mg/g due to the competitive adsorption (NGUYEN et al., 2015).

**Table 6.4.** Experimental conditions used in the column adsorption studies of Pb<sup>2+</sup> ions on CMC/BG/PDA, at pH 5.5: initial concentration (C<sub>0</sub>), flow rate (v), adsorbent mass (m<sub>ads</sub>) and column height (H). Fitting parameters obtained from Thomas model; K<sub>Th</sub> and q<sub>Th</sub> stand for the rate constant (L mg<sup>-1</sup> min<sup>-1</sup>) and adsorption capacity (mg/g). Literature results for column adsorption studies of Pb<sup>2+</sup> ions on other biowastes.

Experimental conditions					Fitting parameters			Ref.
Single solution Pb <sup>2+</sup>	C <sub>0</sub> (mg/L)	v (mL/min)	m <sub>ads</sub> (g)	H (cm)	K <sub>Th</sub> (L mg <sup>-1</sup> min <sup>-1</sup> ) x10 <sup>-4</sup>	q <sub>Th</sub> (mg/g)	R <sup>2</sup>	
<b>Adsorbent</b>								
<b>CMC/BG/PDA pH 5.5</b>	20	3.0	0.10	0.5	47.4	61.1	0.987	This work
	20	1.5	0.10	0.5	9.35	70.3	0.988	This work
	20	3.0	0.05	0.7	71.8	35.0	0.982	This work
	8	3.0	0.05	0.7	83.9	44.6	0.988	This work
<b>tea waste, maple leaves and mandarin peel at pH 5.5</b>	20	10	10	21	7.49	54.5	0.996	(ABDOL ALI et al., 2017)
	20	20	10	21	9.88	27.6	0.993	
	20	10	5	9.5	22.6	16.3	0.992	
	10	10	10	21	8.71	11.6	0.995	
<b>Agaricus bisporus</b>	20	3.0	-	4	8.57	57.72	0.998	(LONG et al., 2014)
	50	3.0	-	4	5.73	63.06	0.995	
	50	3.0	-	2	8.35	67.72	0.999	
	50	1.0	-	4	4.42	66.76	0.991	
<b>Iron coated zeolite</b>	5	8	40	12	0.54	2.03	0.959	(NGUYE N et al., 2015)

	C <sub>0</sub> (mg/L)	v (mL/min)	m <sub>ads</sub> (g)	H (cm)	K <sub>Th</sub> (L mg <sup>-1</sup> min <sup>-1</sup> ) x10 <sup>-4</sup>	q <sub>Th</sub> (mg/g)	R <sup>2</sup>	Ref.
<b>CMC/BG/PDA pH 5.5</b>								
Pb <sup>2+</sup>	20	3.0	0.05	0.7	87.0	28.3	0.983	This work
Ca <sup>2+</sup>	5	3.0	0.05	0.7	2325	1.4	0.985	This work
Mg <sup>2+</sup>	5	3.0	0.05	0.7	3336	0.66	0.985	This work
<b>Iron coated zeolite</b>								
Pb <sup>2+</sup> in the presence of Zn <sup>2+</sup> , Cd <sup>2+</sup> , Cu <sup>2+</sup> , Cr <sup>3+</sup> at 5 mg/L	5	8	40	12	1.04	0.95	0.954	(NGUYE N et al., 2015)

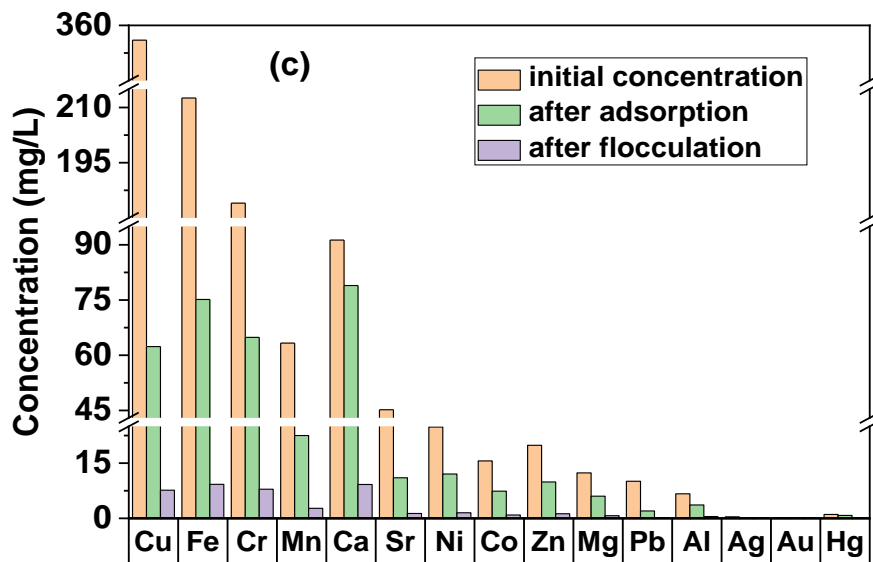
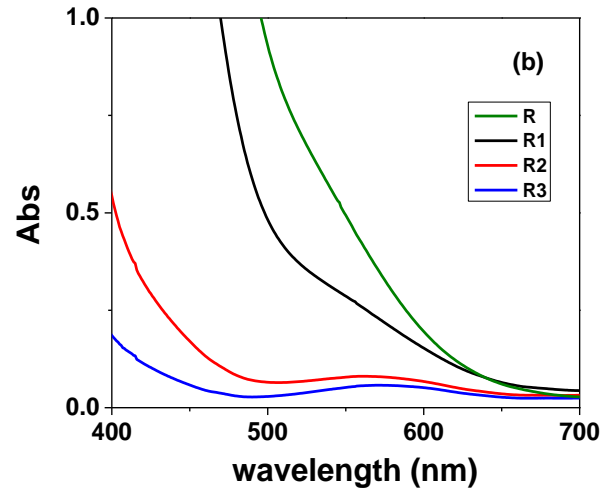
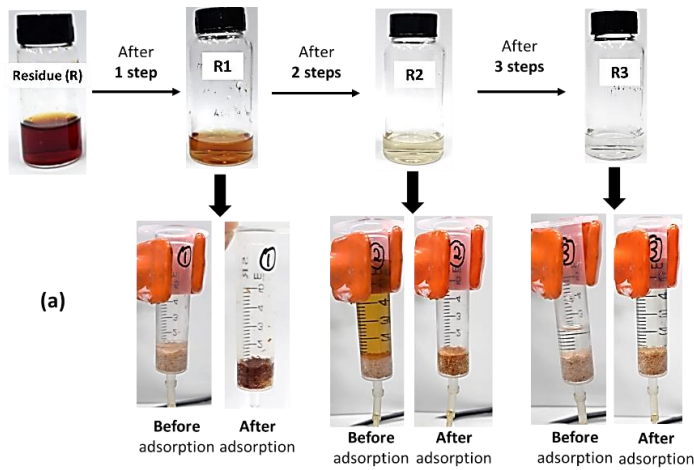
### 6.3.4 Removal of Pb<sup>2+</sup> ions from undergraduate laboratory waste

In order to evaluate the adsorption capacity of CMC/BG/PDA for Pb<sup>2+</sup> ions from a real complex mixture, an undergraduate laboratory waste, containing 17 elements at pH 1, was injected ( $V_{residue} = 5$  mL) in three columns at  $v = 1.0$  mL/min and  $m_{ads} = 0.2242 \pm 0.0024$  g (each), consecutively. The  $C_0$  (mg/L) values determined by ICP-OES for each element are the following: Pb (10), Ca (91.3), Mg (21.0), K (5597), Na (2601), Sr (45.2), Cr (184), Mn (63.3), Fe (212), Co (15.6), Ni (24.8), Cu (356), Zn (19.8), Al (6.66), Ag (0.418), Au (0.0646) and Hg (1.05).

After each adsorption step on the CMC/BG/PDA adsorbents, the outlet became lighter brown; after three consecutive steps, it was visually colorless (**Figure 6.8a**). Consequently, the adsorbents became darker than they were originally (**Figure 6.8a**). The electronic spectra (**Figure 6.8b**) showed the absorbance decrease in the visible region after each adsorption process, indicating that CMC/BG/PDA retained the metal ions and their complexes that absorb in the visible region.

**Figure 6.8c** presents the Removal (%) for each element after three consecutive steps of adsorption. The removal of Pb<sup>2+</sup> was  $80 \pm 5$  % in the complex mixture at pH 1.0. This extremely acid condition is used for general chemistry and analytical chemistry classes to avoid metal ions precipitation during the analyses. In the batch adsorption studies, HCl 0.1 mol/L was used for desorption (**Figure 6.4**), but in this complex mixture the acid medium did not hinder the removal of Pb<sup>2+</sup>. The high concentration of chloride in the laboratory waste favors the formation of negatively charged metal-chloride complexes (LOMMELEN et al., 2019). Probably negatively charged complexes  $[PbCl_3]^-$  and  $[PbCl_4]^{2-}$  adsorbed on the protonated hydroxyl groups belonging to BG and CMC. The removal capacity decreased in comparison to that observed for pure Pb<sup>2+</sup> ions ( $\sim 97\%$ , **Figure 6.4**) due to the competitive adsorption (**Figure 6.4b**). The other 16 metal ions compete for the adsorption sites on CMC/BG/PDA adsorbents. The Removal (%) values achieved simultaneously for the other elements were: Ag (99 %), Cu (83 %), Au (77 %), Sr (75 %), K (73 %), Mg (71 %), Cr

(65 %), Mn (64 %), Fe (64 %), Co (53 %), Ni (52 %), Zn (50 %), Al (47 %), Na (35 %), Hg (24%) and Ca (14 %), **Figure 6.8c** and **Table 6.5** shows the concentration of each element before and after the three consecutive adsorption processes; the concentration of Na and K was reduced to 1693 mg/L and 1503 mg/L, respectively.



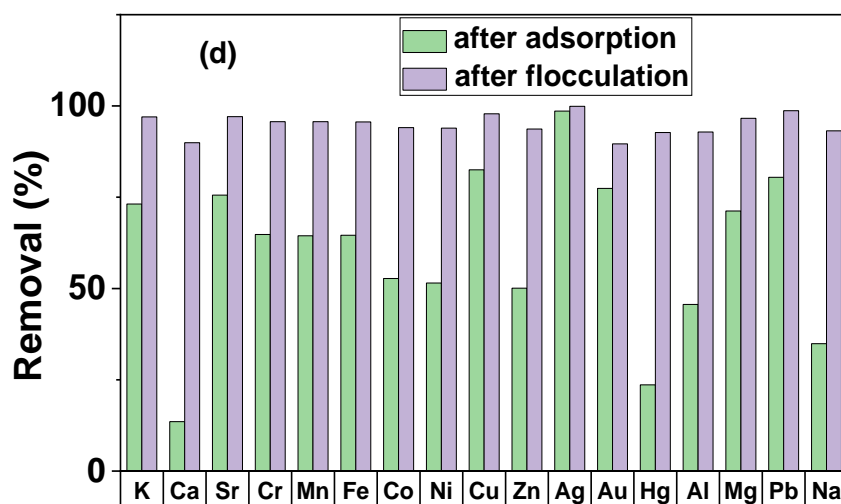


**Figure 6.8.** (a) Photographs of the residue after 3 sequential adsorption steps, using a new adsorbent in each step ( $m_{ads} = 0.2242 \pm 0.0024$  g), and of the CMC/BG/PDA adsorbents before and after each step. (b) Electronic spectra obtained for the original waste (R) after the first (R1), second (R2) and third (R3) steps of adsorption. (c) Concentration of each element found in the undergraduate laboratory waste before and after three adsorption steps. The concentration of Na and K was reduced to 1693 mg/L and 1503 mg/L, respectively. (d) Removal% after three adsorption steps (light green) followed by flocculation with PDDA (light purple).

Considering the large number of metal ions present in the undergraduate laboratory waste competing for the adsorbing sites on CMC/BG/PDA adsorbents, the results achieved were satisfactory. In the case of real complex mixtures, it is very difficult to eliminate all contaminants by only one type of process. Often the combination of two or more process are necessary to clean the waste. For instance, the combination of adsorption and flocculation processes might be successful strategies to wastewater treatment (SHABEER et al., 2014; ZHOU et al., 2015). Poly(diallyl dimethylammonium chloride) (PDDA) is a polycation widely used as flocculant (VEREZHNIKOV et al., 2002) and for water purification (ASSOCIATION; EDZWALD, 2011). Instantaneous flocculation of the remaining metal ions was achieved by adding PDDA to the filtrate. **Figure 6.8** and **Table 6.5** shows that after flocculation with PDDA, 98.7% of  $Pb^{2+}$  ions was removed and the removal of all other elements was larger than 90%, demonstrating that the combination of adsorption by CMC/BG/PDA and flocculation with PDDA is a successful strategy to clean complex laboratory waste. The metal complexes  $[MeCl_3]^-$  and  $[MeCl_4]^{2-}$  probably

interact with PDDA by electrostatic interactions. In order to evaluate if the process sequence plays an important role, in a separate set of experiments, the original residue was first flocculated with PDDA (at 5 g/L) and then the supernatant was injected in the column containing CMC/BG/PDA adsorbents. The results are presented as **Supplementary Material 16**. The removal of Pb<sup>2+</sup> ions was ~ 35% after flocculation and 80% after sequential adsorption, whereas the removal of the other elements was in average 50%, indicating that the highest efficiency was achieved when adsorption was followed by flocculation with PDDA. The flocculation seems to be more efficient for low concentrations of metal complexes.

**Table 6.5.** Concentration of 17 metals present in the undergraduate laboratory waste before treatment, after three steps of adsorption on the CMC/BG/PDA adsorbent and after the flocculation step with PDDA. Removal% after adsorption and flocculation.

<b>Meta l</b>	<b>Initial Concentratio n (C<sub>0</sub>)</b>	<b>Concentratio n after adsorption (mg/L)</b>	<b>Concentratio n after flocculation (mg/L)</b>	<b>Remova l (%)</b>
Pb	10.07	2.016	0.1335	98.7
K	5597	1503	168.5	97.0
Ca	91.30	78.95	9.198	90.0
Sr	45.18	11.03	1.319	97.1
Cr	184.2	64.86	7.928	95.7
Mn	63.3	22.51	2.723	95.7
Fe	212.3	75.15	9.259	95.6
Co	15.61	7.377	0.9280	94.1
Ni	24.81	12.03	1.503	93.9
Cu	356.1	62.35	7.658	97.9
Zn	19.84	9.905	1.252	93.7
Ag	0.4182	0.00585	0.00047	99.9
Au	0.0646	0.01459	0.00671	90.0
Hg	1.049	0.8011	0.07645	92.7

Al	6.663	3.623	0.47593	92.9
Mg	20.95	6.028	0.7118	96.6
Na	2601	1694	177.6	93.2

## 6.4 CONCLUSIONS

CMC/BG/PDA adsorbents are cost-competitive, eco-friendly and its processing involved no carbon emission. Their outstanding chemical and dimensional stability in aqueous media from pH 1 to pH 8.5 were achieved by the combination of adhesive properties of PDA and crosslinking reaction with citric acid. Batch adsorption studies of  $Pb^{2+}$  ions on CMC/BG/PDA revealed that the  $q_{max}$  values of  $(27.4 \pm 2.8)$  mg/g decreased slightly to  $(25.9 \pm 1.8)$  mg/g due to the presence of  $Ca^{2+}$  and  $Mg^{2+}$  ions. The interactions between the metal ions and CMC/BG/PDA hydroxyl groups are the main driving force for the adsorption process, as revealed by the thermodynamic study and XPS analyses. The column adsorption studied indicated that low flow rate and high adsorbent mass favored the adsorption. The highest adsorption capacity achieved for  $Pb^{2+}$  ions in individual system was  $q_{Th} = 70.3$  mg/g ( $v = 1.5$  mL/min,  $m_{ads} = 0.102$  g), but it was slightly reduced in the presence of  $Ca^{2+}$  and  $Mg^{2+}$  ions due to competitive adsorption.

The cost to produce CMC/BG/PDA adsorbents at lab scale was estimated at US\$ 0.25/g, considering the local prices for CMC, citric acid and DOPA, water and energy. BG was biowaste from a local market. The removal of  $Pb^{2+}$  ions ( $80 \pm 5$  %) and other 16 metal ions from an undergraduate laboratory waste disclosed the potential of CMC/BG/PDA adsorbents to be applied in the treatment of wastewater at large scale in combination with flocculation. The combination of adsorption and flocculation with a polycation elevated to 98.7% the removal of  $Pb^{2+}$  ions and to more than 90% the removal of other metal ions. Recycling the adsorbents by desorption does not seem to



be a reasonable destination for the adsorbents because more concentrated waste will be generated. Thus, the application of adsorbents and flocculated materials in the civil construction field is on the scope of a future investigation.

## 6.5 REFERENCES

ABDOLALI, A. et al. Application of a breakthrough biosorbent for removing heavy metals from synthetic and real wastewaters in a lab-scale continuous fixed-bed column. *Bioresource Technology*, v. 229, p. 78–87, 2017. Disponível em: <<http://dx.doi.org/10.1016/j.biortech.2017.01.016>>.

AL-GHOUTI, M. A.; DA'ANA, D. A. Guidelines for the use and interpretation of adsorption isotherm models: A review. *Journal of Hazardous Materials*, v. 393, n. January, p. 122383, 2020. Disponível em: <<https://doi.org/10.1016/j.jhazmat.2020.122383>>.

ALAVARSE, A. C. et al. Crosslinkers for polysaccharides and proteins: Synthesis conditions, mechanisms, and crosslinking efficiency, a review. *International Journal of Biological Macromolecules*, v. 202, n. January, p. 558–596, 2022. Disponível em: <<https://doi.org/10.1016/j.ijbiomac.2022.01.029>>.

ARBABI, M.; HEMATI, S.; AMIRI, M. Removal of lead ions from industrial wastewater: A review of Removal methods. *International Journal of Epidemiologic Research*, v. 2, n. 2, p. 105–109, 2015. Disponível em: <[http://ijer.skums.ac.ir/article\\_11812\\_2023.html%5Cnhttp://ijer.skums.ac.ir/pdf\\_11812\\_9b89af683a567da8c6e9b9b85c124cb4.html](http://ijer.skums.ac.ir/article_11812_2023.html%5Cnhttp://ijer.skums.ac.ir/pdf_11812_9b89af683a567da8c6e9b9b85c124cb4.html)>.

ARTEMENKO, A. et al. Reference XPS spectra of amino acids. *IOP Conference Series: Materials Science and Engineering*, v. 1050, p. 012001, 2021.

ASSOCIATION, A. W. W.; EDZWALD, J. *Water Quality & Treatment: A Handbook*

on *Drinking Water, Sixth Edition*. 6th ed. ed. New York: McGraw-Hill Education, 2011.

BARROS, M. A. S. D.; ARROYO, P. A.; SILVA, E. A. General Aspects of Aqueous Sorption Process in Fixed Beds. In: *Mass Transfer - Advances in Sustainable Energy and Environment Oriented Numerical Modeling*. [s.l.] IntechOpen, 2013. p. 361–383.

BISWAS, S. et al. Semifluidized Bed Adsorption Column Studies for Simultaneous Removal of Aqueous Phase  $Pb^{2+}$  and  $Cd^{2+}$  by Composite Adsorbents: an Experimental and Mass Transfer Dynamic Model–Based Approach. *Water Air and Soil Pollution*, v. 232, n. 8, p. 1–17, 2021.

BRIFFA, J.; SINAGRA, E.; BLUNDELL, R. Heavy metal pollution in the environment and their toxicological effects on humans. *Heliyon*, v. 6, n. 9, p. e04691, 2020. Disponível em: <<http://dx.doi.org/10.1016/j.heliyon.2020.e04691>>.

CHANG, R. *Physical chemistry for the chemical and biological sciences*. [s.l.] University Science Books, 2000.

CHEN, C. T. et al. Polydopamine and eumelanin molecular structures investigated with ab initio calculations. *Chemical Science*, v. 8, n. 2, p. 1631–1641, 2017.

CHEN, H. et al. Polydopamine modified cyclodextrin polymer as efficient adsorbent for removing cationic dyes and  $Cu^{2+}$ . *Journal of Hazardous Materials*, v. 389, n. 130, p. 121897, 2020.

CHEN, T.; DA, T.; MA, Y. Reasonable calculation of the thermodynamic parameters from adsorption equilibrium constant. *Journal of Molecular Liquids*, v. 322, n. 2, p. 114980, 2021. Disponível em: <<https://doi.org/10.1016/j.molliq.2020.114980>>.

CHEN, Y. et al. Synthesis of high-performance sodium carboxymethyl cellulose-based adsorbent for effective removal of methylene blue and  $Pb(II)$ . *International Journal of Biological Macromolecules*, v. 126, p. 107–117, 2018.

CHOWDHURY, I. R. et al. *Removal of lead ions ( $Pb^{2+}$ ) from water and wastewater: a review on the low-cost adsorbents*. [s.l.] Springer International Publishing, 2022. v. 12

CHU, K. H. Fixed bed sorption: Setting the record straight on the Bohart-Adams and Thomas models. *Journal of Hazardous Materials*, v. 177, n. 1–3, p. 1006–1012, 2010. Disponível em: <<http://dx.doi.org/10.1016/j.jhazmat.2010.01.019>>.

CRINI, G.; LICHTFOUSE, E. Advantages and disadvantages of techniques used for wastewater treatment. *Environmental Chemistry Letters*, v. 17, n. 1, p. 145–155, 2019. Disponível em: <<https://doi.org/10.1007/s10311-018-0785-9>>.

CRUZ-OLIVARES, J. et al. Inside the removal of lead(II) from aqueous solutions by De-Oiled Allspice Husk in batch and continuous processes. *Journal of Hazardous Materials*, v. 181, n. 1–3, p. 1095–1101, 2010. Disponível em: <<http://dx.doi.org/10.1016/j.jhazmat.2010.05.127>>.

DELLA VECCHIA, N. F. et al. Building-block diversity in polydopamine underpins a multifunctional eumelanin-type platform tunable through a quinone control point. *Advanced Functional Materials*, v. 23, n. 10, p. 1331–1340, 2013.

DOS SANTOS, V. C. G. et al. Assessment of chemically modified sugarcane bagasse for lead adsorption from aqueous medium. *Water Science and Technology*, v. 62, n. 2, p. 457–465, 2010.

EWULONU, C. M. et al. Lignin-Containing Cellulose Nanomaterials: A Promising New Nanomaterial for Numerous Applications. *Journal of Bioresources and Bioproducts*, v. 4, n. 1, p. 3–10, 2019. Disponível em: <<https://doi.org/10.21967/jbb.v4i1.186>>.

FAKHRE, N. A.; IBRAHIM, B. M. The use of new chemically modified cellulose for heavy metal ion adsorption. *Journal of Hazardous Materials*, v. 343, p. 324–331, 2018. Disponível em: <<https://doi.org/10.1016/j.jhazmat.2017.08.043>>.

FU, B.; XIE, F. Facile in situ synthesis of cellulose microcrystalline-manganese dioxide nanocomposite for effective removal of Pb(II) and Cd(II) from water. *Environmental Science and Pollution Research*, v. 27, n. 5, p. 5108–5121, 2020.

FURTADO, L. M.; ANDO, R. A.; PETRI, D. F. S. Polydopamine-coated cellulose acetate

butyrate microbeads for caffeine removal. *Journal of Materials Science*, v. 55, n. 8, p. 3243–3258, 2020.

GE, Y.; QIN, L.; LI, Z. Lignin microspheres: An effective and recyclable natural polymer-based adsorbent for lead ion removal. *Materials and Design*, v. 95, p. 141–147, 2016. Disponível em: <<http://dx.doi.org/10.1016/j.matdes.2016.01.102>>.

GODIYA, C. B. et al. Carboxymethyl cellulose / polyacrylamide composite hydrogel for cascaded treatment / reuse of heavy metal ions in wastewater. *Journal of Hazardous Materials*, v. 364, n. October 2018, p. 28–38, 2019. Disponível em: <<https://doi.org/10.1016/j.jhazmat.2018.09.076>>.

HALYSH, V. et al. Effect of oxidative treatment on composition and properties of sorbents prepared from sugarcane residues. *Industrial Crops and Products*, v. 139, p. 111566, 2019. Disponível em: <<https://doi.org/10.1016/j.indcrop.2019.111566>>.

HAMZA, I. A. A. et al. Adsorption studies of aqueous Pb(II) onto a sugarcane bagasse/multi-walled carbon nanotube composite. *Physics and Chemistry of the Earth*, v. 66, p. 157–166, 2013. Disponível em: <<http://dx.doi.org/10.1016/j.pce.2013.08.006>>.

HAN, W.; LUO, L.; ZHANG, S. Adsorption of bisphenol A on lignin: Effects of solution chemistry. *International Journal of Environmental Science and Technology*, v. 9, n. 3, p. 543–548, 2012.

HEINZE, T.; KOSCHELLA, A. Carboxymethyl ethers of cellulose and starch - A review. *Macromolecular Symposia*, v. 223, p. 13–40, 2005.

IRAWAN, C. et al. The amine functionalized sugarcane bagasse biocomposites as magnetically adsorbent for contaminants removal in aqueous solution. *Molecules*, v. 26, p. 5867, 2021.

KANIKIREDDY, V. et al. Carboxymethyl cellulose-based materials for infection control and

wound healing: A review. *International Journal of Biological Macromolecules*, v. 164, p. 963–975, 2020. Disponível em: <<https://doi.org/10.1016/j.ijbiomac.2020.07.160>>.

KARNITZ, O. et al. Adsorption of Cu ( II ), Cd ( II ), and Pb ( II ) from aqueous single metal solutions by mercerized cellulose and mercerized sugarcane bagasse chemically modified with EDTA dianhydride ( EDTAD ). *Carbohydrate Polymers*, v. 77, n. 3, p. 643–650, 2009. Disponível em: <<http://dx.doi.org/10.1016/j.carbpol.2009.02.016>>.

KHOO, R. Z.; CHOW, W. S.; ISMAIL, H. Sugarcane bagasse fiber and its cellulose nanocrystals for polymer reinforcement and heavy metal adsorbent: a review. *Cellulose*, v. 25, n. 8, p. 4303–4330, 2018. Disponível em: <<https://doi.org/10.1007/s10570-018-1879-z>>.

KLOSTERMAN, L.; RILEY, J. K.; BETTINGER, C. J. Control of heterogeneous nucleation and growth kinetics of dopamine-melanin by altering substrate chemistry. *Langmuir*, v. 31, n. 11, p. 3451–3458, 2015.

KREMPEL, M.; GRIFFIN, K.; KHOURYIEH, H. *Hydrocolloids as emulsifiers and stabilizers in beverage preservation*. [s.l.] Elsevier Inc., 2019.

KUMAR, A. et al. Lead toxicity: Health hazards, influence on food Chain, and sustainable remediation approaches. *International Journal of Environmental Research and Public Health*, v. 17, p. 2179, 2020.

LEE, H. et al. Mussel-Inspired Surface Chemistry for Multifunctional Coatings. *Science*, v. 318, n. 5849, p. 426–430, 2007.

LIN, Q. et al. Adhesion mechanisms of the mussel foot proteins mfp-1 and mfp-3. *Proceedings of the National Academy of Sciences of the United States of America*, v. 104, n. 10, p. 3782–3786, 2007.

LOMMELEN, R. et al. Model for Metal Extraction from Chloride Media with Basic Extractants: A Coordination Chemistry Approach. *Inorganic Chemistry*, v. 58, n. 18, p. 12289–

12301, 2019.

LONG, Y. et al. Packed bed column studies on lead(II) removal from industrial wastewater by modified *Agaricus bisporus*. *Bioresource Technology*, v. 152, p. 457–463, 2014. Disponível em: <<http://dx.doi.org/10.1016/j.biortech.2013.11.039>>.

LÓPEZ, G. P.; CASTNER, D. G.; RATNER, B. D. XPS O 1s binding energies for polymers containing hydroxyl, ether, ketone and ester groups. *Surface and Interface Analysis*, v. 17, n. 5, p. 267–272, 1991.

LUO, R. et al. Improved immobilization of biomolecules to quinone-rich polydopamine for efficient surface functionalization. *Colloids and Surfaces B: Biointerfaces*, v. 106, p. 66–73, 2013. Disponível em: <<http://dx.doi.org/10.1016/j.colsurfb.2013.01.033>>.

MAHMOOD, T. et al. Comparison of different methods for the point of zero charge determination of NiO. *Industrial and Engineering Chemistry Research*, v. 50, n. 17, p. 10017–10023, 2011.

MARTÍN-LARA, M. Á. et al. Modification of the sorptive characteristics of sugarcane bagasse for removing lead from aqueous solutions. *Desalination*, v. 256, n. 1–3, p. 58–63, 2010. Disponível em: <<http://dx.doi.org/10.1016/j.desal.2010.02.015>>.

MARTINS, D. et al. Bacterial Cellulose-Carboxymethyl Cellulose (BC:CMC) dry formulation as stabilizer and texturizing agent for surfactant-free cosmetic formulations. *Colloids and Surfaces A: Physicochemical and Engineering Aspects*, v. 617, n. September 2020, p. 126380, 2021. Disponível em: <<https://doi.org/10.1016/j.colsurfa.2021.126380>>.

MENESES, I. P. et al. CTAB-modified carboxymethyl cellulose/bagasse cryogels for the efficient removal of bisphenol A, methylene blue and Cr(VI) ions: Batch and column adsorption studies. *Journal of Hazardous Materials*, v. 421, p. 126804, 2022.

MICILLO, R. et al. Eumelanin broadband absorption develops from aggregation-modulated

chromophore interactions under structural and redox control. *Scientific Reports*, v. 7, n. December 2016, p. 1–12, 2017. Disponível em: <<http://dx.doi.org/10.1038/srep41532>>.

MPATANI, F. M. et al. Uptake of micropollutant-bisphenol A, methylene blue and neutral red onto a novel bagasse- $\beta$ -cyclodextrin polymer by adsorption process. *Chemosphere*, v. 259, p. 127439, 2020. Disponível em: <<https://doi.org/10.1016/j.chemosphere.2020.127439>>.

NGUYEN, T. C. et al. Simultaneous adsorption of Cd, Cr, Cu, Pb, and Zn by an iron-coated Australian zeolite in batch and fixed-bed column studies. *Chemical Engineering Journal*, v. 270, p. 393–404, 2015. Disponível em: <<http://dx.doi.org/10.1016/j.cej.2015.02.047>>.

NOVAES, S. D.; OLIVEIRA, P. V.; PETRI, D. F. S. Hydroxypropyl methylcellulose-sugarcane bagasse adsorbents for removal of 17 $\alpha$ -ethinylestradiol from aqueous solution and freshwater. *Environmental Science and Pollution Research*, n. 0123456789, 2022. Disponível em: <<https://doi.org/10.1007/s11356-022-20345-4>>.

OLADOYE, P. O. Natural, low-cost adsorbents for toxic Pb(II) ion sequestration from (waste)water: A state-of-the-art review. *Chemosphere*, v. 287, n. P2, p. 132130, 2022. Disponível em: <<https://doi.org/10.1016/j.chemosphere.2021.132130>>.

PALIN, D. et al. Evaluation of Pb (II) biosorption utilizing sugarcane bagasse colonized by Basidiomycetes. *Environmental Monitoring and Assessment*, v. 188, n. 279, p. 1–14, 2016. Disponível em: <<http://dx.doi.org/10.1007/s10661-016-5257-8>>.

PUTRA, W. P. et al. Biosorption of Cu ( II ), Pb ( II ) and Zn ( II ) Ions from Aqueous Solutions Using Selected Waste Materials : Adsorption and Characterisation Studies. *Journal of Encapsulation and Adsorption Sciences*, v. 4, p. 25–35, 2014.

SAMYN, P. A platform for functionalization of cellulose, chitin/chitosan, alginate with polydopamine: A review on fundamentals and technical applications. *International Journal of Biological Macromolecules*, v. 178, p. 71–93, 2021. Disponível em:

<<https://doi.org/10.1016/j.ijbiomac.2021.02.091>>.

SHABEER, T. P. A. et al. Simultaneous removal of multiple pesticides from water : Effect of organically modified clays as coagulant aid and adsorbent in coagulation – flocculation process. *Environmental Technology*, v. 35, n. 20, p. 2619–2627, 2014.

SHIBI, I. G.; ANIRUDHAN, T. S. Polymer-grafted banana (*Musa paradisiaca*) stalk as an adsorbent for the removal of lead(II) and cadmium(II) ions from aqueous solutions: Kinetic and equilibrium studies. *Journal of Chemical Technology and Biotechnology*, v. 81, n. 3, p. 433–444, 2006.

SLUITER, A. et al. Determination of Structural Carbohydrates and Lignin in Biomass. *Biomass Analysis Technology Team Laboratory Analytical Procedure*, n. August, p. 1–14, 2004.

SUN, G. et al. In Situ Infrared Spectroscopic Monitoring and Characterization of the Growth of Polydopamine (PDA) Films. *Physica Status Solidi (B) Basic Research*, v. 256, n. 2, p. 1–8, 2019.

TAKA, A. L. et al. Removal of cobalt and lead ions from wastewater samples using an insoluble nanosponge biopolymer composite: adsorption isotherm, kinetic, thermodynamic, and regeneration studies. *Environmental Science and Pollution Research*, v. 25, n. 22, p. 21752–21767, 2018.

TATY-COSTODES, V. C. et al. Removal of lead (II) ions from synthetic and real effluents using immobilized *Pinus sylvestris* sawdust: Adsorption on a fixed-bed column. *Journal of Hazardous Materials*, v. 123, n. 1–3, p. 135–144, 2005.

TOLEDO, P. V. O. et al. Carboxymethyl cellulose/poly(acrylic acid) interpenetrating polymer network hydrogels as multifunctional adsorbents. *Cellulose*, v. 26, n. 1, p. 597–615, 2019. Disponível em: <<https://doi.org/10.1007/s10570-018-02232-9>>.

VERA, L. M. et al. Fixed bed column modeling of lead(II) and cadmium(II) ions biosorption on sugarcane bagasse. *Environmental Engineering Research*, v. 24, n. 1, p. 31–37, 2019.



VEREZHNIKOV, V. N. et al. Flocculating power of poly-N,N-dimethyl-N,N-diallylammonium chloride of various molecular weights. *Russian Journal of Applied Chemistry*, v. 75, n. 3, p. 461–464, 2002.

VIEIRA, W. T. et al. Removal of endocrine disruptors in waters by adsorption, membrane filtration and biodegradation. A review. *Environmental Chemistry Letters*, v. 18, n. 4, p. 1113–1143, 2020. Disponível em: <<https://doi.org/10.1007/s10311-020-01000-1>>.

WORLD HEALTH ORGANIZATION. *Guidelines for Drinking-water Quality*. [s.l.: s.n.]

YANG, J. et al. Environmental pollution effect analysis of lead compounds in China based on life cycle. *International Journal of Environmental Research and Public Health*, v. 17, p. 2184, 2020.

YANG, P. et al. Stimuli-responsive polydopamine-based smart materials. *Chemical Society Reviews*, v. 50, n. 14, p. 8319–8343, 2021.

ZANGMEISTER, R. A.; MORRIS, T. A.; TARLOV, M. J. Characterization of polydopamine thin films deposited at short times by autoxidation of dopamine. *Langmuir*, v. 29, n. 27, p. 8619–8628, 2013.

ZHOU, D. et al. Simultaneous removal of multi-pollutants in an intimate integrated flocculation-adsorption fluidized bed. *Environmental Science and Pollution Research*, v. 22, n. 5, p. 3794–3802, 2015.

## 7 GENERAL CONCLUSIONS

Understanding the physicochemical properties of PDA coatings in the presence and absence of caffeine on substrates with different surface energies enabled the development of a novel fluorescent adsorbent, CAB/PDA microbeads that proved to be efficient adsorbent for caffeine.

The characterization of PDA and PDA/caffeine coatings revealed that the co-adsorption of caffeine and PDA on CAB had the highest stability at pH 1.0, 8.5, and 13. Spectroscopic analyses and DFT calculations supported the hypotheses that interactions between caffeine on PDA are driven by hydrogen bonds by the nitrogen 9 of the caffeine and imidazole N-H group of PDA trimer and the  $\pi$ - $\pi$  interactions between their aromatic rings, this result confirmed the importance of combining theoretical and experimental tools/analyses to elucidate the adsorption mechanism and presented an efficient method for the development of new functional and stable coatings in a wide pH range.

The favorable interactions between cellulose acetate butyrate and caffeine detected in the previous study resulted in the development of a system for sustained release of caffeine from micrometric films of CAB.

Systems partially miscible showed a two-step release process. The first one corresponding to the dissolution and release of caffeine at the film surface and a second one related to the release of caffeine in the internal polymer matrix. CAB/caf 7 wt% films were the most interesting system because they achieved total release of loaded caffeine at pH 7.4 during 48 h.

This feature is particularly advantageous for biomedical applications, where caffeine needs to be released slowly into the skin or bloodstream.

Eco-friendly CMC/BG/PDA adsorbents with no carbon emissions were developed with a competitive cost of US\$ 0.25/g – estimated price considering local prices. They presented outstanding chemical and dimensional stability in aqueous media (pH 1 to pH 8.5), due to PDA adhesive properties and citric acid crosslinking.

Batch adsorption studies with individual solutions of  $\text{Pb}^{2+}$  and ternary mixtures of  $\text{Pb}^{2+}$ ,  $\text{Ca}^{2+}$ , and  $\text{Mg}^{2+}$  ions indicated that metal ion adsorption on CMC/BG/PDA were driven by interactions with hydroxyl groups. And potential application of CMC/BG/PDA adsorbents for wastewater treatment at large scale was explored, combining fixed-bed column adsorption and flocculation with polication for efficient removal of  $\text{Pb}^{2+}$  and other metal ions from an undergraduate laboratory waste reaching 98.7% and more than 90% removal, respectively.

## 8 PERSPECTIVES

Polydopamine continues to be studied, opening pathways as functionalization platform on surfaces in different fields, from the development of adsorbents for water treatment to photothermal materials for cancer treatment. However, Liu and co-authors reported that there is a lack of studies regarding scaling up the production of PDA-based materials (LIU et al., 2022).

Hence, pilot-scale studies should be explored for the production and application of CMC/BG/PDA absorbent for the treatment of undergraduate laboratory waste in the Institute of Chemistry at the University of São Paulo. As well as the implementation of new methods of dopamine oxidation, to optimize the time of adsorbent preparation. One of the strategies that might be used is the oxidation of DOPA through microwave irradiation, which reduces the oxidation time from 6 h to 15 min, keeping the amount of oxygen solubilized in an aqueous medium (LEE; PARK; LEE, 2020).

The fluorescence property of CAB/PDA microbeads should be applied in the development of sensors for the detection of organic pollutants, keeping in mind the quenching effect. The fluorescent solution of CAB and PDA can be easily applied by spraying, spin-coating, and casting method to obtain nanometric or micrometric coatings on gold and glassy carbon electrodes. Recently, Rocha et al. reported that polydopamine has been responsible for improving the selectivity, sensitivity, and hydrophilicity of devices in the electrochemical sensors and biosensors field, and fluorescent polydopamine nanoparticles incorporated in polyvinyl alcohol (PVA) hydrogel has been applied to fluorescence imaging-guided photothermal cancer therapy. (LEE et al., 2022; ROCHA; HASIMOTO; SANTHIAGO, 2023).

The circular economy is gaining attraction within organizations, especially with the demands of ESG (Environmental, Social and Corporate Governance), where companies that trade shares on the stock exchange need to incorporate ESG features (AHMED; GAO; SATCHELL, 2021). The

academic community will need to keep an eye on what is happening in the corporative environment to prepare human capital in universities to be used at its highest potential and to contribute to the evolution of our society towards the development of sustainable practices with a positive impact on human beings life quality and in nature that is our source of life.

I wish my work continues in this pathway, as well as the work of researchers who reached the end of this reading.

## REFERENCES

AHMED, M. F.; GAO, Y.; SATCHELL, S. Modeling demand for ESG. *European Journal of Finance*, v. 27, n. 16, p. 1669–1683, 2021. Disponível em: <<https://doi.org/10.1080/1351847X.2021.1924216>>.

LEE, H. A.; PARK, E.; LEE, H. Polydopamine and Its Derivative Surface Chemistry in Material Science: A Focused Review for Studies at KAIST. *Advanced Materials*, v. 32, n. 35, p. 1–20, 2020.

LEE, K. K. et al. Polydopamine Nanoparticle-Incorporated Fluorescent Hydrogel for Fluorescence Imaging-Guided Photothermal Therapy of Cancers. *Biochip Journal*, v. 17, n. 1, p. 85–92, 2022. Disponível em: <<https://doi.org/10.1007/s13206-022-00091-y>>.

LIU, F. et al. Polydopamine-based polysaccharide materials for water treatment. *Cellulose*, v. 29, n. 15, p. 8025–8064, 2022. Disponível em: <<https://doi.org/10.1007/s10570-022-04787-0>>.

ROCHA, J. F.; HASIMOTO, L. H.; SANTHIAGO, M. Recent progress and future perspectives of polydopamine nanofilms toward functional electrochemical sensors. *Analytical and Bioanalytical Chemistry*, n. 0123456789, 2023. Disponível em: <<https://doi.org/10.1007/s00216-023-04522-z>>.

# 9 APPENDICES

## 9.1 Permissions

### 9.1.1 Chapter 1:

14/12/2022 18:45

RightsLink Printable License

#### SPRINGER NATURE LICENSE TERMS AND CONDITIONS

Dec 14, 2022

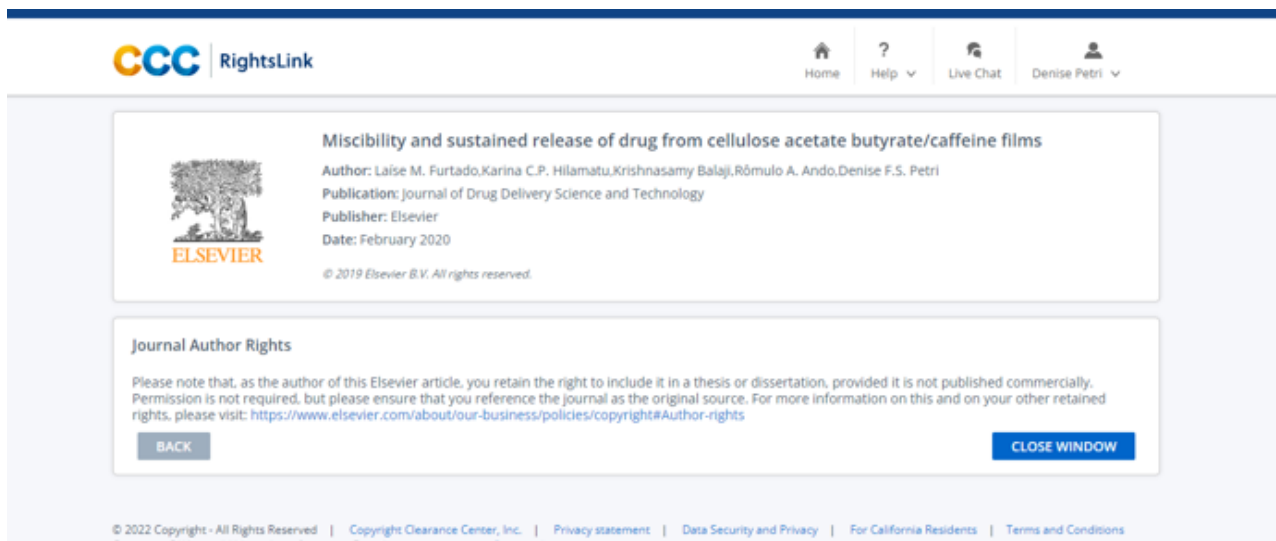
---

---

This Agreement between Universidade de Sao Paulo -- Denise Petri ("You") and Springer Nature ("Springer Nature") consists of your license details and the terms and conditions provided by Springer Nature and Copyright Clearance Center.

License Number	5447820434270
License date	Dec 14, 2022
Licensed Content Publisher	Springer Nature
Licensed Content Publication	Journal of Materials Science
Licensed Content Title	Polydopamine-coated cellulose acetate butyrate microbeads for caffeine removal
Licensed Content Author	Laise Moura Furtado et al
Licensed Content Date	Nov 7, 2019
Type of Use	Thesis/Dissertation
Requestor type	academic/university or research institute
Format	print and electronic
Portion	full article/chapter
Will you be translating?	no
Circulation/distribution	1 - 29

## 9.1.2 Chapter 2:



The screenshot shows the CCC RightsLink interface. At the top, there is a navigation bar with the CCC RightsLink logo on the left and links for Home, Help, Live Chat, and a user profile for Denise Petri on the right. The main content area is divided into two sections. The first section, titled "Miscibility and sustained release of drug from cellulose acetate butyrate/caffeine films", includes an Elsevier logo, the article title, author list (Laise M. Furtado, Karina C.P. Hiamatu, Krishnasamy Balaji, Rômulo A. Ando, Denise F.S. Petri), publication information (Journal of Drug Delivery Science and Technology, Elsevier, February 2020), and a copyright notice (© 2019 Elsevier B.V. All rights reserved.). The second section, titled "Journal Author Rights", contains a disclaimer about the author's retained rights and a link to the Elsevier copyright policy. At the bottom of this section are "BACK" and "CLOSE WINDOW" buttons. A footer at the very bottom contains copyright and privacy information.

## 9.1.3 Chapter 4:

### Author Rights for Scholarly Purposes

I understand that I retain or am hereby granted (without the need to obtain further [permission](#)) the Author Rights (see description below), and that no rights in patents, trademarks or other intellectual property rights are transferred to Elsevier Ltd.

The Author Rights include the right to use the [Preprint](#), [Accepted Manuscript](#) and the [Published Journal Article](#) for [Personal Use](#) and [Internal Institutional Use](#). They also include the right to use these different versions of the Article for [Scholarly Sharing](#) purposes, which include sharing:

- the Preprint on any website or repository at any time;
- the Accepted Manuscript on certain websites and usually after an embargo period;
- the Published Journal Article only privately on certain websites, unless otherwise agreed by Elsevier Ltd.

In the case of the Accepted Manuscript and the Published Journal Article the Author Rights exclude Commercial Use (unless expressly agreed in writing by Elsevier Ltd), other than use by the author in a subsequent compilation of the author's works or to extend the Article to book length form or re-use by the author of portions or excerpts in other works (with full acknowledgment of the original publication of the Article).

### Publishing Agreement

I am one author signing on behalf of all co-authors of the manuscript

I am signing on behalf of the corresponding author.

**Name/Job title/Company:** Denise Freitas Siqueira Petri, Full professor, University of Sao Paulo

**E-mail address:** [dfsp@iq.usp.br](mailto:dfsp@iq.usp.br)

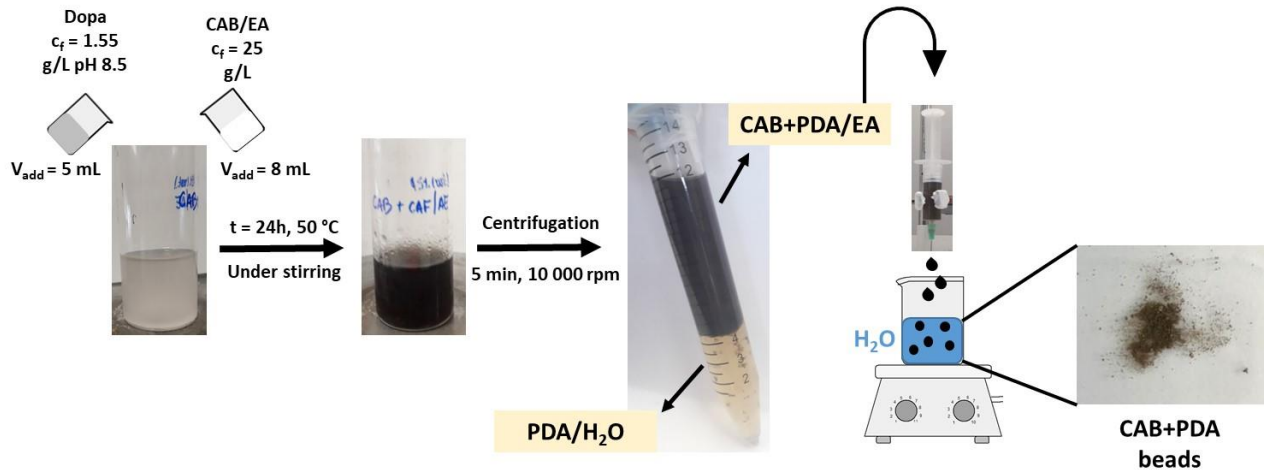
I may post the accepted manuscript in my institutional repository and make this public after an embargo period. To ensure the sustainability of peer-reviewed research in journal publications, I may not share the final article publicly, for example on ResearchGate or Academia.edu. Further details on [Elsevier Sharing Policy](#) [here](#).

Based on information provided the embargo period/end date is 24 months.

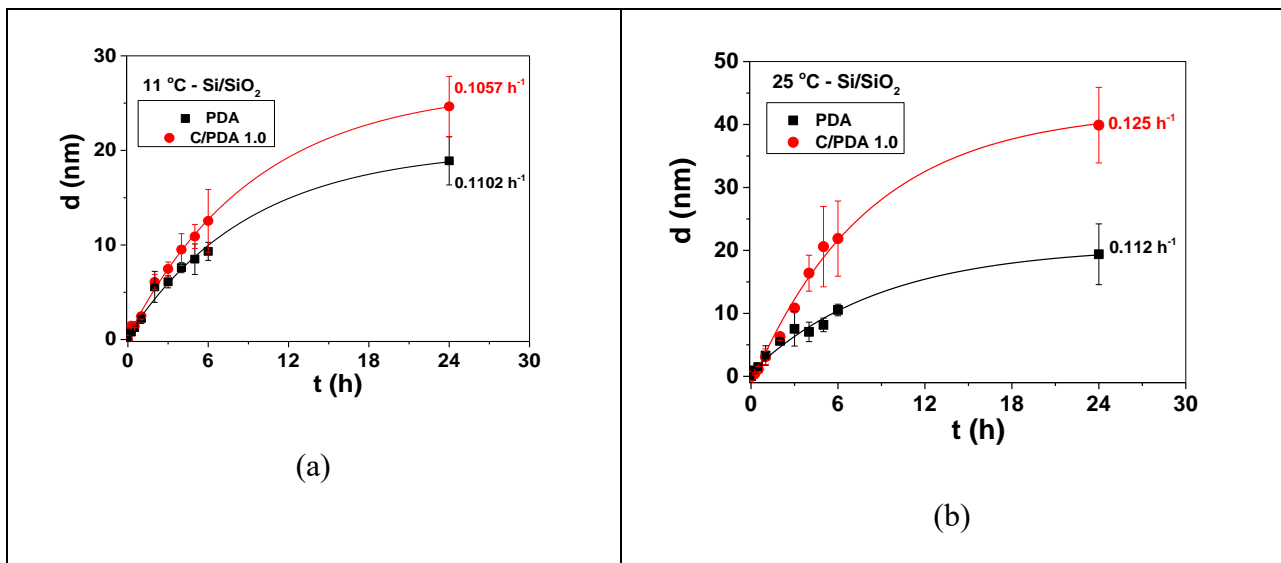
## 9.2 Supplementary Material

### 9.2.1 Chapter 1:

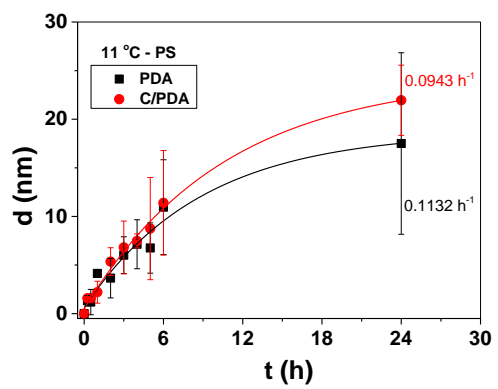
#### SI1. Preparation of CAB/PDA microbeads for caffeine adsorption.



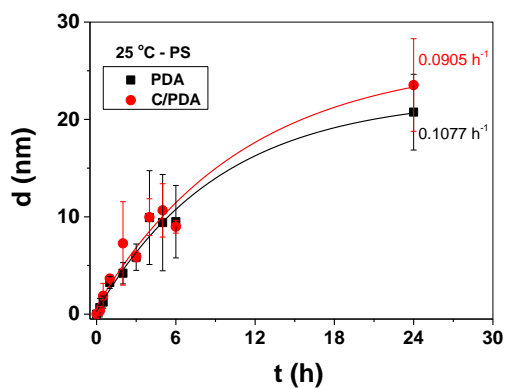
SI2. Mean thickness ( $d$ ) values determined for the deposition of PDA and C/PDA 1.0 on (a, b) Si/SiO<sub>2</sub> wafers, (c, d) PS films, (e, f) CAB films, at (a)  $11 \pm 1$  °C and (b)  $25 \pm 1$  °C, at pH 8.3, as a function of time. The solid lines are the fitting curves with equation (3).



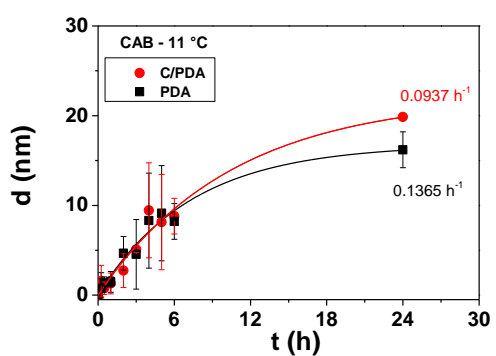




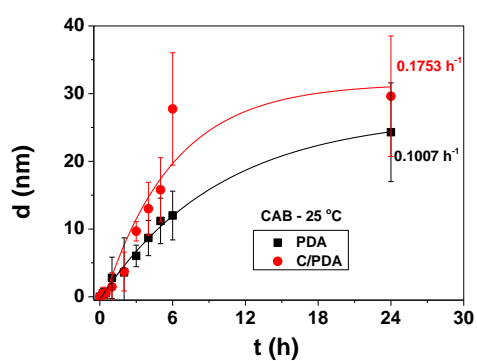
(c)



(d)

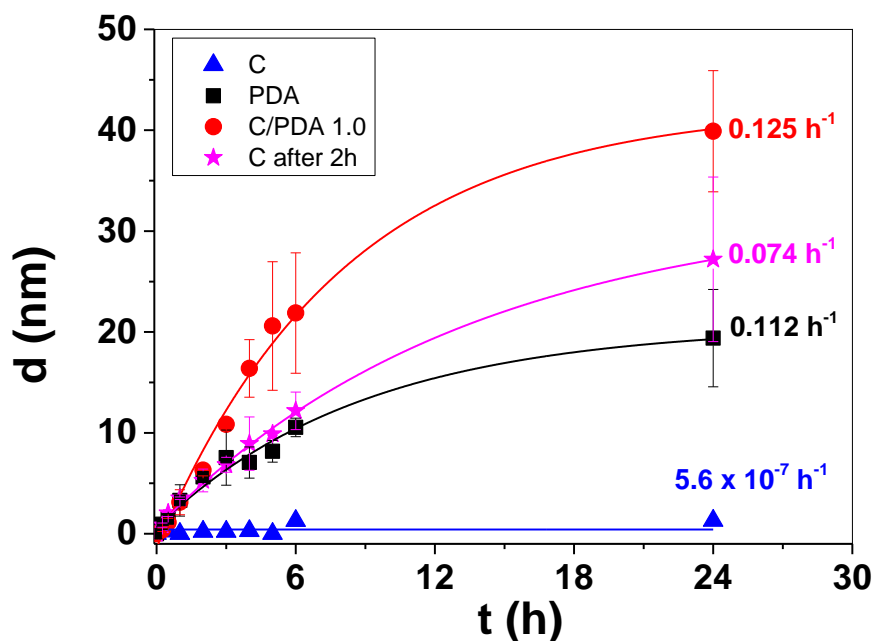


(e)



(f)

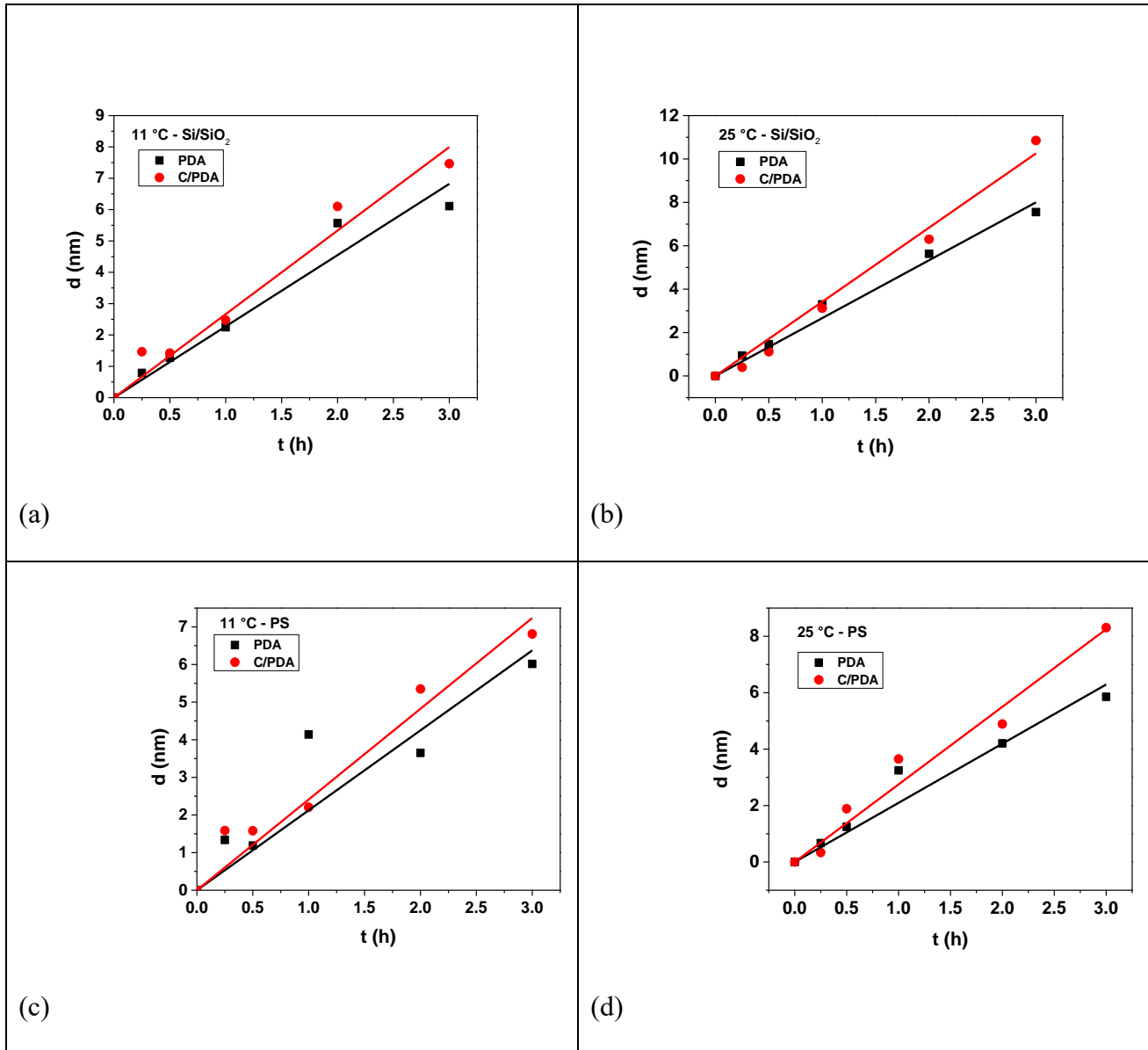
**SI3:** Mean thickness ( $d$ ) values of adsorbed PDA (square), caffeine, C, (triangle), C/PDA (circle), addition of caffeine after 2 h PDA deposition (star) onto Si/SiO<sub>2</sub> wafers at  $25 \pm 1$  C ° and pH 8.3, as a function of time. The solid lines are the fit curves with equation (3), the  $k$  values are indicated for each system.

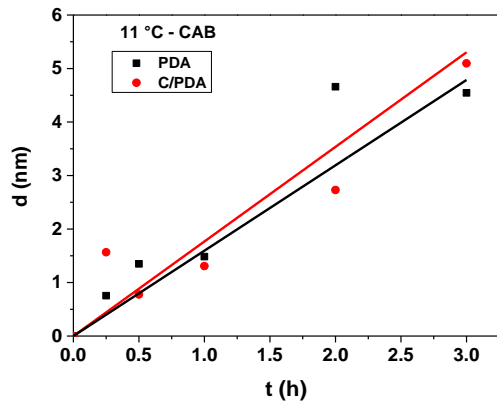


Fitting parameters determined with equation (3.3).

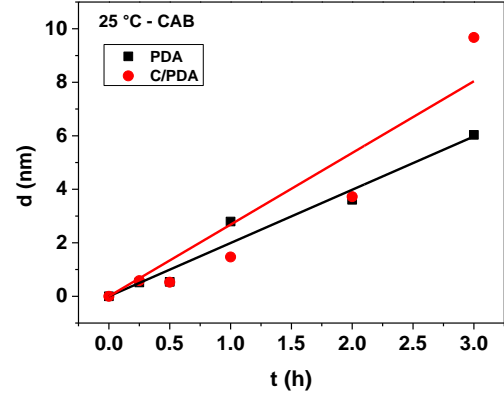
System	$d_0$ (nm)	$d_{max}$ (nm)	$k$ (h <sup>-1</sup> )	$R^2$
C	0.42	$2.6 \cdot 10^{-5}$	$5.6 \cdot 10^{-7}$	-0.2883
PDA	0.63	20	0.11	0.9784
C/PDA 1.0	-1.4	44	0.12	0.9898
C after 2 h	0.57	32	0.07	0.9967

**SI4:** Mean thickness ( $d$ ) values determined for the deposition of PDA and C/PDA 1.0 on (a, b) Si/SiO<sub>2</sub> wafers, (c, d) PS films, (e, f) CAB films, at (a) 11 ± 1 °C and (b) 25 ± 1 °C, at pH 8.3, as a function of time. The solid lines are the fitting curves for deposition rate calculation.





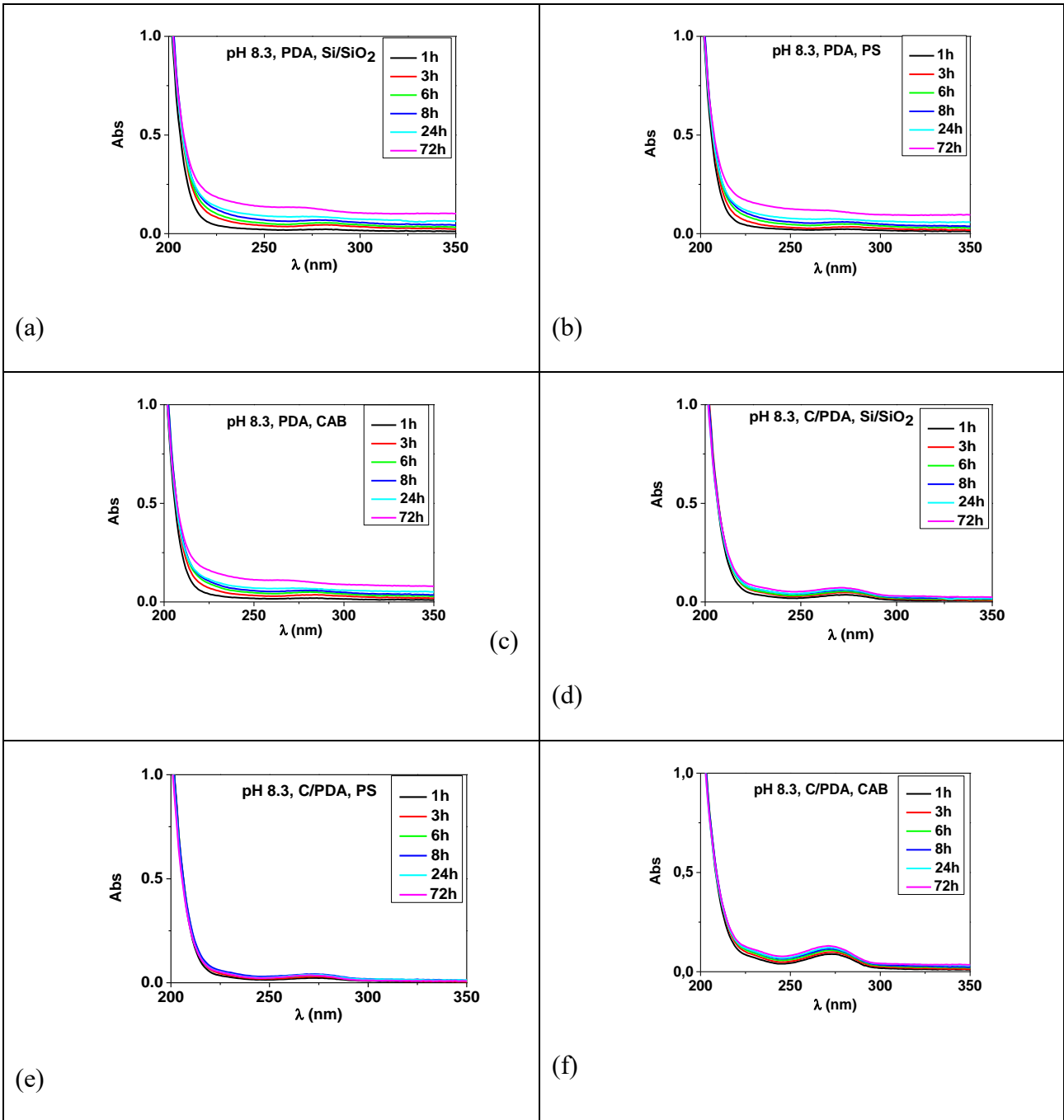
(e)



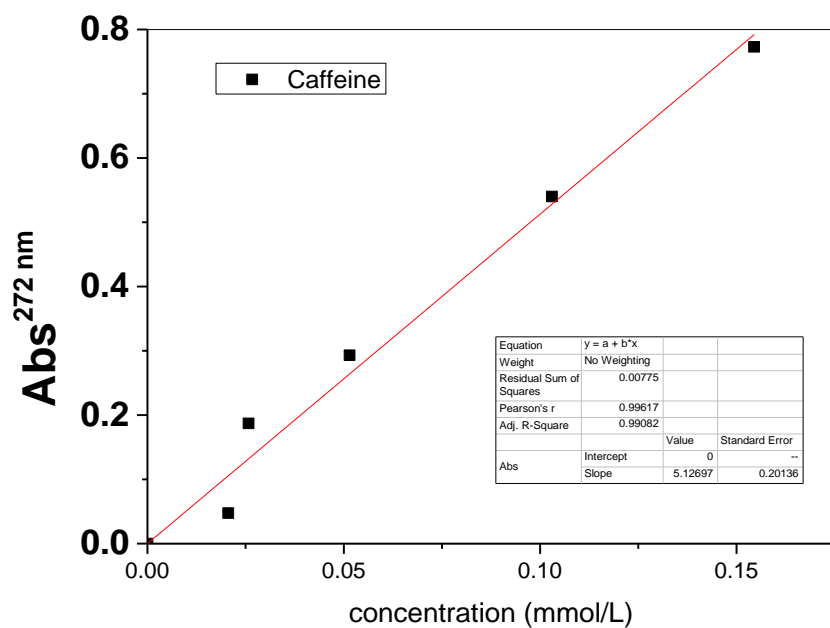
(f)

**SI5.** UV spectra determined for the supernatants of (a), (b) and (c) PDA and (d), (e) and (f)

C/PDA coatings after 1 h, 3 h, 6 h, 8 h, 24 h and 72 h contact with Tris buffer (pH 8.3).

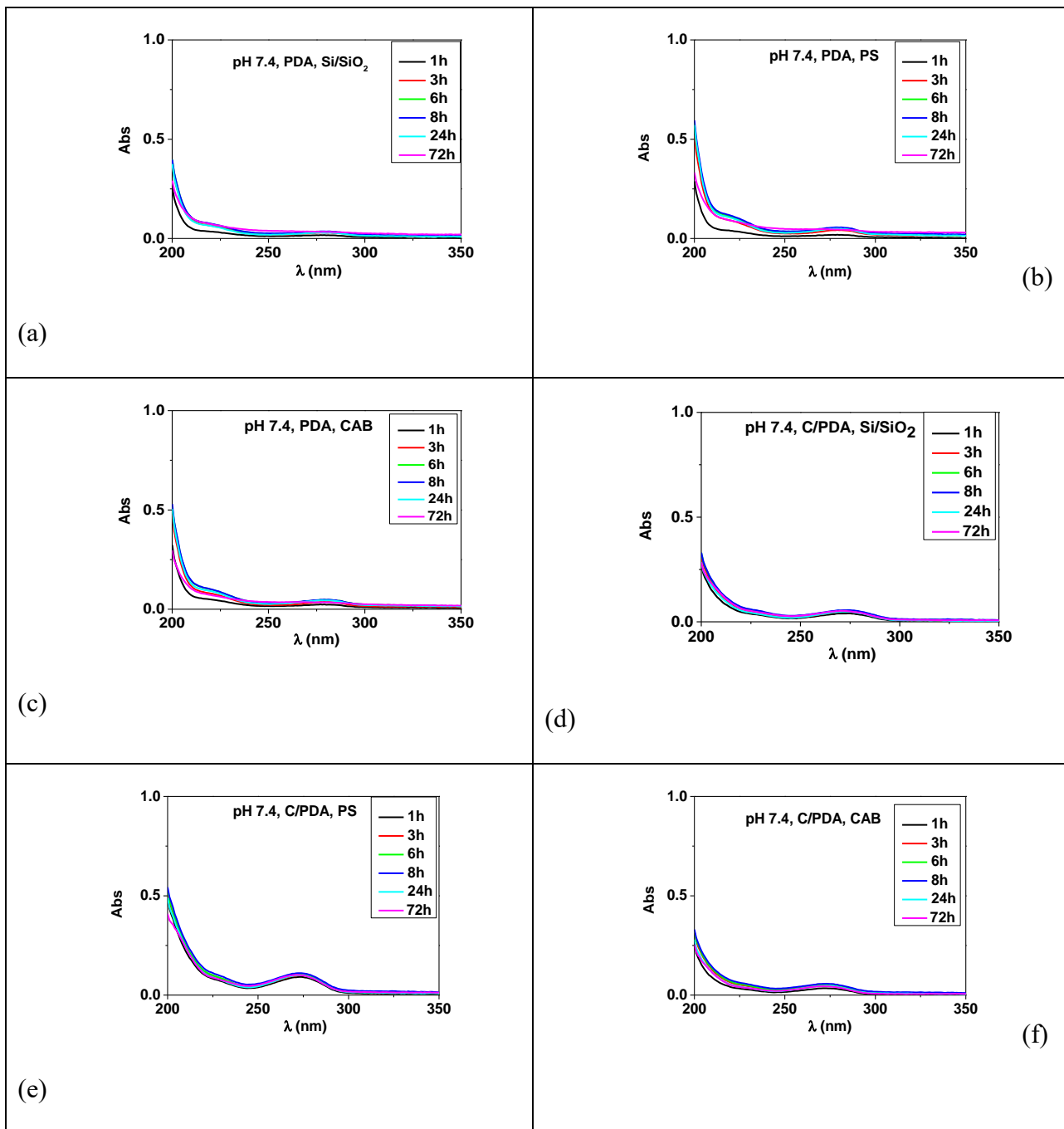


SI6. Calibration curve of caffeine taken at 272 nm and pH 8.3.

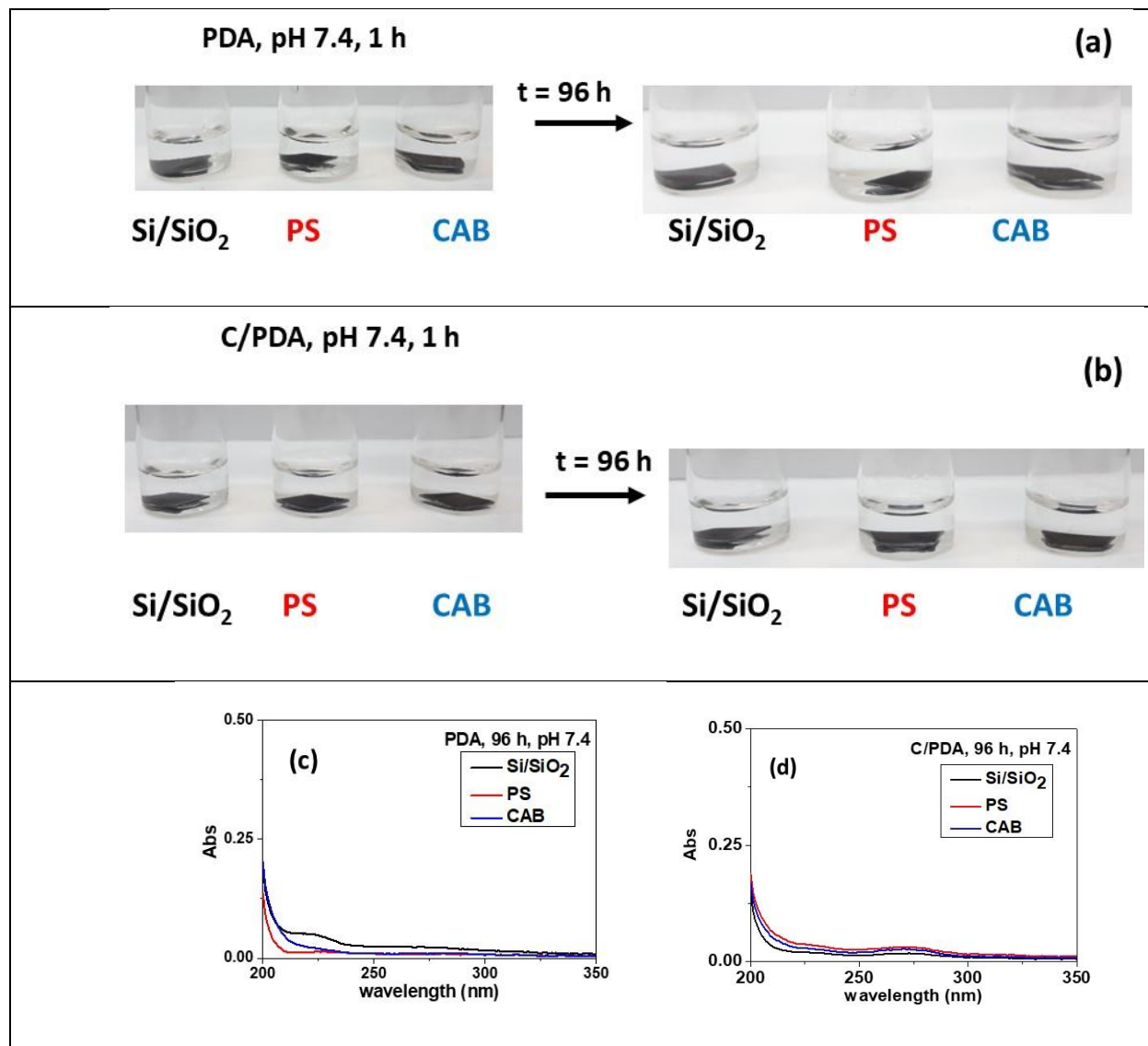


SI7. UV spectra determined for the supernatants of (a), (b) and (c) PDA and (d), (e) and (f)

C/PDA coatings after 1 h, 3 h, 6 h, 8 h, 24 h and 72 h contact with PBS buffer (pH 7.4).



**S18.** Photographs of (a) PDA and (b) C/PDA coatings on Si/SiO<sub>2</sub> wafers, PS and CAB films, respectively, taken after 1 h and 96 h contact with PBS buffer (10 mmol/L, pH 7.4). UV spectra determined for the supernatants of (c) PDA and (d) C/PDA coatings after 96 h contact at pH 7.4





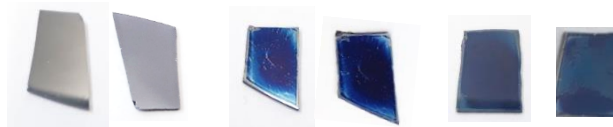
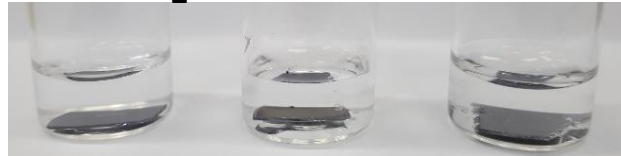
**SI9.** Photographs of the vials with Si/SiO<sub>2</sub> wafers, PS and CAB films before (0 min) and after 10 min contact with NaOH 0.1 mol/L (pH 13).

### Control experiment, pH 13

**Si/SiO<sub>2</sub>**

**PS**

**CAB**

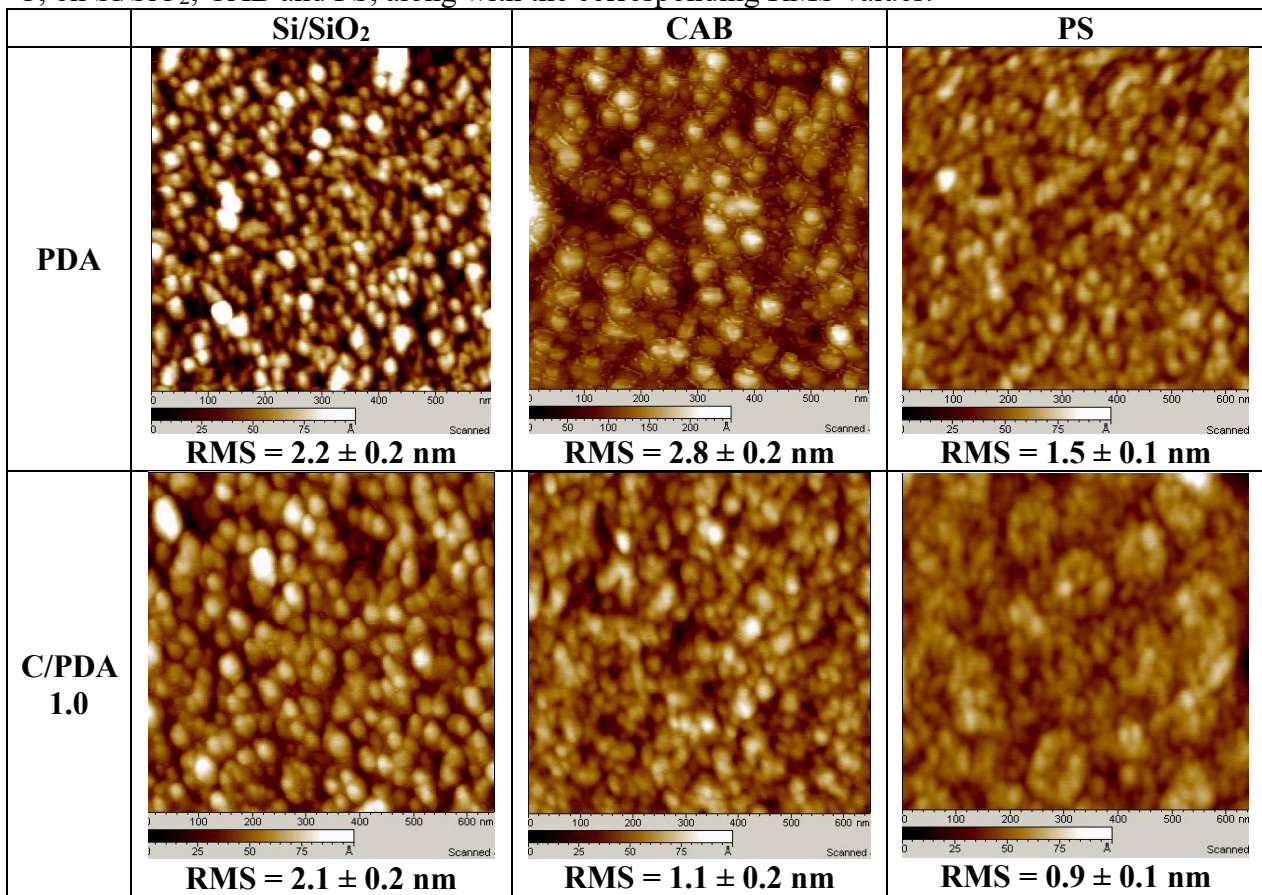


**0min 10min**

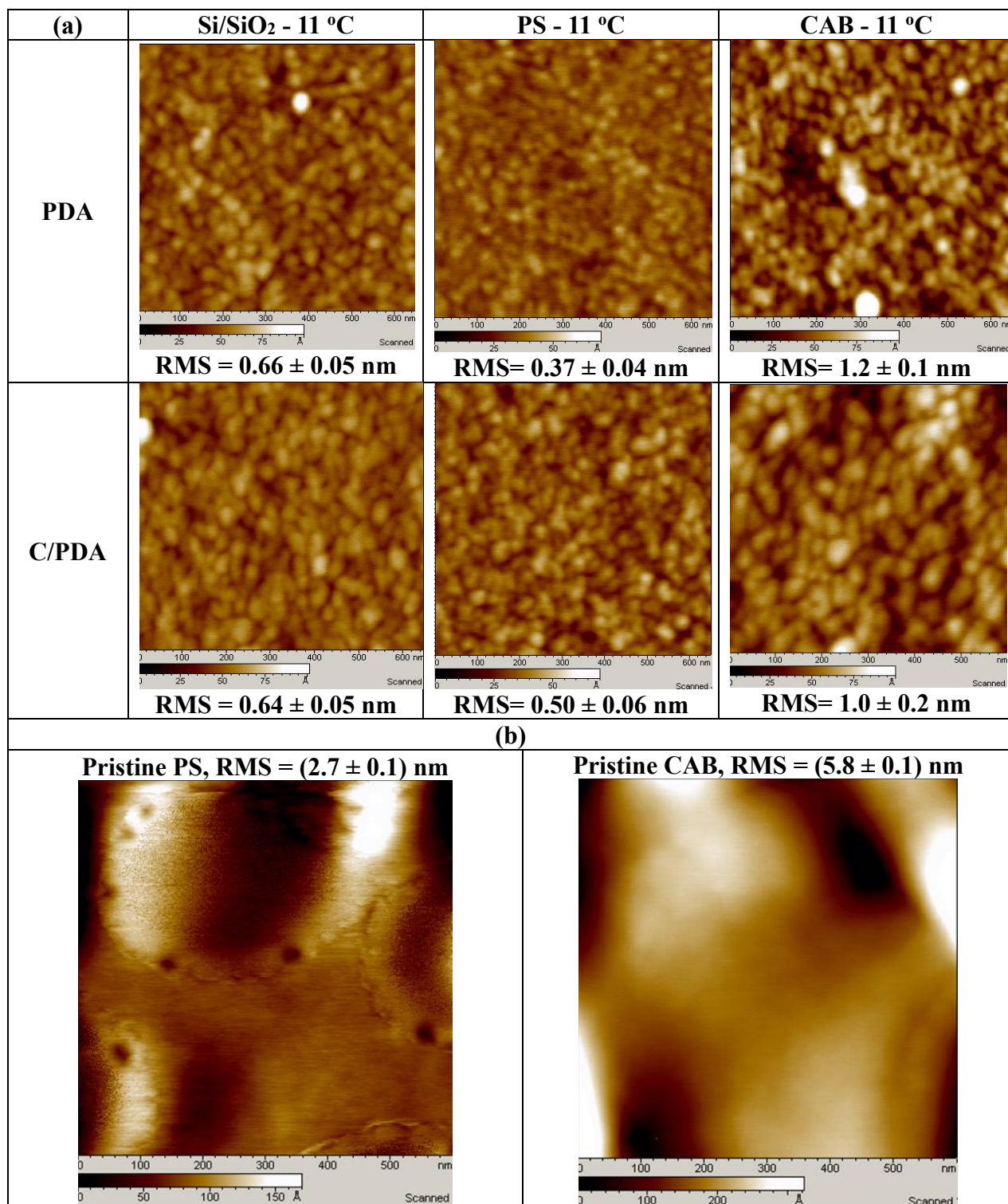
**0min 10min**

**0min 10min**

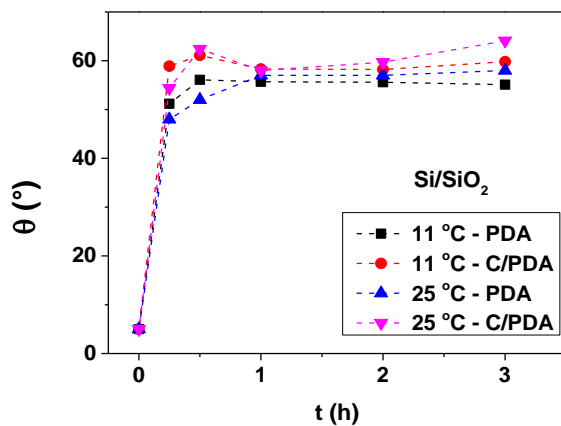
**SI10.** AFM images (600 nm x 600 nm) of PDA and C/PDA 1.0 after 2 h deposition at  $25 \pm 1$  °C, on Si/SiO<sub>2</sub>, CAB and PS, along with the corresponding RMS values.



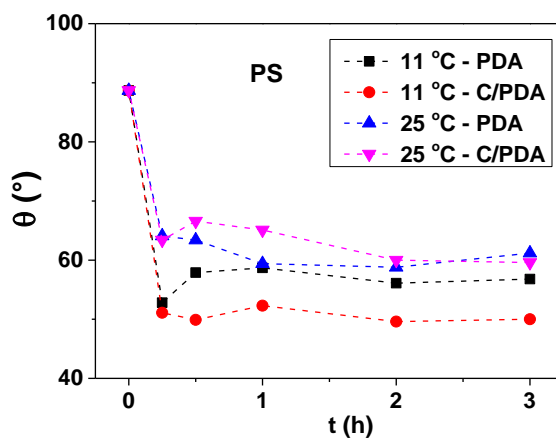
**SI11.** AFM images (600 nm x 600 nm) of (a) PDA and C/PDA 1.0 after 2 h deposition at  $11 \pm 1$  °C, on Si/SiO<sub>2</sub>, PS and CAB, and (b) pristine PS and CAB surfaces, along with the corresponding RMS values.



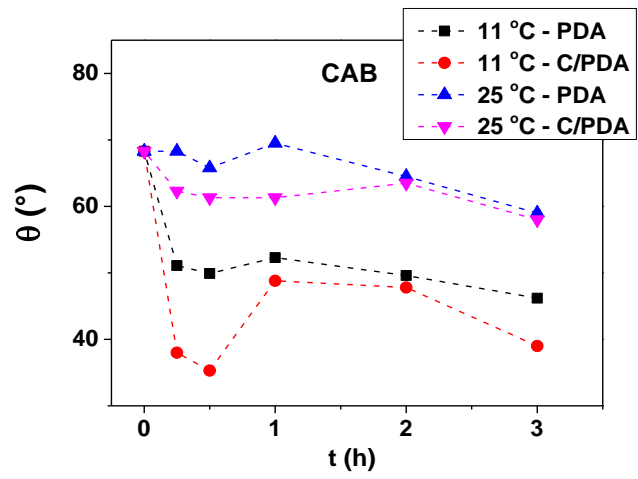
**SI12.** Contact angle ( $\theta$ ) values determined for water droplet (10  $\mu\text{L}$ ) on PDA and C/PDA deposited on (a) Si/SiO<sub>2</sub>, (b) PS and (c) CAB films, at  $11 \pm 1$  °C, as a function of deposition time.



(a)

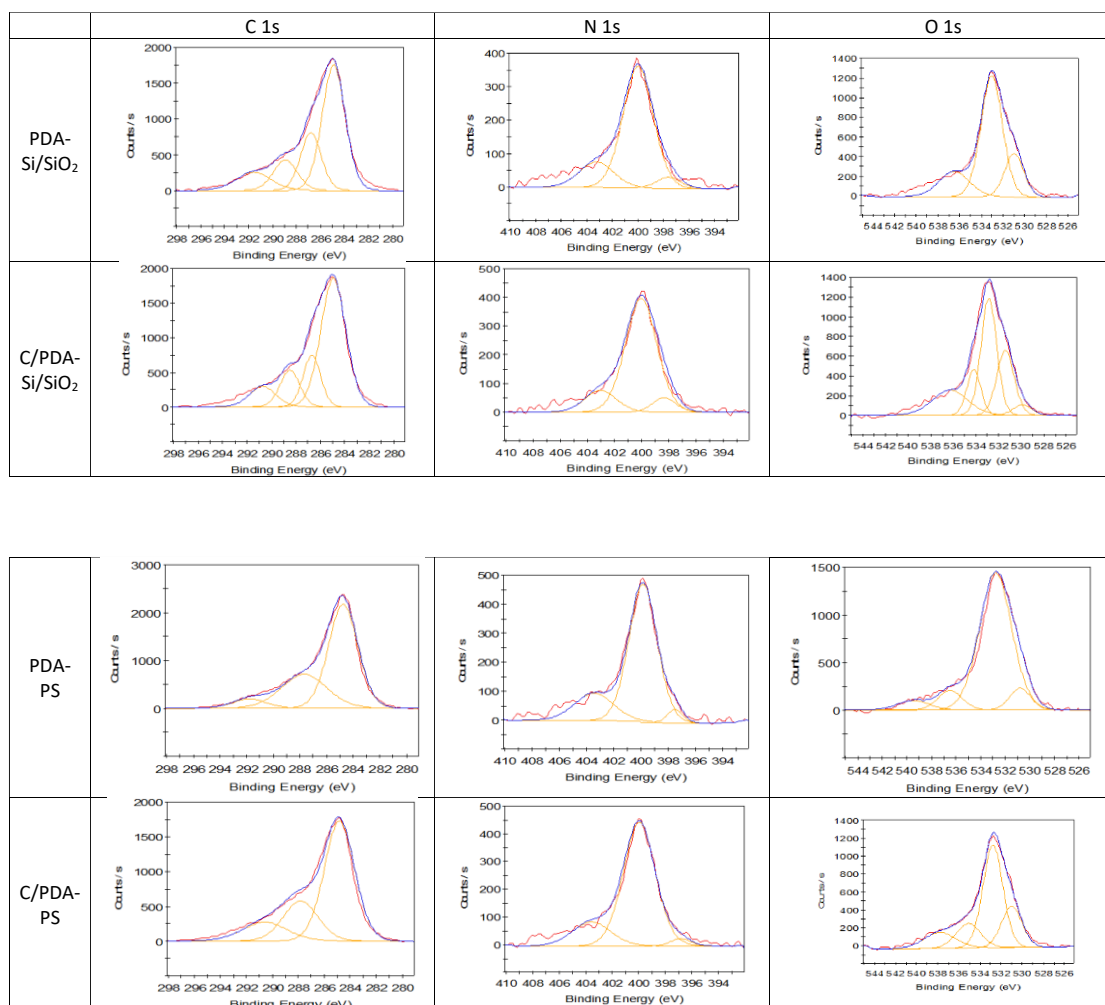


(b)



(c)

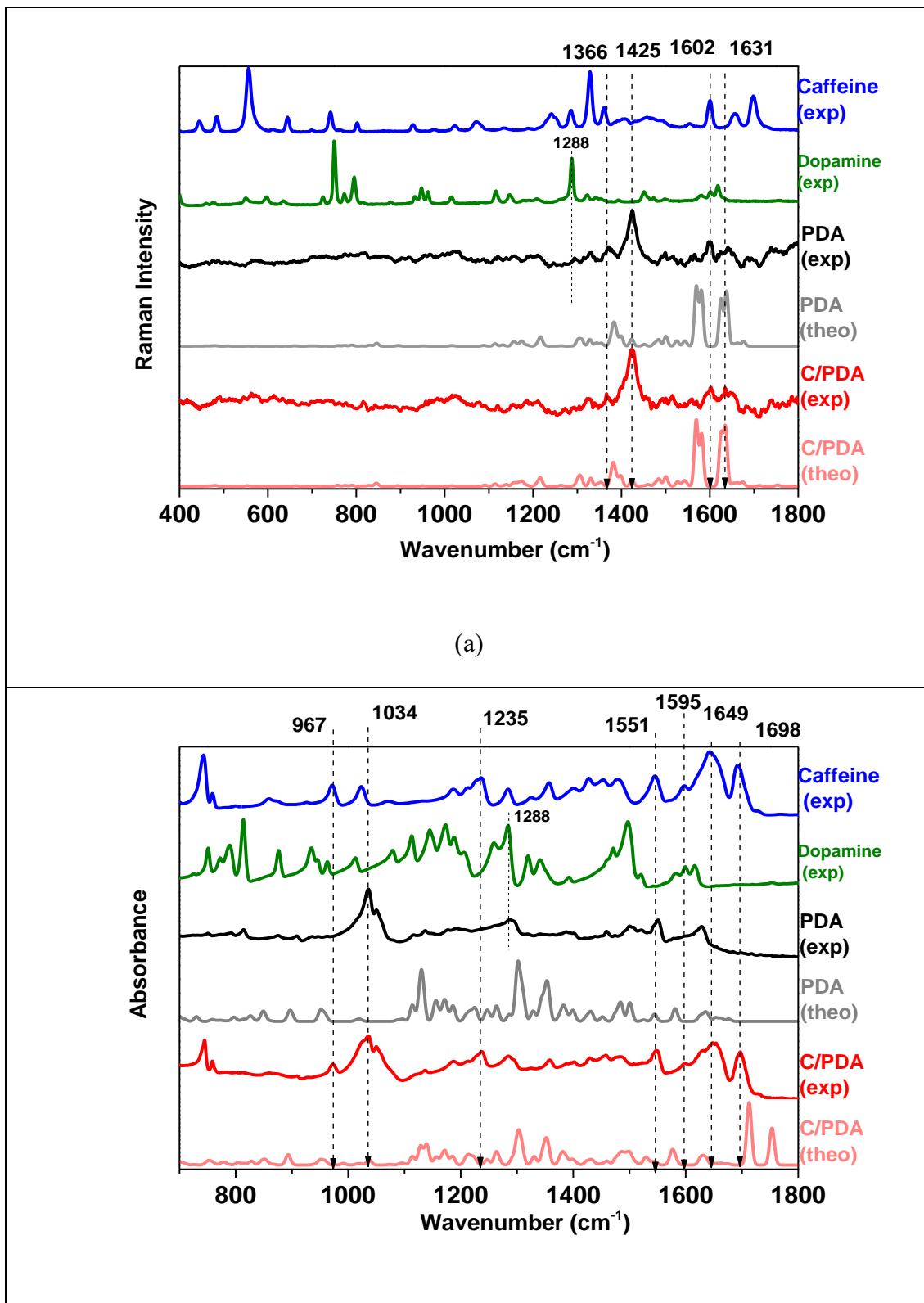
**SI13.** XPS high-resolution spectra of C 1s, N 1s and O 1s and their deconvolutions for PDA and C/PDA deposited on Si/SiO<sub>2</sub> and PS, 24 h, 25 ± 1 °C.



**SI14.** Binding energy of elements in chemical functions of PDA and C/PDA deposited (24 h) at 25 ± 1 °C on Si/SiO<sub>2</sub> and PS. The peak assignments followed references 36, 38-41.

	Peak position, eV	PDA on Si/SiO <sub>2</sub> (%)	C/PDA on Si/SiO <sub>2</sub> (%)	PDA on PS (%)	C/PDA on PS (%)
<b>C 1s</b>	284.8 ± 0.1 (C=C, C-C, CH <sub>x</sub> )	41	44	48	50
	286.8 ± 0.1 (C-O)	17	12 ↓	-	-
	288.0 ± 0.1 (C=O-NH-C, amide or O=C-O <sup>-</sup> carboxylate)	-	-	22	14 ↓
	288.7 ± 0.2 (C=O-OH, carboxylic acid)	10	9.9	-	-
	290.5-291.6 (π π* shake up)	9.0	6.3 ↓	4.7	10 ↑
<b>N 1s</b>	398.5 ± 0.2 (=N-R, imino groups)	0.59	0.74	-	-
	400 ± 0.1 (substituted amine R-NH-R or indole groups)	1.7	4.4 ↑	3.8	4.1
	401.8 ± 0.2 (R-NH <sub>3</sub> <sup>+</sup> )	0.72	2.2	-	-
	402.7 (C-NH <sub>3</sub> <sup>+</sup> )	-	-	-	0.75
<b>O 1s</b>	531.2 ± 0.4 (C=O, aromatic or O=C-N)	4.0	4.7	1.6	3.2 ↑
	532.9 ± 0.2 (C-OH)	13.2	8.8 ↓	16	11 ↓
	534.2 (-COOH)	-	2.7	-	-
	535-536.5 (adsorbed H <sub>2</sub> O)	2.9	3.8	1.7	3.7
	537.8 (adsorbed H <sub>2</sub> O)	-	-	-	2.6
	539.5 (-OH, aromatic)	-	-	1.1	-

SI15. Experimental and theoretical (a) Raman and (b) FTIR spectra determined for caffeine, dopamine, PDA and C/PDA.



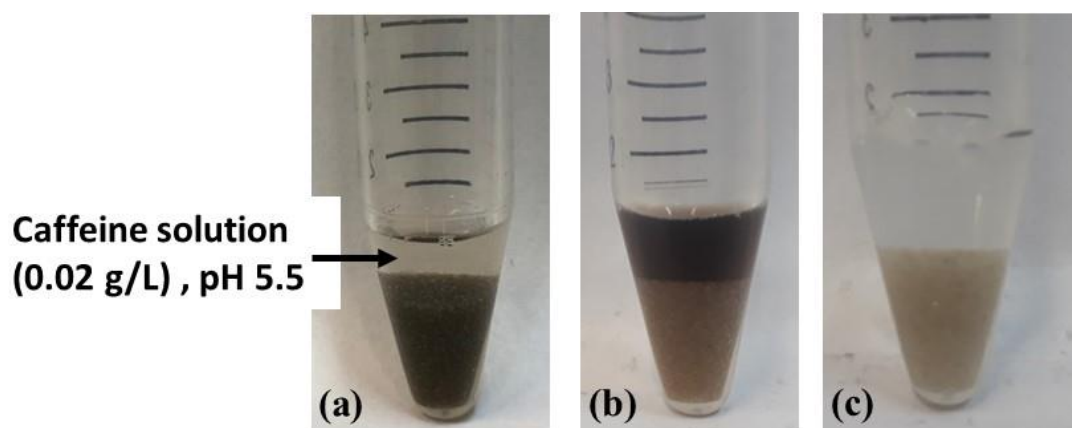


(b)

**SI16:** Assignment of main bands observed in the experimental FTIR and Raman spectra shown in **Figure 4a**.

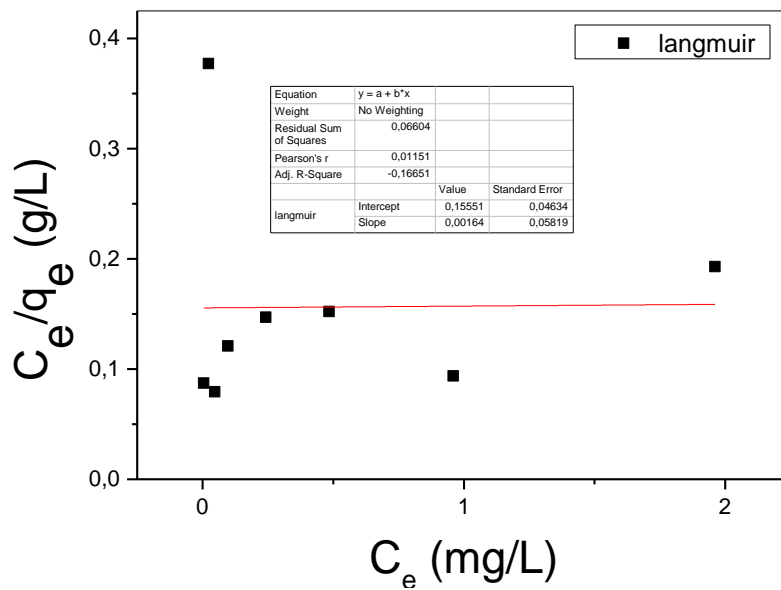
Wavenumber (cm <sup>-1</sup> )	Assignment
1698 (FTIR)	C=O symmetric stretching (caffeine)
1649 (FTIR)	C=O asymmetric stretching ( caffeine )
1631 (Raman)	C=C stretching (PDA)
1602 (Raman)	C=C bending and C-N bending (PDA)
1551 (FTIR)	C=C stretching ( caffeine )
1425 (Raman)	O-H bending, C=C stretching (PDA)
1288 (FTIR and Raman)	Catecholic C-OH stretching (dopamine)

**SI17** – PDA coated glass microbeads (~ 200 μm) (a) just after adding them to caffeine solution 0.02 g/L (pH 5.5), (b) after 24 h contact with caffeine solution and (c) after rinsing the microbeads with MilliQ water.

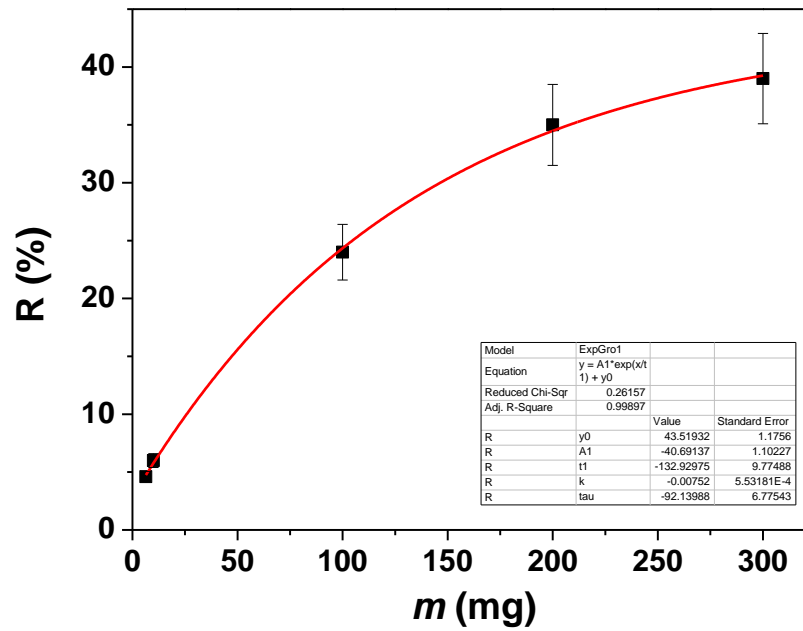


**SI18.** Lack of fit of experimental data to the Langmuir model.

<b>Langmuir</b>	$q_e = \frac{q_{\max}K_L}{1 + K_L C_e}$ <p><math>K_L =</math> adsorption equilibrium constant</p> <p>Linearized form: <math>\frac{C_e}{q_e} = \frac{C_e}{q_{\max}} + \frac{1}{q_{\max}K_L}</math></p> <p>Plot: <math>\frac{C_e}{q_e}</math> as a function of <math>C_e</math></p>
-----------------	---



**SI19.** Removal capacity,  $R$  (%), as a function of CAB/PDA microbeads mass ( $m$ ), for initial concentration ( $C_0$ ) of caffeine at  $1.0 \text{ g L}^{-1}$ .

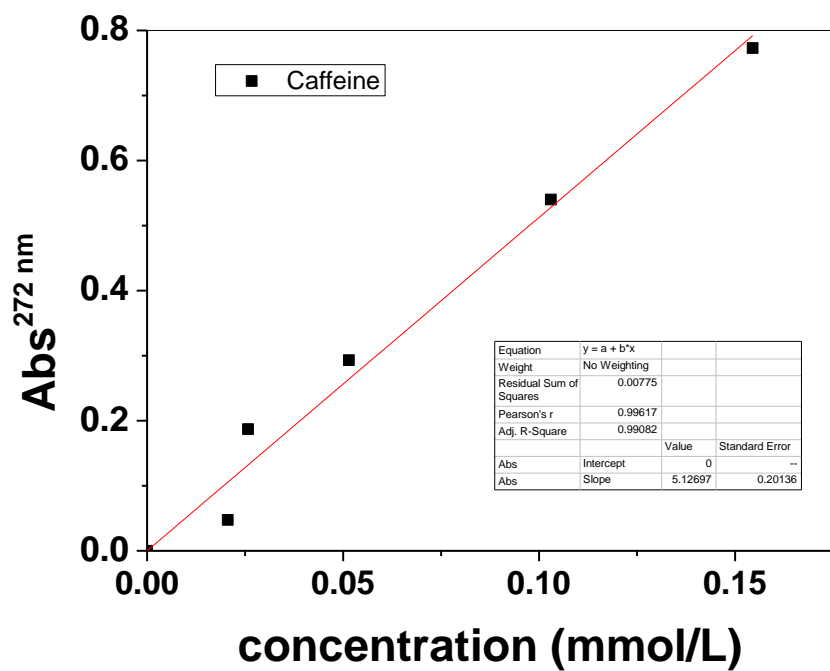


### 9.2.2 Chapter 2:

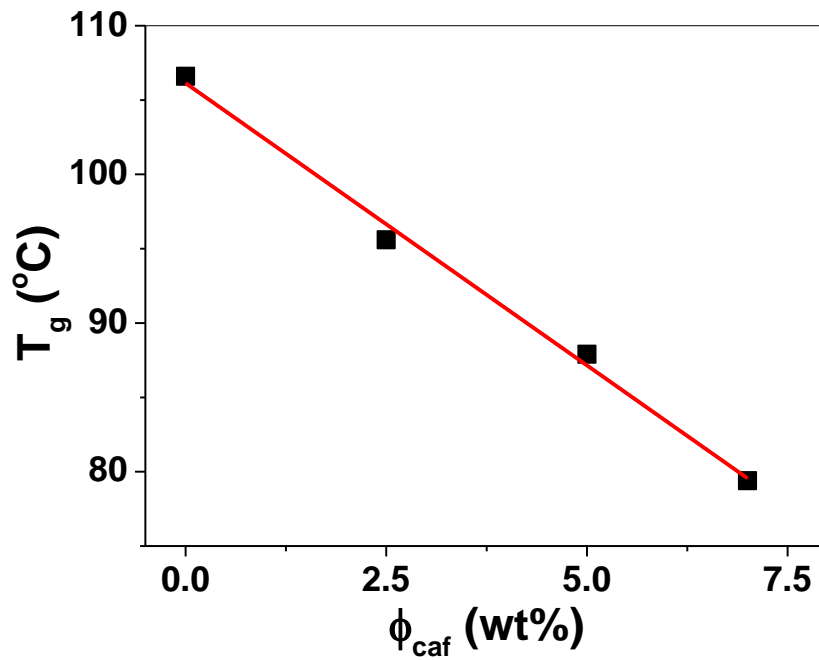
**SM1.** Concentrations of CAB and caffeine in the solutions used to prepare the micrometric films and the caffeine content ( $\phi_{\text{caf}}$ ) in the resulting films.

<b>CAB (g L<sup>-1</sup>)</b>	<b>caf (g L<sup>-1</sup>)</b>	<b><math>\phi_{\text{af}}</math> (wt%)</b>
20	0.02	0.1
20	0.51	2.5
20	1.05	5.0
20	1.5	7.0
20	2.2	10.0
20	3.5	14.9
20	5.0	20.0

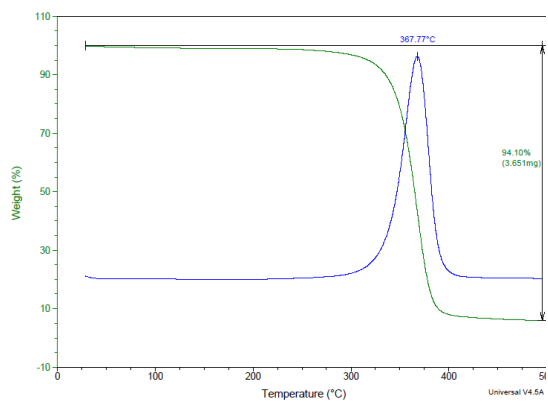
SM2. Calibration curve of caffeine at 272 nm.



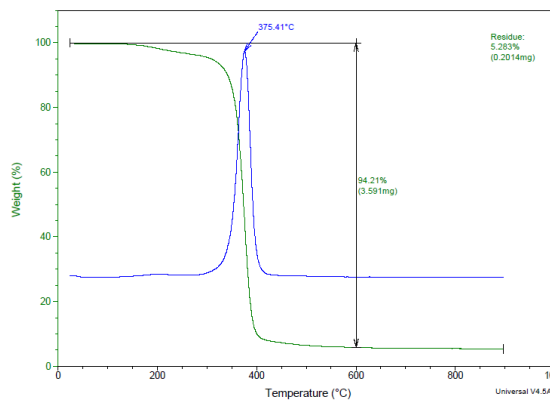
**SM3.** Glass transition temperature ( $T_g$ ) values determined for pure CAB and CAB/caf films as a function of caffeine content ( $\phi_{caf}$ ). The red line corresponds to the linear fit  $y = 106.1 - 3.8x$ ,  $R^2 = 0.9929$ . The experimental data are mean values of duplicates, with standard deviations below 3%.



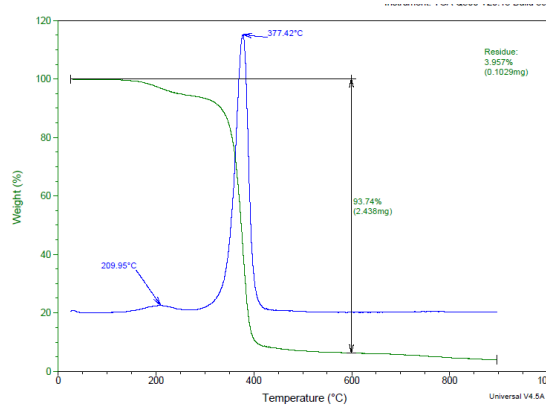
**SM4.** Thermogravimetric curves and the corresponding 1<sup>st</sup> derivatives determined for (a) pure CAB, (b) CAB/caf 2.5 wt%, (c) CAB/caf 5 wt% and (d) CAB/caf 7 wt% films



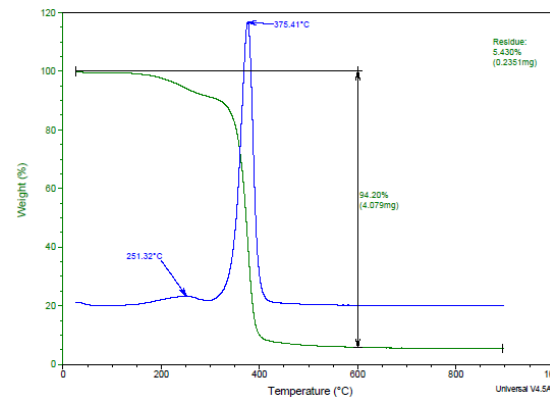
(a)



(b)

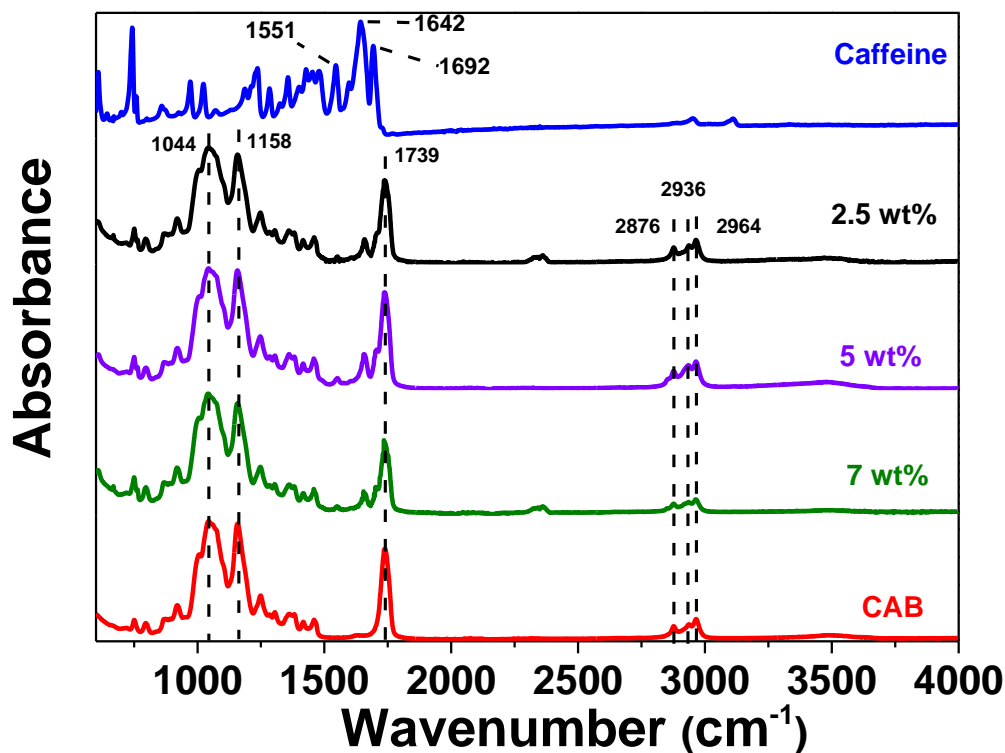


(c)



(d)

**SM5.** FTIR-ATR spectra obtained for pure caffeine, pure CAB (powder), CAB/caf 2.5 wt%, CAB/caf 5 wt% and CAB/caf 7 wt% films, in the spectral range from 600  $\text{cm}^{-1}$  to 4000  $\text{cm}^{-1}$ .



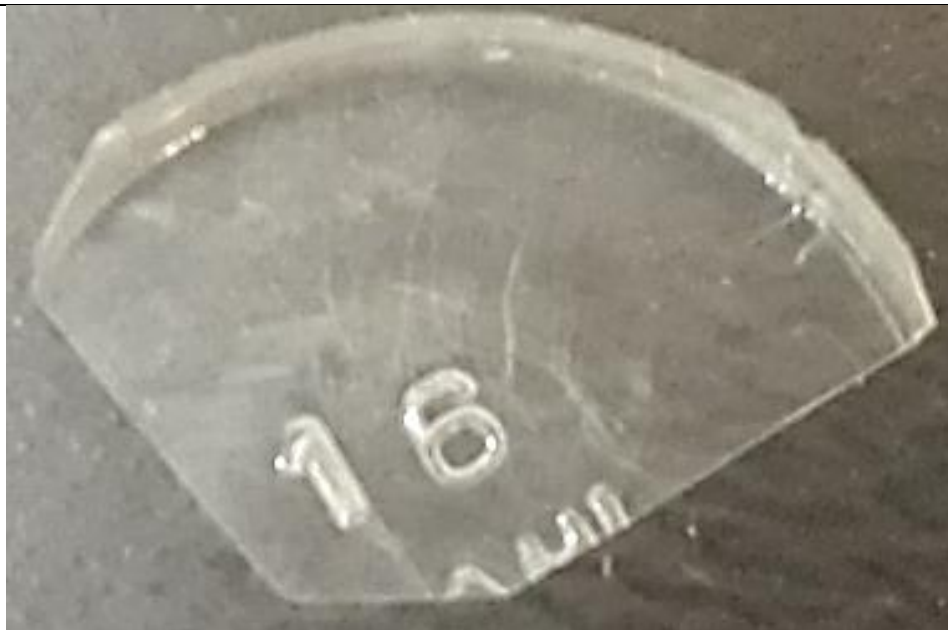
Bands assignment related to the FTIR-ATR spectra of pure CAB films, neat caffeine powder, CAB/caf films. The figures in the brackets represent the wavenumber increase relative to pure caffeine.

Wavenumber ( $\text{cm}^{-1}$ ), assignment	Systems
$\sim 1000 - 1200$ , glucosidic ring vibrations	CAB, CAB/caf films
1551, C=C ring stretch	Caffeine powder
1642, stretch of conjugated C=O(6)	Caffeine powder
1654, stretch of conjugated C=O(6) [+12]	CAB/caf 7 wt%
1657, stretch of conjugated C=O(6) [+15]	CAB/caf 5 wt%
1658, stretch of conjugated C=O(6) [+16]	CAB/caf 2.5 wt%
1692, stretch of isolated C=O(2)	Caffeine powder
1707, stretch of isolated C=O(2) [+15]	CAB/caf films



1739, stretch C=O	CAB, CAB/caf films
2936, asymmetric stretch CH <sub>2</sub>	CAB, CAB/caf films
2876, symmetric stretch CH <sub>3</sub>	CAB, CAB/caf films
2964, asymmetric stretch CH <sub>3</sub>	CAB, CAB/caf films

**SM6.** Photographs of (a) CAB/caf 2.5 wt% films and (b) CAB/caf 7 wt% films and after 48 h release, at pH 7.4.

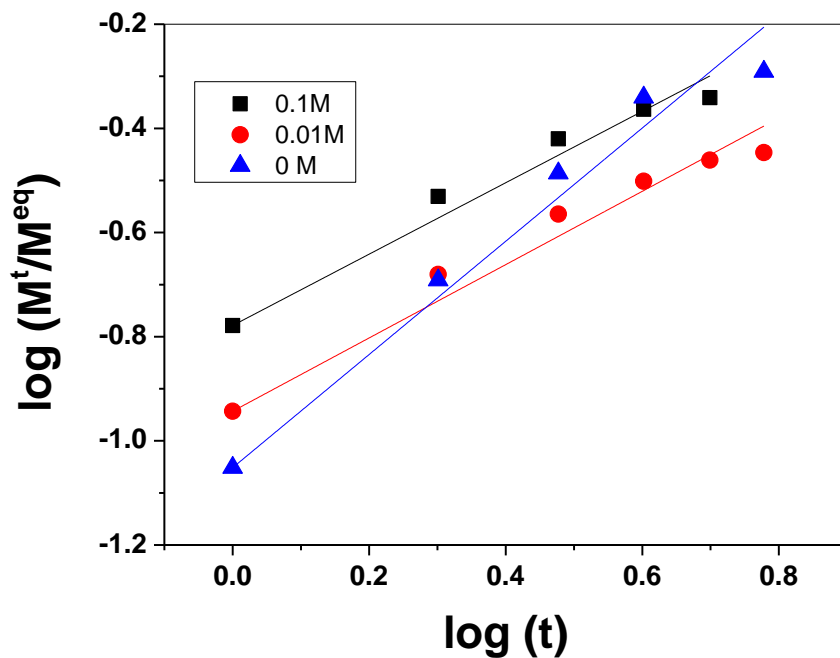


**(a)**



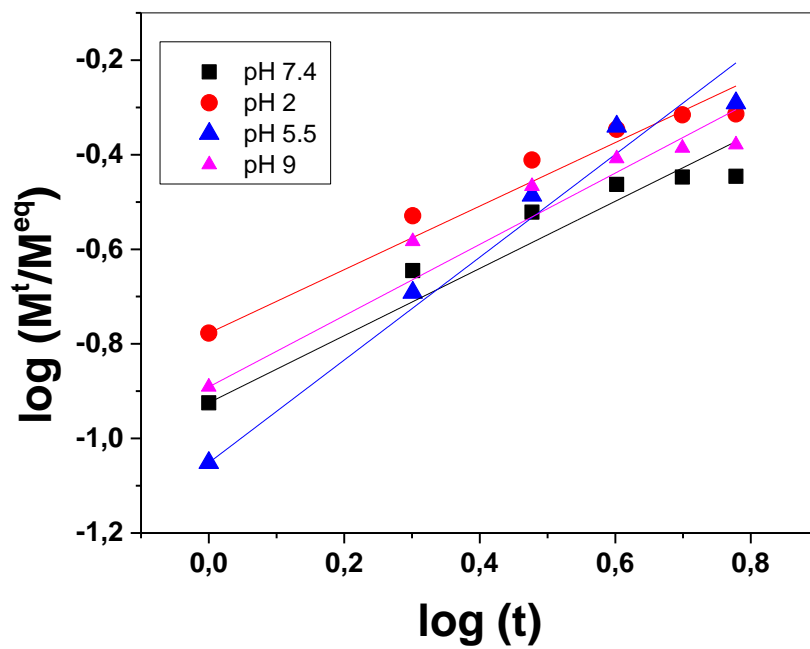
**(b)**

SM7. Fittings of caffeine release from CAB/caf 5 wt% with Korsmeyer-Peppas empirical model at different (a) ionic strength and (b) pH.



(a)

[NaCl] (M)	0.1	0.01	0
R <sup>2</sup>	0.9958	0.9962	0.9915
n	0.686	0.704	1.09

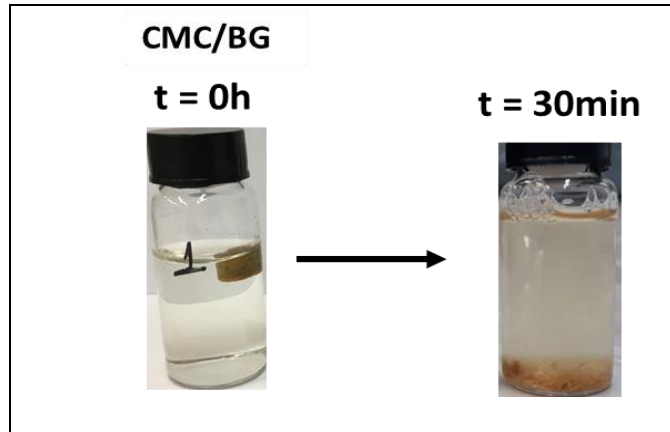


(b)

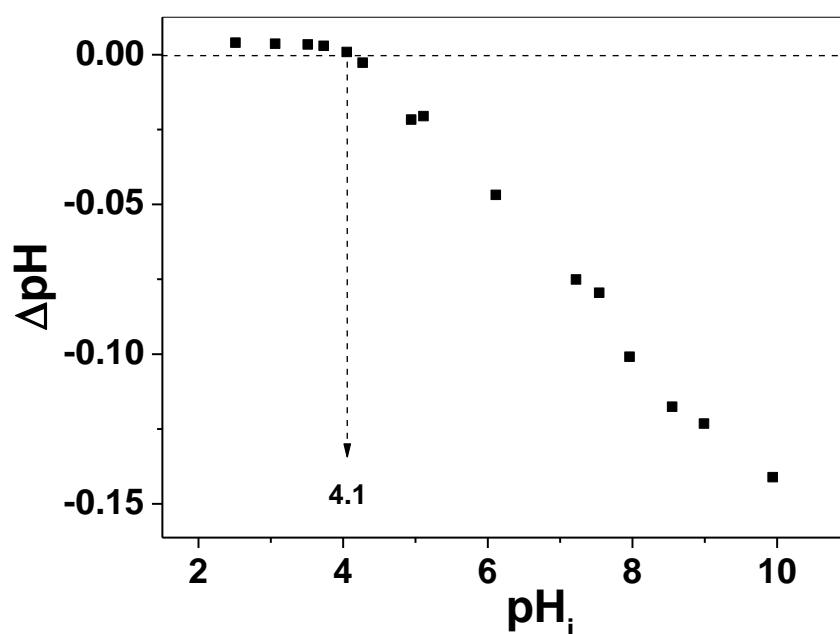
pH	2	5.5	7.4	9
$R^2$	0.9926	0.9915	0.9914	0.9883
n	0.672	1.09	0.710	0.754

### 9.2.3 Chapter 4

**SM1.** Photographs of CMC/BG adsorbent after 30 min under shaking in aqueous medium at pH 5.5.



**SM2. Determination of pzc by titration.** CMC/BG/PDA adsorbents (~ 35 mg) were inserted in aqueous media with pH adjusted to an initial pH value of 2.51, 3.06, 3.51, 3.73, 4.05, 4.27, 4.94, 5.11, 6.11, 7.22, 7.54, 7.74, 7.96, 8.55, 8.99 or 9.94 using either 0.1 mol/L HCl or 0.1 mol/L NaOH and a Digimed pHmeter. Each vial was shaken for 24 h, at  $(24 \pm 1)$  °C. After that, the final pH of each medium was measured. The  $\Delta\text{pH}$  (the difference between final and initial pH) values were normalized by the mass of the corresponding adsorbent, then plotted against the initial pH values. The initial pH at which  $\Delta\text{pH}$  is zero was taken to be the PZC (Mahmood et al., 2011)



### SM3. Specification of ICP-OES set up.

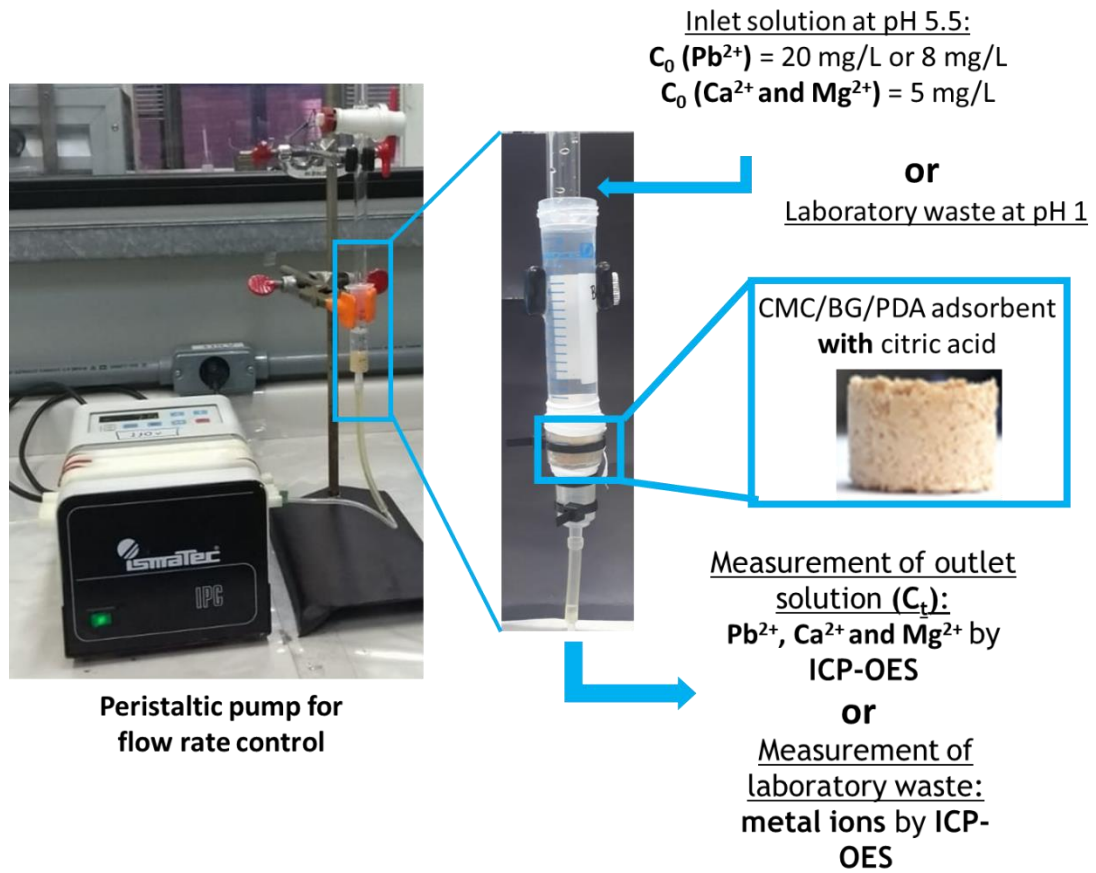
An optical emission spectrometer, model iCAP 7400 Duo, with radial and axial view, CID (Charge Injection Device) detector, which allows coverage wavelength from 166.4 to 847.0 nm a focal length of 383 mm that provides an optical resolution from 19 pm to 200 nm. Echelle polychromator with  $52.91 \text{ mm}^{-1}$  lines and 27.12 MHz radiofrequency sources, being able to adjust the applied power from 750 to 1350 W. Argon (99.998% v v<sup>-1</sup>) was used to generate and maintain the plasma and to aerosol introduction.

#### *Instrumental set up of ICP OES for Pb determination*

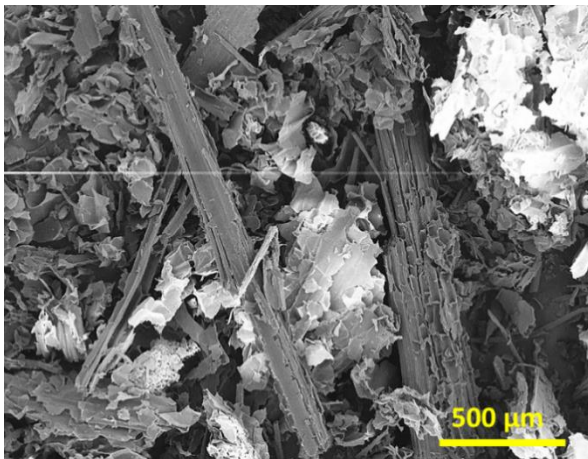
Parameter	Selected condition
Power supply	1350 W
Nebulizer	Meinhard
Spray chamber	Cyclonic
Plasma gas-flow	12 L min <sup>-1</sup>
Auxiliary gas-flow	0,2 L min <sup>-1</sup>
Nebulizer gas-flow	0,5 L min <sup>-1</sup>
Sample introduction	1.5 - 3 mL min <sup>-1</sup>
Wavelength	Pb (I) 220.353 nm

(I) Ionic emission

SM4. Photographs of the experimental setup used for fixed-bed column adsorption studies.

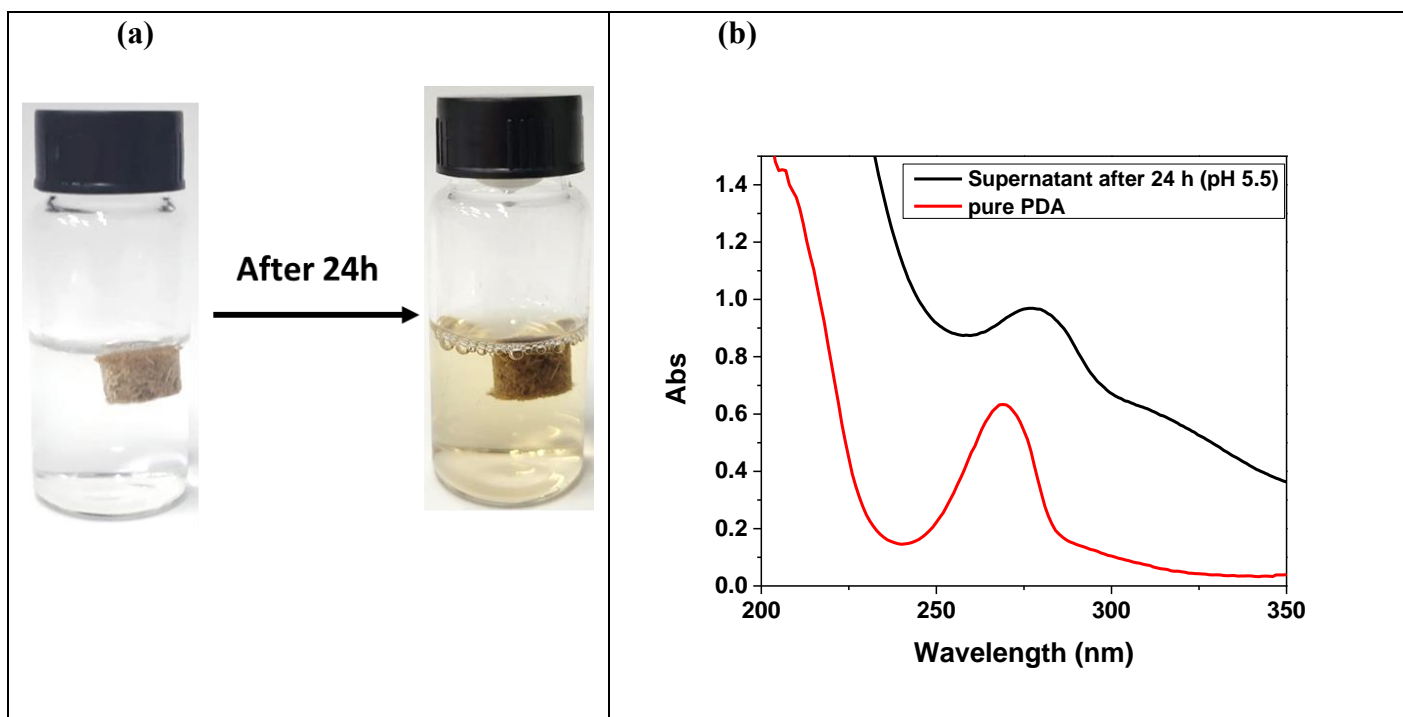


SM5. Typical SEM image of BG microparticles.



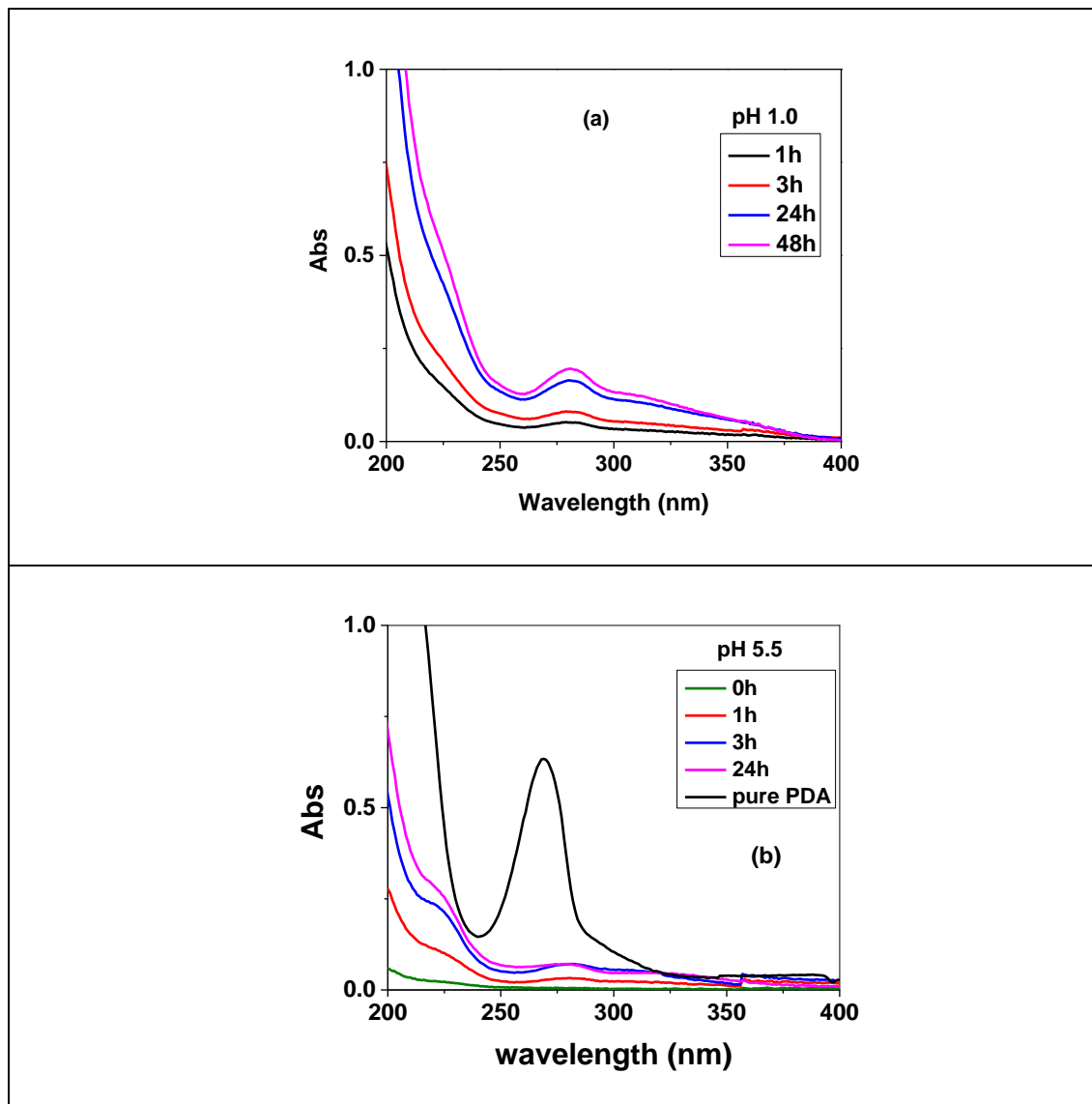


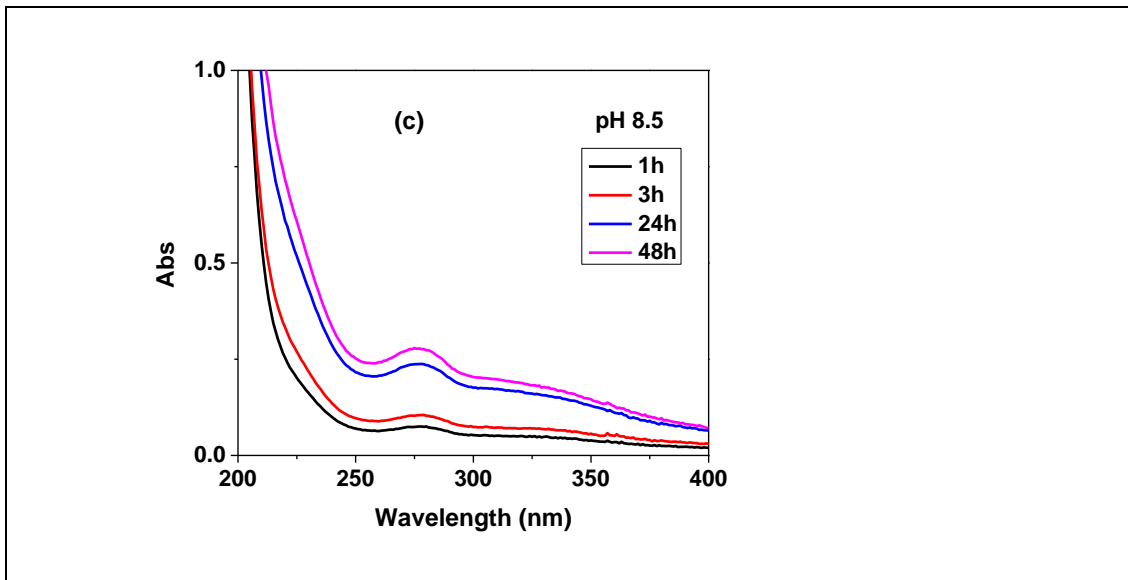
**SM6. (a)** Photographs of CMC/BG/PDA adsorbent without citric acid (crosslinker) in aqueous medium at pH 5.5, before and after 24 h under constant stirring. The adsorbent became darker due to the oxidation of DOPA to PDA and the medium became yellowish, indicating the release of PDA. **(b)** UV-Vis spectra of pure PDA (red line) and the supernatant (black line) after 24 h contact in water at pH 5.5.



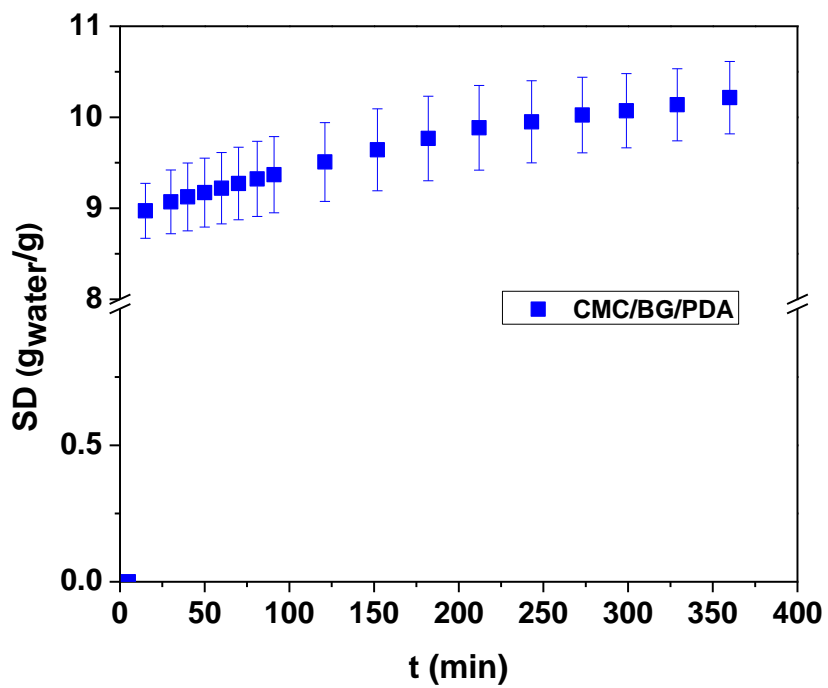
**SM7.** UV spectra obtained for the supernatants after contact with CMC/BG/PDA adsorbents

at (a) pH 1, (b) pH 5.5 and (c) pH 8.5, for 0 h, 1 h, 3 h, 24 h and 48 h.

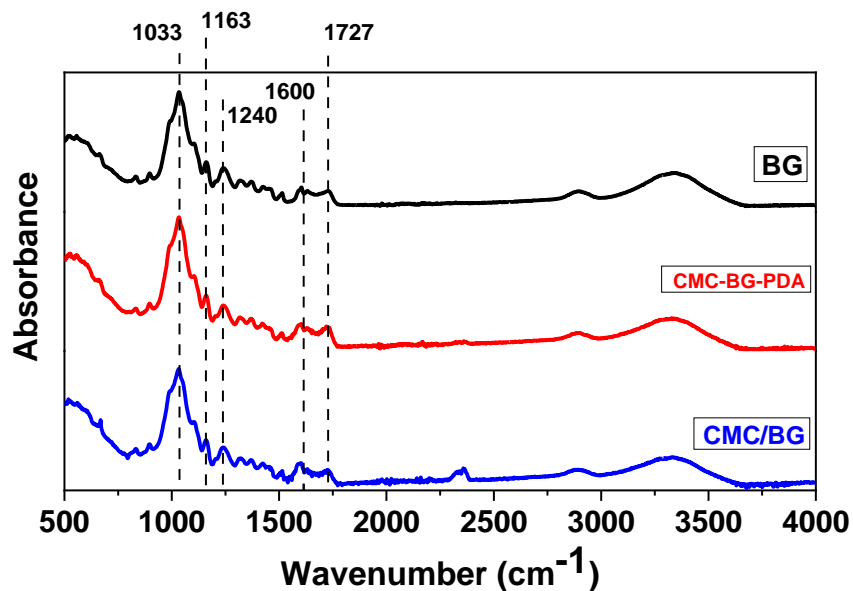




SM8. Swelling degree (SD) as a function of time determined at pH 5.5 for CMC/BG/PDA adsorbents.



**SM9. (a)** FTIR-ATR absorbance spectra of BG, CMC/BG and CMC/BG/PDA and **(b)** Assignment of the main bands observed in the spectra of the CMC/BG, CMC/BG/PDA adsorbents and BG microparticles.

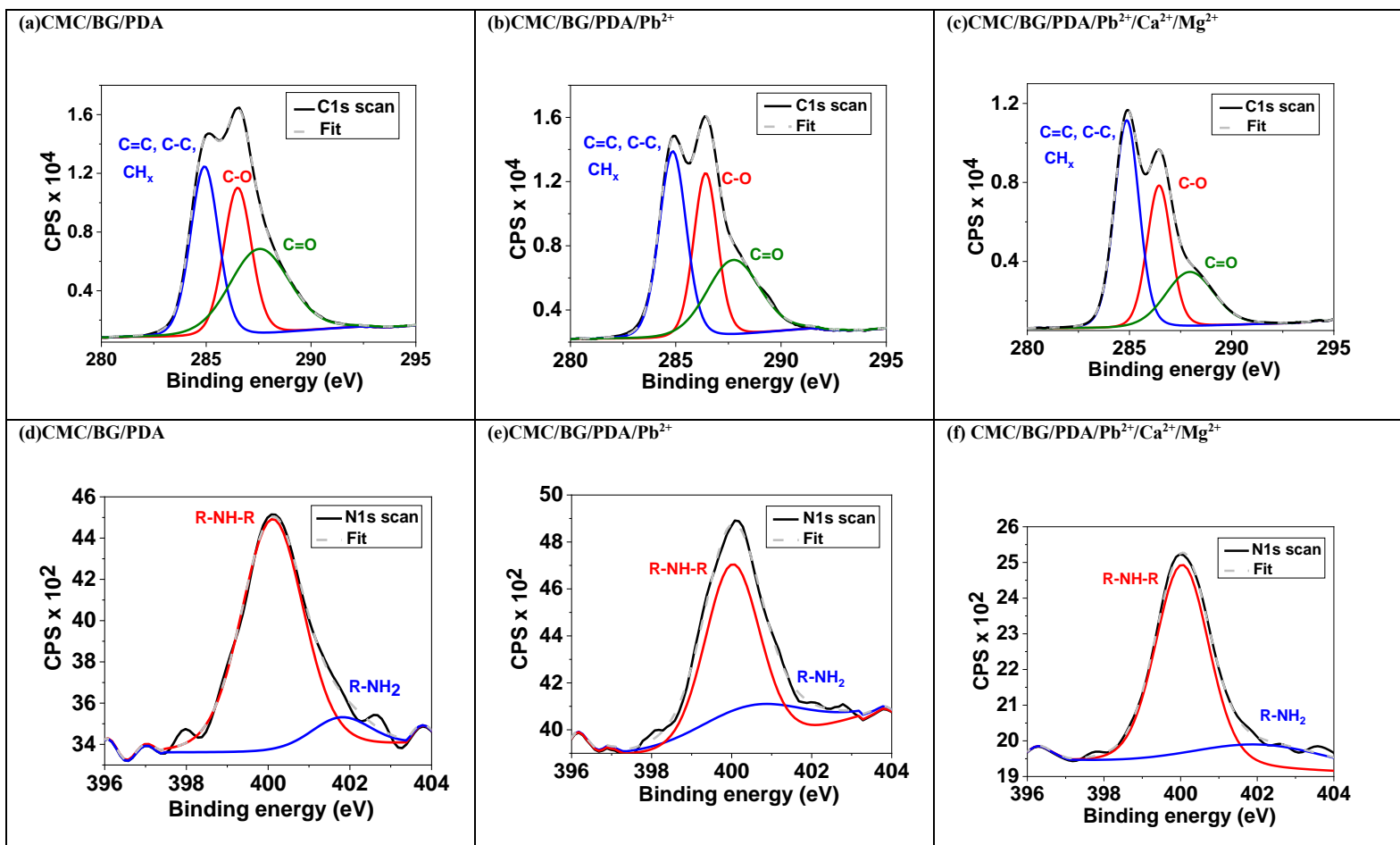


**(a)**

wavenumber (cm <sup>-1</sup> )	Assignment
1727	C=O stretching (carboxylic groups - hemicellulose and ester linkages)
1600	C=C stretching, aromatic ring (lignin)
1240	C-O stretching (phenolic-lignin groups)
1163	C-O-C stretching
1033	C-O/C-C stretching

**(b)**

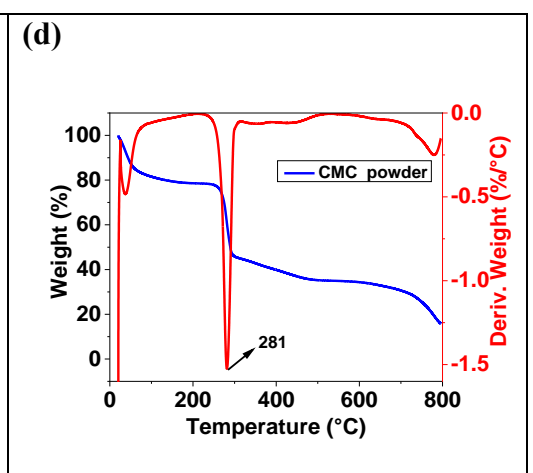
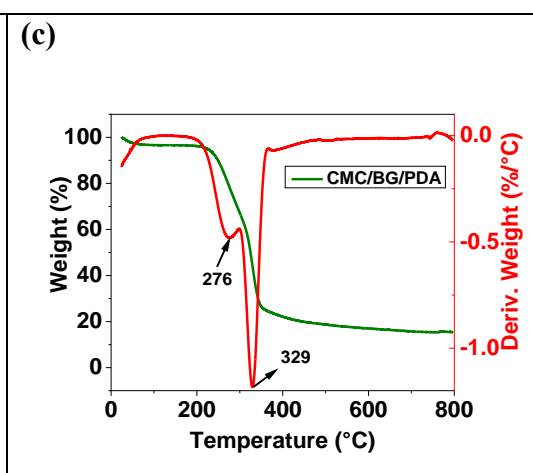
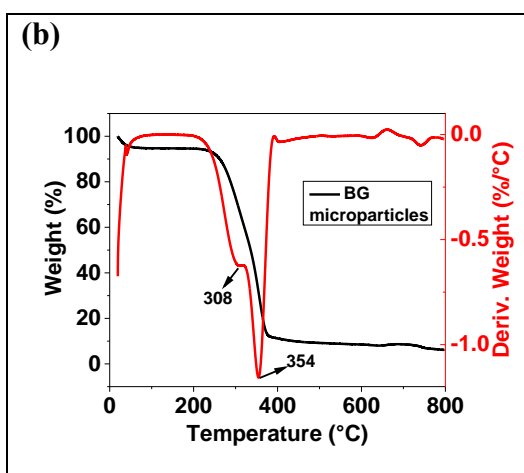
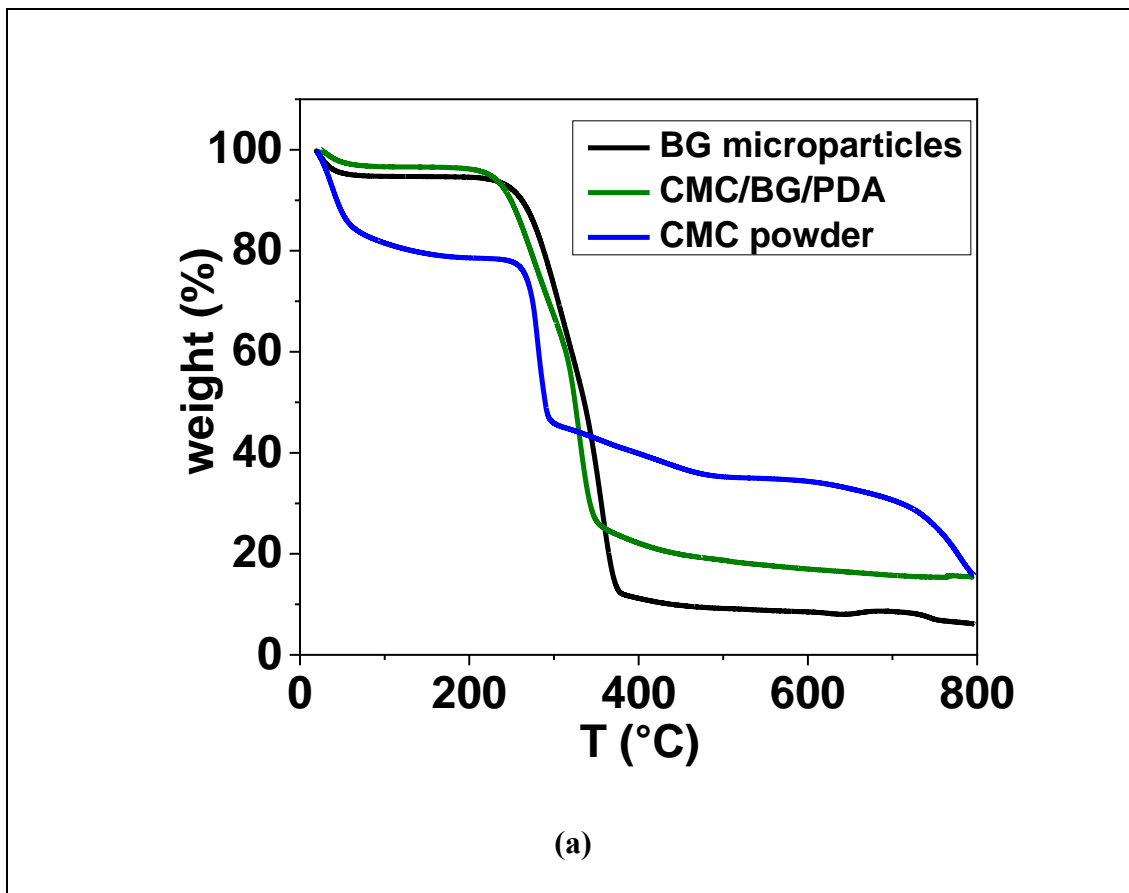
**SM10.** XPS high resolution spectra with the corresponding deconvolutions of C 1s for (a) CMC/BG/PDA before adsorption, (b) after adsorption of  $Pb^{2+}$  in the absence and (c) in the presence of  $Ca^{2+}$  and  $Mg^{2+}$  ions; N 1s (d) before adsorption and after adsorption of  $Pb^{2+}$  (e) in the absence and (f) in the presence of  $Ca^{2+}$  and  $Mg^{2+}$  ions



**SM11.** Table of binding energy (BE, eV) and area (%) values corresponding to the deconvoluted peaks and references used for the assignments of the C 1s and N 1s binding energy values. The BE and area values are mean values with standard deviations from measurements in three different points on the surface, for this reason, the sum of areas might larger than 100%.

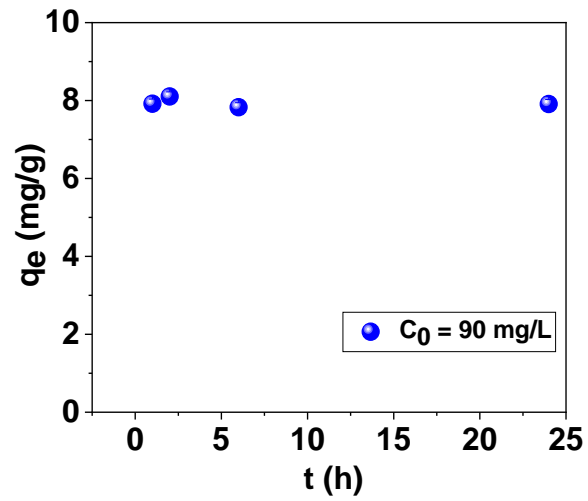
	<b>Peak position, eV</b>	<b>Area (%)</b>	<b>Area (%)</b>	<b>Area (%)</b>
		<b>CMC/BG/PDA</b>	<b>CMC/BG/PDA/Pb<sup>2+</sup></b>	<b>CMC/BG/PDA/ Pb<sup>2+</sup> Ca<sup>2+</sup> Mg<sup>2+</sup></b>
<b>C 1s</b>	<b>285.0 ± 0.1 (C=C, C-C, CH<sub>x</sub>)</b>	38 ± 7	35 ± 3	58 ± 2
	<b>286.6 ± 0.2 (C-O</b>	26 ± 3	32 ± 2	30 ± 5
	<b>288.0 ± 0.2 (C=O- NH-C, amide or O=C-O<sup>-</sup> carboxylate)</b>	28 ± 15	30 ± 3	20 ± 5
<b>N 1s</b>	<b>400.2 ± 0.2 (substituted amine R-NH-R or indole groups)</b>	62 ± 14	83 ± 3	79 ± 3
	<b>402.1 ± 0.4 (R-NH<sub>2</sub>)</b>	12 ± 1	24 ± 3	15 ± 4

SM12. (a) Thermogravimetric curves of BG microparticles, CMC/BG/PDA and CMC powder. TG/DTG curves for (b) BG microparticles, (c) CMC/BG/PDA and (d) CMC powder.

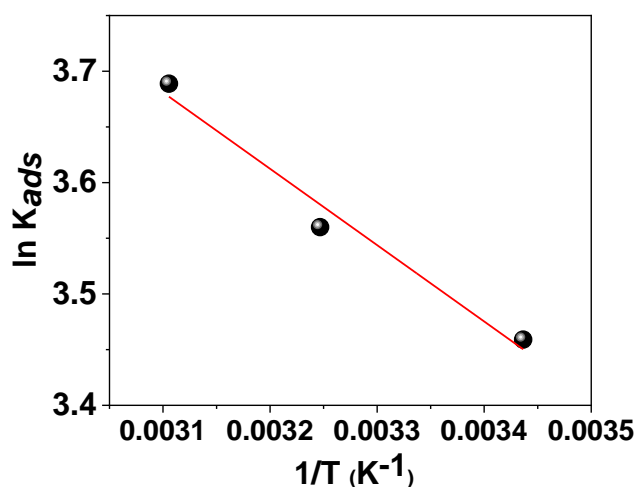




**SM13.** Adsorption kinetics experiments of  $\text{Pb}^{2+}$  ions ( $C_0 = 90 \text{ mg/L}$ ) on CMC/BG/PDA adsorbents ( $53 \pm 5 \text{ mg}$ ) performed at  $(23 \pm 1) \text{ }^\circ\text{C}$ , using  $V = 5 \text{ mL}$ .

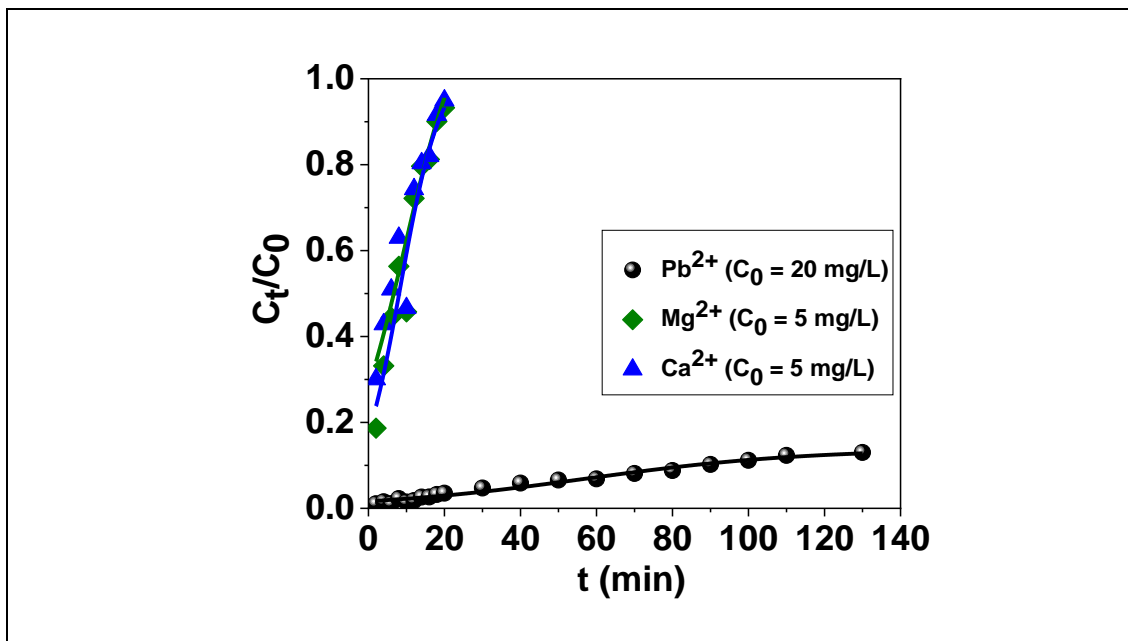


**SM14.** Dependence of  $\ln K_{ads}$  on  $1/T$  (van't Hof equation) determined for the adsorption of  $Pb^{2+}$  on CMC/BG/PDA adsorbents along with the linear fitting (red line). The slope and the intercept yielded the values of adsorption enthalpy change ( $-\Delta H_{ads}/R$ ) and entropy change ( $\Delta S_{ads}/R$ ), respectively.  $K_{ads}$ ,  $\Delta G_{ads}$ ,  $\Delta H_{ads}$  and  $\Delta S_{ads}$  values determined for the adsorption of  $Pb^{2+}$  on CMC/BG/PDA adsorbents



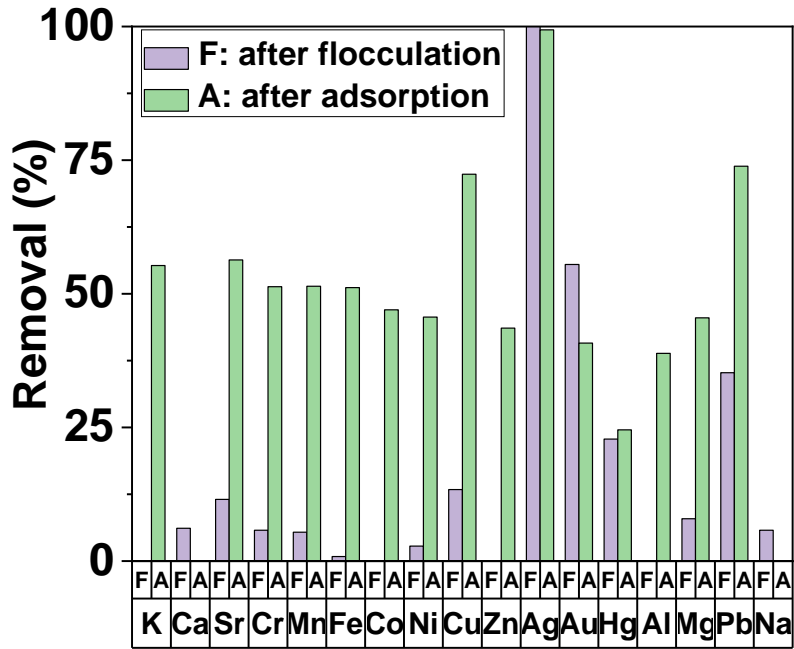
Temperature	$K_{ads}$ (L/mol)	$\Delta G_{ads}$ (kJ/mol)	$\Delta H_{ads}$ (kJ/mol)	$\Delta S_{ads}$ (J/K.mol)
18 °C (291 K)	31.8	-8.36	5.7	48.3
35 °C (308 K)	35.2	-9.18		
40 °C (313 K)	40.0	-9.42		

**SM 15.** Breakthrough curves for  $\text{Pb}^{2+}$  ions on CMC/BG/PDA at pH 5.5 in the presence of the  $\text{Ca}^{2+}$  and  $\text{Mg}^{2+}$  ions. Column operational conditions  $\nu = 0.5 \text{ mL/min}$  and mass of adsorbent = 240 mg.



**SM16.** Removal% after flocculation with PDDA (light purple) followed by 3 adsorption steps

(light green).



## 9.3 Curricular Summary

### PERSONAL DATA

**Name:** Laíse Moura Furtado.

**Date and place of birth:** 03/06/1995, Natal, Rio Grande Norte, Brasil.

### EDUCATION BACKGROUND

#### **B.S. in Chemistry (2013-2016)**

Institute of Chemistry, Federal University of Rio Grande do Norte, Natal, Rio Grande Norte, Brasil.

### MOST RELEVANT SCIENTIFIC RESULTS

Furtado, L. M.; Yee, M.; Fernandes, R.; Valera, T. S.; Itri, R.; Petri, D. F.S. Rheological and mechanical properties of hydroxypropyl methylcellulose-based hydrogels and cryogels controlled by AOT and SDS micelles. JOURNAL OF COLLOID AND INTERFACE SCIENCE, v. 648, p. 604-615, 2023.

Furtado, L. M.; Fuentes, D. P.; ANDO, R. A.; Oliveira, P. V.; Petri, D. F.S. Carboxymethyl cellulose/sugarcane bagasse/polydopamine adsorbents for efficient removal of Pb<sup>2+</sup> ions from synthetic and undergraduate laboratory wastes. JOURNAL OF CLEANER PRODUCTION, v. 380, p. 134969, 2022.

Dezotti, R. S.; Furtado, L. M.; Yee, M.; Valera, T. S.; Krishnasamy, B.; ANDO, R. A.; Petri, D. F.S. Tuning the Mechanical and Thermal Properties of Hydroxypropyl Methylcellulose Cryogels with the Aid of Surfactants. GELS, v. 7, p. 118-135, 2021.

Calheiros, T. F.; Furtado, L. M.; Carmona, A. M. R.; Ando, R. A.; Petri, D. F. S. Physicochemical and antifungal properties of waterborne polymer nanoparticles synthesized with caffeine. COLLOID AND POLYMER SCIENCE, v. 298, p. 341-353, 2020.

Furtado, L. M.; Hilmatu, K. C. P.; Krishnasamy, B.; Ando, R. A.; Petri, Denise F.S. Miscibility and sustained release of drug from cellulose acetate butyrate/caffeine films. JOURNAL OF DRUG DELIVERY SCIENCE AND TECHNOLOGY **JCR**, v. 55, p. 101472, 2019.

Furtado, L. M.; ANDO, Ando, R. A.; Petri, Denise F.S. Polydopamine-coated cellulose acetate butyrate microbeads for caffeine removal. JOURNAL OF MATERIALS SCIENCE **JCR**, v. 55, p. 3243-3258, 2019.